# UNIVERSITÀ DEGLI STUDI DI TRIESTE

## XXXVII CICLO DEL DOTTORATO DI RICERCA IN CHIMICA

# Rheological and Low Field NMR properties of hepatic tissue and polymeric gels in the study of deubiquitinase inhibitors against liver fibrosis

Settore scientifico-disciplinare: **ING-IND/24**


DOTTORANDO / A
**ALICE BIASIN**

COORDINATORE
**PROF. ENZO ALESSIO**

SUPERVISORE DI TESI
**PROF. MARIO GRASSI**

CO-SUPERVISORE DI TESI
**PROF. GABRIELE GRASSI**

CO-SUPERVISORE DI TESI
**DOTT.SSA BARBARA TOFFOLI**

CO-SUPERVISORE DI TESI
**DOTT.SSA MICHELA ABRAMI**

CO-SUPERVISORE DI TESI
**PROF. DARIO VOINOVICH**


**ANNO ACCADEMICO 2023/2024**

UNIVERSITÀ
DEGLI STUDI
DI TRIESTE

# UNIVERSITÀ DEGLI STUDI DI TRIESTE

## XXXVII CICLO DEL DOTTORATO DI RICERCA IN CHIMICA

# Rheological and Low Field NMR properties of hepatic tissue and polymeric gels in the study of deubiquitinase inhibitors against liver fibrosis

Settore scientifico-disciplinare: **ING-IND/24**


DOTTORANDO / A
**ALICE BIASIN**

COORDINATORE
**PROF. ENZO ALESSIO**

SUPERVISORE DI TESI
**PROF. MARIO GRASSI**

CO-SUPERVISORE DI TESI
**PROF. GABRIELE GRASSI**

CO-SUPERVISORE DI TESI
**DOTT.SSA BARBARA TOFFOLI**

CO-SUPERVISORE DI TESI
**DOTT.SSA MICHELA ABRAMI**

CO-SUPERVISORE DI TESI
**PROF. DARIO VOINOVICH**


**ANNO ACCADEMICO 2023/2024**

# List of abbreviations

α-SMA - alfa-Smooth Muscle Actin

ALT - Alanine ammino transferase

AST - Aspartate amino transferase

BIL DIR - Direct Bilirubin

BIL TOT - Total Bilirubin

BMI - Body Mass Index

BSA - Bovine Serum Albumin

CF - Cystic Fibrosis

CLDs - Chronic Liver Diseases

DMSO - Dimethyl sulfoxide

DUBs - Deubiquitinases or deubiquitinating enzymes

ECM - Extracellular Matrix

EMA - European Medicined Agency

E2F1 - E2F Transcription Factor 1

FDA - Food and Drug Administration

FN - Fibronectin

FS - Frequency Sweep test

Glyc - Glycemia

GGT - Gamma glutamyl transpeptidase

HBV - Hepatitis B Virus

HCC - Hepatocellular Carcinoma

HCV - Hepatitis C Virus

HF-NMR - High Field-Nuclear Magnetic Resonance

HRP - Horseradish Peroxidase

HSCs - Hepatic Stellate Cells

LDH - Lactate Dehydrogenase

LF - Liver Fibrosis

LF-NMR - Low Field-Nuclear Magnetic Resonance

MAFLD - Metabolic-associated fatty liver disease

mHSCs - murine Hepatic Stellate Cells

MMPs - Metalloproteases

NAFLD - Non-alcoholic fatty liver disease

NASH - Non-alcoholic steatohepatitis

ON - Overnight

PBS - Phosphate-Buffer Salin

RT - Room Temperature

RT-qPCR - Quantitative Reverse Transcription Polymerase Chain Reaction

SEM - Standard Error of the Mean

SDS - Sodium Dodecyl Sulphate

SS - Stress Sweep test

TIMPs - Tissue Inhibitors of metalloproteinases

UCHL1 - Ubiquitin C-terminal hydrolase 1

UCHL5 - Ubiquitin C-terminal hydrolase 5

UPS - Ubiquitin-Proteosome System

USP9X - Ubiquitin-specific peptidase 9X

VEGF - Vascular-Endothelial Growth Factor

WB - Western Blot

# Abstract

Liver fibrosis (LF) is a major concern for public health worldwide, with more than 800 million people affected and a mortality rate of approximately 2 million deaths per year (Asrani et al., 2019; Marcellin and Kutala, 2018; Ye et al., 2022). In Italy, the death rate for liver fibrosis/cirrhosis is of about 10.8/100˙000 inhabitants (Stroffolini et al., 2017). To date, there is still a great need to develop novel therapeutic strategies to treat LF. Moreover, liver fibrosis is one of the most well-known predisposing cause of hepatocellular carcinoma (HCC): clinical findings indicate that > 80% of HCCs develop in the contest of liver fibrosis/cirrhosis (Affo et al., 2017).

Chronic infection of hepatitis B/C virus, alcohol abuse and non-alcoholic fatty liver disease are the major causes inducing liver fibrosis (Lan et al., 2023). This process consists in the increased deposition of extracellular matrix (ECM) into the liver tissue (Acharya et al., 2021). A major player in the deposition of pathological ECM is represented by the hepatic stellate cells (HSCs) (Khanam et al., 2021a). These cells are localized in the sub-endothelial space between the basolateral surface of hepatocytes and the anti-luminal side of fenestrated sinusoidal endothelial cell layer (space of Disse). Upon activation by pathological stimuli, HSCs change from a quiescent to a proliferative phenotype becoming similar to myofibroblasts (activated HSCs) that secrete excessive amount of pathological ECM. Pathological ECM differs from the normal one as the non-fibrogenic type IV collagen is replaced by fibrogenic type I and II collagen; moreover an augmented secretion of fibrotic markers such as fibronectin and α-smooth muscle actin (α-SMA) (Acharya et al., 2021) occurs. Accumulation of type I collagen fibers causes major structural changes in the liver, leading to mechanical rigidity and disrupting liver function (Iwakiri, 2014).

So far, no effective therapeutic approaches are available for liver fibrosis. Thus, the main aim of this thesis was to study novel drugs with anti-fibrotic potential. To this end, we have used a class of deubiquitinases (DUBs) inhibitors named 2C and DUDC3, that we successfully employed to down regulating the growth of ovarian cancer cells (Maddaloni et al., 2024). To explore DUBs inhibitors effectiveness, we have considered three different experimental models: in the first where DUBs inhibitors effectiveness was studied in HSCs cultivated in standard plastic dishes, in the second DUBs inhibitors were tested in HSCs grown in 3D structures (spheroids) and in the third DUBs inhibitors were evaluated in HSCs cultivated on surfaces able to mimic the normal and pathological liver viscoelastic properties.

The first model employed, i.e. plastic dishes, does not resemble the real environment of the fibrotic liver for several reasons among which the fact plastic dishes exhibits significantly different mechanical properties than a cirrhotic liver (Mazza et al., 2017). In this regard, it is known that the increase of the stiffness and, therefore, the elastic properties promotes cells activation and differentiation (Olsen et al., 2011; Van Grunsven, 2017). Despite this limitation, plastic dishes have the advantage of the easiness of cell culturing and of the further processing to study cell phenotype and molecular effects. The spheroid model has the advantage to explore the effects of the drugs in a 3D structure somehow resembling the 3D structure of the liver, although with a simplified tissue architecture. Finally, the third model allows studying the effects of the drugs in cell cultivated on surfaces with realistic viscoelastic properties, i.e. those represented by the normal and the pathological fibrotic liver. This model is of particular relevance, as it is known that increased surface stiffness promotes cells activation and differentiation. As very few data about human liver viscoelastic properties are available in the literature, here we have determined them in samples obtained from normal and pathological liver. For this purpose, rheology technique was employed and the outcoming results were compared to those descending from the Low Field NMR characterization. The data obtained were used to prepare cell-culturing surface made by the polymer alginate, either with normal or pathological viscoelastic properties. Our data indicate that, in the three models employed, the drugs considered have the power to down regulating HSCs growth and fibrotic activation. While the three models have each some limitations, taken together they can provide data with a significant predictive power for studies performed in animal models of liver fibrosis. In this regard, the *in vivo* studies are ongoing in the lab of prof. Truong Hai Nhung (University of Sciences, Ho Chi Minh City, Vietnam) in the frame of the common project “A novel molecular approach to liver fibrosis” financed by the Ministry of Foreign Affairs and International Cooperation (MAECI) to Prof. Gabriele Grassi.

# Table of contents

# 1. Introduction

## 1.1. Rheology

Rheology (from the Greek verb ρεω meaning to flow) is the discipline that studies the flow properties of materials.

The theory of elasticity and Newtonian fluid mechanics are effective for describing simple mechanical behaviors. In both cases, a single physical property – elastic modulus or viscosity – is sufficient to characterize the deformation or flow conditions induced by stresses on the material. Due to their simplicity, these approaches are applicable only to a limited class of materials. Many real substances exhibit more complex behaviors that lie between the extremes defined by Hooke's and Newton's linear models. This complexity necessitates the field of rheology, which has emerged as an independent science to describe phenomena and solve problems beyond the scope of classical approaches.

Rheology aims to define appropriate equations or models that consider the observed stress-strain relationships in real systems. Another objective is to correlate the macroscopic behavior of a material with its microscopic structure. Real materials possess a microstructure resulting from the spatial distribution and interactions of elementary units such as macromolecules, solid particles, droplets, and micelles. This is particularly true for concentrated and dispersed polymeric systems, whose microstructures are often complex and can undergo significant changes under imposed motion and deformation conditions. Consequently, rheology seeks to establish a relationship between microstructural processes and macroscopic behavior (Grassi et al., 2006).

Rheology deals with a wide variety of materials having very different molecular or microscopic structures and thus exhibiting quite different behaviors that can only be properly described by using more than one physical quantity and by resorting to different and more complex constitutive equations than linear relationships. A given material may behave more like an elastic solid or a viscous liquid depending on the applied stress and the time scale of the deformation process. Therefore, the conventional classification between solid and liquid materials should be supplemented with liquid-like and solid-like properties (Grassi et al., 2006). All these considerations are relevant for materials such as gels, emulsions, cosmetic and pharmaceutical formulations (emulsions, unguents, pastes), but also for biological soft tissues (Kobayashi et al., 2020). These are all materials with viscoelastic properties, as they

combine both viscous and elastic properties. In particular, in this thesis the rheological analysis was applied to characterize liver tissue samples and hydrogels realized with alginate.

### 1.1.1 Strain, deformation and flow

Stress is defined as the ratio between the force F applied to a material and the surface A on which F is applied. If F acts perpendicular to the surface, we speak of normal stress σ, while we speak of shear stress τ if F acts parallel to the surface:

$$\sigma = F/A \tag{1.1}$$

$$\tau = F/A \tag{1.2}$$

Both stresses are measured in Pascals (Pa = $N/m^2$).

The deformation of a continuous body is any change in the geometric configuration of the body that leads to a change in its shape or dimensions following the application of a stress. One can define a linear deformation or elongation ε and a shear deformation γ (representing the tangent of the angle formed between the original direction of the sample and the direction assumed by the sample once deformed) depending on if the force acts normally or parallel to the surface, respectively:

$$\varepsilon = \frac{L - L_0}{L} \tag{1.3}$$

$$\gamma = \frac{S}{h} \tag{1.4}$$

where L represents the length of the material after application of σ and $L_0$ the length at rest; while S represents the displacement of the plane of application of τ and h indicates the thickness of the material (Figure 1). Linear and shear deformations are dimensionless quantities.

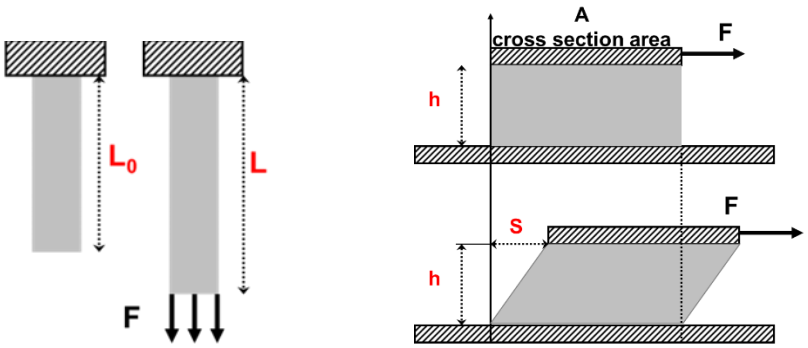


Figure 1: Schematic representation of linear deformation and shear deformation caused by force applied perpendicularly and parallel to the material surface, respectively.

Rheology applied to liquid or semi-solid systems essentially studies the flow, while rheology applied to solid systems (and very consistent semi-solids) deals with deformation. Flow is the sliding of a material in which its adjacent constituent elements move relative to one another. If these elements move one behind or on top of the other, we speak of shear flow, which is generated by applying a shear stress to a liquid or semi-solid. This flow can be imagined as a series of parallel planes sliding over each other. The layers closest to the surface, where the stress is applied, flow faster than those below, and in the simplest case, the difference in speed is proportional to the distance. In this way, the speed difference of each layer is constant. This parameter is called the shear rate $\dot{\gamma}$ and is measured in $s^{-1}$.

### 1.1.2 Basic rheological properties

*Elasticity*

Elasticity is the tendency of a solid material to deform temporarily when subjected to a stress and to regain its original shape and size when the stress is removed.

For small deformations, Hooke's law, the simplest constitutive relation for the behavior of elastic materials, applies. It establishes a direct proportionality between stress and deformation through Young's modulus E (or modulus of elasticity) or shear modulus G, both measured in Pascals, depending on whether the applied stress is normal or shear:

$$\sigma = E\varepsilon \tag{1.5}$$

$$\tau = G\gamma \tag{1.6}$$

For incompressible solid materials, the relationship applies:

$$E = 3G \tag{1.7}$$

For a purely elastic solid, deformation is instantaneous and completely reversible. Following the application of external forces, it is deformed until it reaches a new equilibrium form in which the external forces are perfectly balanced by the internal ones. All the stored energy provided by the external stimuli is completely returned upon removal of the stimulus with a corresponding instantaneous return to the original form.

Rheological behavior is schematized using mechanical models. In this case, the ideally elastic solid is represented by a spring. The load applied to the spring determines its immediate deformation (elongation or compression) and the entity of the deformation depends on the spring's elastic modulus. Once the load is removed, the spring regains its original size.

*Viscosity*

Viscosity $\eta$ expresses the resistance of a fluid to flow under the action of a shear stress. In fact, highly viscous fluids offer high resistance, while low-viscosity fluids offer low resistance.

Newton's law relates the applied shear stress τ and the strain rate or deformation rate $\dot{\gamma}$ (shear rate):

$$\tau = \eta\dot{\gamma} = \eta\frac{d\gamma}{dt} \tag{1.8}$$

The constant of proportionality between shear stress τ and shear rate $\dot{\gamma}$ is called viscosity and is related to the flow resistance of a material. From equation (1.8), a measure of viscosity, also called dynamic viscosity, can be derived, which is measured in $(Pa \cdot s)$:

$$\eta = \frac{\tau}{\dot{\gamma}} \tag{1.9}$$

For a purely viscous fluid, sliding is time-dependent and irreversible. All the mechanical energy applied to induce sliding is entirely dissipated in the form of heat and friction. Therefore, the behavior of a purely viscous liquid is schematized, through the use of mechanical models, by a damper (piston or dashpot). The load applied to the piston causes the liquid to flow with a certain speed that depends on the viscosity of the liquid. Once the load is removed, the piston does not recover its original position.

Viscosity is a function of the conditions of motion ($\dot{\gamma}$), temperature (T) and structure. When viscosity does not depend on the strain rate, the fluid is called Newtonian (water is the typical Newtonian fluid); otherwise, it is called non-Newtonian. Many polymeric and dispersed systems do not obey Newton's law due to their structural complexity and, therefore,

their viscosity depends not only on temperature and pressure but also on the intensity and duration of flow.

The classification of non-Newtonian fluids is traditionally based on the functional dependence of viscosity on shear rate $\eta(\dot{\gamma})$. A typical fluid-dynamic effect of non-Newtonian fluids is the behavior known as shear thinning: as the strain rate increases, the viscosity decreases (pseudoplastic behavior). In most polymeric solutions/fluids, as the deformation rate increases, the polymer chains orient themselves in the direction of motion, thus reducing the cross-section perpendicular to the direction of motion and offering less resistance to sliding. There are various mathematical models describing this phenomenon.

Viscoelasticity

When a purely elastic solid is subjected to a given deformation, its tensional state changes instantaneously; in fact, the internal stresses are proportional to the deformation applied at each instant. Therefore, if the deformation is kept constant, the tensional state does not change either. If the flow of a purely viscous liquid is stopped, the deformation state remains unchanged, while the internal stresses relax instantaneously and completely.

The actual behavior of materials differs from such models. In everyday practice, materials are classified as elastic solids or viscous liquids considering their mechanical response to low stresses on the ordinary time scale of minutes or seconds. However, when applying a very wide range of stresses over a wide time spectrum, liquid-like properties can be observed in solids and solid-like properties in liquids. Therefore, a given material can behave as a solid or a liquid depending on the time scale of the deformation process (Grassi et al., 2006).

A material is considered viscoelastic when it possesses behavior that is intermediate to that expected of a perfectly elastic solid or a purely viscous fluid. In this case, the material does not respond instantaneously to stress or deformation, but its response develops over time.

In the case of a viscoelastic liquid to which a constant stress is applied, the deformation increases over time until it reaches a potentially infinite value. Conversely, in the case of a viscoelastic solid, the deformation reaches a certain value and then becomes constant (Figure 2). In both cases, with a constant stress, the deformation develops over time.

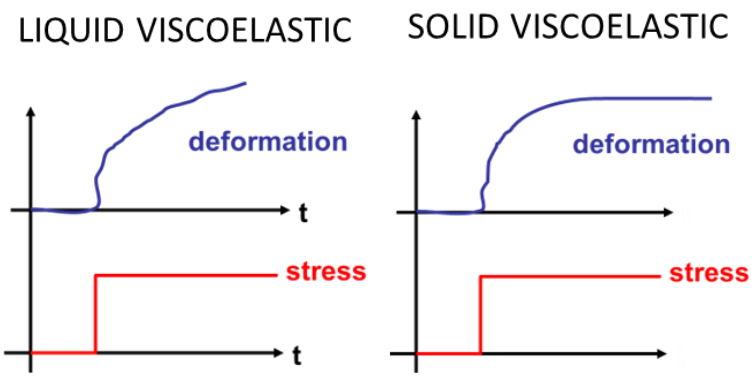


Figure 2: Representation of the deformation trend as a function of time in the case of a viscoelastic liquid (left) and a viscoelastic solid (right) to which a constant stress has been applied.

The model that considers polymeric solutions/melts characterized by polymer chains whose mass is concentrated in non-deformable regions (Kuhn segments) connected by elastic springs with a certain constant explains the viscoelastic behavior of such materials. Indeed, by applying a constant stress, the elastic component reacts instantaneously while the viscous component develops a response over time due to friction between the polymer chains and that between the chains and solvent molecules.

*Thixotropy and Antithixotropy*

The dependence of rheological properties (e.g., viscosity) on the applied stress field is governed by structural mechanisms linked to the primary constituent components (simple molecules, polymer chains, dispersed particles) and, when present, to higher-order structures formed by molecules and particles through their reciprocal attractive and/or repulsive interactions. The more abrupt the changes in the applied stress field, the more pronounced the observed time-dependent rheological properties, which are intrinsically related to the kinetic characteristics of shear-induced structural processes.

Time-dependent behavior is primarily governed by the breaking and formation of inter-particles or inter-chains bonds. The magnitude and kinetics of these processes depend on the strength of the attractive interactions, their degree of cooperation, and the magnitude of the imposed stress changes. If reversible, the resulting time-dependent properties are classified as thixotropic (Grassi et al., 2006).

Thixotropy is the property of certain pseudoplastic fluids where viscosity decreases over time under constant temperature and strain rate conditions. Conversely, antithixotropic behavior, characterized by increasing viscosity under the same conditions, is typical of highly concentrated particle suspensions. These phenomena occur as the motion conditions alter the

micro- and nano-structure of the system. While time-dependent viscoelastic behavior arises because the response of stresses or strains in the fluid following changes in imposed strains or stresses, respectively, is not instantaneous, in a thixotropic fluid, this response is instantaneous, and time-dependent properties arise solely due to changes in the fluid structure following shear stresses.

However, despite the distinction between thixotropy and viscoelasticity as separate phenomena, many real fluids such as weak gels and concentrated dispersed systems exhibit both types of time-dependent behavior, even simultaneously. In general, thixotropic effects prevail when stresses and deformation rates are relatively large; conversely, at small deformations only linear viscoelastic properties manifest themselves and their measurement is very useful for examining the microstructure of the system under investigation (Grassi et al., 2006).

### 1.1.3 Rheometer

The rheometer (Figure 3) is an instrument used to measure the rheological properties of materials. It consists of several components, including a fixed lower part and a mobile upper part, called the head. These two parts are connected by two vertical guides, which, with the help of an electric motor, allow the head to move up and down.


Figure 3: The rheometer HAAKE MARS III (Thermo-Scientific) (https://www.rheologysolutions.com/thermo-scientific-haake-mars-iii/)

The head is connected to the upper part of the measuring element, represented by a metal plate (or cone) attached to a rod that screws into the head housing. The lower part, on the other hand, is connected to the lower part of the measuring element (metal plate) by means

of a screw ring. While the lower part of the measuring element is fixed, the upper part is rotated around its axis by the action of a magnetic field generated in the head. To minimize friction between the rotating metal parts (the head and the upper part of the measuring element), compressed air at 1.6 atm is used to create an air cushion that suspends the upper part of the measuring element. In this way, the only friction present is between the metal parts and the air, which is negligible for rheological measurements.

The measurement is made by placing the sample on the lower plate of the measuring element and lowering the head until the upper part of the measuring element encounters the sample.

At this point, the application of the magnetic field causes a torque that rotates the upper part of the measuring element, which then applies a shear stress τ to the sample. The angular amplitude of the rotation θ, which determines the shear deformation γ of the sample, depends on the rheological properties of the sample and is measured using a laser beam that passes through a perforated ring at the top of the head, fixed to the measuring element. Based on the number of holes the laser passes through, a sensor records the value of θ and the speed at which the rotation θ occurs ($\dot{\theta}$). Given θ and $\dot{\theta}$, it is possible to determine γ and the deformation rate ($\dot{\gamma}$) experienced by the sample due to the application of τ. The relationship between τ, γ, and $\dot{\gamma}$ allows for the measurement of the sample's various rheological properties.

### 1.1.4 Rheological analysis: Oscillatory tests

Utilizing this apparatus, we can perform different rheological tests. These tests can be broadly classified into two categories: tests where a constant shear stress ($\tau$) or strain ($\gamma$) is applied and tests where $\tau$ or $\gamma$ exhibits a sinusoidal behavior. In the context of this thesis, due to the specific nature of the materials under investigation (namely gels and hepatic samples), we employed tests where $\tau$ or $\gamma$ follows a sinusoidal pattern. These are referred to as tests in the oscillatory regime. Oscillatory tests are particularly advantageous as they facilitate the examination of viscoelastic properties within the linear regime in a relatively straightforward manner. These tests necessitate the application of a sinusoidal stimulus ($\tau$ or $\gamma$). In the case of stress, we have:

$$\tau = \tau_0 \sin(\omega t) \tag{1.10}$$

where:

- $\tau$ is the applied shear stress,
- $\tau_0$ is the maximum shear stress,

- $t$ is the time,

- $\omega$ (rad/s) (expressed in rad/s) denotes the angular frequency, which is defined as the rate of change of the phase of a sinusoidal waveform. It represents the velocity at which one complete cycle of a wave, equivalent to a 2π radian rotation, is completed.

Within the domain of linear viscoelasticity, characterized by infinitesimal stresses and strains, we can invoke Boltzmann's principle of superposition. This principle posits that the response of a viscoelastic material to a complex deformation can be predicted by summing the responses to simpler, individual deformations. Consequently, to induce a sinusoidal strain in a sample, it necessitates the application of a sinusoidal stress, that is phase-shifted by an angle δ:

$$\tau = \tau_0 \sin(\omega t + \delta) \tag{1.11}$$

Developing eq. (1.11) according to the rules for the sum of arcs, we obtain:

$$\tau = \tau_0(\cos\delta)\sin(\omega t) + \tau_0(\sin\delta)\cos(\omega t) \tag{1.12}$$

As can be seen from eq. (1.12), the stress is the sum of two terms, the first of which is in phase and the second out of phase by $\pi/2$ with respect to the deformation (γ). In fact, $\cos(\omega t) = \sin(\omega t + \pi/2)$. Rewriting eq. (1.12) more conveniently, we have:

$$\tau(t) = \gamma_0 \left( \frac{\tau_0(\cos\delta)}{\gamma_0} \sin(\omega t) + \frac{\tau_0(\sin\delta)}{\gamma_0} \cos(\omega t) \right) \tag{1.13}$$

By defining $\frac{\tau_0(\cos\delta)}{\gamma_0}$ and $\frac{\tau_0(\sin\delta)}{\gamma_0}$ as the elastic or storage modulus (G') and viscous or loss modulus (G''), respectively, we underscore the dual dependence of a viscoelastic material's response on both its elastic and viscous properties. G' is connected to the elastic energy stored in the material upon deformation. G'' is associated to the energy dissipated due to internal friction inside the fluid (viscosity). For a purely elastic material, where the stress response is instantaneous, we have G'' = 0, δ = 0, and G' = $\tau_0/\gamma_0$. In contrast, for a purely viscous material, where the stress response is phase-shifted by π/2, we have G' = 0, δ = π/2, and G'' = $\tau_0/\gamma_0$. We can rewrite eq. (1.13) as follows:

$$\tau(t) = G'\gamma_0 \sin(\omega t) + G''\gamma_0 \cos(\omega t) \tag{1.14}$$

From these considerations, we can define the complex modulus G*, the magnitude of which is given by:

$$|G^*| = \frac{\tau_0}{\gamma_0} = \sqrt{(G')^2 + (G'')^2} = \sqrt{\left(\frac{\tau_0 cos\delta}{\gamma_0}\right)^2 + \left(\frac{\tau_0 sin\delta}{\gamma_0}\right)^2}$$

(1.15)

where the loss angle δ can be defined as:

$$\tan(\delta) = \frac{G''}{G'}$$

(1.16)

### 1.1.5 Stress Sweep tests

The Stress Sweep (SS) test is a rheological examination that involves subjecting the material to oscillatory stress by incrementing the stress amplitude $\tau_0$, while maintaining a constant frequency *f* (typically, *f* = 1 Hz) or pulsation $\omega$ (typically, $\omega = 2\pi f = 2\pi$ rad/s). The rheometer yields the values of the storage modulus G' and the loss modulus G'' as a function of the changing stress amplitude $\tau_0$.

This test is crucial as it allows the delineation of the linear viscoelastic region, within which the material's structure remains unaltered by the applied stress. In essence, as long as G' and G'' remain invariant with increasing $\tau_0$, it can be ascertained that the material is within the linear viscoelastic region. Conversely, any increase or decrease in G' and/or G'' signifies a transition into the non-linear region. An example is reported in the Figure 4, where the red line indicates approximately the point where the material in no longer in the viscoelastic region. As usual in rheology field the x and y axes are reported with a logarithmic scale. Indeed, from the rheological view point what matters is the logarithmic variation of physical parameters (e.g. G', G'' and τ).

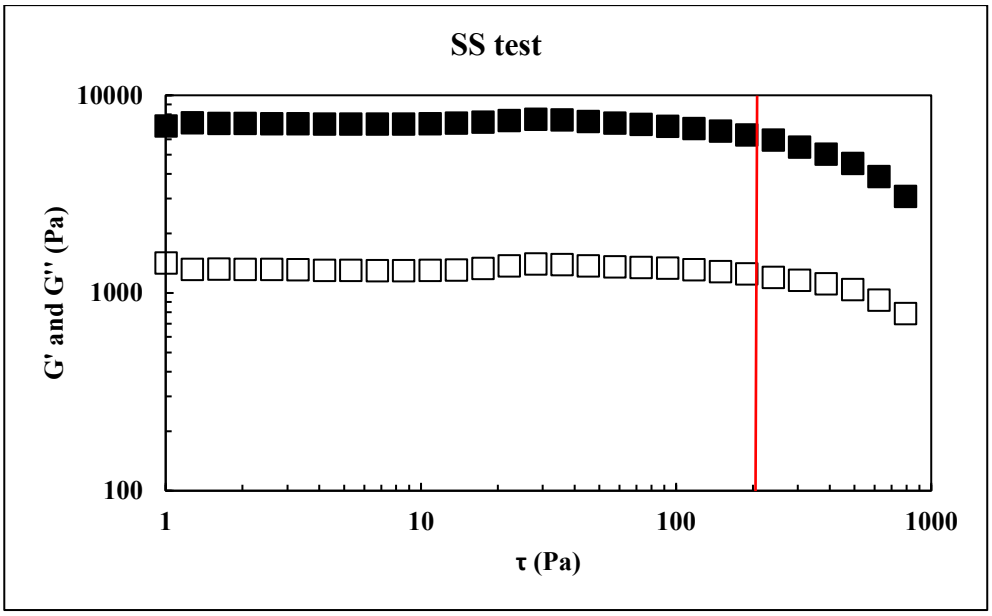


Figure 4: Typical graphic of a Stress Sweep test, where the elastic modulus G' (black square) and the viscous modulus G'' (white square) are independent from the shear stress τ. However, after the critical deformation $\gamma_c$ (here approximately indicated by the red line), the linear viscoelastic zone is exceeded and both the moduli decrease.

### 1.1.6 Frequency Sweep tests

A Frequency Sweep (FS) test involves applying a sinusoidal stress with a constant amplitude $\tau_0$ and varying frequency, typically ranging from 100 to 0.01 Hz. The stress amplitude is selected within the linear viscoelastic region. The plot of G' and G'' versus angular frequency ω (ω = 2π*f*) is known as the mechanical spectrum. The typical mechanical spectrum of a gel is characterized by constant G' and G'' values across ω. Additionally, G' is approximately ten times higher than G'' throughout the frequency range. Figure 5 shows a typical mechanical spectrum of a gel. Conversely, solutions are characterized by G' < G''. An ideal elastic material is characterized by G'' = 0, while an ideal liquid material is characterized by G' = 0. The sol-gel transition occurs when G' ≈ G''. As usual in rheology field the x and y axes are reported with a logarithmic scale. Indeed, from the rheological view point what matters is the logarithmic variation of physical parameters (G', G'' and ω).

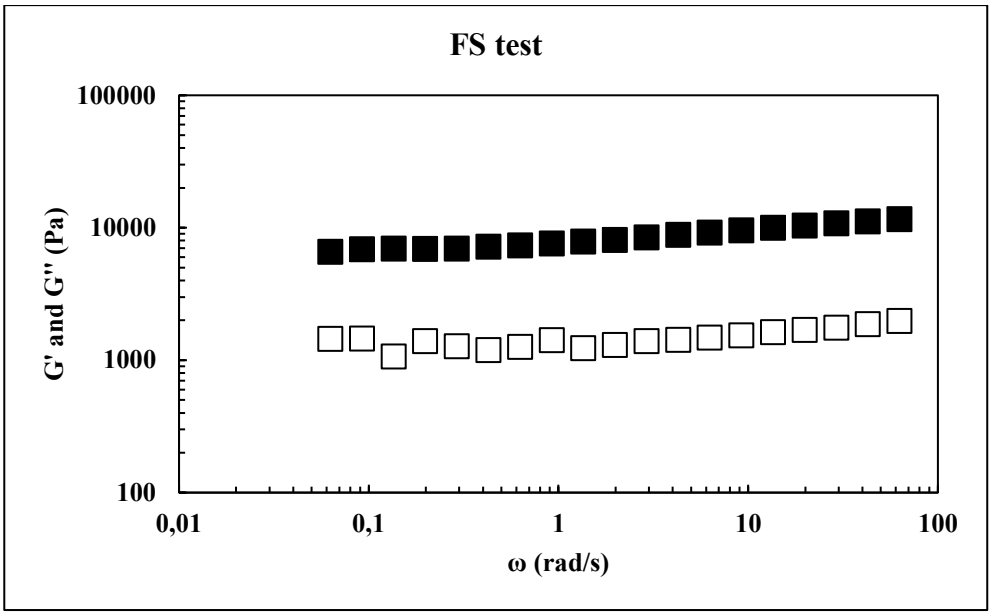


Figure 5: Typical hydrogel mechanical spectrum. The elastic modulus G' (black square) is bigger than the viscous one G'' (white square), and both of them are independent from the pulsation ω.

### 1.1.7 Correlation models: Maxwell model and Generalized Maxwell model

Several models are used in theoretical rheology to describe the viscoelastic behavior of materials. One of the most popular theories for interpreting mechanical spectra of viscoelastic materials is Maxwell's model. According to this theory, the response of viscoelastic materials can be represented by an elastic element (spring with constant G) in series with a dashpot (viscous element - piston containing a fluid of constant viscosity η) (Figure 6).

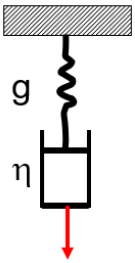


Figure 6: Maxwell element.

The constitutive equation representing the viscoelastic behavior of the Maxwell element is given by equation (1.17):

$$\tau + \frac{\eta}{G}\frac{\partial \tau}{\partial t} = \eta\dot{\gamma} \tag{1.17}$$

where τ is the stress, $\dot{\gamma}$ is the shear rate, t is time, η is the dashpot viscosity, G is the spring constant, and λ = η/G is the Maxwell element relaxation time, representing a characteristic time. In the case of sinusoidal deformation $\gamma = \gamma_0 \sin(\omega t)$, eq. (1.17) implies the following expression for the stress:

$$\tau = \gamma_0 \left(G' sen(\omega t) + G'' \cos(\omega t)\right) \tag{1.18}$$

$$G'(\omega) = \frac{G(\lambda\omega)^2}{1+(\lambda\omega)^2} \qquad G''(\omega) = \frac{G\lambda\omega}{1+(\lambda\omega)^2} \tag{1.19}$$

When ω = 1/λ, G' = G'' and this condition corresponds to the maximum value of G''.

Generally, the mechanical response of a viscoelastic material requires a more complex model than the simple Maxwell element. For this purpose, the rheological data (e.g. the data obtained from the frequency sweep test) can be interpreted using the generalized Maxwell model, consisting of *n* Maxwell elements in parallel with the addition of a purely elastic element $G_0$ (spring – infinite relaxation time), is considered (Figure 7). The elastic element is considered to describe the solid-viscoelatic behavior according to which the sample cannot indefinitely deform under the action of a constant stress. On the contrary, when the purely elastic element is absent, the liquid viscoelastic behavior (infinite deformation caused by the application of a constant stress) is described. Each element is characterized by a relaxation time $\lambda_i$ and a viscosity $\eta_i$ (or alternatively, the storage moduli $G_i = \eta_i/\lambda_i$). The expressions for G' and G'' read:

$$G'(\omega) = G_0 + \sum_{i=1}^{n} G_i \frac{(\lambda_i\omega)^2}{1+(\lambda_i\omega)^2} \tag{1.20}$$

$$G''(\omega) = \sum_{i=1}^{n} G_i \frac{\lambda_i\omega}{1+(\lambda_i\omega)^2} \tag{1.21}$$

Simultaneous fitting of eqs. (1.20) and (1.21) to the experimental G' and G'' vs ω data allows for the determination of the generalized Maxwell model unknown fitting parameters ($G_i$, $\lambda_i$), that represent the "relaxation spectrum." Typically (Lapasin and Pricl, 1995), to speed up the fitting procedure, the relaxation times of the various elements are assumed to be related to each other via the following expression:

$$\lambda_{i+1} = 10 \cdot \lambda_i \tag{1.22}$$

By scaling the various $\lambda_i$ by a factor of 10, therefore, $\lambda_1$ becomes the only fitting parameter for what concerns the relaxation times. Therefore, in the case of one Maxwell element, the fitting parameters are two: $\lambda_1$ and $G_1$. For each Maxwell element that is added to the model, a further fitting parameter must be considered, namely the corresponding shear modulus $G_i$.

The proper number of Maxwell elements $n$ to be considered is determined by a statistical procedure (Draper and Smith, 1998), where the optimal $n$ minimizes the product $\chi^2(1+n)$. $\chi^2$ is the sum of the squared errors from the simultaneous fitting of eqs. (1.20) and (1.21) to the experimental G' and G''.

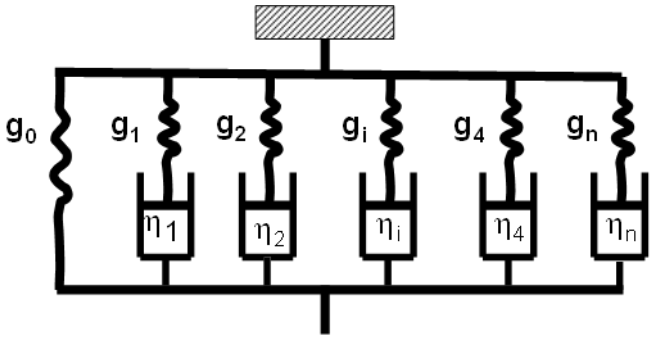


Figure 7: Generalized Maxwell model in which element 0 is degenerated into a spring.

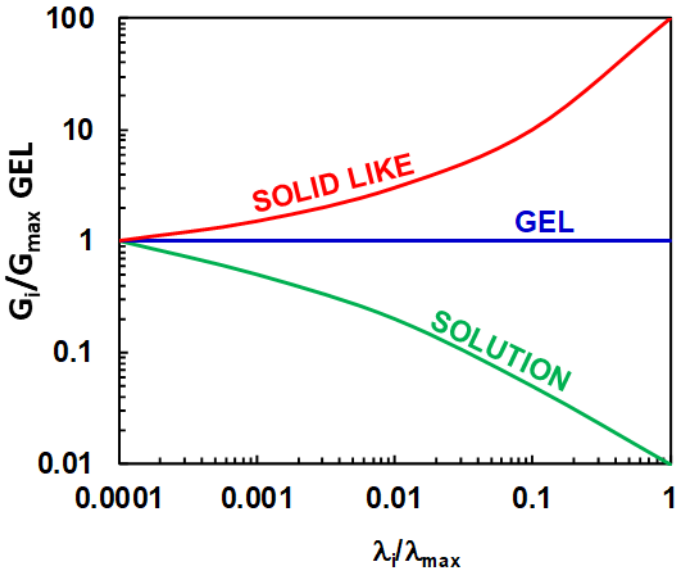


Figure 8: Typical relaxation spectra of liquid (e.g. solution), gel and solid-like materials.

Figure 8 shows the classic shape of relaxation spectra for solid-like materials, gels and solution-like (viscous liquids). Knowledge of $G_0$, $G_1$, … $G_n$, makes it possible to determine a

very important parameter, namely the shear modulus of the material (indicated as G or $\Sigma G_i$), which can be calculated as the sum of the terms $G_0$, $G_1$, … $G_n$.

It is interesting to note that, within the linear viscoelastic regime, the superposition of effects principle, or, Boltzman's principle, makes it possible to predict the behavior of a material subjected to a constant stresses on the basis of its relaxation spectrum ($\lambda_i$, $G_i$) obtained from oscillatory (FS) tests. Indeed, in the case of *creep* tests, in which the material is subjected to a constant stress $\tau_0$, the corresponding deformation is given by:

$$\gamma(t) = \frac{\tau_0}{G_0 + \sum_{i=1}^{n} \frac{\lambda_i G_i}{t+\lambda_i}} \qquad J(t) = \frac{\gamma(t)}{\tau_0}$$

(1.23)

where $\lambda_i$ and $G_i$ are the same parameters as in eqs. (1.20) (1.21) and J(t) is called compliance. Similarly, in *relaxation* tests the sample undergoes a constant deformation $\gamma_0$ and the stress required is given by:

$$\tau(t) = \gamma_0 \left( G_0 + \sum_{i=1}^{n} G_i e^{-\frac{t}{\lambda_i}} \right)$$

(1.24)

### 1.1.8 Determining the average mesh size

Once the macroscopic behavior of a system (the relaxation spectrum and the limit of the linear viscoelastic regime) has been obtained, it is possible to relate the macroscopic and micro/nanoscopic properties of the material to derive the average mesh size.

*Flory Theory*

Flory's theory (Flory, 1953) assumes that gels consist of a solid phase, typically represented by polymer chains (constituted by non-deformable units called Kuhn segments), swollen by a solvent phase.

Equilibrium conditions are met when the chemical potential of the mobile component (solvent, typically water) in the gel phase is equal to the chemical potential of the solvent in the external solvent phase. Therefore, if the number of water molecules leaving the gel phase is equal to the number of water molecules entering the gel phase from the solvent phase, the chemical potential difference ($\Delta$) is zero:

$$\Delta = \Delta_M + \Delta_E + \Delta_I = 0$$

(1.25)

where $\Delta_M$, $\Delta_I$ and $\Delta_E$ are, respectively, the mixing, the ionic, and the elastic contribution to $\Delta$. $\Delta_E$ expression reads:

$$\Delta_E = -RT\rho_x \left(\frac{\nu_p}{\nu_{p0}}\right)^{\frac{1}{3}}$$

(1.26)

where $\nu_p$ is the volume fraction of polymer; whereas $\nu_{p0}$ represents the polymer volume corresponding to the condition in which polymeric chains cross-linking occurred. R is the universal gas constant deriving from the statistical thermodynamics approach used by Flory to describe the polymeric network as done for gas molecules. T is the absolute temperature (in this thesis 310°K, which corresponds to 37°C). If the system has undergone neither swelling nor contraction (by exposure to pure solvent) from the state in which cross-linking occurred, then, $\nu_p=\nu_{p0}$. A key parameter appearing in eq. (1.26) is the cross-linking density $\rho_x$ (moles of cross-linking points per unit volume), that can be determined by the following equation:

$$\rho_x = \frac{G}{RT}\left(\frac{\nu_p}{\nu_{p0}}\right)^{\frac{2}{3}}$$

(1.27)

Therefore, there is a direct correlation between the cross-linking density $\rho_x$ and the shear modulus G of the system. Assuming that the value of the shear modulus is equal to the value that the modulus assumes at the initial instant in a relaxation experiment, which corresponds to an infinite frequency in a frequency sweep experiment, we can write:

$$G = \sum_{i=1}^{n} G_i$$

(1.28)

Thus, Flory's theory allows to link a macroscopic property of the system (shear modulus) to a microscopic property (cross-linking density) and to determine its value.

Although, in general, gels made of biopolymers only remotely resemble those theorized by Flory, studies have shown that in the linear viscoelastic field, the theory reasonably describes reality.

*Schurz's Equivalent network theory*

The equivalent network theory developed by Schurz (Schurz, 1991) makes it possible to relate the cross-linking density to the average mesh size. Since, in most cases, the polymer chains in the gel phase form an uneven structure, the actual topology of the polymer network is complex to describe. Therefore, we assume the existence of an equivalent ideal cubic

network that has in common with the real network only the cross-linking density. Then, we associate to each crosslink a sphere with a diameter equal to the distance between two adjacent crosslinks ξ, i.e. the average mesh size of the reticle (Figure 9).

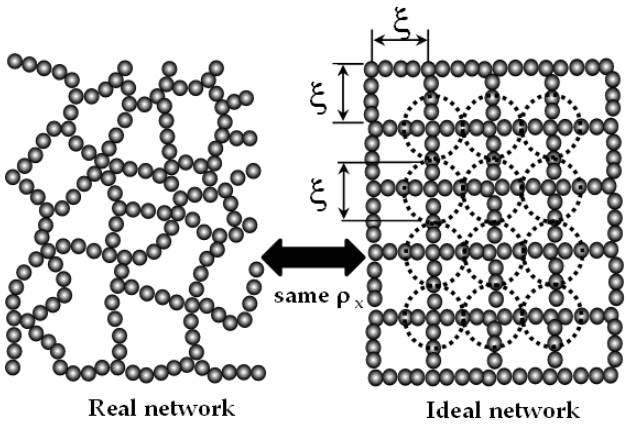


Figure 9: Schematic representation of the real network and the equivalent network assumed in the equivalent network theory.

The product of the crosslink density and the Avogadro's number ($N_A$) represents the number of crosslinks per unit volume. Therefore, the inverse of this product coincides with the volume per cross-linking point:

$$\frac{4}{3}\pi\left(\frac{\xi}{2}\right)^3 = \frac{1}{\rho_x N_A} \tag{1.29}$$

It follows that the average mesh size ξ is:

$$\xi = \sqrt[3]{6/\pi\rho_x N_A} \tag{1.30}$$

In conclusion, thanks to Flory's theory and Schurz's equivalent network theory, it is possible to link a nanoscopic property of the system (ξ) and a macroscopic property (G).

### 1.1.9 Correlation models: Soskey-Winter model

In order to determine the limit of the viscoelastic regime, the value of the critical strain $\gamma_c$ can be determined by fitting the Soskey-Winter equation (Soskey and Winter, 1984) to the experimental stress sweep data:

$$Z = \frac{Z_0}{1 + (b\gamma)^n} \tag{1.31}$$

where Z can be G*, G', or G'' and $Z_0$ is the Z value for a vanishing deformation ($\gamma \approx 0$). $b$ and $n$ are two fitting parameters. The value of $\gamma_c$ is calculated by eq. (1.31), setting $Z = 0{,}95 \times Z_0$ (Sacco et al., 2020). The corresponding value of the critical stress $\tau_c$ was evaluated according to the usual equation:

$$\tau_c = \gamma_c \sqrt[2]{(G_c')^2 + (G_c'')^2} = \gamma_c G_c^* \tag{1.32}$$

### 1.1.10 Cell adhesion and rheological characteristics of the substrate

Studies that relate cellular behavior to the rheological characteristics of the substrate with which they interact have developed over the last 20 years. Until around 2011, the prevailing view was that the most important rheological characteristic was the stiffness of the matrix, represented by the shear modulus G. For example, Yeung and co-workers (Yeung et al., 2005), working on fibroblasts and endothelial cells, find that G significantly influences cell morphology, cytoskeleton structure and adhesion on the substrate. Li and co-workers (Li et al., 2007) note that G regulates the activation of portal fibroblasts in culture. Evans and co-workers (Evans et al., 2009) find that G is able to influence the early stages of differentiation of embryonic stem cells. This evidence is also taken up by Huebsch and co-workers (Huebsch et al., 2010) who note that G values between 3 and 10 kPa favor the formation of osteocytes while adipocytes are obtained on softer substrates (G ~ 1-2 kPa). Finally, Olsen and co-workers (Olsen et al., 2011) observe that hepatic stellate cells require a rigid environment to differentiate into myofibroblasts.

From 2011 onwards, however, it is hypothesized that not only G but, more generally, all viscoelastic aspects of the substrate play an important role in the cellular response. In other words, not only G, but the entire relaxation spectrum of the substrate ($\lambda_i$, $G_i$) plays an important role in driving the cellular response. Cameron and co-workers (Cameron et al., 2011), studying mesenchymal stem cells, state that the cells seem to be more affected by G'' (viscous or loss modulus) rather than G' (elastic or storage modulus), i.e. that the cells are affected more by the viscous component (G'') of the substrate rather than the elastic component (G'). Chaudhuri and co-workers (Chaudhuri et al., 2015) perform an interesting experiment in which they realize a substrate by cross-linking an aqueous alginate solution. In the first case, they proceed with a covalent cross-linking between the polymer chains, while in the second, the cross-linking is ionic. The result is that the covalently cross-linked alginate has practically no viscous component (G'' ~ 0) and, therefore, subjected to a deformation does not relax, whereas the ionically cross-linked alginate (in a similar manner to what was done in

this thesis work) does. They verify, therefore, that cells are only able to migrate onto the substrate if it allows relaxation following its deformation by cellular action. In fact, the authors see that cells only migrate on the ionically cross-linked substrate. In conclusion, they state that both elasticity (G) and viscosity (i.e. the entire relaxation spectrum ($\lambda_i$, $G_i$)) play an important role for cells behaviour. It is important to emphasize that these conclusions are not only based on experimental evidence but also on the output of a mathematical model created to describe the motion of a viscoelastic object (the cell) on a viscoelastic medium (the substrate). Using another mathematical model, Gong and co-workers (Gong et al., 2018) come to similar conclusions, namely that cell behavior is not only influenced by the stiffness of the substrate (G) but also by its viscous properties. Finally, Sacco and co-workers (Sacco et al., 2020), on the basis of an in-depth rheological analysis of different substrates made by cross-linking different types of chitosan, define the molar energy of dissipation $E_d$, as the ratio between the work, per volume unit, that the cell has to perform to cause a critical surface deformation ($\gamma_c$) of the substrate and the cross-linking density $\rho_x$ (eq. (1.27)) of the substrate. On an experimental basis, the authors find that cell adhesion and migration are inversely proportional to $E_d$.

$E_d$ suggests that cells must be able to remodel the substrate in order create a favorable environment (the "nest") where to live. Thus, it would be extremely interesting to theoretically evaluate the work required to provoke the substrate critical deformation ($\gamma_c$), the minimum work necessary for substrate re-modelling. As, unfortunately, work is not a state function, this target implies to know the kinematics of the stress applied by cell on substrate, i.e. a constant stress $\tau_0$, a stress proportional to deformation or something different (sinusoidal?). The paper by Du Roure and co-workers (Du Roure et al., 2005), one of the most interesting on this topic, shows a very complex scenario as the stress exerted by the cell modifies with time and position, being maximum in correspondence of the cell rim. In the light of this complexity and in order to draw general conclusions, the authors simplify the frame reasoning on average stress values, implicitly suggesting that the assumption of a constant stress is reasonable. On the contrary, the mathematical model proposed by Gong and co-workers (Gong et al., 2018) suggests that the stress exerted by the cell on the substrate can be considered proportional to substrate deformation. Thus, a constant stress ($\tau_0$) and a stress proportional to deformation will be considered in this thesis for the theoretical evaluation of the work performed by the cell.

Assuming that the cell exerts a constant radial stress ($\tau_0$) on a circular substrate portion of initial radius $r_0$ (two-dimensional cells culture), the work done will be:

$$W = \int_{r_0}^{r} F * dr = \int_{r_0}^{r} \tau_0 \pi r^2 dr = \int_{0}^{\gamma} \tau_0 \pi r_0^3 (1+\gamma)^2 d\gamma = \pi \tau_0 r_0^3 (\gamma + \gamma^2 + \gamma^3)$$

(1.33)

where:

$$\gamma = \frac{r - r_0}{r_0} \qquad\qquad dr = r_0 d\gamma$$

(1.34)

being F is the total force exerted on the surface $\pi r^2$. If the deformation is small, the quadratic and cubic terms of the deformation are negligible compared to γ, so that eq. (1.33) can be approximated by the following equation:

$$W \approx \pi \tau_0 r_0^3 \gamma(t) \qquad\qquad w = \frac{W}{\pi r_0^3} \approx \tau_0 \gamma(t) = \tau_0^2 J(t)$$

(1.35)

*w* being the work per unit volume and J(t) the compliance (eq. (1.23)) of the substrate after a time t from the application of the stress $\tau_0$. Assuming that the deformation γ coincides with the critical deformation $\gamma_c$ (which marks the limit from the linear viscoelastic regime) and dividing *w* by the cross-linking density $\rho_x$ (eq. (1.27)) we obtain $E_d$.

In the case of an applied stress proportional to deformation (γ), we can assume:

$$\tau = G^* \gamma \qquad\qquad G^* = \sqrt[2]{(G')^2 + (G'')^2}$$

(1.36)

where *G** is the substrate complex shear modulus whose dependence on g can be given by the Soskey-Winter model (Soskey and Winter, 1984), see eq. (1.31) whose fitting parameters ($G_0^*$, *b* and *n*) can be determined by eq. (1.31) fitting to experimental data referring to strain sweep test. According to eq. (1.31) and (1.36), the expression of the work performed by the cell (eq. (1.33)) becomes:

$$W = \int_{r_0}^{r} \tau(\gamma) \pi r^2 dr = \pi r_0^3 \int_{0}^{\gamma} \frac{G_0^*}{1 + (b * \gamma)^n} \gamma \, (1+\gamma)^2 d\gamma$$

(1.37)

or, equivalently:

$$w = \frac{W}{\pi r_0^3} = \int_{0}^{\gamma} \frac{G_0^*}{1 + (b\gamma)^n} \gamma \, (1+\gamma)^2 d\gamma$$

(1.38)

Unfortunately, the integral appearing in eq. (1.38) does not lead to an analytical solution, even if its numerical determination is very easy and not particularly time consuming

in virtue of the small computational duty required. However, when *n* can be assumed equal to 1, eq. (1.38) analytical solution exists and it reads:

$$\mathrm{w} = \frac{G_0^*}{b^2}\left[\gamma^3\left(\frac{b}{3}\right) + \gamma^2\left(\frac{2b-1}{2}\right) + \gamma\left(\frac{(b-1)^2}{b}\right) - \left(\frac{b-1}{b}\right)^2 ln(1+b\gamma)\right]$$

(1.39)

When $\gamma = \gamma_c$, both eq. (1.33) and eq. (1.38) (or eq. (1.39) when n = 1 in eq. (1.38)) provide the minimum work necessary to remodel the substrate. Interestingly, both eq. (1.33) and eq. (1.38) (or eq. (1.39)) hold also for $\gamma > \gamma_c$, i.e. in the not linear viscoelastic range. In addition, both eq. (1.33) and eq. (1.38) (or eq. (1.39)) can be extended to a three-dimensional cell culture (3D substrate) by simply remembering that the surface of a sphere of radius *r* is 4 times the surface of a circle of the same radius. Thus, in the 3D case, eq. (1.33) and eq. (1.38) (or eq. (1.39)) still hold once the work expression is multiplied by a factor 4.

Finally, relaying on all these equations ((1.33) and (1.38) or (1.39)), it is possible estimating the elastic (recoverable - $w_e$) and the viscous (dissipated - $w_v$) part of *w*. Indeed, whatever the kinetics of the applied stress, if we imagine removing the applied solicitation (stress) once a fixed deformation has been attained ($\gamma_f$), the substrate will be able to recover only part of the deformation so that a residual deformation will persist forever ($\gamma_\infty$). Thus, $w_v$ and $w_e$ will read:

*constant stress* ($\tau_0$)

$$w_v = \tau_0\,\gamma_\infty \qquad\qquad w_e = w - w_v$$

(1.40)

*linear stress* ($\tau = G\gamma$)

$$w_v = \int_0^{\gamma_\infty} \frac{G_0^*}{1+(b\gamma)^n}\gamma\,(1+\gamma)^2 d\gamma \qquad\qquad w_e = w - w_v$$

(1.41)

When a constant stress is considered, provided that $\gamma_f \leq \gamma_c$, $\gamma_\infty$ can be analytically evaluated according to the generalized Voigt model in series with a Maxell element (see Figure *10*).

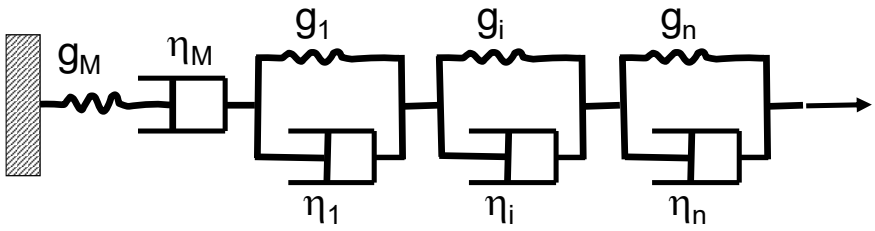


Figure 10: Generalized Voigt Model (made up by a series of spring and dashpot in parallel) plus one Maxwell element. gi and ηi are, respectively, spring constant and dashpot fluid viscosity. $g_M$ and $\eta_M$ are, respectively, the spring constant and the dashpot fluid viscosity pertaining to the Maxwell element.

Indeed, according to this mechanical model, the deformation increases upon the application of a constant stress $\tau_0$ (creep) is given by:

$$\gamma(t) = \gamma_M(t) + \sum_{i=1}^{n} \gamma_i(t) = \tau_0 \left( \frac{1}{g_M} + \frac{t}{g_M \lambda_M} + \sum_{i=1}^{n} \frac{\left(1 - e^{-\frac{t}{\lambda_i}}\right)}{g_i} \right) \tag{1.42}$$

where $\gamma$ is the global deformation, $\gamma_M$ and $\gamma_i$ are, respectively, the Maxwell element and the i$^{th}$ Voigt element deformation, $t$ is time, $\lambda_M$ and $\lambda_i$ are, respectively, the characteristics time pertaining to the Maxwell element and to the i$^{th}$ Voigt element while $\tau_0$ is the applied constant stress. On condition that $\gamma \leq \gamma_c$ (limit of the linear viscoelastic regime; i.e. $t \leq t_c$), eq. (1.42) enables the determination of the deformation at time $t = t^*$, after which the stress is removed so that the recovery phase starts. The time variation of $\gamma$ during the recovery phase is given by:

$$\gamma(t) = \frac{\tau_0}{\lambda_M g_M} t^* + \tau_0 \sum_{i=1}^{n} \frac{e^{-\left(\frac{t}{\lambda_i}\right)}}{g_i} \left[ e^{\left(\frac{t^*}{\lambda_i}\right)} - 1 \right] \tag{1.43}$$

It is easy to verify that, for a very long time, the not recoverable deformation ($\gamma_\infty$) is simply given by $(\tau_0\, t^*)/(\lambda_M\, g_M)$ with $0 < t^* \leq t_c$. Thus, $w_v$ evaluation is straightforward (eq. (1.40). Obviously, the determination of $\lambda_M$ and $g_M$ (beside that $g_i$ and $\lambda_i$) requires the generalized Voigt model fitting to experimental creep-recovery data. Alternatively, all these parameters can be determined by model fitting to experimental data referring to the pulsation ($\omega$) dependence on the elastic ($J'$) and the viscous ($J''$) compliances. Indeed, according to the generalized Voigt model plus one Maxwell element, the theoretical expression of $J'$ and $J''$ read:

$$J' = \frac{1}{g_M} + \sum_{i=1}^{n} \frac{1/g_i}{1+(\lambda_i \omega)^2} \qquad J'' = \frac{1}{g_M \lambda_M \omega} + \sum_{i=1}^{n} \frac{\lambda_i \omega / g_i}{1+(\lambda_i \omega)^2}$$

(1.44)

Although $\tau_0$ determination is more difficult, the experimental outcomes from the work by Du Roure and co-workers (Du Roure et al., 2005) can help a lot in setting reasonable $\tau_0$ values. Obviously, in the case of a linear stress, the evaluation of $\gamma_\infty$ requires the numerical solution of the Generalized Voigt model in series with a Maxwell element. Finally, when $\gamma$ exceeds $\gamma_c$, the only way to evaluate $\gamma_\infty$ consists in its experimental determination according to a creep-recovery experiment.

On the basis of what discussed at the beginning of this section, it is reasonable to suppose that cell behavior can depend on both $w(\gamma_c)$ and $w_v(\gamma_f)/w(\gamma_f)$ ratio, representing the un-recoverable fraction of the work performed by cells and due to viscous dissipation and substrate structure disruption when $\gamma_f$ exceeds $\gamma_c$.

## 1.2. Low Field-Nuclear Magnetic Resonance (LF-NMR)

In contrast to the high field-Nuclear Magnetic Resonance technique (HF-NMR), which involves a range of magnetic field of 7.5 T < B < 37 T, low field-Nuclear Magnetic Resonance (LF-NMR) conditions are fulfilled when: 0.37 T < B < 2.43 T. In the former case, the use of intense magnetic fields allows systems at the atomic scale to be studied but in a small region of space; conversely, lower magnetic field values allow systems at the nanoscale or micrometer scale to be studied over larger volumes ($mm^3$ or $cm^3$). In fact, LF-NMR analysis allows structural information to be deduced in the range of lengths from 1 nm to ~ 300 nm, in contrast to HF-NMR, that provides information on much smaller length scales (Å). For this reason, HF-NMR is used to study the chemical structure of a system or chemical reactions; conversely, LF-NMR is a useful investigation technique to study the physical structure of solids, liquids, solutions, suspensions, emulsions and gels. In particular, in this thesis the LF-NMR analysis was applied to characterize liver tissue samples and hydrogels relaying on alginate.

*Theoretical background*

Regardless of the magnetic field strength, the operating principle is the same in both HF-NMR and LF-NMR. Some atoms, such as hydrogen, by virtue of their electronic configuration (odd number of protons and/or neutrons), behave like permanent magnets, i.e. they are characterized by a permanent magnetic moment $\mu_i$ (magnetic dipole moment). Thanks to the presence of $\mu_i$, it is possible, from a magnetic point of view, to consider each atom of hydrogen as defined by the vector $\mu_i$. If a system consisting of a multiplicity of hydrogen atoms is immersed in a zero magnetic field $B_0$, the orientation of the magnetic moments of these atoms is random (Figure 11). Therefore, with $B_0 = 0$, the induced magnetization vector M, given by the vector sum of all magnetic moments, is zero:

$$B_0 = 0 \qquad \Rightarrow \qquad M = \sum_{i=1}^{N} \mu_i = 0 \tag{1.45}$$

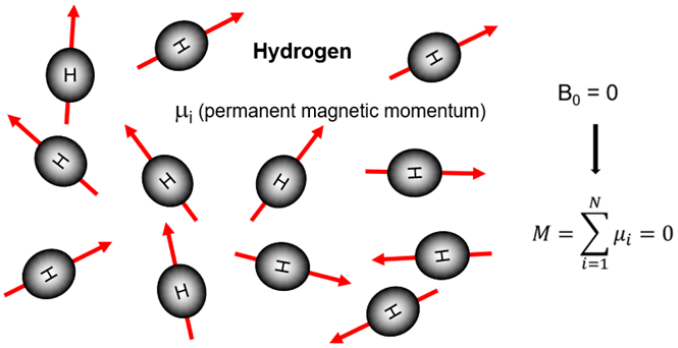


Figure 11: H atoms immersed in a null external magnetic field $B_0$, where the orientation of the permanent magnetic moments is random.

Conversely, if the system is immersed in a non-zero magnetic field $B_0$, the magnetic moments of the atoms tend to orient themselves in the direction of $B_0$, forming, however, a characteristic angle with respect to the axis identified by the direction of $B_0$. In fact, the precession phenomenon is generated such that the magnetic moments of the atoms begin to rotate around the direction of $B_0$, describing a double cone (Abrami et al., 2018) (Figure 12). The frequency $\nu_0$ at which the magnetic moments rotate is called the Larmor frequency, and depends on the magnetic field strength $B_0$ and the gyromagnetic ratio of the hydrogen atom $\gamma$ ($\gamma = 2.67*10^8$ rad/Ts for the H atom):

$$\nu_0 = \gamma B_0 \tag{1.46}$$

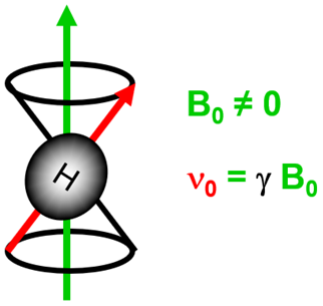


Figure 12: Schematic representation of the Larmor precession phenomenon.

From eq. (1.46) follows that a reduction or increase in the intensity of $B_0$ changes the value of the rotation frequency but does not alter the characteristic angle of rotation of the atom. Furthermore, when $B_0 \neq 0$, the magnetic moments of the atoms can also align in the direction antiparallel to that of the field, thus providing a negative contribution to the total magnetization. However, since the parallel direction is energetically more stable, most of the

magnetic moments tend to orient themselves parallel to the direction of $B_0$. Therefore, the vector sum of all magnetic moments is still not zero:

$$B_0 \neq 0 \qquad \Rightarrow \qquad M = \sum_{i=1}^{N} \mu_i \neq 0$$

(1.47)

Assuming that the external magnetic field $B_0$ is oriented along the z-axis, the component of the magnetization along the z-axis ($M_Z$) is not zero; on the contrary, the component in the xy-plane ($M_{XY}$), and thus perpendicular to the direction of $B_0$, is zero.

If, starting from the configuration just described in which $B_0 \neq 0$, at the instant $t = t_0$ a magnetic field $B_1$ is applied to the system, which is a radio frequency pulse that is in the xy-plane (perpendicular to $B_0$) and rotates around the z-axis with frequency $\nu_0$, the magnetization M undergoes a rotation of an angle $\Delta\theta$ that brings it into the xy-plane (Figure 13). The angle of rotation $\Delta\theta$ depends on the gyromagnetic ratio $\gamma$, the magnetic field strength $B_1$ and the radio frequency application time $t_p$:

$$\Delta\theta = \gamma B_1 t_p$$

(1.48)

The rotation of M in the xy-plane, caused by the application of $B_1$, causes the z-component of the magnetization to cancel out and, at the same time, the xy-component to become different from zero: $B_1$ at $t = t_0 \quad \Rightarrow \quad M_Z = 0;\ M_{XY} \neq 0$.

If at time $t = t_1 > t_0$ the magnetic field $B_1$ is removed, the magnetization vector M returns to its initial configuration and, therefore, we have that: $M_{XY} = 0$ and $M_Z \neq 0$.

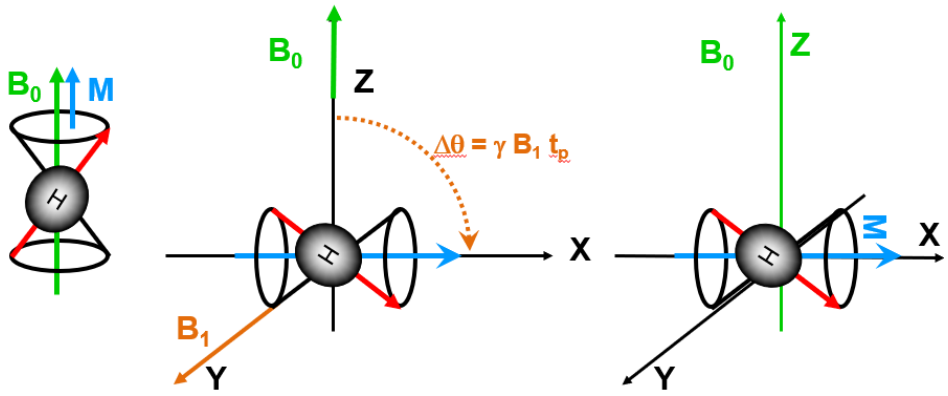


Figure 13: Magnetization vector M directed along the z-axis in the presence of $B_0 \neq 0$ (left); application of a radio frequency pulse $B_1$ and rotation of M in the xy-plane (center); removal of $B_1$ and return of M along z-axis (right).

The return of the magnetization vector M from the perturbed configuration to its original configuration is called *magnetic relaxation*, a phenomenon that is particularly

important because it allows to get information about the nano-microstructure of a system. In fact, the physical-chemical environment around hydrogen atoms can alter the way in which M returns to the equilibrium configuration.

The trajectory described by M during the process of rotation in the xy-plane and relaxation is illustrated in Figure 14. It is observed that the magnetization vector returns to the initial configuration with a complex spiral motion that extends in space and time.

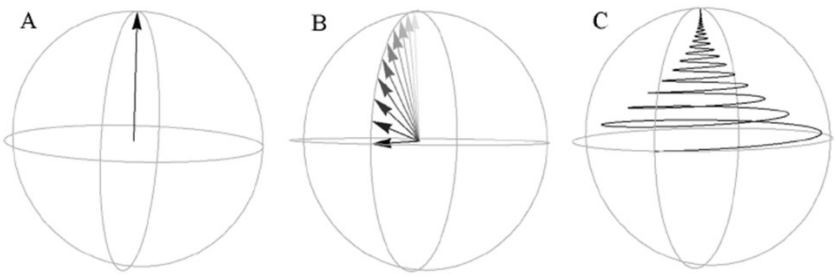


Figure 14: Initial equilibrium configuration of M along the z-axis in the presence $B_0 \neq 0$ (image A); rotation of M in the xy-plane induced by the application of $B_1$ (image B); return of M along the z-axis following the removal of $B_1$ (image C).

From an experimental point of view, the instrument records the magnetic relaxation phenomenon according to two mechanisms (Figure 15):

- *spin-lattice relaxation* (longitudinal relaxation): mechanism by which the longitudinal component of the magnetization vector $M_Z$ increases over time; it is characterized by the spin-lattice or longitudinal relaxation time, a time constant known as $T_1$;
- *spin-spin relaxation* (transverse relaxation): mechanism by which the transverse component of the magnetization vector $M_{XY}$ is reduced over time; it is characterized by the spin-spin or transverse relaxation time, a time constant known as $T_2$.

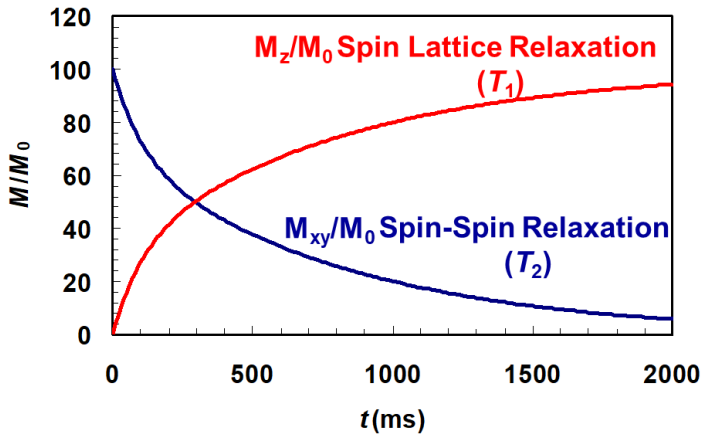


Figure 15: Relaxation curve of the $M_Z$ and $M_{XY}$ components of the magnetization over time during the magnetic relaxation process describing the spin-lattice relaxation and the spin-spin relaxation, respectively.

These two constants $T_1$ and $T_2$, although useful for describing the same phenomenon, have different physical meanings. In fact, $T_1$ relates to the exchange of energy between $\mu_i$ (spin) and the surrounding environment (lattice) to bring the entire system to a condition of minimum energy, while $T_2$ relates to the order-disorder transition (entropy change of the system). Although the instrument can track both longitudinal and transverse relaxation, for purely technical reasons, tracking transverse relaxation, and thus measuring $T_2$, is much faster.

*Fanning out and the CPMG sequence*

However, the $T_2$ measurement presents a little technical problem. In fact, since it is not possible to create a perfectly homogeneous magnetic field, the spins (magnetic moments) of the various atoms will rotate with different frequencies. This means that, once they are flipped onto the xy-plane, those that precede faster will return to the vertical position by travelling (rotating) clockwise, while those that precede slower will do so by travelling (rotating) counterclockwise. Thus, the so-called *fanning out* occurs, which implies such a reduction of the signal in the xy-plane that the instrument would not be able to record anything. In the fanning out event, M fans out according to the different velocities of the magnetic moments of which it is formed. To overcome this problem, the Carr-Purcell-Meiboom-Gill (CPMG) sequence is used, which can be understood as a Hahn spin-echo sequence repeated several times. After applying the magnetic field $B_1$, which causes the rotation of M by 90° (xy-plane), and after allowing a time $\tau$ to elaps, a further magnetic field is applied, again along the x-axis, which causes the vectors of the magnetic moments (slow and fast) to rotate by 180° around the x-axis (Figure 16). Since this rotation does not change the rotation direction of the magnetic moments around z, the slow and fast magnetic moments will rejoin resulting in a signal measurable by the instrument. At this moment, the Hahn spin-echo sequence is concluded: 90°-$\tau$-180°-$\tau$-echo (Figure 17). In order to follow the entire relaxation process (i.e. the fall of $M_{XY}$), it is necessary to apply *n* times the $B_1$ pulse in the x-direction (each one separated by a time interval $\tau$) and rotate M a further 180° (Figure 18). After a further time $\tau$ from the reapplication of $B_1$, the slow and fast signals will merge again allowing the measurement of $M_{XY}$ as shown in Figure 19. This is the so-called CPMG pulse sequence: 90°-$[\tau$-180°-$\tau$-(echo)$]_n$. The CPMG sequence ends when $M_{XY}$ vanishes (basically, it only needs to reach about 2.5% of its initial value) (Abrami et al., 2018).

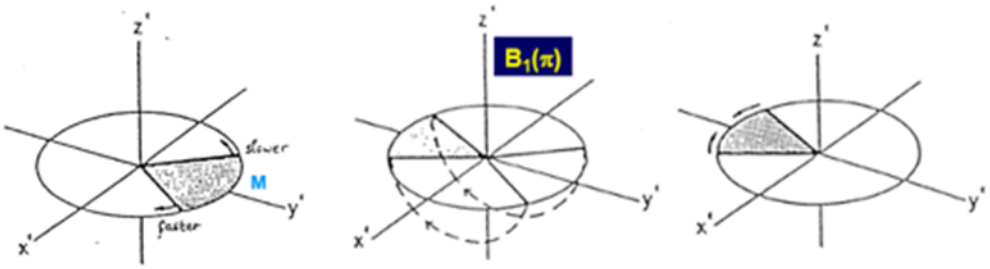


Figure 16: Three-dimensional development of the Hahn spin-echo sequence.

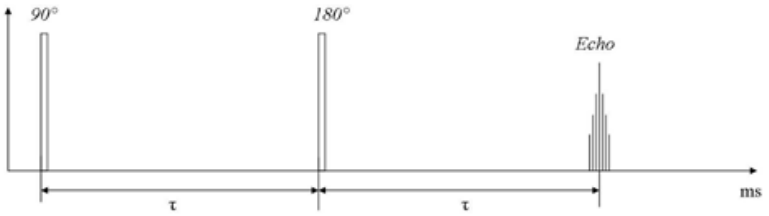


Figure 17: Schematic of the Hahn spin-echo sequence.

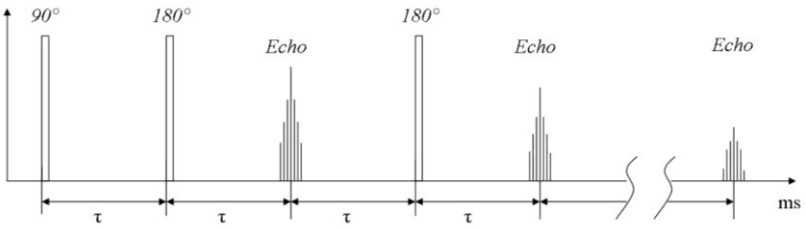


Figure 18: Schematic of the CPMG sequence.

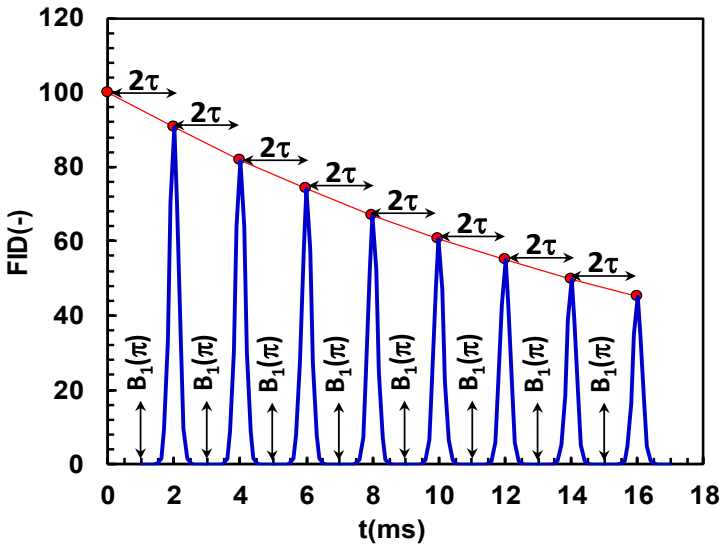


Figure 19: Time course of the signal intensity (FID – Free Induction Decay) with the CPMG sequence (blue line). The instrument records the intensity at the red dots (instants of reconnection of the signals corresponding to the slow and fast magnetic moments).

The value of the relaxation time $T_2$ is a function of temperature, the magnetic field strength $B_0$, the hydrogenated fluid being analyzed (water, alcohol, etc.), and the presence of solid surfaces. In fact, if in the case of pure fluids, such as water, the decay (relaxation) of $M_{XY}$ is exponential, in the case of more complex systems such as gels, suspensions and living tissue, for example, a single relaxation time is not sufficient to describe the relaxation of $M_{XY}$ and it is therefore necessary to consider a greater number. This results in the description of the decay of $M_{XY}$ as a summation of exponentials:

$$I(t) = \sum_{i=1}^{n} A_i e^{\left(-t/T_{2i}\right)} \tag{1.49}$$

where $t$ is time, I(t), also called FID (Free Induction Decay), denotes the ratio $M_{XY}(t)/M_0$, $T_{2i}$ represents the $i^{th}$ transverse relaxation time (or spin-spin), while $A_i$ denotes the number of magnetic moments that relax with $T_{2i}$. From (1.49), one can define important parameters such as the average relaxation time, $T_{2m}$, and the average value of its inverse, $(1/T_2)_m$, and the percentage (in volume, moles or number), of magnetic moments that relax with $T_{2i}$, $A_{i\%}$:

$$T_{2m} = \sum_{i=1}^{m} A_i T_{2i} / \sum_{i=1}^{m} A_i \qquad \left(\frac{1}{T_2}\right)_m = \sum_{i=1}^{m} \frac{A_i}{T_{2i}} / \sum_{i=1}^{m} A_i \qquad A_{i\%} = 100 A_i / \sum_{i=1}^{m} A_i \tag{1.50}$$

The set of pairs ($T_{2i}$, $A_{i\%}$) is called the magnetic relaxation spectrum and matches the mechanical relaxation spectrum ($\lambda_i$, $G_i$) seen in the rheology overview.

Determining the parameters of eq. (1.49), i.e. the magnetic relaxation spectrum, as already seen for the mechanical spectrum ($\lambda_i$, $G_i$), involves fitting eq. (1.49) to the experimental relaxation data. Fitting, in turn, involves minimizing the quadratic deviation ($\chi^2$), which measures the "distance" between the experimental data and the model represented by eq. (1.49). The criterion used to statistically define the number $n$ of exponentials appearing in eq. (1.49), is identical to that set out in the case of rheological relaxation. In fact, $n$ is chosen to minimize the product $\chi^2 \cdot 2n$, where $2n$ indicates the number of fitting parameters appearing in eq. (1.49).

*Surface effect on $T_{2m}$*

Solid surfaces have an effect on the relaxation of the hydrogenated fluid analyzed by LF-NMR and this is important to obtain nano-structural information on the systems under investigation. For this purpose, we must consider the theory of Brownstein and Tarr

(Brownstein and Tarr, 1977), which aims to explain and simulate the effect of a surface on the relaxation of $\mu_i$ near the surface. This theory argues that the presence of paramagnetic substances on the surface in contact with the fluid and/or the topological constraint of the surface on the mobility (rotation) of the fluid molecules in its vicinity make the surface itself a magnetization absorber. This means that in the presence of a solid surface, the $\mu_i$ hydrogens of solvent molecules (water in general) relax faster than those belonging to hydrogens of molecules distant from the surface. The mechanical analogue of this situation is a bar embedded rigidly in a wall. Imagine hitting by a hammer the free end of a rod that is embedded in the wall for a small fraction of its length. We will see that the rod will begin to oscillate and slowly return to its equilibrium condition (non-oscillating rod). If we repeat the same experiment by embedding the rod in the wall for a much larger section of its length, we will see that the oscillations will be smaller in amplitude and of greater frequency so that the rod will reach the equilibrium position more quickly. The rod that is more constrained in the wall behaves qualitatively like the hydrogenated molecules near the surface, although the principles governing the two phenomena (magnetic and mechanical relaxation) are different.

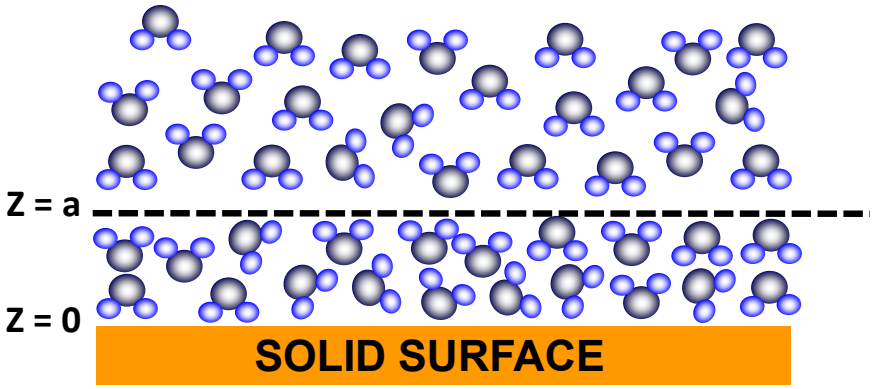


Figure 20: Hydrogenated molecules close to the surface ($Z \leq a$) are said to be "bound" and relax rapidly with a low relaxation time $T_{2s}$. Hydrogenated molecules far from the surface ($Z > a$) are not affected by the surface at all and relax slowly with a relaxation time $T_{2b} >> T_{2s}$.

From the solution of the magnetization diffusion equation, Brownstein and Tarr derive an interesting relationship between the parameters of the system under investigation:

$$\left(\frac{1}{T_2}\right)_m = \frac{S}{V}\mathcal{M} + \frac{X_{FW}}{T_{2b}} = \frac{Sa}{V}\frac{1}{T_{2s}} + \frac{X_{FW}}{T_{2b}} \tag{1.51}$$

where S is the solid surface in contact with the volume V of hydrogenated molecules, $T_{2b}$ is the relaxation time of the hydrogenated fluid molecules in the absence of S (i.e. the relaxation time of fluid molecules far from the surface, the "free" molecules), $X_{FW}$ denotes the

fraction of "free" fluid (i.e. the volumetric fraction of fluid far from the surface), while $\mathcal{M}$ is a parameter called relaxivity. It represents the ratio between the thickness of the layer "a" of molecules close to the surface (the "bound" molecules) and their relaxation time $T_{2s}$.

To be precise, due to the inhomogeneity of $B_0$ (as discussed earlier in connection with the CPMG sequence), a third term ($1/T_{2D}$), related to the movement (diffusion) of the hydrogenated molecules, should appear on the right-hand side of eq. (1.51). However, it can easily be shown that, in general, as in this case, this term is negligible, being approximately 0.003% of $1/T_{2b}$ (Kopač et al., 2022).

Therefore, eq. (1.51) tells us that the average value of the inverse of the relaxation time is the volume-weighted average of the inverse of the relaxation times $T_{2s}$, of the "bound" fluid, and $T_{2b}$, of the "free" fluid. Since, usually, $X_{FW} \sim 1$, eq. (1.51) is practically always given in its approximate form:

$$\left(\frac{1}{T_2}\right)_m \approx \frac{S}{V}\mathcal{M} + \frac{1}{T_{2b}} \tag{1.52}$$

*Ferromagnetic effect on $T_{2m}$*

A ferromagnetic material (such as iron, cobalt and nickel) has a magnetic moment even at zero applied field and a paramagnetic material (i.e. aluminum, platinum) has a magnetic moment proportional to the applied field. In fact, paramagnetism refers to materials which become magnetized in a magnetic field, but their magnetism disappears when the field is removed. Ferromagnetism refers to materials that can retain their magnetic properties when the magnetic field is removed, becoming a permanent magnet. Both types of magnetism may contribute to the net field experienced by the nuclear spins (Tayler et al., 2019).

In fact, a ferromagnetic material affects the relaxation times ($T_{1m}$ and $T_{2m}$) due to the alteration of the magnetic environment. For this reason, in the presence of ferromagnetic substances, LF-NMR analysis does not yield nano-structural information but instead highlights the quantity of these ferromagnetic materials.

## 1.3. Biomedical approach of the rheological characterization and the LF-NMR

Rheological analyses and LF-NMR characterization are widely use in different biomedical areas, such as the study of biomaterials (e.g. hydrogels) with potential application in the biomedical field, pharmaceutical formulations and biological soft tissue. Hydrogels are used as biosensors, drug delivery vectors, and carriers or matrices for cells in tissue engineering (Chai et al., 2017). Rheology and LF-NMR are useful to understand their mechanical behavior and the complex structure of their polymeric networks. Moreover, rheology and LF-NMR techniques can evaluate the mesh size of hydrogels designed for drug delivery. Rheology is also used to study biological soft tissue, in fact, their mechanical behavior is a major concern in bioengineering and biomechanical research. Many mechanical models have been proposed to describe the behavior of soft tissues. Among them, brain tissue has been the most extensively studied. Available data on other soft tissues is comparatively sparse and more recent (renal and hepatic tissue) (Nicolle et al., 2010). In this thesis we will apply these techniques to the study of biological soft tissues, liver tissues, in healthy and pathological conditions, and alginate hydrogels used as *in vitro* models that can mimic healthy and fibrotic liver tissue mechanical behavior.

Recently, my research group applied rheology and LF-NMR also as a diagnostic tool in a lung disease, cystic fibrosis (CF). CF is an autosomal recessive disease caused by mutations in a single gene, located on the long arm of chromosome 7, which encodes a transmembrane glycoprotein named “Cystic Fibrosis transmembrane conductance regulator” (CFTR) (Chen et al., 2021). The airways are among the tissues with the highest expression of CFTR, hence dysfunctional CFTR causes several alterations into airway secretions. The pathological increase of proteins, mucin and biological polymers determines their arrangement into a three-dimensional polymeric network, affecting the whole mucus. These alterations lead to poorly hydrate and hyper-concentrated mucus that impairs muco-ciliary clearance, favoring the pathological invasion of microorganisms (Tildy and Rogers, 2015). These features of CF mucus (hyper-concentration and dehydration) affect the rheology and the mean relaxation time ($T_{2m}$) of water hydrogens of sputum samples. The combined use of rheology and LF-NMR has shown to be very useful to study the nanostructure and the mesh size distribution of the sputum from CF patients, giving synergic results from the determination of the mechanic and magnetic relaxation spectra (Abrami et al., 2021). These techniques show also to be useful to explore the effects of chest physiotherapy on CF sputum characteristic and to monitor lung conditions (Abrami et al., 2022). Moreover, obtaining a deeper understanding of

the mesh length distribution in CF sputum, is essential for drug delivery. In fact, the dense and adhesive nature of mucus in CF airways presents a significant obstacle to drug delivery, impeding drug penetration into lung tissues, thereby diminishing their effectiveness. To ensure drugs reach their intended targets in the lungs, it is important to deeply study this mucous barrier.

## 1.4. Liver fibrosis (LF)

*Liver*

The liver is the largest solid organ in the human body and has two major sources of blood supply, namely the portal vein, which brings venous blood from the intestine and spleen, and the hepatic artery, which brings arterial blood from the celiac axis. The liver is encapsulated by the Glisson's capsule, composed of connective tissue, and divided into microscopic polygonal sections called lobules, which are also separated by connective tissue (Acharya et al., 2021). Each lobule has a characteristic hexagonal structure with the central vein in the center and in the edges the hepatic portal vein, hepatic artery and biliary ducts. Hepatocytes are the main parenchymal cells and are responsible for a large proportion of the liver function, such as detoxification of xenobiotics, urea cycle and the synthesis of plasma proteins. In the lobules, the hepatocytes are arranged in rows radiating outwards from the central vein, toward the edge of the lobule (Figure 21). The gaps between the hepatocyte rows are known as sinusoids which are lined with endothelial cells (liver sinusoidal endothelial cells - LSECs), and contain Kupffer cells (KCs, the resident macrophages), hepatic stellate cells (HSCs), and extracellular matrix (ECM) material such as the non fibrogenic type IV collagen. HSCs, KCs, LSECs, together with portal fibroblasts and non-resident immune cells constitute the liver's non-parenchymal cell fraction (Campana et al., 2021). The hepatic portal vein, hepatic artery and biliary tree are the major vessels feeding into the sinusoids and the exchange of blood gases, nutrients and other signaling molecules occurs in the sinusoids.

This elegant arrangement of the lobules is disturbed during liver fibrosis and is completely damaged during cirrhosis.

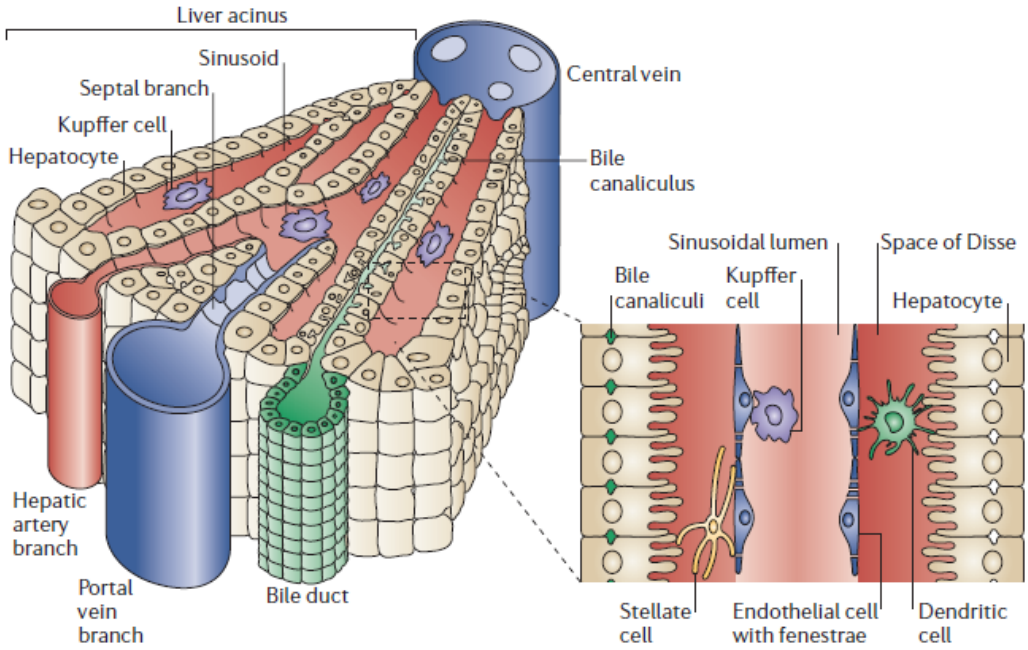


Figure 21: Structure of a liver lobule. Blood enters the liver lobules via the hepatic artery, which then forms hepatic sinusoids that drain into the central vein. The portal vein is an additional source of blood, bringing nutrient- and antigen-rich blood from the gastrointestinal system to the liver. Blood from hepatic artery and portal vein mix in the sinusoids. The sinusoids are formed by unique endothelial cells, that are characterized by the absence of tight junctions, the absence of a recognizable basement membrane and the presence of open fenestrae. Kupffer cells, which are phagocytic cells, are found within or below the fenestrated sinusoidal endothelium (pictured here within the sinusoids). These cells serve important filtering function, removing and processing antigens that arrive from the gastrointestinal tract. In the space of Disse (the space just below the endothelium), there are extracellular matrix proteins and other stromal cells, including stellate cells and dendritic cells. Hepatocytes form rows and between these rows the biliary canaliculi are located (Adams and Eksteen, 2006).

*Liver fibrosis*

Interacting with components of circulation arriving from the rest of the body, liver is exposed to injury of external agents, leading to the activation of the natural fibrogenic wound healing response of the body. But a long-term injury of liver components and a consistent activation of the fibrogenic response results in the liver fibrosis (LF). LF results from chronic liver injury of different etiologies. Hepatitis C Virus (HCV) infection, Hepatitis B Virus (HBV) infection, metabolic-associated fatty liver disease (MAFLD), hereditary hemochromatosis, porphyria and alcohol or hepatotoxic medications abuse as well as non-alcoholic fatty liver disease (NAFLD) and its more aggressive form non-alcoholic steatohepatitis (NASH) are all liver diseases which if not treated, lead to chronic injury and chronic liver diseases (CLDs) (Mazza et al., 2017). Indeed, indifferent from etiology, if left untreated these factors will cause the development of liver fibrosis and subsequently cirrhosis, which in turn can evolve into hepatocellular carcinoma (HCC).

During fibrogenesis, crosstalk between parenchymal and non-parenchymal cells, activation of different immune cells and release of several inflammatory mediators take place, resulting in inflammation. Excessive inflammation drives HSCs activation, which plays a

crucial role in liver fibrosis and in the ECM deposition (Khanam et al., 2021b). HSCs are mesenchymal cells which lie in the space of Disse, between the hepatic sinusoidal endothelium and the rows of hepatocytes. These cells are rich in vitamin A, which is stored in the form of retinol esters within cytoplasmic droplets (Iredale et al., 2013). During liver injury HSCs encounter various morphological and functional changes, transforming into proliferative and ECM-producing myofibroblasts. When activated to a myofibroblast-like phenotype, these cells proliferate, express α-smooth muscle actin (α-SMA) and secrete fibrillar collagens (e.g. collagen I), elastin and ECM proteins to form a fibrous scar (Iredale et al., 2013; Khanam et al., 2021a). As a result, in LF the composition and density of the extracellular matrix (ECM) change, interfering with hepatic function. Non-fibrogenic type IV collagen is replaced by fibrogenic type I and II collagen and there is additional secretion of fibronectin, hyaluronic acid and α-SMA into the ECM (Acharya et al., 2021). Moreover, studies have demonstrate that in cirrhotic liver, beside the disproportionate increase in the fibrogenic collagens, there are increases in laminin, elastins and proteoglycans (Iredale et al., 2013).

The long-term fibrogenic response in liver and the modifications in the ECM result also in alterations in the mechanical properties of the liver tissue, such as increased stiffness. In turn, stiffness mechanotransduction amplifies fibrogenesis (Kostallari et al., 2022). Indeed, hepatic stellate cells require a stiff environment for myofibroblastic differentiation (Olsen et al., 2011), thus initiating a domino effect leading to impaired liver function.

*Interaction ECM-HSC*

The transdifferentiation of HSCs into myofibroblasts results in ECM accumulation and disrupts its remodeling, leading to an increase in ECM stiffness. This augmented stiffness may play a critical role in the progression of fibrosis, as it is detected by surface receptors on HSCs, such as integrins, which in turn activate cellular processes (Caliari et al., 2016).

HSCs activation is driven by the TGF-β1 signaling pathway, which is also considered the most relevant liver fibrogenic cytokine. Furthermore, TGF-β1 is linked to the ECM. In fact, TGF-β1 is synthesized as a latent precursor with its prodomain and stored in the ECM as part of a large complex. It is activated by mechanical force that induce the conformational changes of the latent complex and release of active TGF-β. The two main elements that promote the release of the active TGF-β are the augmented contractility of activated HSCs and the increased mechanical strength of ECM due to its accumulation and consequent higher tissue stiffness. Integrins are essential in this process, as they convey the actin cytoskeleton

contraction force to the prodomain of the large latent inactive TGF-β complex located in the ECM. It follows that the interaction between ECM and the actin cytoskeleton through integrins promotes the release of TGF-β from the latent TGF-β binding protein complex. The activation of this pathway regulates the transcription of genes that allow the maintenance of the HSCs' fibrotic state, driving fibrogenesis and ECM production through a domino effect of a paracrine activation of HSCs (Ortiz et al., 2021).

*Extracellular matrix degradation during liver fibrosis*

Abundant matrix synthesis by myofibroblasts undeniably plays a significant role in the development of fibrosis. However, evidence now suggests that fibrosis progression is also influenced by changes in the pattern of matrix degradation.

In fact, as fibrosis advances, HSCs not only proliferate and secrete ECM proteins but also modify the balance between metalloproteases (MMPs) and their inhibitors, the tissue inhibitors of metalloproteinases (TIMPs). Even during progressive liver fibrosis, there is evidence suggesting for matrix degradation primarily mediated by MMPs. MMPs are zinc and calcium-dependent endopeptidases produced in the liver by hepatocytes, HSCs, KCs, neutrophils, and recruited hepatic macrophages. MMPs are meant to sustain tissue homeostasis by degrading old proteins for renewal and actively target key ECM components, including fibrillar and non-fibrillar collagens, as well as elastin. Notably, the types of MMPs expressed by HSCs and macrophages change with specific phenotypic alterations associated with *in vivo* fibrogenesis. Collagenases, a subgroup of MMPs, play a critical role in reshaping fibrotic tissue by cleaving the native helix of fibrillar collagens, which converts them into a gelatin form that is more easily degraded by other MMPs. The activity of MMPs in the extracellular environment is tightly regulated at multiple stages to prevent potential damage from these powerful proteases. This regulation occurs primarily at the gene level, influenced by various cell signals including growth factors and cytokines such as TNFα, PDGF, EGF, IL-1 and TGF-β1. Moreover, active MMPs can be inhibited by TIMPs, which are soluble proteins that noncovalently bind to MMPs, effectively blocking their enzymatic function (Iredale et al., 2013; Ortiz et al., 2021).

*Fibrosis resolution*

Large-scale trials of antiviral treatments for hepatitis B and C provide strong evidence that spontaneous resolution of liver fibrosis can occur in humans, demonstrating fibrosis remodeling and a partial return to normal liver architecture. Some studies also suggest that

matrix remodeling may be possible even in advanced cirrhosis, though not all advanced cases may be entirely reversible, leaving this area controversial (Iredale et al., 2013).

At the cellular level, the resolution of liver fibrosis always involves HSCs. In fact, a key defining feature of the spontaneous resolution of liver fibrosis is the apoptosis of myofibroblast-like hepatic stellate cells (Iredale, 2001). However, other studies have also shown evidence of some phenotypic reversion to quiescence in these cells (Kisseleva et al., 2012; Troeger et al., 2012) (Figure 22).

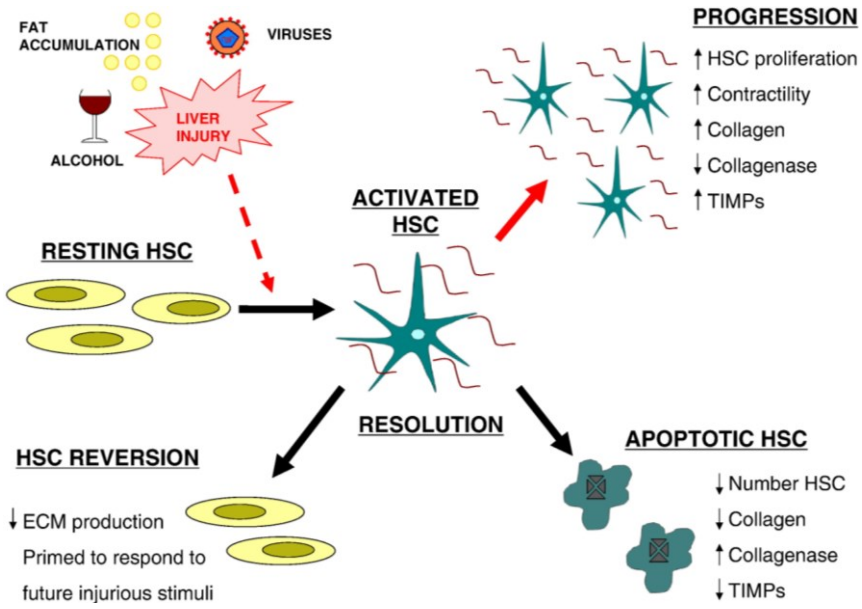


Figure 22: Liver injury activates quiescent HSCs into activated HSC (liver myofibroblasts), leading to the secretion of extracellular matrix proteins, such as fibrillar collagens. Repeated liver injury amplifies this process, ultimately resulting in cirrhosis. In contrast, during the resolution of liver fibrosis, HSC can either undergo programmed cell death (apoptosis) or revert to a deactivated state, which reduces ECM production (Iredale et al., 2013).

.

*Metabolic disorders: NAFLD and NASH*

The metabolic syndrome, linked to obesity and type 2 diabetes mellitus, elevate cardiovascular risks and can lead to NAFLD (Acharya et al., 2021). NAFLD is characterized by excessive fat accumulation in the liver, which is associated with insulin resistance. It is defined by the presence of steatosis in more than 5% of hepatocytes as determined by histological analysis or through imaging techniques. NAFLD includes two distinct pathological forms: non-alcoholic fatty liver (NAFL) and non-alcoholic steatohepatitis (NASH). NASH exhibits a wider range of disease severity and can progress to complications such as steatosis, fibrosis, cirrhosis, and HCC (European Association for the Study of the Liver et al., 2016).

Recently, the term NAFLD is moving to the term MAFLD, metabolic-associated fatty liver disease. The diagnosis of MAFLD is based on the presence of hepatic steatosis and at

least one between these three conditions: type 2 diabetes mellitus, obesity or metabolic dysregulation (Boccatonda et al., 2023). However, in this thesis we will refer to NAFLD term.

NAFLD pathogenesis is complex but centers on the conversion of HSCs into profibrogenic myofibroblasts via TGF-β signaling, which regulates multiple cellular processes, including hepatocyte injury and fibrosis (Acharya et al., 2021). Emerging research suggests several genes and pathways, particularly in lipogenesis and inflammatory signaling, are involved at various stages of NAFLD progression to NASH and HCC (Locke et al., 2008; Ryaboshapkina and Hammar, 2017). Limited proteomics studies emphasize the importance of PPAR signaling, ECM interactions, and oxidative phosphorylation in NAFLD, indicating a complex interplay of metabolic and inflammatory processes at work (Yuan et al., 2020).

In fact, the accumulation of free fatty acids in the liver leads to the production of reactive oxygen species (ROS) and oxidative stress, which are crucial in promoting fibrosis through various pathways. Oxidative stress prevents the replication of mature hepatocytes, causing an increase in immature progenitor cells. Moreover, ROS contributes to fibrosis in NAFLD and NASH by triggering the release of pro-inflammatory cytokines and transforming cholangiocytes (the epithelial cells of the bile ducts) into fibrogenic myofibroblasts (Khanam et al., 2021a).

NAFLD is reaching epidemic levels globally, affecting about 25% of the population and up to 60% among obese and type 2 diabetes patients. NASH has a global prevalence of 2-6% and is associated with significant hepatic inflammation, fibrosis, and an increased risk of cirrhosis and HCC. Recently reported trends in the incidence of NAFLD over time suggest that NAFLD will become the leading cause of end stage liver disease in the decades to come (Acharya et al., 2021).

*Iron metabolism in liver fibrosis*

As we have already discussed, liver fibrosis occurs as a result of an excessive wound healing response to ongoing liver injury, disrupting liver structure and function, and is commonly seen in untreated CLDs such as haemochromatosis, viral hepatitis (such as hepatitis B and C), alcoholic liver disease (ALD), NAFLD, NASH, and diabetes. A common feature of all these conditions that promote LF is elevated iron levels (Kowdley, 2016), indicating that iron loading may increase the risk of disease progression and worsen liver pathology.

Iron is vital for normal physiology, but excess iron is toxic as it can enhance the Fenton reaction, producing harmful ROS that damage cells and tissues. Maintaining iron homeostasis

is crucial because the body lacks a mechanism to remove excess iron. Hepcidin, an iron-regulating hormone produced by hepatocytes, controls systemic iron levels. It is released in response to rising iron saturation of plasma transferrin (the glycoprotein that binds and mediate the transport of iron through blood plasma), increased hepatic iron stores, or inflammation, and negatively feeds back to reduce iron availability. In fact, hepcidin binds to and degrades ferroportin (the transmembrane iron-exporter protein), on the iron-storing macrophages and hepatocytes, thereby reducing iron entry into circulation. Hepcidin also decreases intestinal iron absorption by interacting with ferroportin on enterocytes and downregulating the expression of divalent metal transporter DMT-1 protein, that mediates the iron uptake on the apical surface of enterocytes (Hilton et al., 2023; Mehta et al., 2019). A deficiency or resistance to hepcidin due to genetic mutations can lead to hereditary hemochromatosis, characterized by excessive iron absorption from the duodenum, unregulated iron release from macrophages and deposition in various organs. Additionally, excess iron is observed in several non-hereditary liver pathologies, where it can accelerate the progression of liver fibrosis to cirrhosis and hepatocellular carcinoma, regardless of disease etiology. In non-hereditary CLDs the exact role of iron is unclear, raising questions about whether iron overload is a cause, consequence, or mediator of disease progression (Mehta et al., 2019).

Thus, iron enhances fibrogenic responses and is a cofactor in the development of liver damage. In fact, in iron loading HSCs activation and excessive ECM deposition are cumulative consequences of direct and indirect effect of iron on the HSCs (Mehta et al., 2019). For the first time, Ramm et al. (Ramm et al., 1997) demonstrated a correlation between liver iron concentration (LIC) and HSCs activation in humans, resulting in increased expression of α-SMA and collagen deposition in patients with haemochromatosis. In animal studies, iron raised collagen gene expression in HSCs and increased TGF-β expression in rats (Houglum et al., 1994), induced collagen deposition in gerbil (Carthew et al., 1991) and promoted cirrhosis in mice (Arezzini et al., 2003). Moreover, in rat HSCs iron increased HSCs proliferation, selectively increased collagen synthesis (Gardi et al., 2002), and increased expression of α-SMA and collagen I (Bridle et al., 2003). Rat HSCs, when treated with ferritin, demonstrated a pro-inflammatory cascade by nuclear factor kappa-B signalling (Ruddell et al., 2009). In murine HSCs showed transferrin-induced elevations in α-SMA, collagen secretion and vimentin (Mehta et al., 2018). Furthermore, iron loading in CLDs predominantly occurs in the hepatocytes and Kupffer cells, and this supports the indirect

effect of iron on HSCs for which iron-damaged hepatocytes and macrophages release humoral factors that activate the HSCs (Mehta et al., 2019).

In different studies, a correlation between excessive hepatic iron accumulation and liver diseases, such as NASH associated with increased fibrosis (George et al., 1998), HCC developed on NASH (Sorrentino et al., 2009). Elevated LIC is observed in about 33% of adult NAFLD patients (Kowdley, 2016) and it is suggested to be associated with increased fibrosis (George et al., 1998).

Moreover, in a recent clinical study serum ferritin (the main protein involved in iron storage, mainly found in the liver and spleen) level was an independent factor predicting advanced fibrosis in NAFLD participants in a non-obese Chinese population (Yao et al., 2019).

A different situation occurs in obese patients. In fact, obesity has been closely linked to important perturbations in iron metabolism and is associated with iron deficiency, and, eventually, to anemic state. This is because every component involved in the main regulatory pathway controlling hepcidin synthesis is exacerbated in obesity, including the enzyme (furin) involved in the cleavage of the active form of this peptide hormone (González-Domínguez et al., 2020). For this reason, patients with obesity have higher hepcidin levels which rise with BMI. High levels of hepcidin reduce the iron uptake by enterocytes and the release from iron-storing macrophages and hepatocytes, resulting in iron deficiency (Hilton et al., 2023).

*Diagnosis for liver fibrosis*

Liver biopsy is the gold standard for the diagnosis of liver fibrosis. Histochemical staining can be used to stain the cells or the extracellular matrix proteins to identify liver fibrosis. Common histological staining methods for liver fibrosis evaluation are hematoxylin-eosin staining. Moreover, non-invasive techniques (e.g. elastography scanning) and biomarkers (e.g. platelet ratio or transaminases levels, such as aspartate amino transferase (AST), alanine amino transferase (ALT) and gamma glutamyl transpeptidase (GGT)) can be applied for diagnosing liver fibrosis (Zhang et al., 2023).

In the EASL (European Association for the Study of the Liver) Clinical Practice Guidelines on non-invasive tests for evaluation of liver disease severity and prognosis, updated to 2021 (European Association for the Study of the Liver et al., 2021), the liver stiffness can be measured with magnetic resonance elastography and shear wave ultrasound elastography techniques, that allow to estimate tissue mechanical properties *in vivo* by

exploiting the relationships between the viscoelastic properties of a material and its wave propagation. However, there are several factors that affect the measurements. These include patient factors like the presence of obesity (due to the impact of abdominal wall thickness on measurement accuracy), fasting, blood pressure, position, medications, and co-morbidities (Barr, 2018). Moreover, soft tissue rheology is very complex; soft tissues are nonlinearly viscoelastic, inhomogeneous, and often anisotropic, and their apparent stiffness can vary with the current loading state and the water content (Bilston, 2018).

As an anticipation of the work presented in this thesis, our research group set out to measure the mechanical properties of liver tissues using a different approach, that is a direct measurement of the mechanical behavior per means of the rheometer of liver biopsies (permission of the university ethics committee obtained at its meeting on 1-12-22 record no. 126). This is a direct approach that by-passes all the problems of an *in vivo* measurement and permits an accurate mechanical characterization of the liver tissue.

*Therapies for liver fibrosis*

Many treatments for liver fibrosis have been investigated in clinical trials, including dietary supplementation (e.g. vitamin C), biological treatment (e.g. simtuzumab), drug (e.g. pegbelfermin), genetic regulation (e.g. non-coding RNAs), and transplantation of stem cells (e.g. hematopoietic stem cells). However, at the present day, there are no drugs approved either by the Food and Drug Administration (FDA) or by the European Medicines Agency (EMA), hence there is an urge to develop liver antifibrotic therapies as well as anti-NASH therapy (Kumar et al., 2021; Zhang et al., 2023).

Thus, current therapeutic options for liver fibrosis are to prevent the initial causing factors for liver inflammation, hepatocyte cell death and oxidative stress. Currently, promising treatments for liver fibrosis are still the preventive strategies, such as treatment of hepatitis viral infection, inhibition of the progression of MAFLD and obesity (e.g. physical activity, dietary change (such as mediterranean diet or calorie-restricted diet), dietary supplementation (such as vitamin C, prebiotics), and bariatric surgery). Unfortunately, the reverse of liver fibrosis is slowly and frequently impossible for advanced fibrosis or cirrhosis. Liver transplantation is the only therapeutic option for the late stage of liver cirrhosis and cancer (Khanam et al., 2021a; Zhang et al., 2023). As there is a disproportion between the high demand and the low availability of livers for transplantation, cirrhosis is a major cause of morbidity and mortality globally, imposing a heavy health burden on many countries (Yan et al., 2021). Globally, an estimated 1.16 million people die every year from liver cirrhosis,

being the 11th most common cause of death (Asrani et al., 2019). Hepatic fibrosis is therefore associated with significant mortality and is therefore of particular interest to national health systems (Yan et al., 2021).

While we currently lack effective strategies for treating liver fibrosis, pre-clinical and clinical evaluations for new treatments are essential. The development of innovative *in vitro* models may enhance the discovery of compounds with anti-fibrotic properties (Mazza et al., 2017). Additionally, new delivery systems can improve the efficacy of treatments and minimize therapy side effects. Additional clinical studies are also needed to confirm the safety and effectiveness of treatments.

As an anticipation, this thesis presents an *in vitro* model that mimics liver fibrosis tissue and analyzes novel compounds to treat this condition.

## 1.5. Alginate hydrogels as *in vitro* models for liver fibrosis

The development of advanced *in vitro* models has the potential to significantly improve the process of discovering new compounds that possess anti-fibrotic properties. By simulating the fibrotic environment more accurately, researchers can better evaluate how different compounds affect fibrosis and potentially identify effective treatments. These models can mimic the biological conditions of fibrotic tissues, allowing for more precise screening and understanding of the mechanisms by which these compounds work, ultimately leading to the development of effective therapies for liver fibrosis (Mazza et al., 2017).

On the other hand, cell cultures on traditional plastic surfaces offer various advantages: they are relatively easy to set up and maintain, have been widely used for decades, and, for this reason, they lead to well-established protocols that facilitate reproducibility and comparison between studies. Furthermore, they require few specialized pieces of equipment and materials, making them more affordable. However, when considering cell cultures of HSCs, these types of cultures on plastic surfaces present some limitations. Indeed, cells adopt an unnatural flat and elongated shape when cultured on plastic, and a large portion of the cell surface is in contact with the plastic. Moreover, the stiffness of the plastic material (> 2 GPa) differs significantly from that of liver tissues (~ 1-20 kPa), whether physiological or pathological. Ultimately, traditional plastic surfaces lack ECM-specific bioactive cues (Mazza et al., 2017). All these disadvantages can affect the translatability of results to *in vivo* scenarios. For all these reasons, we prepared hydrogel surfaces for cell culture to better mimic the ECM environment and to resemble the rheological characteristics of liver tissue.

Usually, *in vitro* models for cell tests are designed with biomaterials that can mimic the extracellular matrix. ECM surrounds cells within tissues, providing mechanical support and regulating cellular behavior by storing adhesion molecules, growth factors, and cytokines (Ortiz et al., 2021). For this purpose, we hydrogel surfaces with alginate polymer.

Alginates are natural hydrophilic polysaccharides made of linear polymers typically obtained by extraction from brown algae (*Phaeophyceae*) by treatment with aqueous alkali solutions, typically with NaOH. Alginates can be synthetized also from bacteria, such as *Azotobacter* and *Pseudomonas*. Alginates are often the subject of research due to their numerous advantages: biocompatibility, low toxicity, low cost, possibility of ionic gelation (Lee and Mooney, 2012).

The structure of alginates is composed of linear copolymers consisting of blocks of D-mannuronic acid (M) and L-guluronic acid (G) arranged consecutively (MMMM/GGGG) or

alternately (GMGMGM). The content of M and G residues can vary, which allows for a wide choice of alginates with different mechanical properties (Augst et al., 2006).

Only the G residues of alginate engage in intermolecular cross-linking with divalent cations (e.g. $Ca^{2+}$) to create hydrogels, resulting in an ionic crosslinking with the typical structure of egg-box (Figure 23). Consequently, critical factors influencing the physical properties of alginate and its resulting hydrogels include the composition (i.e. M/G ratio), sequence, G-block length, and molecular weight. Typically, the mechanical properties of alginate gels improve with an increase in G-block length and molecular weight. To obtain an alginate hydrogel, the process of gelation of the aqueous alginate solution is required. The most common methodology uses as ionic cross-linking agents calcium ions, which only interact with the G monomers, forming intermolecular bonds between neighboring polymeric blocks, resulting in a gel-like structure. Generally, a calcium chloride solution ($CaCl_2$) is used to provide calcium ions, even though it leads to immediate and therefore poorly controlled gelation from a mechanical point of view. In fact, the gelation rate can vary the strength and uniformity of the resulting hydrogel (Lee and Mooney, 2012).

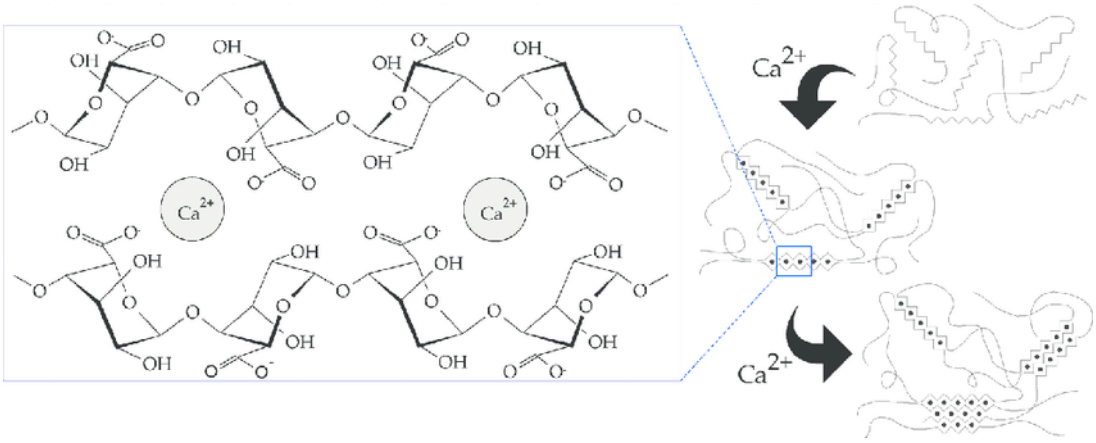


Figure 23: Alginate polymer chains crosslink with calcium ions, forming the typical egg box structure (https://www.researchgate.net/figure/The-egg-box-model-of-gelation-of-alginate-by-calcium_fig3_312344348).

Alginate hydrogels are increasingly used as model systems for 2D- or 3D-cell cultures. Alginate alone would not allow cell adhesion as it lacks essential components for cell binding. However, it is possible to add RGD peptide sequences for cell adhesion. In this way, alginate hydrogels can mimic not only mechanically but also chemically the microenvironment in which cell live, grow, differentiate and interact with the ECM and one to each other. In the specific case of this thesis, alginates have been used for their ability to mimic the viscoelastic properties of both physiological and pathological liver tissue and, therefore, for their influence on how cells behave.

## 1.6. Deubiquitinase (DUBs) inhibitors

In this thesis, compounds with deubiquitinase inhibiting activity were took into consideration. These compounds were synthesized at the bio-organic chemistry laboratory of Prof. Benedetti and Prof. Felluga (Dipartimento di Scienze Chimiche e Farmaceutiche of the University of Trieste).

*Ubiquitin-proteosome system (UPS)*

The ubiquitin-proteasome system (UPS) is the major proteolytic system that controls protein degradation and it regulates many cellular processes, such as cell cycle, DNA repair and stress response. The UPS is made up of specific enzymes that modify proteins by attaching ubiquitin and 26S proteasomes responsible for proteolysis of ubiquitin-tagged proteins (Park et al., 2020). This process can be divided into two parts, the first being ATP-dependent and the second not relying on the ATP availability (Nandi et al., 2006).

Ubiquitination is a post-translational modification that influences protein function, localization, protein-protein interaction, and protein stability. The UPS regulates protein homeostasis, involving the covalent bonding of one or multiple ubiquitin molecules to promote proteolysis of a protein that is set to be eliminated. Moreover, the UPS aims to degrade misfolded and damaged proteins, cell-cycle regulators, oncogenic proteins, and oncosuppressor proteins, and to regulate antigens expression and transcription factors activity (Wertz and Murray, 2019).

The process of adding ubiquitin to a protein involves a series of steps with three types of enzymes: E1, E2, and E3. First, the ubiquitin-activating enzymes (E1) use energy from ATP to form a thioester bond between the carboxyl-terminal of a ubiquitin and a cysteine residue in the E1 enzyme. This activated ubiquitin is then transferred to the ubiquitin-conjugating enzymes (E2), where another thioester bond is formed. Finally, the E2 enzymes work with the ubiquitin ligases (E3) to attach the activated ubiquitin to the target protein (Park et al., 2020).

Ubiquitin binds covalently to cellular target proteins through an isopeptide bond between the carboxyl-terminal glycine of the ubiquitin and ε-amino groups of lysins present in target proteins (Shaid et al., 2013).

There are three types of ubiquitination, with the most common being monoubiquitination, Lys48-linked polyubiquitination, and Lys63-linked polyubiquitination. The effects of ubiquitination differ based on the type. Monoubiquitination enhances protein identification, allosteric regulation, and the formation of protein complexes. In contrast, Lys48-linked polyubiquitination signals for proteasomal degradation, while Lys63-linked

polyubiquitination is non-degradative and contributes to cellular signaling and intracellular trafficking. For this reason, ubiquitin receptors possess multiple ubiquitin-binding domains (UBDs) that allow them to recognize various ubiquitin signals (Mevissen and Komander, 2017).

After ubiquitination, proteins with the opportune ubiquitination are degraded by the 26S proteasome, a complex made up of the 20S core particle with catalytic activity, which is covered by one or two 19S regulatory particle. The 19S controls the entry of proteins into the degradation machine, ensuring that only targeted proteins are degraded. In fact, the sub-complex 19S recognizes and binds polyubiquitin chains with high affinity, thus enabling correct recognition of target substrates. This sub-complex consists of a series of Rpn proteins, among which Rpn10, that contains two C-terminal motifs that interact with ubiquitin and cooperate to bind polyubiquitin chains, Rpn13, that binds to Lys48-linked diubiquitin with high affinity, and Rpn11, a deubiquitinase (DUBs) responsible for the removal of the substrate-bound ubiquitin chain before they enter the proteosome (Bard et al., 2018).

*Deubiquitinases or deubiquitinating enzymes (DUBs)*

The ubiquitination process is highly dynamic and can be reversed by the action of specialized enzymes known as isopeptidase. Isopeptidases can be viewed as E3-ligase antagonists, however, they have additional functions, such as maturation of ubiquitinis. The isopeptidase family includes deubiquitinating enzymes (DUBs), which in principle should be specifically devoted to the rupture of ubiquitin linkages (Cersosimo et al., 2015). Deubiquitinases are enzymes that are mainly involved in the regulation of the ubiquitin pool within the cell. In fact, the deubiquitination involves the removal of ubiquitin, the disassembly of ubiquitin chains to inhibit their signal and the recycle of ubiquitin for subsequent conjugation. DUBs are a superfamily of cysteine proteases and metalloproteases that cut the bond established between ubiquitin and protein. Their action is performed by hydrolyzing the bond formed between the carboxyl group at the C-terminus of the ubiquitin molecule and the ε-amino group of the Lys present on the protein. These enzymes are also involved in other complex processes such as DNA repair, cell cycle regulation, genome stability, redox regulation and apoptosis (Varca et al., 2021). Consequently, DUBs dysregulation leads to severe complications, including neurological disorders and cancer (e.g. mesotheliomas, melanomas, renal cell carcinomas, glioblastomas, ovarian carcinoma, breast carcinoma) (Antao et al., 2020; Snyder and Silva, 2021).

At the level of the proteasome complex, the activity of DUBs is required to regulate the protein degradation and the recycling of ubiquitin molecules. In other cases, they are involved in the remodeling of ubiquitin tails bound to target proteins in the process of ubiquitination in which they stabilize erroneously ubiquitinated protein substrates by preventing their proteasome-dependent degradation or modulate the amount and type of polyubiquitin chain bound to substrates (Bard et al., 2018; Snyder and Silva, 2021).

DUBs have three different mechanisms of action:

- the generation/release of free ubiquitin (De Novo Ub Synthesis), where ubiquitin is transcribed as a sequential chain of by the ribosome and the release of free ubiquitin is generated by the DUBs activity.
- the cleavage of polyubiquitinated chains, where DUBs' cleavage along the ubiquitin chains has different outcomes depending on their location. In this way, DUBs and E3 enzymes regulate protein degradation.
- the complete removal of ubiquitin chains, where proteins are stabilized and do not undergo UPS degradation. The action of DUBs releases ubiquitin portions which go through recycling to maintain the ubiquitin homeostasis (Farshi et al., 2015).

DUBs can be distinguished into two major classes, cysteine proteases and metalloproteases. Most DUBs catalyze a proteolytic reaction between an ε-amino Lys group and a carboxyl group corresponding to the C-terminus of ubiquitin.

DUBs, which are cysteine proteases, employ a catalytic mechanism based on the catalytic triad consisting of Cys-His-Asp/Asn to hydrolyze the ubiquitin bonds. The activity of the cysteine protease DUBs is dependent on whether the Cys residue contains an inactive thiol (-SH) or reactive thiolate ($-S^-$) group. Specifically, the Asp/Asn residue depolarizes and orients the His residue. The His, depolarized by the aspartate, deprotonates the Cys, converting its side chain from thiol to the reactive thiolate. In this way, His acts first as a base to Cys, activating it for nucleophilic attack on the acyl carbon of the ubiquitin isopeptide bond. After thiolate of Cys undergoes a nucleophilic attack on the isopeptide bond, there is a formation of a tetrameric intermediate, that is negatively charghed. The isopeptide bond is cleaved as the amide group of the isopeptide bond deprotonates the Hys (that in this case acts as an acid that donates a proton to the ε-amine group of Lys), freeing the substrate from the ubiquitin, which is still bound as an intermediate with the Cys. The mechanism proceeds through the nucleophilic attack of a water molecule to the Cys acyl intermediate resulting in

the release of the C-terminal carboxylate. The intermediate bond between the ubiquitin and Cys is broken, reforming the ubiquitin monomer and thiolate (the enzyme is regenerated). Finally, the ubiquitin monomer and substrate are released from the DUB (Snyder and Silva, 2021) (Figure 24).

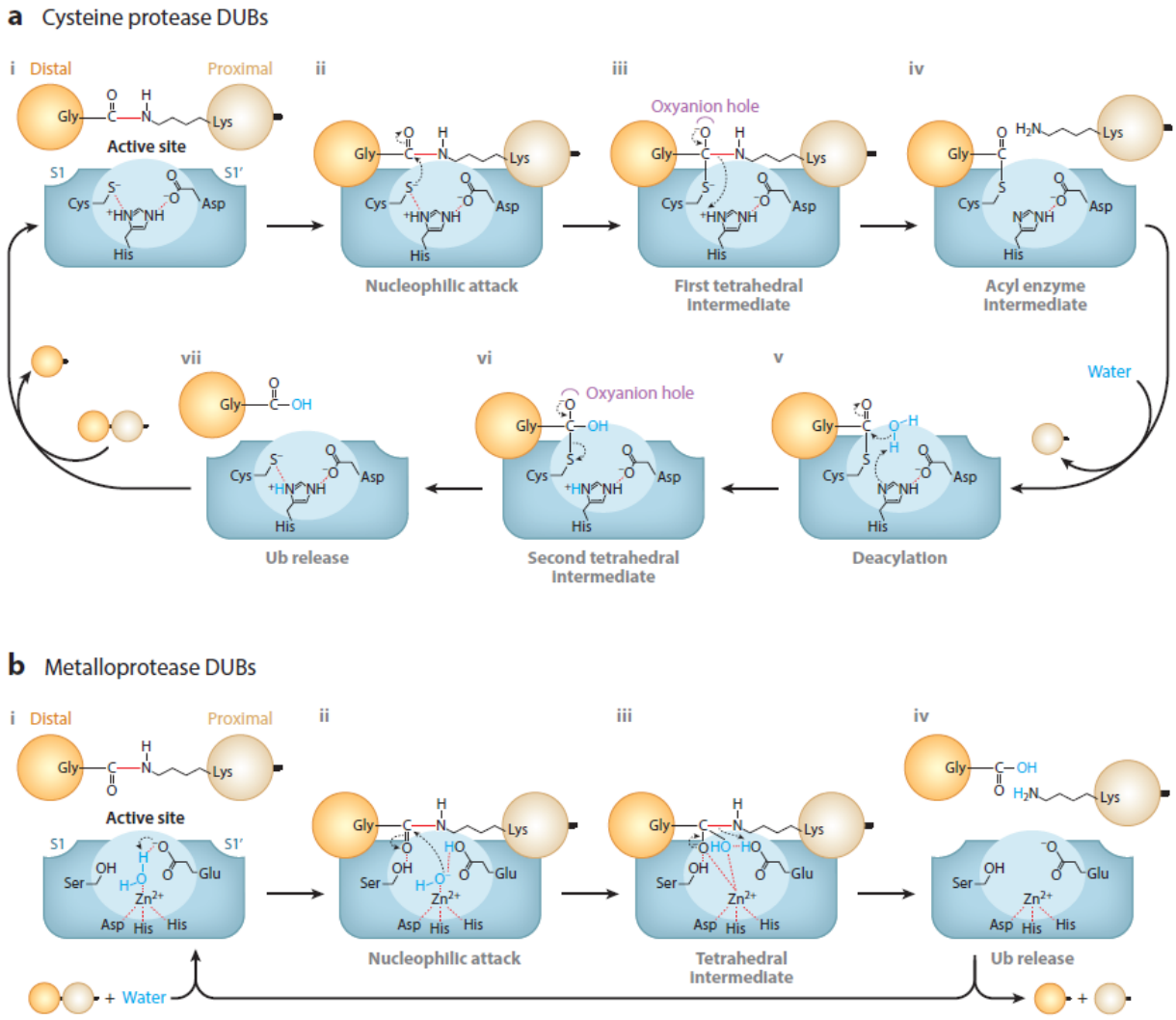


Figure 24: Cysteine protease DUBs and metalloprotease DUBs catalytic mechanisms (Mevissen and Komander, 2017).

On the other hand, metalloprotease DUBs utilize a catalytic site (an aspartate, a serine, and two histidine residues) and a zinc ion cofactor to catalyze isopeptide hydrolysis. The zinc ion is coordinated by the aspartate and the histidine residues. Once activated, a water molecule leads to a nucleophilic attack to the acyl group of the C-terminal of the ubiquitin isopeptide bond. Consequently, there are the formation of a covalent intermediate and the cleavage of the isopeptide bond. Ubiquitin is released, and the DUB enzyme is regenerated (Mevissen and Komander, 2017) (Figure 24).

DUBs regulate various aspects of cell physiology, and defects in these processes have significant clinical implications, including cancer. Examples of these dysregulations include the BRCA1-associated protein 1 (BAP1), commonly mutated in mesotheliomas, melanomas, and renal cell carcinomas; USP6 translocation in aneurysmal bone cysts; USP9X mutations leading to developmental disorders and dysregulated expression in cancer; USP15 overexpression in certain glioblastomas, ovarian cancer, and breast cancer; and mutations in cylindromatosis (CYLD). Given the role of ubiquitin mechanism components in various cancers, inhibitors targeting DUBs are garnering attention from pharmaceutical industries, with several candidates already identified as promising therapeutic targets (Antao et al., 2020).

*DUBs and liver fibrosis*

Liver fibrosis progression include alterations in the cellular phenotype and in cell cycle, which promote myofibroblast proliferation and the spread of fibrosis. The trans-differentiation of HSCs into myofibroblasts during fibrogenesis is an epigenetically regulated process that induces changes in gene expression that allow the cell to adopt its profibrogenic functions including proliferation, migration and expression/secretion of large amounts of ECM proteins. To acquire these functions, trans-differentiated HSCs must also undergo fundamental alterations in protein turnover and post-translational regulatory (e.g. addition of ubiquitin) mechanisms that control protein localization and function.

Ubiquitin plays crucial role in the pathogenesis of CLD through dynamic post-translational modifications exerting diverse cellular outcomes such as protein degradation through UPS and autophagy, and regulation of signal transduction (Park et al., 2021). Indeed, it has been observed that ubiquitin C-terminal hydrolase 1 (UCHL1) is highly induced after HSCs activation, thus representing a potential therapeutic target for fibrosis. UCHL1 expression is highly upregulated upon HSC activation and is involved in the regulation of HSCs proliferation (Wilson et al., 2015). Furthermore, a recent study showed that ubiquitin-specific peptidase 9X (USP9X) regulates the TGF-β signaling cascade by deubiquitination, highlighting its crucial role in fibrogenesis. Indeed, USP9X was found to be a critical deubiquitinating enzyme for the stability and high activity of NRP1 (a transmembrane receptor involved in the VEGF (Vascular-Endothelial Growth Factor) signaling cascade) and NRP1 deubiquitination mediated by USP9X enhanced HSCs activation and liver fibrosis. NRP1 promotes HSC activation via the cytokine TGF-β1, VEGFA, and PDGF-BB. In fact,

NRP1 influences HSC motility and migration and NRP1 gene that has been shown to be particularly expressed in the liver of liver fibrosis patients and in the mouse fibrosis model. NRP1 deubiquitination mediated by USP9X enhances HSCs activation, implying that targeting NRP1 or USP9X potentiates novel options in the treatment of liver fibrosis (Zhao et al., 2023). Moreover, USP9X acts as a DUB for SMAD4, promoting its association with SMAD2 and positively regulating TGF-β (Antao et al., 2020).

Therefore, the importance of DUBs as key regulators in liver fibrosis has made them attractive targets for the development of new therapeutic strategies.

*DUBs inhibitors*

The development and approval of bortezomib, a drug that targets the UPS, for treating relapsed multiple myeloma and mantle cell lymphoma has opened the field to new inhibitors targeting critical enzymes of UPS, among which DUBs have gained interest as possible pharmaceutical targets (Cersosimo et al., 2015).

Bortezomib is a reversible inhibitor of the β5 subunit, located in the 20S catalytic core of the proteasome. This molecule causes an intracellular accumulation of unfolded or misfolded proteins (mainly immunoglobulins) resulting in cell cycle arrest and activation of apoptotic caspases, as well as in an inhibitory effect on the transcription factor NF-κB. Bortezomib has also been tested for the potential treatment of other cancers, such as the treatment of HCC. It showed an inhibitory effect on cell proliferation of HCC cell lines by inducing a post-transcriptional decrease in cyclin E1 with a transcriptional-mediated decrease in the transcription factor E2F1 (Baiz, 2014).

However, side effects of bortezomib, represented by peripheral neuropathy and thrombocytopenia (Field-Smith et al., 2006), prompted the development of new UPS inhibitors. In particular, DUBs are attracting particular attention due to their ability to make the ubiquitination process reversible, so a therapeutic strategy based on their inhibition could be an effective method for the treatment of several diseases, including liver fibrosis.

On the basis of the specific target selectivity, DUBs inhibitors can be divided into two classes: selective inhibitors, acting on a specific enzyme or on a limited number of enzymes, and nonselective isopeptidase inhibitors (N-SIIs), which in principle can affect the activity of several isopeptidases. The two classes offer different and complementary advantages. The first class guarantees advantages in terms of selectivity when survival of a specific disease/tumor depends on a specific isopeptidase. On the other hand, the second class, affecting more enzymes and multiple pathways, may offer advantages in terms of

effectiveness on different diseases/tumors. A subclass of N-SIIs includes molecules characterized by the presence of a α,β-unsaturated dienone with two sterically accessible electrophilic β-carbons that can act as Michael acceptors to target nucleophiles, like the catalytic cysteine of several DUBs (Cersosimo et al., 2015). These molecules can form covalent adducts with free thiols in active sites of cysteine DUBs, resulting in the inhibition of the catalytic site (Santos and Moreira, 2007).

*2C and DUDC3 compounds*

The compound 2C (4-hidroxy-2,6-bis (4-nitro benzylidene) cyclohexanone 2) was synthetized in the laboratory of Prof. Benedetti and Prof. Felluga (Department of Pharmaceutical and Chemical Sciences of the University of Trieste) (Figure 25). Compound 2C is an irreversible non-selective DUBs inhibitor, characterized by the presence of a bis(arylidene)cyclohexanone group which presents two potential binding sites for catalytic cysteines of cysteine DUBs. In fact, 2C inhibited representative deubiquitinases with micromolar IC50 (e.g. UCHL1, UCHL5, and USP18) (Cersosimo et al., 2015). However, cysteine-dependent DUBs are not the unique target of 2C, but inhibition of the UPS is likely the major component of the observed antitumor activity (Ciotti et al., 2018).

2C displays an -OH group on the cyclohexanone ring in position 4, allowing further modifications to the central scaffold, therefore, it consents to bond to an extended pool of molecules to improve its delivery and pharmaceutical properties. In fact, to improve 2C solubility, its derivative DUDC3 was synthetized modifying this position (Figure 26).

Inhibiting DUBs, 2C impairs UPS causing the accumulation of polyubiquitinated proteins, leading to proteotoxic stress and cell apoptosis (Cersosimo et al., 2015; Iuliano et al., 2022; Maddaloni et al., 2024). 2C showed proapoptotic activity in different cancer cell lines of glioblastoma and ovarian cancer cell (Cersosimo et al., 2015; Maddaloni et al., 2024). Moreover, 2C is effective in downregulating the viability of primary ovarian cancer cells isolated from patients and cultured in 2D and in organoids and 2C is effective also in a subcutaneous xenograft mouse model of ovarian cancer, in vivo (Maddaloni et al., 2024).

Furthermore, 2C interferes the expression of the transcription factor E2F1 (a member of a family of transcription factors named E2Fs), involved in the regulation of cell proliferation. In fact, 2C reduces ovarian cancer cell growth also by down-regulating the level of the transcription factor E2F1 (Maddaloni et al., 2024). Interestingly, E2F1 is an activator that can promote HCC (Farra et al., 2019) and LF (Zhang et al., 2014).

Therefore, considering together the importance of ubiquitin and DUBs in the pathogenesis of CLD and LF (Antao et al., 2020; Park et al., 2021) and the importance of the marker E2F1 in LF, 2C seems to be a promising compound to test on LF *in vitro* models.

The mechanism of action of 2C involving apoptosis is interesting too. In fact, apoptosis seems an important mechanism to reduce the numbers of activated stellate cells during the resolution phase of hepatic fibrosis. Activated stellate cells seem to be more susceptible to apoptotic stimuli than their quiescent counterparts (Taimr, 2003). Activated stellate cells have the capacity to undergo apoptosis both spontaneously (e.g. the resolution phase of stellate cell activation (see paragraph 1.4)) and by specific targeting with apoptotic agents, such as the compound 2C.

For all these reasons we considered 2C and its derivative DUDC3 in the context of liver fibrosis. DUDC3 was considered because of its potent anti-proliferative effects in ovarian carcinoma cells (Maddaloni et al., 2024).

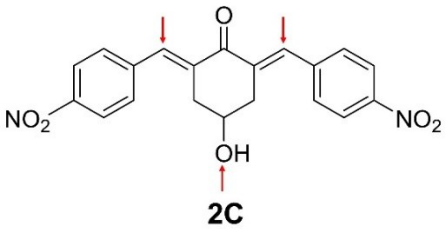


**2C**

Molecular Weight: 380,36

Figure 25: Molecular structure of 2C compound. The upper red arrows indicate two potential binding sites for catalytic cysteines of DUBs enzymes. The lower red arrow displays an -OH group that consents to bond to an extended pool of molecules to improve its delivery and pharmaceutical properties.

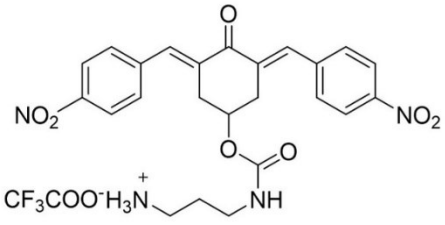


Molecular Weight: 113,02

**DU-DC3**

Molecular Weight: 481,48

Figure 26: Molecular structure of DUDC3, a derivative of 2C compound.

# 2. Aim of the thesis

Liver fibrosis (LF) is a chronic inflammation of the liver that can result from numerous causes and, if not adequately treated, can progress to cirrhosis and eventually hepatocellular carcinoma (HCC). Clinical findings indicate that > 80% of HCCs develop in the contest of LF or cirrhotic livers, suggesting an important role of liver fibrosis in the premalignant environment of the liver (Affo et al., 2017). Globally, liver fibrosis is associated with high mortality, causing around 2 million deaths each year (Marcellin and Kutala, 2018). To date, there is still a great need to develop new therapeutic strategies to slow down or stop the fibrotic process that would otherwise lead to failure of liver function.

The main aim of this thesis was to study novel drugs with anti-fibrotic potential and the role of the liver viscoelastic properties on the disease progression. To this end, we have used a class of deubiquitinases (DUBs) inhibitors named 2C and DUDC3, we successfully employed to down regulating the growth of ovarian cancer cells (Maddaloni et al., 2024). To characterize the therapeutic potential of 2C and DUDC3 we have considered three experimental *in vitro* models: cell culturing on plastic dishes, cell culturing in 3D structures (spheroids) and cell culturing on surfaces able to mimic the normal and pathological liver viscoelastic properties. The use of plastic dishes have the advantage of the easiness of cell culturing and of the further processing for cell phenotype and molecular effects characterization; however this model cannot resemble the viscoelastic properties of the fibrotic liver (Mazza et al., 2017) that are known to affect HSCs phenotype. The spheroid model has the advantage to explore the effects of the drugs in a 3D structure somehow resembling the 3D structure of the liver, although with a simplified tissue architecture. Finally, cell culturing on surface with the appropriate mechanical properties of the normal and fibrotic liver, considered these important variables in drug testing. Hydrogel substrates were designed to mimic the viscoelastic properties of the extracellular matrix of the healthy and fibrotic liver. In addition, it was performed the theoretical evaluation of the work the cell is required to perform in order to modify the substrate in the attempt of building up a proper nest where to live. To realize hydrogels, it was decided to focus on alginate, a biomaterial, with excellent peculiarities including biocompatibility and versatility. As very few data about human liver viscoelastic properties are available in the literature, we have determined them in samples obtained from normal and pathological liver. Prof. Silvia Palmisano, a bariatric surgeon at Cattinara Hospital in Trieste, and Prof. Fabrizio Zanconati, the director of the Department of Pathological Anatomy at the same institution, kindly provided us the liver tissue biopsies

(healthy and pathological). Normal and pathological liver samples were characterized by rheology and Low Field-Nuclear Magnetic Resonance (LF-NMR) (permission of the university ethics committee obtained at its meeting on 1-12-22 record no. 126). These types of analyses allowed us an accurate study of the viscoelastic properties of liver tissue and the evaluation of the iron content in the tissue samples.

While the three models considered to test 2C/DUDC3 anti fibrotic potential have each some limitations, taken together they can generate data with a significant predictive power for studies performed in animal models of liver fibrosis. In this regard, the *in vivo* studies are ongoing in the lab of prof. Truong Hai Nhung (University of Sciences, Ho Chi Minh City, Vietnam) in the frame of the common project "A novel molecular approach to liver fibrosis" financed by the Ministry of Foreign Affairs and International Cooperation (MAECI) to Prof. Gabriele Grassi.

# 3. Material and methods

## 3.1 Rheological characterization

For this thesis, a HAAKE MARS III (Thermo-Scientific) (Figure 3) rheometer was used, fitted with a 20 mm diameter knurled plate system. The knurling is essential to prevent possible slippage between the sample and the two parts of the measuring element. After switching on the instrument, the working temperature (e.g. 5°C for liver samples or 37°C for gels) and the correct approach of the two plates in the 'Automatic zero' position must be carried out.

Before performing rheological tests, the placement of the sample between the stationary and rotating parts of the sensor is a crucial step. For systems that cannot be spread, such as gels, the sample is first cut into a disc matching the sensor diameter, placed on the stationary plate, and then the mobile part of the sensor is lowered until it contacts the sample. Insufficient contact can result in inaccurate modulus values (typically lower than the actual ones), while an excessively small gap can cause internal fractures in the sample, leading to unreliable property measurements.

The optimal gap is determined through short Stress Sweep (sSS) tests, which involve setting an initial gap value, measuring G', reducing the gap, and measuring G' again until a slight decrease (~10% of the maximum G' value) is observed. sSS is performed within the linear viscoelastic region, typically at a shear stress range of 1-5 Pa and a frequency of 1 Hz. The determined gap is then maintained for all subsequent tests.

Specifically, we employed three types of oscillatory rheological examinations, namely the stress sweep (SS) test, the frequency sweep (FS) test and the time sweep (TS) test.

The following parameters were used for the SS measurement:

- shear stress $\tau$ = 1-1000 Pa,

- frequency $f$ = 1 Hz.

While the following parameters were used for the FS measurement:

- shear stress $\tau$ = 1 or 5 Pa, according to the wideness of the sample's linear viscoelastic region,

- frequency $f$ = 0.1-10 Hz.

The obtained data were analyzed by means of the generalized Maxwell model (see paragraph 1.1.7).

We used also the TS with liver samples, as an initial step to choose the correct temperature for the analyses. In the time sweep the time is the variable, while temperature (5°C or 37°C), frequency (1 Hz) and shear stress (5 Pa) are held constant throughout the test.

## 3.2 LF-NMR analysis

First, the instrument must be subjected to a 'Daily Check' to check that it is working properly, and then the working temperature (37°C) can be set. After the sample has been placed in its housing, analysis is carried out; the first measurement is usually a test to understand the behavior of the sample; some parameters can then be adjusted such as the number of points considered or the 'gain', which allows the initial intensity of the signal reading to be modulated. Generally, the final signal intensity (FID) should be below 5% of the initial intensity.

## 3.3 Liver sample preparation

Solid biopsies of human liver tissue (permission was granted by the University Ethics Committee at the University of Trieste during the session on 01/12/2022, verbal reference number 126) can be subjected to rapid deterioration due to blood clotting. For this reason, freshly isolated human liver biopsies were kept on ice until experimental analysis. Under a laminar flow hood, pieces of adequate size were obtained for both rheological and LF-NMR analysis.

For rheological characterization, a specialized glass apparatus known as a 'solvent trap' was employed to minimize water evaporation from the sample (Figure 27). This device created an approximately water-saturated environment around the sample, thereby preventing alterations in the rheological properties that could occur due to water evaporation from the biological samples. Short Stress Sweep tests ($\tau$ 1-5 Pa) were then performed to correctly identify the value of the distance (gap) between the moving and fixed parts of the sensor, with the procedure previously described in paragraph 3.1. The set temperature for rheological analysis of liver samples was 5°C, to prevent degradation of the sample.

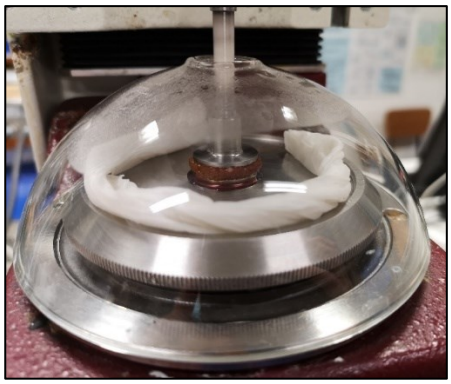

Figure 27: Image of a liver sample placed in the rheometer, utilizing a ‘solvent trap’.

For the NMR analysis, the liver samples were placed inside an appropriate glass tube and subjected to measurement. However, the liver contains a significant amount of iron, which affects the relaxation times ($T_{1m}$ and $T_{2m}$) due to the alteration of the magnetic environment. Indeed, iron is a ferromagnetic substance that can become intensely magnetized in the presence of an external magnetic field and retain its magnetism for a prolonged period after the field is removed, effectively becoming a permanent magnet. For this reason, in the presence of ferromagnetic substances such as iron, cobalt, or nickel, LF-NMR analysis does not yield nano-structural information but, on the contrary, highlights the amount of these ferromagnetic materials.

## 3.4 Cell cultures

Hepatic stellate cells (HSCs) are a major fibrogenic cell type that contributes to extracellular matrix deposition (ECM) during chronic liver disease. The HSCs cell lines used as *in vitro* models in this thesis are the LX2 and CFSC.

LX2 derived from primary human HSCs generated by immortalization with the Simian Vacuolating Virus 40 (SV40) transforming antigen and subsequent propagation in low serum conditions (1% fetal bovine serum, FBS). The phenotype of LX2 is most like that of activated HSCs *in vivo*. LX2 have a fibroblastic morphology with a spindle-shaped form. They express α-smooth muscle actin (α-SMA) under all culture conditions, vimentin, the intermediate filament protein glial fibrillary acidic protein (GFAP), key receptors regulating hepatic fibrosis, including platelet derived growth factor (PDGF) receptor β (βPDGF-R), and proteins involved in matrix remodeling, as matrix metalloproteinase-2 (MMP-2), suggesting that LX2 retain key features of transdifferentiated HSC. Therefore LX2 must be regarded as at least partially activated even after immediate replating (Castilho-Fernandes et al., 2011; Taimr, 2003; Weiskirchen et al., 2013; Xu et al., 2005).

CFSC cells are a spontaneously immortalized HSCs cell line derived from adult male cirrhotic rat livers induced by carbon tetrachloride. In this thesis a subclones of CFSC was used, the clonal cell line CFSC-2G. For simplicity, in this work we will always abbreviate CFSC-2G in CFSC. CFSC cells have a fusiform fibroblastic morphology and express typical HSCs markers including fibronectin, α-SMA, collagen I, and vimentin, in agreement with a fibrogenic phenotype. Furthermore, CFSC are capable of uptaking and accumulating fat in intracellular lipid droplets, that are other important hallmarks of HSCs, physiologically acting as professional retinoid-storing cells (Nanda et al., 2022).

Beside HSCs cell lines, we also considered WS1, human fibroblast cell line.

WS1 cells are fibroblasts derived from skin. They grow adherent and in a fibroblastoid form. This line was chosen because it has a phenotype that mimics rather well that of activated HSCs (myofibroblasts), largely responsible for liver fibrosis.

LX2 and WS1 cells were cultured in DMEM High Glucose with sodium pyruvate (Euroclone) supplemented with 100 U/ml penicillin and 100 μg/ml streptomycin (Euroclone) and 2 mM L-glutamine (Euroclone) and containing heat-inactivated FBS (Euroclone) in percentage of 2% for LX2 or in percentage of 10% for WS1.

CFSC cells were grown in DMEM High Glucose (Sigma-Aldrich) supplemented with 1 mM sodium pyruvate (Sigma-Aldrich), 100 U/ml penicillin and 100 μg/ml streptomycin (Sigma-Aldrich), 2 mM L-glutamine (Sigma-Aldrich), and 10 % heat-inactivated FBS (Sigma-Aldrich). In the medium for CFSC cells were also added 1% MEM Non-Essential Amino Acids (Gibco).

All the cell lines were grown at 37°C in a humidified atmosphere at 5% $CO_2$. Medium exchange was conducted every second day and cells were subcultured using Accutase solution (Sigma-Aldrich). The cell lines resulted negative for the mycoplasma test.

Cell lines were generously provided by Prof. Ralf Weiskirchen.

## 3.5 Preparation of alginate gels

We prepared hydrogel surfaces with alginate polymer suitable for cell culture to better mimic the ECM environment and to resemble the rheological characteristics of liver tissue.

Alginate (Sigma-Aldrich) solution, was prepared by pouring the polysaccharide in non-complete Dulbecco's Modified Eagle Medium (DMEM) to promote cell adhesion to the alginate gels. For the formation of the alginate gels, we used a calcium chloride (Sigma-Aldrich) solution, which provides the divalent ions that act as gelling agent. The calcium

chloride, in its solid granular form, was solubilized in Phosphate-Buffer Salin (PBS) to get the required concentration (the range of concentrations used is 1-9 mg/ml of calcium ions).

The formation of the gel is contingent upon finding the optimal balance between the concentrations of alginate and calcium chloride solution to replicate physiological and pathological stiffness of the liver tissue. The selected alginate concentrations are 2% and 3% m/V solutions. These specific concentrations were chosen on the basis of rheological test results, which confirmed the attainment of the targeted stiffness, namely the desired shear modulus (G).

To promote cell adhesion on alginate gel surfaces, it was necessary to add some ECM element, such as fibronectin (Sigma-Aldrich), collagen I (Sigma-Aldrich) or Geltrex (Gibco). These elements were added to the alginate and mixed in a proportion of 1:10, ECM element to alginate. More in detail, the mixed solution of alginate and ECM elements (fibronectin, collagen I, or Geltrex) was placed in 24-well plates and crosslinked with a calcium chloride solution for 5 minutes. Afterward, the calcium chloride solution was removed, and the alginate hydrogels were used as culture surfaces for LX2 cells, which were seeded at a density of $60.0 * 10^3$ cells/well.

## 3.6 Isolation and Culturing of Primary mouse Hepatic Stellate Cells (mHSC)

In the RWTH Aachen University, primary HSCs from wild type adult mice (B6/J-(Plin5)tm) were isolated by pronase and collagenase perfusion as described by Nevzorova et al., with the modification that animals were sacrificed before cell isolation (Nevzorova et al., 2012). The liver tissue was homogenized and digested in a solution containing DNase I. The resulting cell suspensions were filtered through a nylon strainer, centrifuged and washed in Gey's Balanced Salt Solution (GBSS). HSCs were further purified by a single-step density gradient centrifugation with 14.5% (w/v) Nycodenz (Axis-Shield Point-of-Care Division). HSC were collected by aspiration of the white top layer of the gradient.

Freshly isolated mHSCs were cultivated at 37°C in 5% $CO_2$ in DMEM High Glucose (Sigma-Aldrich) supplemented with 1 mM sodium pyruvate (Sigma-Aldrich), 10 % FBS (Sigma-Aldrich), 100 U/ml penicillin and 100 µg/ml streptomycin (Sigma-Aldrich), 4 mM L-glutamine (Sigma-Aldrich).

## 3.7 Cell counting and vitality assay

To evaluate the morphology and the viability of cultured cells and the number of cells that have to be sown, it is necessary to perform an examination by optical microscope (we used Nikon Eclipse TS100).

Trypan Blue Exclusion Test of Cell Viability is the most common method used to determine the number of viable cells present in a cell suspension. Trypan Blue (Figure 28) is a 960 kDa molecule that is cell membrane impermeable, therefore viable cells with intact membranes do not take up this dye. However, Trypan Blue can enter in dead cells with compromised membranes. The dye exclusion test is based upon the concept that viable cells exclude this impermeable dye, whereas dead cells do not. After entering in the cell, Trypan Blue binds to intracellular proteins giving the cells a blue color. This test enables to enumerate the viable unstained cells and the dead blue cells in a given population.

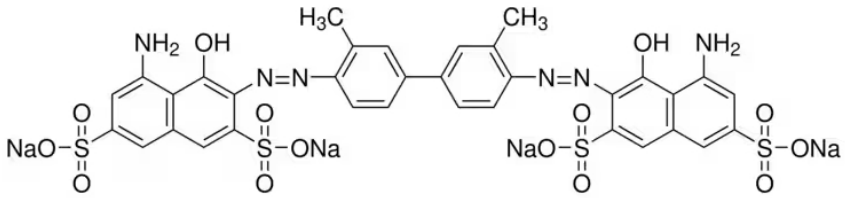


Figure 28: Trypan Blue (https://www.sigmaaldrich.com/IT/en/product/sigma/t6146)

In this test, a cell suspension is simply diluted 1:1 with an equal volume of 0.04% of Trypan Blue solution in 1X PBS (NaCl 137 mM, KCl 2.7 mM, $Na_2HPO_4$ 8.1 mM, $KH_2PO_4$ 1.47 mM, pH 7.4). Then, it is possible to perform a cell counting loading 15 µl of the cell dilution with the dye in Thoma's counting chamber (Exacta-Optech) and observing under the optical microscope.

After several independent cell counts, it is possible to obtain the number of cells in 1 milliliter of the initial suspension using the following formula:

$$cells/ml = n * 2 * 10^4$$

where n is the mean of the independent counts, 2 represent the dilution factor of Trypan Blue and $10^4$ is the conversion factor of Thoma's chamber.

## 3.8 3D cell culture system

In 3D cell culture systems cells establish connections with many other cells and with extracellular matrix components, in contrast to what happen in classical 2D monolayer culture systems. Spheroids, an example of 3D culture system, permits to generate tissue-like cellular

aggregates for the measurement of biomechanical properties or for molecular and biochemical analysis in a physiologically relevant model (Foty, 2011). In particular, we used cell spheroids to examine the ability of DUBs inhibitors to diffuse in a system with ECM components, by means of a cell viability test designed for 3D cell cultures (CellTiter assay, see paragraph 3.15). This procedure was conducted in the laboratory of Prof. Flavio Rizzolio in C.R.O. Aviano and with Dr. Salvatore Parisi.

3D spheroids were prepared by encapsulating LX2 within collagen I (from rat tail, Serva) and using the method of hanging drops. Firstly, a cell solution with final concentration of 2 mg/ml collagen I and pH ~ 7.4 was prepared. The pH was measured with a sterile litmus paper and corrected using NaOH 0,1 M. Single drops of this cell-collagen solution containing $2.0 * 10^3$ cells/each were placed on the bottom of the wells of a 96-well plate. Each well contained a single drop. The drops were allowed to solidify by placing the plate upside-down into a standard cell culture incubator (37° C) for a period of 20 minutes. After that, culture medium was added to the wells.

## 3.9 Dil Labeling of cell membranes

FAST Dil oil (Invitrogen) is lipophilic fluorescent tracer that does not appreciably affect cell viability, development, or basic physiological properties. According to the manufacturer, it is weakly fluorescent in water but highly fluorescent and quite photostable when incorporated into membranes. Once applied to cells, this dye diffuses in the cell membrane, resulting in staining of the entire cell. Dil exhibit orange fluorescence that highlight the cells and their morphology.

The cells were prepared in a serum-free culture medium suspension. Serum proteins and lipids should be removed from the medium because they may bind the dyes and reduce the effective dye concentration. Then, we added the dye to the cell suspension to achieve a final dilution of 1:300. We mixed by gentle pipetting and incubated at 37°C for 15 minutes. The stained cells were separated from the staining solution by centrifugation at 1000 rpm for 5 minutes. Then we removed the supernatant, resuspend the cells in fresh medium at 37°C, and seeded on alginate substrates prepared in 12-well plate at the density of $120.0 * 10^3$ cells/well.

We used this labeling to monitor the viability of the cells when cultivated on alginate substrates. The observation of the cells labeled with Dil dye was carried out using an inverted microscope (Leica DM IRB).

## 3.10 Morphological analyses

HSCs during their pathological activation undergo a morpho-functional modification that leads them to assume a more elongated myofibroblastic morphology than the stellate form that characterizes them under physiological conditions. Morphological analysis of LX2 may therefore be useful to discriminate active from inactive HSCs. To this end, a morphological analysis of LX2 cells grown on alginate gels and labeled with Dil, was performed using ImageJ, an open-source software commonly used for analyzing microscope images. This software allows segmenting single cells and achieving different shape parameters, such as the cell perimeter and area. Single cells were analyzed by ImageJ to obtain the circularity (C) and the aspect ratio (or elongation, AR), two so-called shape factors useful for describing the degree of cell elongation. Specifically, circularity is a parameter indicating how much the cell contour resembles a perfect circle. It ranges from 0 to 1, with 1 indicating a perfect circle (Figure 29b). Circularity is expressed by $C = (4\pi A)/P^2$, where A is the area of cell and P its perimeter. Elongation (or aspect ratio), on the other hand, is obtained from the ratio between the major (a) and minor axis (b) of the ellipse that best describes the cell contour. Aspect ratio is expressed by AR = a/b (Figure 29a). The higher this ratio is (and therefore the greater the major axis is than the minor axis), the more elongated the cell will be (Yu et al., 2013).

LX2 cells were labeled with Dil and seeded on plastic, Alg 2% gels (containing fibronectin in 1:10 with alginate) or Alg 3% gels (containing fibronectin in 1:10 with alginate) in 6-well plates. Cells were seeded with a density of $1*10^5$ cells/well. After 24 hours from seeding, cells images were taken with fluorescent microscope and analyzed with ImageJ. For each condition analyzed, 300 cells from 5 pictures were analyzed. To obtain AR and C values in ImageJ, the cell images were initially converted from the RGB (Red-Blue-Green) format to the 16-bit (greyscale) format to have a clearer recognition of the background. This makes it possible to convert the 16-bit image into a binary image, i.e. with only two colors: white (with a pixel value of 255 and referring to the cell form) and black (with a pixel value of 0 and referring to the background). From the binary image, the program is able to recognize the cell contour and thus calculate its circularity and elongation.

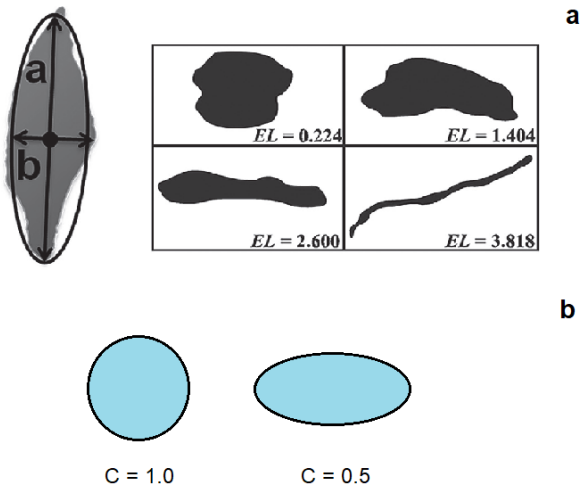


Figure 29: Schematic representation of the aspect ratio, here indicated as EL, and Circularity, indicated as C.

## 3.11 Deubiquitinase (DUBs) inhibitors compounds

The 2C compound (4-hidroxy-2,6-bis (4-nitro benzylidene) cyclohexanone 2) is characterized by the presence of a bis(benzylidenecyclohexanone) group which presents two potential binding sites for catalytic cysteines of deubiquitinating enzymes (upper red arrows, Figure 30). Moreover, it displays an -OH group on the cyclohexanone ring in position 4 (lower red arrow, Figure 30), that allows further modifications to the central scaffold (Cersosimo et al., 2015).

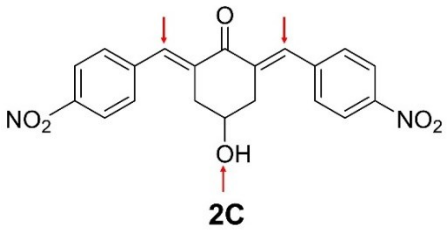


Molecular Weight: 380,36

Figure 30: Molecular structure of 2C compound. The upper red arrows indicate two potential binding sites for catalytic cysteines of DUBs enzymes. The lower red arrow displays an -OH group that consents to bond to an extended pool of molecules to improve its delivery and pharmaceutical properties.

A chemical derivative of 2C was also used. This compound is called DUDC3 ((3E, 5E)-3,5-bis[(4-nitrophenyl)methylidene]-4-oxocyclohexyl N-(3-aminopropyl)carbamate (trifluoro acetate salt)), and it possesses a small positive chain instead of the -OH group (Figure 31).

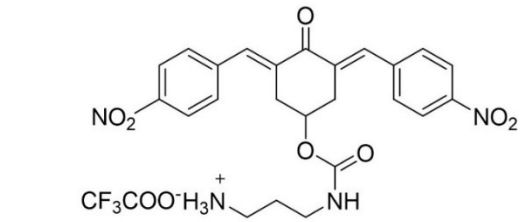


Molecular Weight: 113,02

**DU-DC3**

Molecular Weight: 481,48

Figure 31: Molecular structure of DUDC3 compound, a derivative of 2C.

Another compound used is VV1 ((2E,6E)-2,6-bis[(4-nitrophenyl)methylene]-4-hydroxycyclohexanol), an inactive form of 2C (Figure 32). The reduction of the carbonyl group of the cyclohexanone ring to hydroxyl group leads to the loss of the activity of the original compound (because there are no more binding sites for catalytic cysteines of deubiquitinating enzymes), therefore it was utilized as a control in the experiments performed.

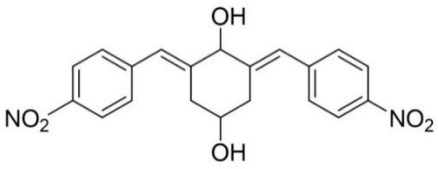


**VV1**

Molecular Weight: 382,37

Figure 32: Molecular structure of VV1 compound, a derivative of 2C.

These compounds were synthesized at the bio-organic chemistry laboratory of Prof. Benedetti and Prof. Felluga (Dipartimento di Scienze Chimiche e Farmaceutiche of the University of Trieste).

To test these compounds, the cells were seeded in multi-well plates of different sizes. After 24 hours, cells were treated with the compound of interest and finally tested through different assays. In particular, after weighing each compound the stock solution was obtained by dissolving them in DMSO, due to the hydrophobic nature of 2C and its derivatives. After this step, a dilution in non-complete DMED was performed to obtain the desired compound concentrations (0.5, 1, 2, 4 and 10 μM) in wells where cells had been previously seeded.

## 3.12 Cellular uptake test with fluorescent compound (2C-Fl)

We used 2C compound labelled by fluorescein (2C-Fl, Figure 33) to evaluate the uptake of 2C from LX2 cells. 1,5 × $10^5$ LX2 cells/well were seeded on glass slides in 6-well plates. 24 hours after seeding, cells were treated with 2 µM of 2C-Fl. At different time intervals, cells were fixed in 4% paraformaldehyde (PFA, Sigma-Aldrich) and stained with DAPI. Images were then taken by a Leica DM2000 fluorescence microscope.

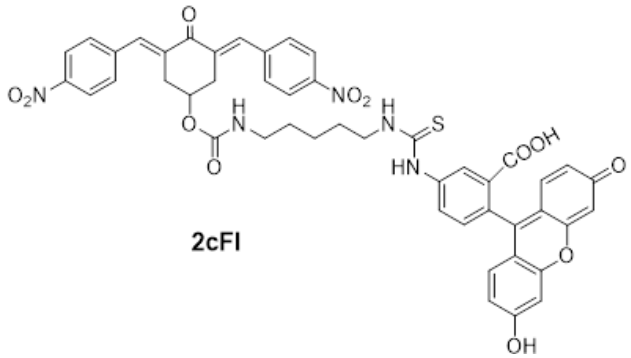


Figure 33: Molecular structure of 2C compound labelled by fluorescein (2C-Fl).

## 3.13 MTT assay

MTT assay is a quantitative test used for assessing cellular metabolic activity as an indicator of cell viability, proliferation, and cytotoxicity. This colorimetric assay is based on the reduction of a yellow tetrazolium salt (3-(4,5-dimethylthiazol-2-yl)-2,5-diphenyltetrazolium bromide or MTT) to purple formazan crystals by metabolically active cells (Figure 34). Indeed, the viable cells contain NAD(P)H-dependent oxidoreductase enzymes at the mitochondrial level which reduce the MTT to the insoluble formazan. The formazan crystals are dissolved using dimethyl sulfoxide (DMSO) and the resulting-colored solution is quantified by measuring absorbance. The absorbance measured is directly proportional to the mitochondrial activity of the cells and thus to the number of viable cells.

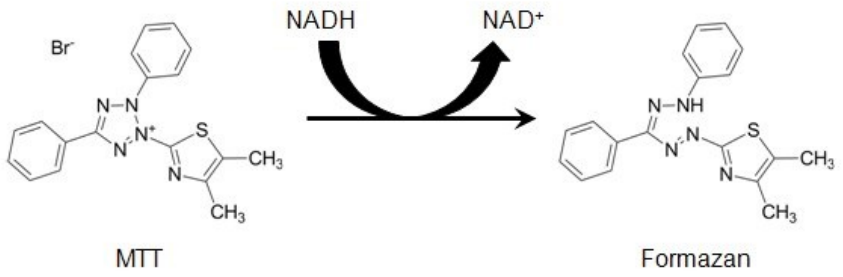


Figure 34: Reduction reaction of MTT to formazan by mitochondrial reductase enzymes (https://www.ncbi.nlm.nih.gov/books/NBK144065/figure/mttassays.F1/)

Regarding DUBs inhibitors treatments, LX2, WS1 and primary mHSC were seeded at 5.0 * $10^3$ cells/well in 96-well plates. CFSC were seeded at 1.0 * $10^3$ cells/well because of their high proliferative rate.

MTT salt was solubilized in PBS, obtaining a yellow solution with concentration of 4 mg/ml, and was administered to the cell cultures at a final concentration of 0,4 mg/ml. After 4 hours of incubation in the dark, in an incubator at 37°C, the cell medium was removed, and the formazan crystals formed inside the cells were solved in DMSO. Absorbance (Abs) was then read at 570 nm using a multi-well spectrophotometer (SpectraMax Plus 384 Molecular Devices).

Cell viability percentage in calculated using the following formula:

$$\%\ of\ viability = \left(\frac{Abs\ treated\ cells}{Abs\ untreated\ cells}\right) * 100 \tag{3.1}$$

We calculated also IC50 (half maximal inhibitory concentration) plotting x-y and fitting the % of viability with a straight line. IC50 value was then estimated using the fitted line, i.e.,

$$y = ax + b$$
$$IC50 = (50 - b)/a \tag{3.2}$$

## 3.14 PrestoBlue assay

Another test that has been used for the determination of viable cells is the assay involving the PrestoBlue HS Reagent (Thermo-Scientific), a resazurin-based solution to quantitatively measure cell viability by using the enzymatic activity of living cells. Resazurin is a non-toxic, cell-permeable, non-fluorescent, blue-colored compound. When added to cells,

the resazurin is modified by the reducing environment of the viable cell to resorufin, a red in color, highly fluorescent compound (Figure 35). This change can be detected using fluorescence or absorbance measurements. In contrast to MTT test, PrestoBlue does not require cell lysis. After the assay, it is possible to remove the reagent from the cells and replace it with growth medium for further proliferation. In particular, we measure the cell viability with PrestoBlue assay in the experiments where cells were seeded on alginate hydrogels. In these experiments was not possible to use MTT assay, because of the difficult solubilization of formazan crystal over the hydrogels.

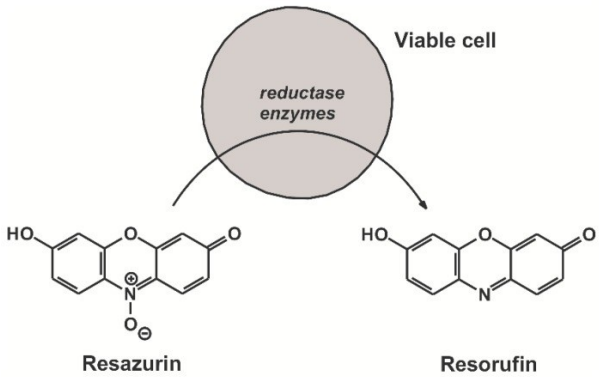


Figure 35: Reductases of viable cells reduce resazurin resulting in the formation of its highly fluorescent metabolic product resorufin (Csepregi et al., 2018).

To carry out the assay, LX2 cells were seeded on alginate substrates prepared in 24-well plate at the density of 60.0 * $10^3$ cells/well. PrestoBlue reagent was added in a 1:10 proportion compared to the medium that was already present in the wells, and after 1 hour of incubation at 37°C the multi-well plate was scanned through a spectrophotometer (TECAN Infinite F200), using 535 nm as excitation wavelength and as 595 nm emission wavelength.

## 3.15 CellTiter assay

The CellTiter-Glo 3D Cell Viability Assay (Promega) is method to determine the number of viable cells in 3D spheroids, because the assay reagent penetrates large spheroids and has lytic capacity. This 3D assay reagent is based on quantitation of the ATP present and generates a luminescent readout. ATP is a marker for the presence of metabolically active cells.

According to the manufacturer's instructions, in this assay the reagent was directly added to cell medium of 3D culture systems with LX2 cells (see paragraph 3.8). Then we mixed by shaking for 5 minutes and incubated for 25 minutes at room temperature. The

incubation of the reagent resulted in cell lysis and generation of a luminescent signal proportional to the amount of ATP present, which is directly proportional to the number of viable cells present in culture. We recorded luminescence with a luminometer (TECAN Infinite F200).

## 3.16 Protein extraction

Protein extraction is the first step to proceed with protein analysis with Western Blot. To perform protein extraction RIPA Lysis Buffer (Millipore) was used. This buffer efficiently lyses cells and tissues, solubilizes proteins, and protects them from degradation during the extraction process. Before the using, it is necessary to dilute the RIPA buffer 10X with water (9 parts of water and 1 part of buffer). Then, the diluted buffer solution must rest at 4°C for 2 hours. After the incubation it is necessary to add protease inhibitor (Sigma-Aldrich) and phosphatase inhibitor (Sigma-Aldrich) in proportion of 1:200 with the buffer solution, for each inhibitor. At this point the RIPA diluted buffer is ready for the using.

To obtain protein extracts, $1.5 * 10^5$ cells/well were seeded on 6-well plates. At the end of the treatments with DUBs inhibitors, cells were collected by centrifugation at 1000 rpm for 5 minutes and rinsed with PBS 1X. After that, cells were lysed with 100 µl of RIPA diluted buffer for every $1 * 10^6$ cells present in the pellet. We incubated the samples with RIPA buffer for 15 minutes on ice. After that, a 10-minute centrifugation at 13000 rpm and 4°C was performed. At the end of the centrifugation, the supernatant was collected into a new tube. Protein extracts were quantified by the Bicinchoninic acid assay (BCA assay) and then stored at -80°C.

## 3.17 Protein extracts quantification by BCA protein assay

The protein content of protein extracts was determined by the Bicinchoninic acid assay (BCA assay), which is an indirect spectrophotometric technique based on two different reactions. Firstly, the peptide bonds in the protein sample reduce $Cu^{2+}$ ions from the $CuSO_4$ solution to $Cu^{+}$, under alkaline conditions. The amount of $Cu^{2+}$ reduced is proportional to the amount of protein present in the solution. Next, two molecules of bicinchoninic acid (BCA) chelate with each $Cu^{+}$ ion, forming a purple-colored complex that strongly absorbs light at a wavelength of 562 nm (Figure 36). Because of this property, the resultant absorbance at 562 nm is directly proportional to the protein concentration. The amount of protein present in a solution can be quantified by measuring the absorption spectra and comparing with protein solutions with known concentrations.

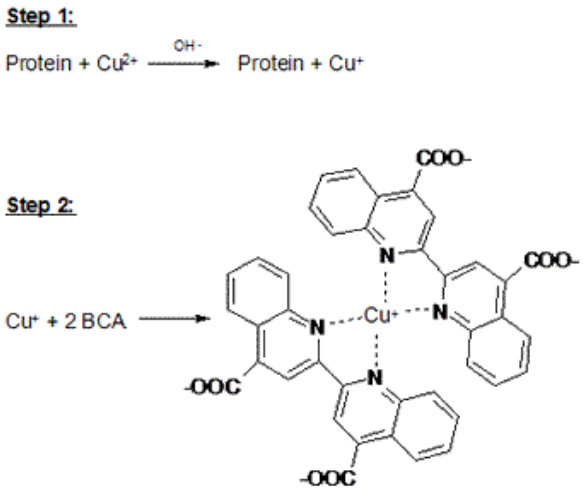


Figure 36: Two reactions of the BCA assay
(https://nfsc4500101groupa.weebly.com/uploads/5/1/2/4/51240965/2154981_orig.gif)

In this test, standard solutions of Bovine Serum Albumin (BSA; 2 µg/ml; Thermo-Scientific) were prepared to obtain a calibration curve in order to determine protein extract concentration. The working solution for the colorimetric reaction was composed by mixing two reagents, reagent A and reagent B (Pierce BCA Protein Assay Kits; Thermo-Scientific), in the proportion 50:1.

2 µl of each standard solution and protein sample, considered in duplicate, were mixed with freshly prepared working solution, plated in 96-well flat-bottomed plates and incubated at 37°C for 30 minutes. After the incubation, the absorbance was measured at 562 nm using a spectrophotometer (SpectraMax Plus 384 Molecular Devices). The concentration of each protein sample was determined by means of the calibration curve.

## 3.18 SDS-PAGE electrophoresis and Western Blot

SDS-PAGE is a technique that allows proteins to be separated according to their molecular weight, exploiting their electrophoretic mobility. The electrophoretic mobility is a specific property that permits molecules to be separated based on molecular weight, conformation, and molecular charge. In SDS-PAGE, the chemical denaturant Sodium Dodecyl Sulphate (SDS) is added to protein to remove protein structure and turn the molecules into an unstructured linear chain. Moreover, it binds with the same stoichiometry to all proteins and gives them the same negative charge. In this way, the proteins move in an electric field towards the positive pole and with different speeds only depending on their molecular weight, because the conformation is denatured, and the negative charge is the same

for all the proteins. After electrophoretic separation, specific proteins can be identifying by Western Blot analysis, in which proteins are transferred to a membrane and then incubated with antibodies specific to the protein of interest.

In particular, the gel prepared for SDS-PAGE electrophoresis consisted of two parts, the so-called stacking gel and the running gel, respectively with 4% and 12% (w/v) of acrylamide (29:1, acrylamide:bis-acrylamide). The gel was fixed to a suitable support (Invitrogen) and immersed in the Running Buffer (0.125 mM of Tris-HCl pH 8.3, 0.96 M of glycine and 0,5% of SDS). 30 μg of protein extract were added with Loading Buffer 4X (NuPAGE LDS Sample Buffer, Thermo-Scientific), denatured at 70°C for 10 minutes, and loaded in the wells of the gel. The electrophoretic run was performed with an electric field of about 14 V/cm.

After that, the proteins were transferred from the gel onto the 0.22-μm nitrocellulose membrane (Schleicher & Schuell) by exploiting the electrical potential created by a semi-dry transblot apparatus (Bio-Rad). To carry out this procedure, the membrane and 6 sheets of filter paper of the same size and corresponding to that of the gel are hydrated with a Transfer Buffer (60 mM of Tris-HCl, 40 mM of glycine containing 0.05% SDS and 10% methanol). After the assembly of sandwich with gel, membrane and filter sheets, protein transfer was performed using electric field of 1 mA/cm for about 1 hour. Membranes were then stained with Ponceau S. (Sigma-Aldrich) to evaluate the transfer efficiency and then blocked with 5% of fat-free dried milk. Subsequently, membranes were incubated with the primary antibodies of interest and then washed twice with PBS containing 0.1% Tween 20 (TBST), before the incubation with the secondary antibody conjugated with horseradish peroxidase (HRP). Finally, membranes were washed thrice in TBST and incubated with the substrate (SuperSignal West Pico Chemiluminescent Substrate; Thermo-Scientific Pierce). The HRP enzyme catalyzes the oxidation of the substrate leading to a chemiluminescence reaction. The measurement of the chemiluminescent protein bands was carried out using the Chemidoc XRS instrument (Bio-Rad), followed by the quantification with Quantity One software.

Anti-GAPDH or anti-β-actin antibody were used as the loading control. The primary antibody specifications and conditions of use are reported in the table below (Table 1). The secondary antibodies used are Goat anti-Mouse IgG (31430; Thermo-Scientific) and Goat anti-Rabbit IgG (31460; Thermo-Scientific). Both are conjugated with HRP and were incubated for 2 hours at RT with the dilution of 1:5000 in 2,5% milk in TBST.

Table 1: Antibodies' specifications. ON indicates Over Night.

| Primary antibody | Cat. Number; Producer | Dilution | Incubation | Secondary antibody |
|---|---|---|---|---|
| PARP | 9532; Cell Signaling | 1:1000 in 2.5% milk in TBST | ON at 4°C | Goat anti-rabbit |
| Fibronectin | AB1954; Sigma-Aldrich | 1:1000 in 2.5% milk in TBST | ON at 4°C | Goat anti-rabbit |
| Collagen I | NB600-408; Novus Biologicals | 1:1000 in 2.5% milk in TBST | ON at 4°C | Goat anti-rabbit |
| α-sma | CBL171-1; Sigma-Aldrich | 1:500 in 2.5% milk in TBST | ON at 4°C | Goat anti-mouse |
| Ubiquitin | P4D1; Cell Signling | 1:1000 in 2.5% milk in TBST | ON at 4°C | Goat anti-mouse |
| Vimentin | ab92547; AbCam | 1:8000 in 2.5% milk in TBST | ON at 4°C | Goat anti-rabbit |
| E2F1 | sc-251; Santa Cruz | 1:200 in 5% milk in TBST | ON at 4°C | Goat anti-mouse |
| LC3B | GTX127375; GeneTex | 1:1000 in 5% milk in TBST | ON at 4°C | Goat anti-rabbit |
| GAPDH | sc-32233; Santa Cruz | 1:1000 in 2.5% milk in TBST | ON at 4°C | Goat anti-mouse |
| β-actin | A5441; Sigma-Aldrich | 1:10000 in 2.5% milk in TBST | ON at 4°C | Goat anti-mouse |

## 3.19 Total RNA extraction

Total RNA was extracted using a column-based purification kit (RNeasy Mini Kit; Qiagen). Briefly, pelleted cells were lysed using RLT Lysis Buffer integrated with β-mercaptoethanol. Afterwards, a 70% ethanol solution was used to precipitate RNA. The solution was loaded to the spin columns and centrifugated for 40 seconds at 11,000 rpm. After that, the columns were washed with Buffer RW1 and RPE. Finally, RNA was eluted in 20 µl of RNase Free Water centrifuging for 60 seconds at 11,000 rpm. The concentration of isolated RNA was measured using a spectrophotometer (NanoDrop ND-100; CelBio).

## 3.20 Quantitative Real-Time PCR

1 µg of each RNA sample was reverse transcribed into cDNA using TaqMan™ Reverse Transcription Reagents (Thermo-Scientific). The master mix for reverse transcription was prepared by adding the reagents in the order and in the proportions as reported below (Table 2).

Table 2: Reverse transcription master mix

| Components (Thermo-Scientific) | Final concentration |
|---|---|
| 10X RT Buffer | 1X |
| 25 mM $MgCl_2$ | 1.75 mM |
| dNTPs mix (dGTP, dATP, dCTP, dTTP) | 0.5 mM each |
| Random Hexamers | 2.5 µM |
| RNase Inhibitor | 1.0 U/µl |
| MultiScribe Reverse Transcriptase | 2.5 U/µl |

Subsequently, cDNA was employed as template for quantitative-PCR using PowerUp SYBR Green Master Mix (Applied Biosystems) on the StepOnePlus Real-Time PCR System (Applied Biosystems). The primer sequences (Eurofins) used in the present thesis are shown Table 3. The expression level of the target genes was normalized to the housekeeping gene (GAPDH or 28S) and analyzed using the $2^{-\Delta\Delta Ct}$ method.

Table 3: Primer used for RT-qPCR

| Gene | Primer pair | Ta |
|---|---|---|
| ACTA2 | FW 5'-CCT TGG TGT GTG ACA ATG GC-3'<br>RV 5'-AAA CAG CCC TGG GAG CAT C-3' | 60°C |
| E2F1 | FW 5'-CCA GGA AAA GGT GTG AAA TC-3'<br>RV 5'- AAG CGC TTG GTG GTC AGA TT-3' | 62°C |
| GAPDH | FW 5'-CCCATCACCATCTTCCAGGAG-3'<br>RV 5'-CTTCTCCATGGTGGTGAAGACG-3' | 60 °C |
| MMP9 | FW 5'-CTG GAG GTT CGA CGT GAA G-3'<br>RV 5'-TCC TGG CAG AAA TAG GCT TTC-3' | 60°C |
| 28S | FW 5'-TGG GAA TGC AGC CCA AAG-3'<br>RV 5'-CCT TAC GGT ACT TGT TGA CTA TCG-3' | 60°C |

## 3.21 Apoptosis Assay – Annexin V Assay

Apoptosis is a physiological genetically programmed process for cell death, that is generally characterized by energy-dependent biochemical mechanisms and distinct morphological characteristics, including loss of plasma membrane asymmetry, plasma membrane blebbing, condensation of cytoplasm and nucleus, separation of cell fragments into apoptotic bodies (Elmore, 2007). Loss of plasma membrane asymmetry is one of the earliest features of apoptosis.

In our samples, apoptosis was evaluated by the RealTime-Glo Annexin V Apoptosis Assay (Promega). In apoptotic cells, the membrane phospholipid phosphatidylserine (PS) translocates from the inner to the outer leaflet of the plasma membrane. Annexin V is a 35 kDa phospholipid-binding protein with high affinity for PS. In this assay, Annexin V-NanoBit Luciferase fusion proteins supplied in the assay reagent bind to flipped-out PS during early apoptosis leading to the emission of a luminescent signal. Indeed, the reagent also contains a time-released luciferase substrate that provides a constant source of substrate over experimental exposure periods.

In this test, LX2 cells were seeded in 96-well plate at a density of 5 * $10^3$ cells/well. After 24 hours cells were treated with DUBs inhibitors and added with the detection reagent. After 24 hours from the treatments, luminescence of samples was measured using a luminometer (BioTek Synergy 2 Plate Reader) according to the manufacturer's instructions.

## 3.22 Cytotoxicity Assay – LDH Assay

Cell death or cytotoxicity is classically evaluated by the quantification of plasma membrane damage. In this thesis, cellular cytotoxicity was evaluated by lactate dehydrogenase (LDH) assay, with LDH-Cytotoxicity Colorimetric Assay Kit (BioVision). This type of assay is based on the measurement of the activity of lactate dehydrogenase, that is released from damaged cells. LDH activity is determined by a coupled enzymatic reaction: LDH oxidizes lactate to pyruvate which then reacts with tetrazolium salt to formazan. The increase in the amount of formazan produced in culture supernatant directly correlates to the increase in the number of lysed cells.

Cells were seeded as in MTT assay protocol. At the end of the appropriate treatment with DUBs inhibitors, 100 µl of cellular supernatant were transferred to an optical clear 96-well plate. 100 µl of the Reaction Solution, containing the catalyst solution and the dye solution at a ratio of 1:45, were then added to each well and incubated for 30 minutes at RT, protecting plate from light. Absorbance of samples was measured at 500 nm (SpectraMax Plus 384 Molecular Devices). As positive control (+ CTR), Triton X-100 (1% final concentration; Sigma-Aldrich) treated cells were considered whereas free medium was used as negative control (– CRT). The percentage of cytotoxicity was determined according to the formula:

$$\%\ Cytotoxicity = \left(\frac{test\ sample - (-\ CTR)}{(+\ CTR) - (-CTR)}\right) * 100 \quad (3.3)$$

## 3.23 Autophagy assay – LC3 Assay

Autophagy is the process by which cells degrade and recycle proteins and organelles to maintain intracellular homeostasis. Normally, autophagy plays a protective role in cells. However, a disruption of autophagy mechanisms or an excessive autophagic flux usually lead to cell death (Liu et al., 2023). In this thesis, we evaluated the autophagic flux by means of the Autophagy LC3 HiBiT Reporter Assay System (Promega). This kit employes a luminescent LC3 reporter to quantitatively measure autophagic flux. The autophagy LC3 reporter consists of a HiBiT tag fused to the human LC3 protein. Upon autophagy induction, the LC3 reporter proteins are sequestered within autophagosomes and subsequently degraded. With addition of the lytic reagent containing LgBiT protein and substrate, LgBiT interacts with the HiBiT tag to reconstitute the luminescent NanoBiT® enzyme. The resulting luminescent signal is directly proportional to the amount of HiBiT-tagged LC3 reporter. An increase in autophagic flux enhances the degradation of the autophagy reporter, leading to a decrease in luminescent signal, while inhibition of autophagy results in elevated reporter levels and a stronger luminescent signal (Promega, 2024). Following the manufacturer's instructions, we transfected the reporter vector into LX2 cells, after 24 hours from the seeding in a 96-well plate (opaque and white plate) with a density of 2,5 * $10^3$ cells/well. After 3 days from transfection, we treated cells with DUBs inhibitors. 24 hours after treatment we added the detection reagent and recorded the luminescence using a luminometer (BioTek Synergy 2 Plate Reader).

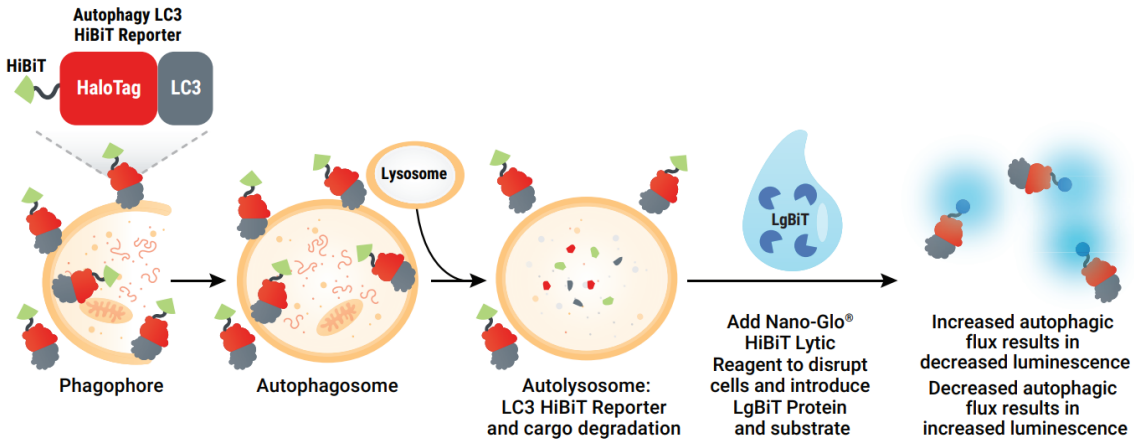


Figure 37: Principle of the Autophagy LC3 HiBiT Reporter Assay (Promega). The Autophagy LC3 HiBiT Reporter, similar to endogenous LC3 protein, becomes targeted to phagophores when autophagy is induced in cells. The reporter molecules captured within the lumen of autophagosomes are subsequently degraded upon autolysosome formation. After cell treatment, the level of intact Autophagy LC3 HiBiT Reporter is indicated by luminescent signal following application of the NanoGlo® HiBiT Lytic Detection System (https://www.promega.co.uk/products/cell-health-assays/autophagy/autophagy-assay).

## 3.24 Immunocytochemistry

LX2 cells were seeded on slides placed in each well of a 6 well plate with a density of 1.5 * $10^5$ cells/well. After the specific treatment, cells were fixed in 4% PFA for 15 minutes at RT. Then cells were washed three times in 1X PBS and were permeabilized with 0.1% Triton X-100 (Sigma-Aldrich) for 5 min. After three washes in 1X PBS, cells were submerged in blocking solution (1% BSA in 1X PBS) for 1 hour, incubated with primary antibodies anti-collagen I (diluted 1:100; ab34710; Abcam), β-tubulin (diluted 1:50; 2128; Cell Signaling Technology), vimentin (diluted 1:50; sc-6260; Santa Cruz) and, fibronectin (diluted 1:50; sc-8422; Santa Cruz) at 4°C overnight, detected with Alexa Flour 488-conjugated secondary antibody (diluted 1:400; Invitrogen) for 45 minutes at room temperature. The nuclei were stained with DAPI (diluted 1:2500; Sigma-Aldrich) for 5 minutes. Finally, cells were mounted using Moviol solution (Mowiol 4-88 Fluka). The images were captured by Fluorescence Microscope (Leica DM200).

## 3.25 Oil Red O staining (ORO staining)

ORO staining permits to stain the lipid droplets. The stock solution of ORO (Sigma-Aldrich) 0.5% was prepared in absolute isopropanol. Before using, the stock ORO was diluted 3:2 in distilled water and left for 10 min at 4°C to obtain the final working solution.

Briefly, the cultured cells were washed with 1X PBS and fixed with 4% PFA for 1 hour at RT. Cells were then washed with isopropanol 60% for 5 minutes, incubated with ORO working solution for 25 min at RT, followed by a three-time rinse with PBS. The nuclei were counterstained with Hematoxylin (Sigma-Aldrich) for 1 min before light microscope observation.

## 3.26 Statistical analysis

Statistical tests are classified into two primary categories: parametric and non-parametric tests. The distinction between these tests is based on the assumptions they make about the underlying distribution of the data.

Parametric tests operate under the assumption that the data are drawn from a specific distribution, typically a Gaussian or normal distribution. These tests are grounded in parameter estimation, where parameters such as the population mean and variance are estimated and used to draw inferences about the population characteristics. Common parametric tests include the t-test, Analysis of Variance (ANOVA), and Pearson's r correlation

coefficient. These tests offer greater statistical power, meaning they have a higher probability of detecting an effect if one truly exists, when their assumptions are satisfied. However, they may lose robustness, or the ability to perform well under a variety of conditions, when these assumptions are violated.

In contrast, non-parametric tests do not impose any assumptions about the distribution of the data. They do not involve the estimation of statistical parameters such as the mean, variance, or standard deviation. Non-parametric tests, including the Wilcoxon test, Mann-Whitney test, and Spearman's correlation coefficient, are often employed when the data fail to meet the requirements imposed by parametric tests.

While parametric tests generally offer greater statistical power, they are contingent upon certain assumptions about the data. If these assumptions are not met, non-parametric tests provide a robust alternative.

In this thesis, the selection of parametric or non-parametric tests was contingent upon the distribution characteristics of the data. Statistical significance was determined using *GraphPad InStat* software.

*F-test e Student's t test*

When a set of experimental data shows a sufficiently strong tendency to group around the most probable value, it is convenient to derive the average value $\bar{x}$, the standard deviation σ (square root of the variance $\nu_a$) and the standard error of the mean (SEM) to establish how the data are dispersed around this value:

$$\bar{x} = \frac{1}{N}\sum_{i=1}^{N} x_i$$

$$\nu_a = \frac{1}{N-1}\sum_{i=1}^{N}(x_i - \bar{x})^2$$

$$\sigma = \sqrt{\frac{1}{N-1}\sum_{i=1}^{N}(x_i - \bar{x})^2}$$

$$SEM = \frac{\sigma}{\sqrt{N}}$$

(3.1)

where $x_i$ represent the value of the i-th experimental data and N is the number of data considered. In statistical analysis, to determine whether two distributions are characterized by different or equal mean values, it is necessary to proceed according to a two-step procedure.

Firstly, the F-test is applied to determine whether the two mean values are characterized by different variances or not. This test consists in evaluating the experimental value of F, defined as the ratio between the higher weighted variance $\nu_{awh}$ and the lower one $\nu_{awl}$:

$$F = \frac{\nu_{awh}}{\nu_{awl}} \qquad \nu_{awh} = \frac{\nu_{ah}}{n_h - 1} \qquad \nu_{awl} = \frac{\nu_{al}}{n_l - 1}$$

(3.2)

where $\nu_{ah}$ and $\nu_{al}$ are, respectively, the highest and lowest variance referred to two different sets of data characterized respectively by $n_h$ e $n_l$ elements. Setting a probability value $p = 1 - \alpha$ of telling the truth (typically 0.95 or 0.99), if the value of F, calculated according to equation (*3.2* with $(n_h - 1)$ degrees of freedom for the numerator and $(n_l - 1)$ degrees of freedom for the denominator, is greater than the tabulated value of F, then $\nu_{ah}$ and $\nu_{al}$ are statistically different; otherwise, they are equal. To determine whether two distributions with the same variance ($\nu_{ah}$ and $\nu_{al}$) are characterized by different mean values, the Student's t-test can be applied. For this purpose, the combined variance is defined as:

$$s_D = \sqrt{\frac{\sum_{i=1}^{n_h}(x_i - \bar{x}_h)^2 - \sum_{i=1}^{n_l}(x_i - \bar{x}_l)^2}{n_h + n_l - 2}\left(\frac{1}{n_h} + \frac{1}{n_l}\right)}$$

(3.3)

It follows that the experimental t value is calculated through:

$$t = \frac{|\bar{x}_h - \bar{x}_l|}{s_D}$$

(3.4)

where the numerator is the absolute value of the difference between the two average values $\bar{x}_h - \bar{x}_l$.

By setting a probability value of $p = 1 - \alpha$ to tell the truth (typically 0.95 or 0.99), if the calculated t value (with $n_h + n_l - 2$ degrees of freedom) is greater than the tabulated t value corresponding to that chosen p value, then the average values $\bar{x}_h$ and $\bar{x}_l$ are statistically different; if the opposite happens, they are equal.

Conversely, if two variances ($\nu_{ah}$ and $\nu_{al}$) are statistically different, the following form of the Student's t-test allows you to decide whether the corresponding average values ($\bar{x}_h$ and $\bar{x}_l$) are equal or not:

$$t = \frac{|\bar{x}_h - \bar{x}_l|}{\sqrt{\frac{\nu_{ah}}{n_h} + \frac{\nu_{al}}{n_l}}}$$

(3.5)

By setting a probability value of $p = 1 - \alpha$ to tell the truth (0.95 or 0.99), if the t value calculated with $dof$ degrees of freedom:

$$dof = RTNI\left(\frac{(\frac{v_{ah}}{n_h} + \frac{v_{al}}{n_l})^2}{\frac{(\frac{v_{ah}}{n_h})^2}{n_h - 1} + \frac{(\frac{v_{al}}{n_l})^2}{n_l - 1}}\right)$$

(3.6)

where $RTNI$ means 'round to the nearest integer', is greater than the tabulated one, then $\bar{x}_h$ and $\bar{x}_l$ are statistically different; otherwise, they are equal.

*Chi-square test: linear regression*

To define a law that expresses the average distance of a mathematical model from the experimental data, it is assumed that this model *f* is characterized by M variable parameters ($a_j$, with $j = 1, \dots, M$) to fit on $N$ data points $(x_i, y_i)$ (with $i = 1, \dots, N$) where $x$ and $y$ are the independent and dependent variables, respectively. It can be shown that the most probable set of model parameters is the one that minimizes the chi-square $\chi^2$:

$$\chi^2 \equiv \sum_{i=1}^{N}\left(\frac{y_i - f(x_i, a_1 \dots a_M)}{\sigma_i}\right)^2$$

(3.7)

where $\sigma_i$ is the standard deviation of the i-th data.

Although equation (3.7) strictly holds when measurement errors are normally distributed, it is also useful if the assumption of normality does not exist. In the simplest case where $f$ is a straight line (linear regression) characterized by the independent variable $x$, the slope $m$, and the intercept $q$:

$$f(x_i, a_1 \dots a_M) = mx + q$$

(3.8)

the equation (3.7) becomes:

$$\chi^2(m, q) \equiv \sum_{i=1}^{N}\left(\frac{y_i - mx_i - q}{\sigma_i}\right)^2$$

(3.9)

The conditions that allow to minimize the $\chi^2$ and, therefore, to calculate $m$ and $q$, are:

$$\frac{\partial \chi^2(m,q)}{\partial m} = -2\sum_{i=1}^{N}\frac{(y_i - mx_i - q)x_i}{{\sigma_i}^2} = 0 \qquad \frac{\partial \chi^2(m,q)}{\partial q} = -2\sum_{i=1}^{N}\frac{(y_i - mx_i - q)}{{\sigma_i}^2} = 0$$

(3.10)

Finally, it is also possible to estimate the uncertainties associated with the parameters $m$ and $q$ ($\delta_m$ e $\delta_q$), which depend on the quality of the experimental data and the ability of the mathematical model to describe such data. An approximate evaluation of these uncertainties is given by:

$$\delta_m = \sqrt{\sum_{i=1}^{N}\left(\frac{y_i - mx_i - q}{\sigma_i}\right)^2/(N-M)} * \sqrt{{\sigma_m}^2}$$

$$\delta_q = \sqrt{\sum_{i=1}^{N}\left(\frac{y_i - mx_i - q}{\sigma_i}\right)^2/(N-M)} * \sqrt{{\sigma_q}^2}$$

(3.11)

where $N$ and $M$ are, respectively, the number of experimental points and fitting parameters of the model (for the line $M = 2$). In order to verify whether the fitting is statistically acceptable or not, the F test is used. In particular, it evaluates whether two particular variances, the mean square regression $MSR$ and the mean square error $MSE$, differ or not:

$$MSR = \frac{\sum_{i=1}^{N}\left(\frac{y_i - \bar{y}}{\sigma_i}\right)^2 - \sum_{i=1}^{N}\left(\frac{y_i - y_i^p}{\sigma_i}\right)^2}{M-1} \qquad \bar{y} = \frac{\sum_{i=1}^{N}\left(\frac{y_i}{{\sigma_i}^2}\right)}{\sum_{i=1}^{N}\left(\frac{1}{{\sigma_i}^2}\right)}$$

$$MSE = \frac{\sum_{i=1}^{N}(\frac{y_i - y_i^p}{\sigma_i})^2}{M-1}$$

(3.12)

where the degrees of freedom associated with $MSR$ are $\nu_1 = M - 1$, while those associated with $MSE$ are $\nu_2 = M - N$. Consequently, the calculated value of $F$ is $F = MSR/MSE$. In the presence of a good data fitting, since only $MSE$ tends to zero, $F$ will be very high. If the calculated value of $F$ (with $\nu_1$ degrees of freedom for the numerator and $\nu_2$ degrees of freedom for the denominator) is greater than the tabulated one corresponding to a fixed probability of $p = 1 - \alpha$ of telling the truth, $MSR$ will be statistically larger than $MSE$. Therefore, the data fitting will be statistically acceptable.

Pearson and Spearman Correlation Indices

The interpretation of experimental results frequently requires the identification of relationships between variables. Specifically, it's vital to ascertain if a functional relationship, like correlation, is present between two variables within a specific data set. Two variables, $x$ and $y$, are considered correlated if the trend of one can be inferred from the trend of the other. This correlation is quantified through a numerical value known as the correlation coefficient, which ranges from -1 to 1. Negative values indicate an inverse correlation, while positive values indicate a direct correlation. The correlation is perfect when the correlation coefficient equals ±1, and the correlation strength decreases as the coefficient approaches 0.

To identify correlations between different variables, the Kolmogorov-Smirnov test (K-S test) is initially performed for each pair of data sets. This test verifies whether one, both, or neither of the data sets follow a Gaussian distribution.

If a pair of data sets passes the normality test, the Pearson correlation index ($r_p$) can be evaluated. This index expresses a potential relationship between two statistical variables. However, if even one data set does not follow a Gaussian distribution, the non-parametric Spearman correlation index ($r_{sp}$) is evaluated. This index measures the correlation strength between two variables when the normality assumption is not met.

The $r_p$, which ranges from -1 to 1, is calculated as the ratio of the covariance of two statistical variables ($D_{XY}$) to the product of their standard deviations:

$$r_p = \frac{D_{XY}}{\sqrt{D_X D_Y}} \tag{3.13}$$

where the covariance $D_{XY}$ and the variances $D_X$ and $D_Y$ are, respectively:

$$D_{XY} = \sum_{i=1}^{N} \frac{1}{\sigma_i^2} \sum_{i=1}^{N} \frac{X_i Y_i}{\sigma_i^2} - \sum_{i=1}^{N} \frac{X_i}{\sigma_i^2} \sum_{i=1}^{N} \frac{Y_i}{\sigma_i^2}$$

$$D_X = \sum_{i=1}^{N} \frac{1}{\sigma_i^2} \sum_{i=1}^{N} \frac{X_i}{\sigma_i^2} - \left( \sum_{i=1}^{N} \frac{X_i}{\sigma_i^2} \right)^2 \qquad D_Y = \sum_{i=1}^{N} \frac{1}{\sigma_i^2} \sum_{i=1}^{N} \frac{Y_i}{\sigma_i^2} - \left( \sum_{i=1}^{N} \frac{Y_i}{\sigma_i^2} \right)^2 \tag{3.14}$$

The t-test with ($N$-2) degrees of freedom allows us to say whether the obtained value of $r_p$ is statistically different from zero, that is, it is statistically significant:

$$t_r = r_p \sqrt{N - 2/(1 - {r_p}^2)} \tag{3.15}$$

To understand whether the possible correlation between the two data sets is linear or not, we use the correlation coefficient ρ defined by:

$$\rho = \sqrt{\sum_{L=1}^{k} n_L(\bar{Y}_L - \bar{Y})^2 \Big/ \sum_{i=1}^{N}(Y_i - \bar{Y})^2}$$

(3.16)

where,

$$\bar{Y} = (\sum_{i=1}^{N} \frac{Y_i}{\sigma_{iY}^2})/(\sum_{i=1}^{N} \frac{1}{\sigma_{iY}^2}) \qquad \bar{Y}_L = (\sum_{j=1}^{n_L} \frac{Y_j}{\sigma_{jY}^2})/(\sum_{i=1}^{N} \frac{1}{\sigma_{jY}^2})$$

(3.17)

In practice, this coefficient analyzes the two distributions at the level of subgroups (in number of $k$) each consisting of $n_L$ elements ($1 \leq L \leq k$) and each characterized by the mean $\bar{Y}_L$. In this case too, the statistical significance of ρ is determined by the t-test:

$$t_r = \rho\sqrt{N - 2/(1 - \rho^2)}$$

(3.18)

If $r_p$ and ρ are statistically equal (F test), then the correlation is linear. If not, then the correlation is not linear.

When dealing with data sets that do not follow a Gaussian (or normal) distribution, it's necessary to use the Spearman correlation coefficient ($r_{sp}$). This coefficient is essentially the Pearson coefficient, but it's calculated based on the ranks of the data in the two series, rather than the actual data values themselves.

*Mann-Whitney U test*

The Mann-Whitney U test is a nonparametric statistical test that is used to compare two unpaired groups with no specific distribution (Mann and Whitney, 1947).

The Mann-Whitney U is intended to determine if two groups (e.g., samples "a" and "b") come from the same population (p), which is a null hypothesis stipulating that the distributions of both populations are equal (McKnight and Najab, 2010). The alternative hypothesis is that the distributions are not equal. To test the null hypothesis, Mann-Whitney test operates by ranking all the values from both groups from 1 to N, without considering to which group each value belongs. N is the total sample size ($n_a + n_b = N$). After ranking, the procedure divides the rank scores by group and calculates the sum of the ranks for each group ($T_a$ and $T_b$). Then, to calculate the U statistic is possible to use the equations here reported:

If $n_a > n_b$: $U = T_a - (n_a(n_a + 1))/2$

(3.19)

If $n_b > n_a$: $U = T_b - (n_b(n_b + 1))/2$

(3.20)

The U statistic follows a discrete or uniform distribution, allowing us to set a critical value, assign a probability to it, and test the null hypothesis. A critical value, often 0.05, helps us determine if differences are due to chance. If the U statistic exceeds this critical value, we reject the null hypothesis, suggesting the samples come from different populations.

# 4. Results

There is a great need to develop novel therapeutic strategies to slow down or stop the fibrotic process that would otherwise lead to liver failure. In addition to the use of *in vitro* model where HSCs are grown on a plastic surface, here we developed a novel *in vitro* system that can take into account the viscoelastic properties of the normal and fibrotic liver. For this purpose, we employed alginates, natural polymers particularly suited to generate surfaces tunable with regard to the viscoelastic properties. Notably, in literature there is a lack of proper information about the mechanical characteristics of the human liver tissue. Indeed, studies conducted on porcine liver tissue are mostly available (Jugé et al., 2023; Nicolle et al., 2010; Wex et al., 2014). To have a better insight on human liver tissue viscoelastic properties, we characterized healthy and pathological liver samples by means of rheology. This characterization allowed also to theoretically evaluate the minimum work that the cell has to perform in order to adhere and, consequently, modify the surrounding substrate.

## 4.1 Liver samples

The liver samples analyzed in this study were kindly provided by Prof. Silvia Palmisano, a bariatric surgeon at Cattinara Hospital in Trieste, and Prof. Fabrizio Zanconati, the director of the Department of Pathological Anatomy at the same institution. The samples are divided into two distinct groups. The first group consisted of 30 biopsies from the same number of obese patients that underwent bariatric surgery, while the second group comprised 10 liver tissue obtained from hepatic resections in the same number of patients with liver cancer. The obese patients' samples, named *pathological samples*, exhibited varying degrees of fibrosis and steatosis as evaluated histologically. In contrast, *healthy samples* were obtained from normal liver enucleated from large cancer resection tissue.

The pathological samples were analyzed histologically by the Department of Pathological Anatomy at Cattinara Hospital and classified according to the Kleiner-Brunt fibrosis and steatosis stages (Kleiner et al., 2005). The scoring systems utilized are detailed in Table 4, and the classification of our pathological samples is presented in Table 5.

Table 4: Fibrosis and steatosis scoring system according to Kleiner-Brunt classification (Kleiner et al., 2005).

| Item | Definition | Score |
|---|---|---|
| **Steatosis** | Evaluation of parenchymal involvement | |
| Grade | < 5% | 0 |
| | 5% - 33% | 1 |
| | > 33% - 66% | 2 |
| | > 66% | 3 |
| **Fibrosis** | | |
| Stage | None | 0 |
| | Perisinusoidal or periportal | 1 |
| | Mild, zone 3, perisinusoidal | 1A |
| | Moderate, zone 3, perisinusoidal | 1B |
| | Portal/periportal | 1C |
| | Perisinusoidal and portal/periportal | 2 |
| | Bridging fibrosis | 3 |
| | Cirrhosis | 4 |

Table 5: Kleiner-Brunt classification of our pathological samples derived from histological analysis conducted from the Department of Pathological Anatomy at Cattinara Hospital in Trieste.

| Sample | Steatosis stages | Fibrosis stages | Sample | Steatosis stages | Fibrosis stages |
|---|---|---|---|---|---|
| **1** | 1 | 0 | **16** | 1 | 1 |
| **2** | 1 | 0 | **17** | 3 | 1A |
| **3** | 0 | 1A | **18** | 0 | 1A |
| **4** | 1 | 1C | **19** | 0 | 0 |
| **5** | 1 | 1C | **20** | 1 | 0 |
| **6** | 1 | 0 | **21** | 2 | 0 |
| **7** | 1 | 0 | **22** | 1 | 0 |
| **8** | 3 | 1A | **23** | 1 | 0 |
| **9** | 1 | 1B | **24** | 1 | 1C |
| **10** | 1 | 1B | **25** | 1 | 0 |
| **11** | 0 | 1B | **26** | 2 | 1 |
| **12** | 0 | 1A | **27** | 0 | 0 |
| **13** | 1 | 2 | **28** | 1 | 0 |
| **14** | 1 | 1 | **29** | 0 | 0 |
| **15** | 0 | 0 | **30** | 1 | 1 |

The majority exhibited steatosis and half of them presented fibrosis. Specifically, 22 samples had a steatosis grade ≥ 1, and 16 samples exhibited a fibrosis stage ≥ 1. The prevalence of steatosis among these samples reflected the pathological condition of obesity of these patients, which had a BMI (see Table 6), higher than the normal range of 18.5 to 24.9 (Caballero, 2019). Moreover, the high incidence of histologic outcome of fibrosis in these samples is due to the fact that fibrosis is directly correlated with increasing weight (Sheka et

al., 2020). In fact, around 40% of NASH patients have progression of their fibrosis over time, at a rate of about 1 stage per decade (Younossi et al., 2016).

Table 6: Clinical data of the 30 obese patients corresponding to the pathological liver samples.

| Patient | height (m) | weight (kg) | ideal weight (kg) | excess weight (kg) | BMI (kg/m$^2$) |
|---|---|---|---|---|---|
| **1** | 1,73 | 143,5 | 74,8 | 68,7 | 47,9 |
| **2** | 1,57 | 90,4 | 61,6 | 28,8 | 36,7 |
| **3** | 1,7 | 113,1 | 72,3 | 40,9 | 39,1 |
| **4** | 1,7 | 96,1 | 72,3 | 23,9 | 33,3 |
| **5** | 1,67 | 108,6 | 69,7 | 38,9 | 38,9 |
| **6** | 1,79 | 144,0 | 80,1 | 63,9 | 44,9 |
| **7** | 1,54 | 96,2 | 59,3 | 36,9 | 40,6 |
| **8** | 1,65 | 115,0 | 68,1 | 46,9 | 42,2 |
| **9** | 1,68 | 133,0 | 70,6 | 62,4 | 47,1 |
| **10** | 1,53 | 79,0 | 58,5 | 20,5 | 33,7 |
| **11** | 1,59 | 88,8 | 63,2 | 25,6 | 35,1 |
| **12** | 1,75 | 144,6 | 76,6 | 68,0 | 47,2 |
| **13** | 1,59 | 91,0 | 63,2 | 27,8 | 36,0 |
| **14** | 1,72 | 140,0 | 74,0 | 66,0 | 47,3 |
| **15** | 1,72 | 117,0 | 74,0 | 43,0 | 39,5 |
| **16** | 1,69 | 121,8 | 71,4 | 50,4 | 42,6 |
| **17** | 1,72 | 126,0 | 74,0 | 52,0 | 42,6 |
| **18** | 1,87 | 140,0 | 87,4 | 52,6 | 40,0 |
| **19** | 1,92 | 122,2 | 92,2 | 30,0 | 33,1 |
| **20** | 1,62 | 108,0 | 65,6 | 42,4 | 41,2 |
| **21** | 1,65 | 103,4 | 68,1 | 35,3 | 38,0 |
| **22** | 1,61 | 119,0 | 64,8 | 54,2 | 45,9 |
| **23** | 1,69 | 127,0 | 71,4 | 55,6 | 44,5 |
| **24** | 1,57 | 97,0 | 61,6 | 35,4 | 39,4 |
| **25** | 1,54 | 107,0 | 59,3 | 47,7 | 45,1 |
| **26** | 1,69 | 108,0 | 71,4 | 36,6 | 37,8 |
| **27** | 1,67 | 127,0 | 69,7 | 57,3 | 45,5 |
| **28** | 1,78 | 125,0 | 79,2 | 45,8 | 39,5 |
| **29** | 1,76 | 120,0 | 77,4 | 42,6 | 38,7 |
| **30** | 1,80 | 130,0 | 81,0 | 49,0 | 40,1 |

To evaluate the liver stiffness, most patients had a liver elastography examination, particularly a shear-wave elastography, an ultrasound elastography technique. The ultrasound elastography techniques are a non-invasive method of estimating the mechanical properties of soft tissues *in vivo* by using the relationships between wave propagation and the elastic properties of materials (Bilston, 2018). The shear-wave elastography is a recent development of the ultrasound elastography, that combines imaging with elastography. With these techniques, it is possible to estimate the degree of liver fibrosis. However, there are several factors that affect the measurements. These include patient factors such as obesity, fasting, blood pressure, position, some medications, co-morbidities like acute or chronic liver disease and vascular congestion from renal or cardiac failure (Barr, 2018). Obesity can interfere with elastographic analysis due to the impact of abdominal wall thickness on measurement accuracy. Specifically, the median liver stiffness values presented in the Table 7 have an over 80% probability of histological-elastographic correspondence when the abdominal wall thickness is less than 2.5 cm. Only 7 out of 26 patients who underwent the examination met this criterion. Moreover, in 3 cases the thickness of the abdominal wall precluded the analysis from being performed. This means that in the case of obese patients, liver elastography often fails to give accurate results.

The median stiffness results obtained from the elastography can be classified into Kleiner-Brunt fibrosis stages (F0-F4) according to this scale (Amernia et al., 2021):

F0: 1–6 kPa,

F1: 6.1–7 kPa,

F2: 7.1–9 kPa,

F3: 9.1–10.3 kPa,

F4: ≥ 10.4 kPa.

Table 7: Liver elastography results, including median stiffness values and corresponding fibrosis stages (F0-F4), were obtained for 23 out of 30 patients. Patients 3, 11, 24, and 30 did not undergo the examination. Patients 6, 7, and 14 had an abdominal wall thickness too high to permit accurate analysis. The highlighted lines of samples represent those with an abdominal wall thickness of ≤ 2.5 cm, which have an over 80% probability of histological-elastographic correspondence.

| Patient | Abdominal wall thickness (cm) | Median stiffness (kPa) | Corresponding Kleiner-Brunt fibrosis stages |
|---|---|---|---|
| **1** | 3,51 | 4,42 | 0 |
| **2** | 2,2 | 5,3 | 0 |
| **3** | - | - | - |
| **4** | 2,07 | 3,76 | 0 |
| **5** | 2,29 | 6,37 | 1 |
| **6** | 4,87 | not executable | not executable |
| **7** | 3,75 | not executable | not executable |
| **8** | 3,2 | 4,81 | 0 |
| **9** | 3,75 | 4,19 | 0 |
| **10** | 1,94 | 4,36 | 0 |
| **11** | - | - | - |
| **12** | 2,8 | 4,97 | 0 |
| **13** | 2,62 | 7,98 | 2 |
| **14** | 3,81 | not executable | not executable |
| **15** | 2,56 | 5,05 | 0 |
| **16** | 3,12 | 4,14 | 0 |
| **17** | 4,51 | 9,77 | 3 |
| **18** | 3,16 | 4,89 | 0 |
| **19** | 2,75 | 4,32 | 0 |
| **20** | 2,94 | 5,42 | 0 |
| **21** | 2,57 | 3,83 | 0 |
| **22** | 4,14 | 6,44 | 1 |
| **23** | 2,82 | 3,81 | 0 |
| **24** | - | - | - |
| **25** | 5,58 | 8,18 | 2 |
| **26** | 3,1 | 8,45 | 2 |
| **27** | 2,52 | 6,13 | 1 |
| **28** | 3,91 | 5,44 | 0 |
| **29** | 2,93 | 6,03 | 0 |
| **30** | - | - | - |

Table 8: Comparison between Kleiner-Brunt stages deduced from liver elastography and from histological analyses. The highlighted grey lines of samples represent those with an abdominal wall thickness of ≤ 2.5 cm, which have an over 80% probability of histological-elastographic correspondence. While green color refers to cases with correspondence between the two classifications, red color refers to cases without correspondance.

| Patient | Abdominal wall thickness (cm) | Kleiner-Brunt stages from elastography | Kleiner-Brunt stages from histological analyses |
|---|---|---|---|
| **1** | 3,51 | 0 | 0 |
| **2** | 2,2 | 0 | 0 |
| **3** | - | - | - |
| **4** | 2,07 | 0 | 1C |
| **5** | 2,29 | 1 | 1C |
| **6** | 4,87 | not executable | 0 |
| **7** | 3,75 | not executable | 0 |
| **8** | 3,2 | 0 | 1A |
| **9** | 3,75 | 0 | 1B |
| **10** | 1,94 | 0 | 1B |
| **11** | - | - | - |
| **12** | 2,8 | 0 | 1A |
| **13** | 2,62 | 2 | 2 |
| **14** | 3,81 | not executable | 1 |
| **15** | 2,56 | 0 | 0 |
| **16** | 3,12 | 0 | 1 |
| **17** | 4,51 | 3 | 1A |
| **18** | 3,16 | 0 | 1A |
| **19** | 2,75 | 0 | 0 |
| **20** | 2,94 | 0 | 0 |
| **21** | 2,57 | 0 | 0 |
| **22** | 4,14 | 1 | 0 |
| **23** | 2,82 | 0 | 0 |
| **24** | - | - | - |
| **25** | 5,58 | 2 | 0 |
| **26** | 3,1 | 2 | 1 |
| **27** | 2,52 | 1 | 0 |
| **28** | 3,91 | 0 | 0 |
| **29** | 2,93 | 0 | 0 |
| **30** | - | - | - |

To examine the accuracy of the elastographic measurement, a comparison was made between the Kleiner-Brunt classification provided by histological analysis and the Kleiner-Brunt stages corresponding to the median stiffness measured by liver elastography. Only in 11 cases a correspondence between the two classifications could be observed (green parameters in

Table *8*), while in 12 cases there was no correspondence (red parameters in Table 8). Among the 12 cases, three exhibited an abdominal wall thickness ≤ 2.5 cm. These cases were expected to have a histological-elastographic correspondence probability exceeding 80%. However, this correspondence was not observed.

## 4.2 Setting temperatures in the rheological characterization of liver samples

In this thesis, we aimed to rheologically characterize the human liver samples previously introduced. To determine the optimal temperature for rheological analysis, we performed Time Sweep measurements for 30 minutes at two different temperatures (5°C and 37°C). This is an oscillatory test to determine whether system rheological properties are time dependent or not. The oscillatory time sweep was performed at constant maximum stress (5 Pa) and frequency of 1 Hz. This test was repeated twice with two different samples (Figure 38 and Figure 39 for the first sample, Figure 40 and Figure 41 for the second sample).

The results indicated that at 37°C, the values of the storage modulus (G') and loss modulus (G'') increased after 1000 seconds, suggesting alterations in the rheological properties and structural integrity of the liver tissue. Conversely, at 5°C, the G' and G'' moduli remained stable, indicating no significant changes in the tissue's rheological properties or structure. Based on these initial findings, we selected 5°C as the temperature for subsequent analyses.

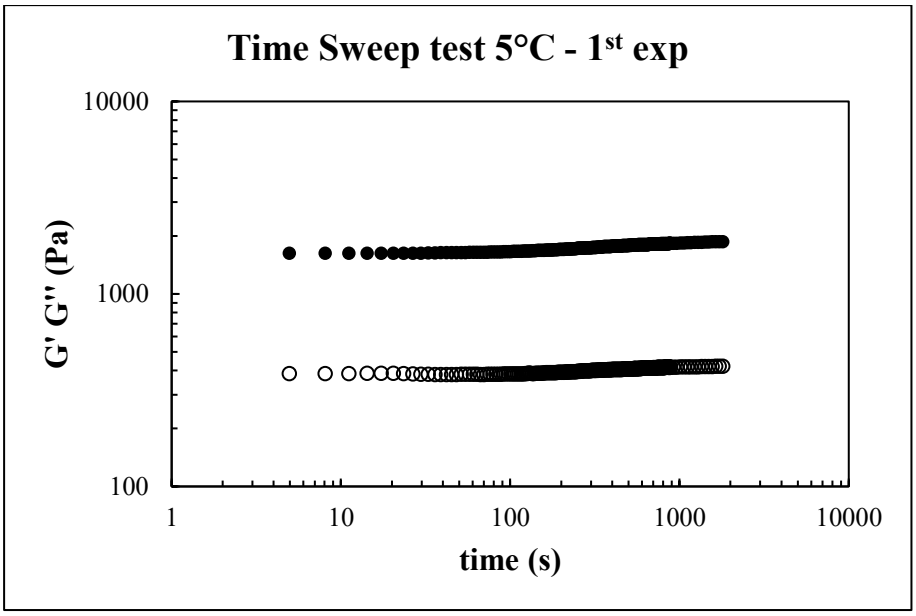


Figure 38: Time Sweep test conducted for 30 minutes at 5°C on the first liver sample. G' (black circle) is parallel to G'' (open circle) and both of them are time independent.

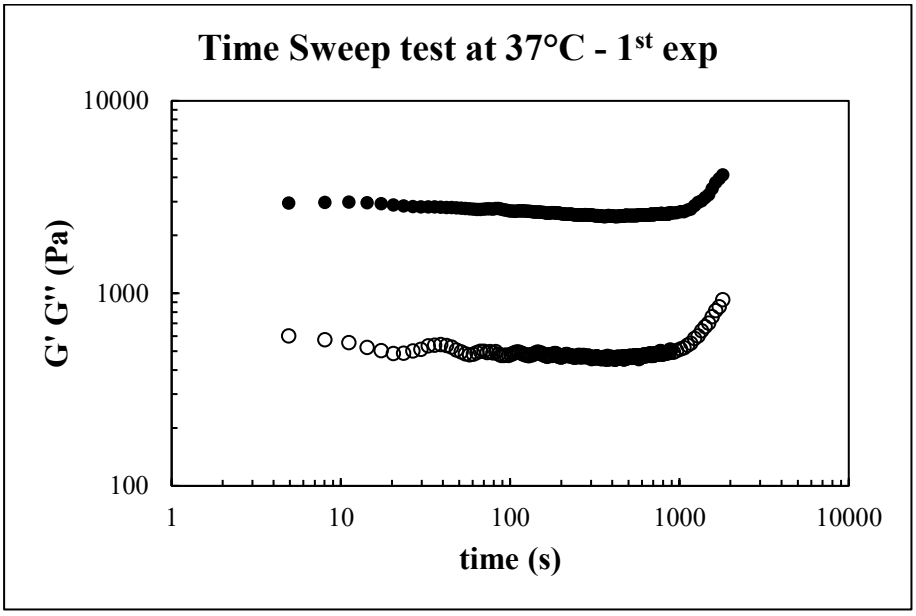


Figure 39: Time Sweep test conducted for 30 minutes at 37°C on the first liver sample. G' (black circle) and G'' (open circle) modify in time.

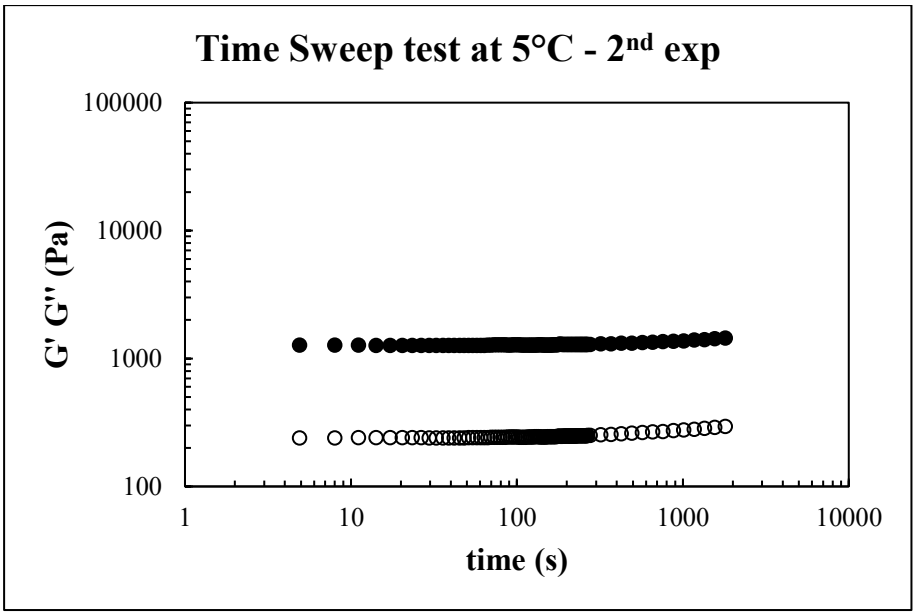


Figure 40: Time Sweep test conducted for 30 minutes at 5°C on the second liver sample. G' (black circle) is parallel to G'' (open circle) and both of them are time independent.

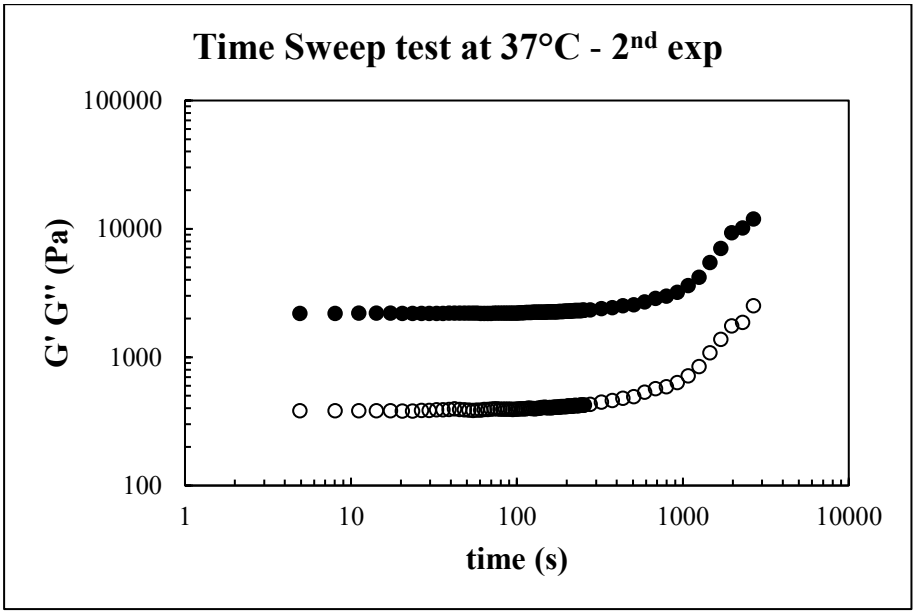


Figure 41: Time Sweep test conducted for 30 minutes at 37°C on the second liver sample. G' (black circle) and G'' (open circle) modify in time.

## 4.3 Rheological characterization of liver samples

Since the elastographic technique shows some problems, as already discussed, in this thesis we performed rheological measurements on liver samples. Stress sweep (SS) and frequency sweep (FS) tests were performed on the pathological and healthy liver samples. In the Figure 42 and Figure 43 are reported the G* modulus coming from the SS and FS tests. We remember that: $|G^*| = \sqrt{(G')^2 + (G'')^2}$.

From both tests, it can be observed that the healthy samples (blue circles connected by a line) are positioned in the lower-middle part, while the pathological samples (brown-yellow circles not connected by a line) are positioned in the upper-middle part. This indicates that the pathological samples are characterized on average by higher G* moduli than the healthy samples. This is also emphasized by the boxplot in Figure 44.

The best-fitting of the Soskey-Winter model to SS data (Table 9) and the best-fitting of the generalized Maxwell model to FS data (Table 10) allow the evaluation of the critical deformation $\gamma_c$, the critical stress $\tau_c$, the critical shear modulus $G_c$, the shear modulus G (also indicated as $\Sigma G_i$) and the relaxation time spectrum. Table 10 reports the percentage of elasticity evaluated as follows:

$$\%\ elasticity = \frac{G_0}{\sum G_i} * 100 \tag{4.1}$$

where $G_0$ is the spring constant of the purely elastic element embedded in the generalized Maxwell model used to fit the FS data.

Stress sweep tests showed that the linear viscoelastic field (the value of the stress $\tau$ at which G' and G'' begin to vary with $\tau$) is always greater than the range of $\tau$ 1-5 Pa, considered to perform frequency sweep tests. Stress sweep tests performed on pathological samples indicated that the linear viscoelastic field extends to a minimum critical strain $\gamma_c$ of $1.97*10^{-3}$ (which corresponds to $G_c$ = 29133 Pa). In terms of critical stress $\tau_c$, this corresponds to 57 Pa. For this reason, the frequency sweep tests on the pathological samples were conducted at 5 Pa, except in a few cases that 1 Pa was used. On the other hand, if we consider healthy samples, stress sweep tests showed that the linear viscoelastic region elongates to a minimum $\gamma_c$ of $9.16*10^{-5}$ (which corresponds to $G_c$ = 2363 Pa). In terms of critical stress $\tau_c$, this corresponds to 0.2 Pa. The frequency sweep tests on the healthy samples were conducted at 1 Pa, except in the case here reported as minimum, in which 0.1 Pa was used.

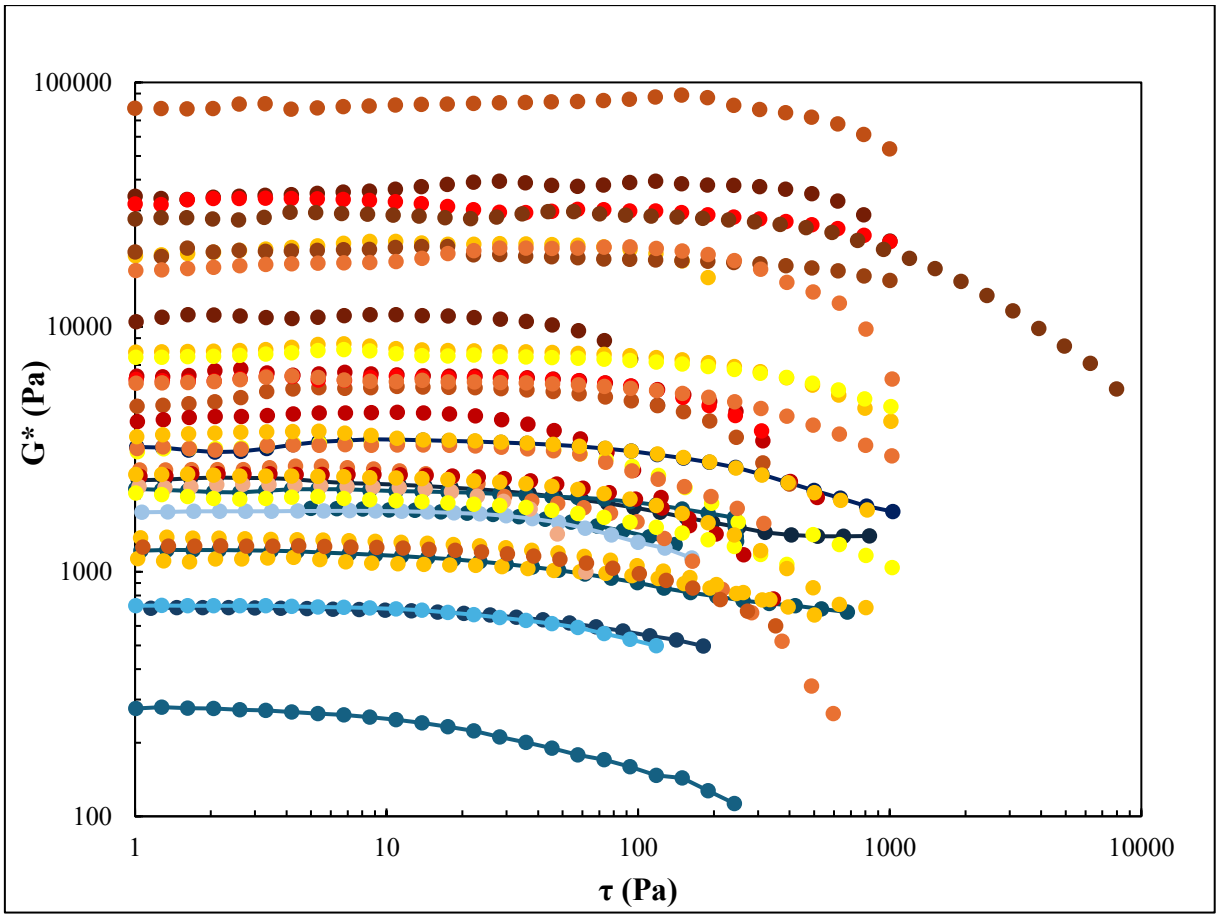


Figure 42: Stress sweep test performed on liver samples at 1 Hz. The moduli are reported as G* (Pa). The circles colored in brown, red or yellow, not connected by a line, represent pathological samples (n = 26). The circles colored in blue or light blue, connected by a line, represent healthy samples (n = 9). Each color represents one sample.

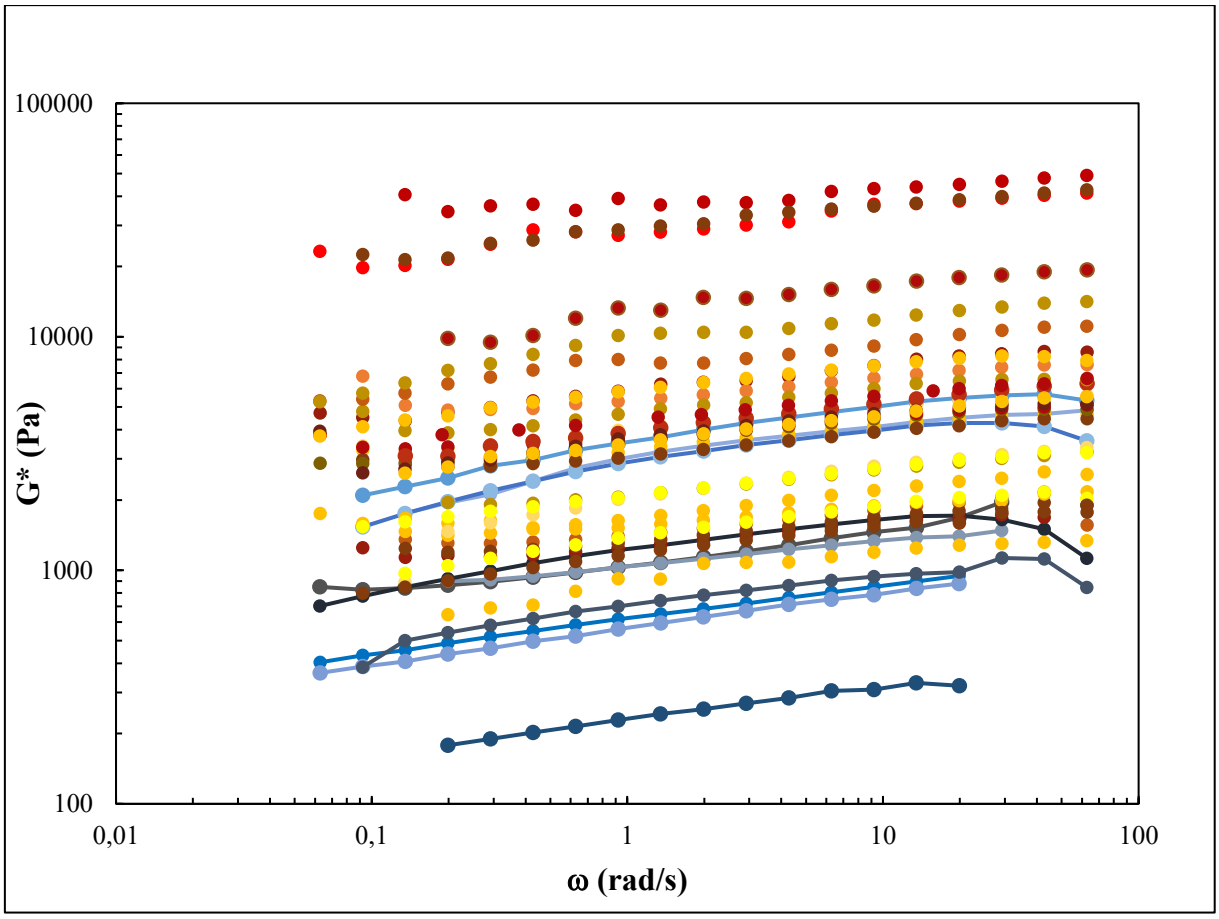


Figure 43: Frequency sweep test performed on liver samples. The moduli are reported as G* (Pa). The circles colored in brown, red or yellow, not connected by a line, represent pathological samples (n = 26). The circles colored in blue or light blue, connected by a line, represent healthy samples (n = 9). Each color represents one sample.

Table 9: Results of SS analysis on healthy (in blue) and pathological (in red) liver samples. *w* is the work (evaluated according to eq. (1.38)) and $\gamma_c$, $G_c$, $\tau_c$, $\gamma^*_c$, $G^*_c$ are the fitting parameters of the Soskey-Winter model.

| Sample | $\gamma_c$ (-) | $G_c$ (Pa) | $\tau_c$ (Pa) | $\gamma^*_c$ (-) | $G^*_c$ (Pa) | *w* (J/m$^3$) |
|---|---|---|---|---|---|---|
| **5** | 0,0065 | 5532 | 36 | 0,0067 | 5371 | 0,14368 |
| **6** | 0,0058 | 20355 | 118 | 0,0062 | 19098 | 0,39783 |
| **7** | 0,0149 | 946 | 14 | 0,0145 | 970 | 0,11687 |
| **8** | 0,0027 | 10553 | 28 | 0,0030 | 11875 | 0,04955 |
| **9** | 0,0058 | 2471 | 14 | 0,0056 | 2536 | 0,04449 |
| **10** | 0,0117 | 4968 | 58 | 0,0123 | 4751 | 0,40017 |
| **11** | 0,0104 | 2230 | 23 | 0,0091 | 2550 | 0,10207 |
| **12** | 0,0031 | 14712 | 45 | 0,0032 | 14081 | 0,07921 |
| **13** | 0,0043 | 71221 | 304 | 0,0043 | 70190 | 0,74780 |
| **14** | 0,0069 | 2590 | 18 | 0,0072 | 2501 | 0,06650 |
| **15** | 0,0167 | 14472 | 241 | 0,0173 | 13927 | 2,84057 |
| **16** | 0,0065 | 8884 | 58 | 0,0070 | 8317 | 0,22526 |
| **17** | 0,0050 | 3578 | 18 | 0,0053 | 4223 | 0,06149 |
| **18** | 0,0143 | 34269 | 490 | 0,0143 | 34326 | 3,70301 |
| **19** | 0,0098 | 3726 | 36 | 0,0106 | 3432 | 0,18293 |
| **20** | 0,0066 | 3399 | 23 | 0,0071 | 3158 | 0,08227 |
| **21** | 0,0037 | 1818 | 7 | 0,0039 | 1750 | 0,01506 |
| **22** | 0,0052 | 2696 | 14 | 0,0054 | 8566 | 0,04403 |
| **23** | 0,0057 | 1251 | 7 | 0,0059 | 1198 | 0,02389 |
| **24** | 0,0106 | 1098 | 12 | 0,0103 | 1129 | 0,06704 |
| **25** | 0,0033 | 3382 | 11 | 0,0034 | 3235 | 0,02085 |
| **26** | 0,0020 | 29133 | 57 | 0,0005 | 32564 | 0,00461 |
| **27** | 0,0078 | 7374 | 58 | 0,0081 | 7126 | 0,26148 |
| **28** | 0,0089 | 8200 | 73 | 0,0100 | 7346 | 0,37730 |
| **29** | 0,0068 | 5297 | 36 | 0,0071 | 6442 | 0,14968 |
| **30** | 0,0201 | 23086 | 465 | 0,0076 | 30167 | 0,85258 |
| **1** | 0,0085 | 1942 | 16 | 0,0089 | 1840 | 0,07229 |
| **2** | 0,0161 | 1854 | 30 | 0,0168 | 1774 | 0,24958 |
| **3** | 0,0051 | 250 | 1 | 0,0030 | 332 | 0,00133 |
| **4** | 0,0180 | 698 | 13 | 0,0399 | 647 | 0,09895 |
| **6** | 0,0184 | 465 | 9 | 0,0184 | 466 | 0,12406 |
| **7** | 0,0001 | 2363 | 0,2 | 0,0001 | 2221 | 0,00001 |
| **8** | 0,0005 | 1928 | 1 | 0,0002 | 4940 | 0,00003 |
| **9** | 0,0127 | 1383 | 18 | 0,0125 | 1400 | 0,16836 |
| **10** | 0,0126 | 3652 | 46 | 0,0136 | 3380 | 0,30344 |

Table 10: Results of FS analysis on healthy (in blue) and pathological (in red) liver samples. $\Sigma G_i$ is the shear modulus, $G_0$, $G_1$, $G_2$, $G_3$, $G_4$ and $\lambda_1$ are the fitting parameters of the generalized Maxwell model.

| Sample | $\lambda_1$ (s) | $G_0$ (Pa) | $G_1$ (Pa) | $G_2$ (Pa) | $G_3$ (Pa) | $G_4$ (Pa) | $\Sigma G_i$ (Pa) | % elasticity | mean G* (Pa) |
|---|---|---|---|---|---|---|---|---|---|
| 1 | 0,0153 | 805,8 | 1735,9 | 848,3 | 805,1 | 1885,9 | 6081,1 | 13,3 | 3719 |
| 2 | 0,0090 | 2518,5 | 1964,6 | 954,4 | 806,3 | 1059,9 | 7303,8 | 34,5 | 4392 |
| 3 | 0,0181 | 612,2 | 1740,9 | 848,1 | 725,0 | 1846,1 | 5772,3 | 10,6 | 3491 |
| 4 | 0,0164 | 3386,8 | 2562,1 | 1488,6 | 1800,2 | 1116,6 | 10354,3 | 32,7 | 6450 |
| 5 | 0,0205 | 1298,0 | 1746,2 | 897,7 | 742,5 | 1509,6 | 6194,0 | 21,0 | 3838 |
| 6 | 0,0162 | 2747,2 | 2954,9 | 1555,2 | 1451,0 | 1500,3 | 10208,6 | 26,9 | 6098 |
| 7 | 0,0234 | 8,0 | 1417,8 | 647,2 | 597,6 | - | 2670,7 | 0,3 | 1046 |
| 8 | 0,0150 | 1864,6 | 2042,1 | 1022,1 | 935,0 | 1088,6 | 6952,3 | 26,8 | 4060 |
| 9 | 0,2517 | 61,0 | 646,0 | 73,0 | 1096,3 | - | 1876,2 | 3,2 | 1420 |
| 10 | 0,0067 | 2002,1 | 3231,5 | 1451,8 | 1136,8 | 1465,2 | 9287,5 | 21,6 | 4571 |
| 11 | 0,0103 | 566,4 | 1341,5 | 432,4 | 388,8 | 615,3 | 3344,4 | 16,9 | 4571 |
| 12 | 0,0065 | 6166,3 | 5897,8 | 2930,2 | 3529,6 | 4895,8 | 23419,9 | 26,3 | 14791 |
| 13 | 0,0142 | 27123,7 | 13146,7 | 9158,8 | 9884,5 | - | 59313,7 | 45,7 | 40532 |
| 14 | 0,0267 | 59,9 | 817,4 | 393,4 | 414,5 | 837,4 | 2522,6 | 2,4 | 1508 |
| 15 | 0,0539 | 3372,6 | 1747,6 | 666,3 | 1090,3 | - | 6876,9 | 49,0 | 5264 |
| 16 | 0,0102 | 2123,4 | 2717,7 | 1394,8 | 1184,2 | 1516,6 | 8936,6 | 23,8 | 5115 |
| 17 | 0,0180 | 1059,4 | 1165,3 | 498,3 | 430,0 | 501,9 | 3654,9 | 29,0 | 1757 |
| 18 | 0,0118 | 1843,8 | 1705,6 | 973,9 | 814,9 | 1260,9 | 6599,1 | 27,9 | 4004 |
| 19 | 0,0113 | 762,0 | 1295,3 | 614,8 | 480,3 | 596,7 | 3749,0 | 20,3 | 1947 |
| 20 | 0,0175 | 1704,9 | 1261,5 | 584,5 | 465,3 | - | 4016,2 | 42,5 | 2458 |
| 21 | 0,0189 | 1325,8 | 1191,5 | 595,1 | 337,6 | 284,4 | 3734,3 | 35,5 | 2342 |
| 22 | 0,0253 | 1081,4 | 1175,3 | 615,8 | 469,3 | 503,6 | 3845,3 | 28,1 | 2349 |
| 23 | 0,0297 | 745,0 | 841,3 | 408,8 | 301,6 | 249,9 | 2546,6 | 29,3 | 1602 |
| 24 | 0,0100 | 683,5 | 953,7 | 340,9 | 324,7 | 268,7 | 2571,5 | 26,6 | 1318 |
| 25 | 0,0156 | 2374,5 | 2015,5 | 901,9 | 722,6 | 570,1 | 6584,6 | 36,1 | 4062 |
| 26 | 0,0131 | 13782,0 | 11736,1 | 7862,9 | 5009,3 | 10980,8 | 49371,1 | 27,9 | 30491 |
| 27 | 0,0139 | 4102,2 | 4421,1 | 1594,7 | 2326,7 | 1888,8 | 14333,4 | 28,6 | 8159 |
| 28 | 0,0137 | 5414,6 | 4463,7 | 1933,9 | 2580,7 | 1784,1 | 16177,0 | 33,5 | 10104 |
| 29 | 0,0143 | 3599,6 | 3291,9 | 1550,6 | 1258,2 | 1045,2 | 10745,5 | 33,5 | 6286 |
| 30 | 0,0145 | 14435,1 | 12924,2 | 7194,6 | 8462,7 | 8108,2 | 51124,8 | 28,2 | 31785 |
| 1 | 0,0434 | 378,3 | 325,8 | 146,7 | 159,9 | - | 1011 | 37,4 | 1172 |
| 2 | 0,0436 | 732,6 | 531,8 | 242,5 | 275,6 | - | 1782 | 41,1 | 1160 |
| 3 | 0,0949 | 108,4 | 138,9 | 67,3 | 66,5 | - | 381 | 28,4 | 256 |
| 4 | 0,0383 | 291,9 | 452,1 | 194,6 | 135,7 | 128,4 | 1203 | 24,3 | 648 |
| 5 | 0,0093 | 324,2 | 594,8 | 251,2 | 163,0 | 135,6 | 1469 | 22,1 | 594 |
| 6 | 0,0304 | 395,0 | 483,5 | 195,0 | 153,2 | 82,5 | 1309 | 30,2 | 782 |
| 7 | 0,0131 | 1803,1 | 1812,8 | 854,4 | 742,3 | 486,7 | 5699 | 31,6 | 3468 |
| 8 | 0,0301 | 622,9 | 868,0 | 383,8 | 295,8 | 208,2 | 2379 | 26,2 | 1271 |
| 9 | 0,0218 | 1385,7 | 1655,3 | 790,1 | 637,6 | 442,4 | 4911 | 28,2 | 3161 |
| 10 | 0,0197 | 1656,3 | 2302,7 | 1179,8 | 1121,7 | 789,0 | 7049 | 23,5 | 4059 |

To facilitate a comparative analysis of the rheological properties between pathological and healthy liver samples, boxplots were utilized to display the following parameters: mean complex modulus G*, shear modulus $\Sigma G_i$, and critical stress $\tau_c$ (Figure 44 and Figure 45). The distributions of these parameters exhibited distinct differences between the two sample types. Specifically, mean G*, $\Sigma G_i$, and $\tau_c$ were statistically significantly lower in healthy liver samples, indicating reduced stiffness. These significant differences suggest that these rheological parameters can effectively differentiate between the two tissue types and provide biomechanical insights into liver tissue integrity. Increased stiffness in pathological samples is associated with pathological changes, lower stiffness attains to healthy liver tissue.

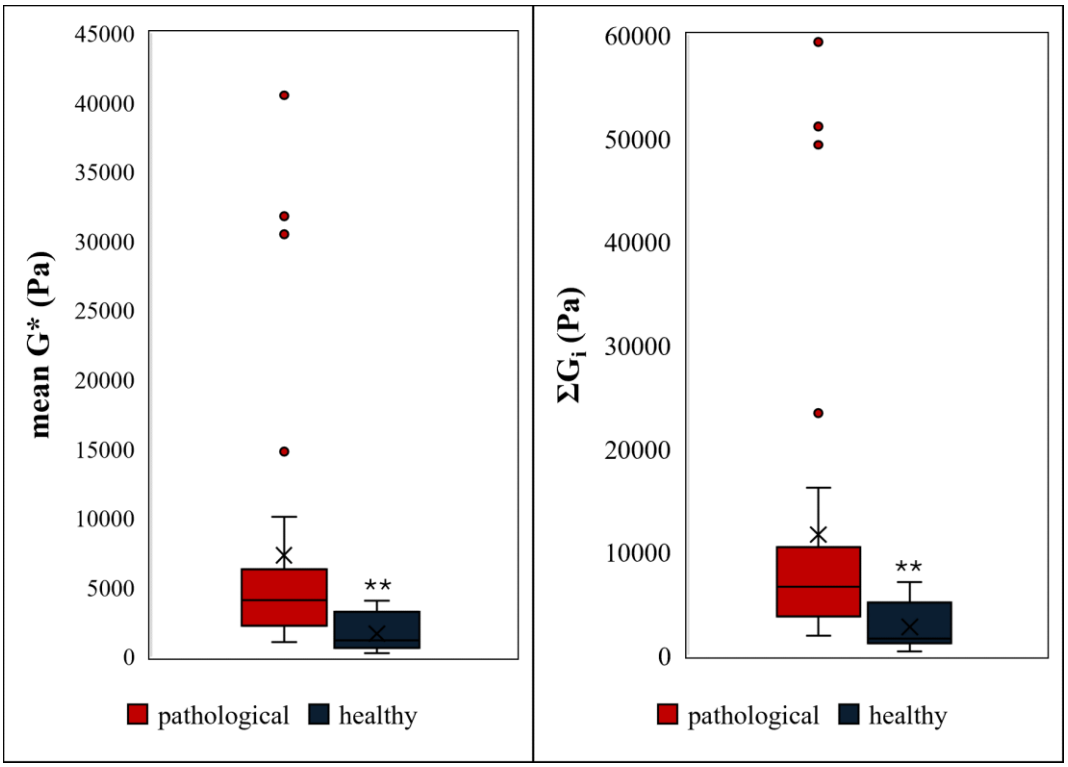


Figure 44: Boxplots with mean G* and shear modulus ΣGi for pathological (red) and healthy samples (blue). X represents the average value. In the case of mean G* the average value ± SEM is (7318 ± 1768) Pa for pathological samples and (1657 ± 432) Pa for healthy samples. The average ΣGi ± SEM for pathological samples is (11672 ± 2723) Pa and for healthy samples it is (2719 ± 728) Pa. Statistical significance was determined by comparing pathological with healthy samples: **$p < 0.001$. Statistical analyses were performed using Mann-Whitney test.

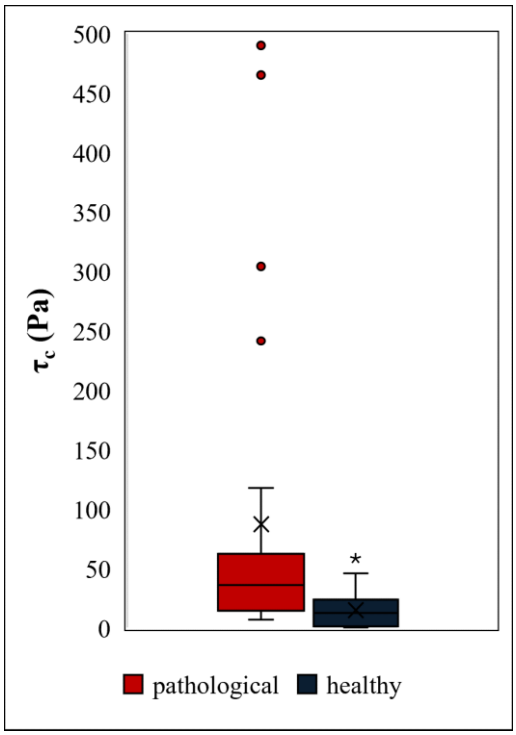


Figure 45: Boxplots with $\tau_c$ for pathological (red) and healthy samples (blue). X represents the average value. The average value ± SEM for pathological samples is (87 ± 26) Pa and for healthy samples is (15 ± 5) Pa. Statistical significance was determined by comparing pathological with healthy samples: *p < 0.01. Statistical analyses were performed using Mann-Whitney test.

To better understand the trend of G' and G'' of liver samples, their trends, referring to some significant samples, are shown in Figure 46 and Figure 47 in conjunction with the corresponding relaxation spectra (Figure 48).

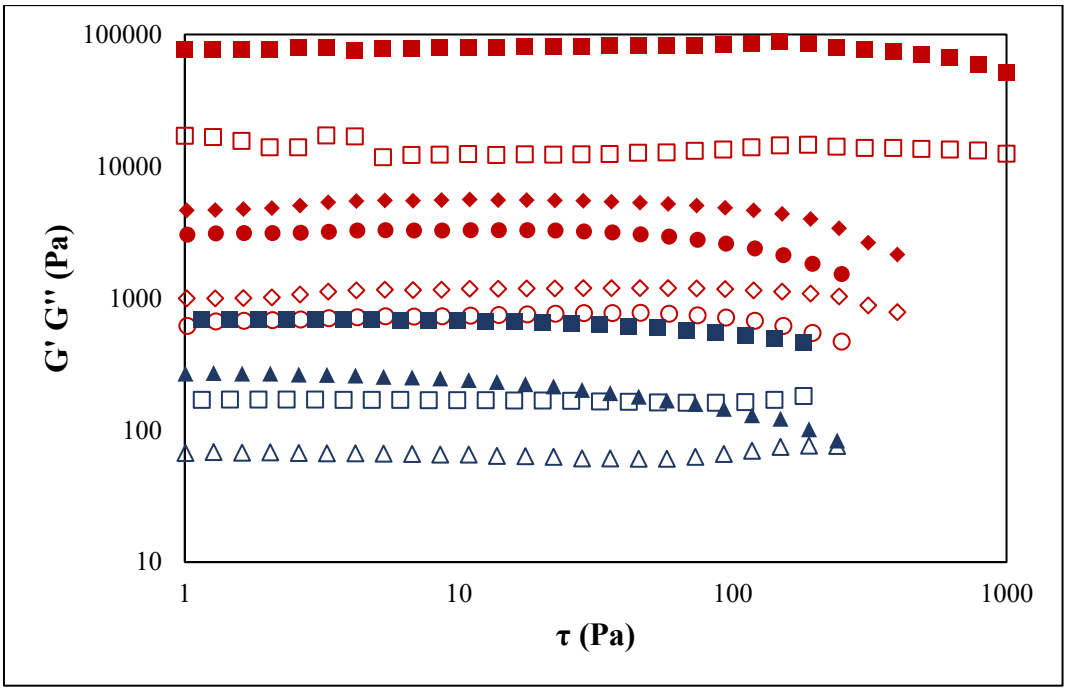


Figure 46: Stress sweep test referring to 3 pathological liver samples (red symbols) and 2 healthy samples (blue symbols). The fully colored symbols represent the G' moduli while open symbols represent the G'' moduli.

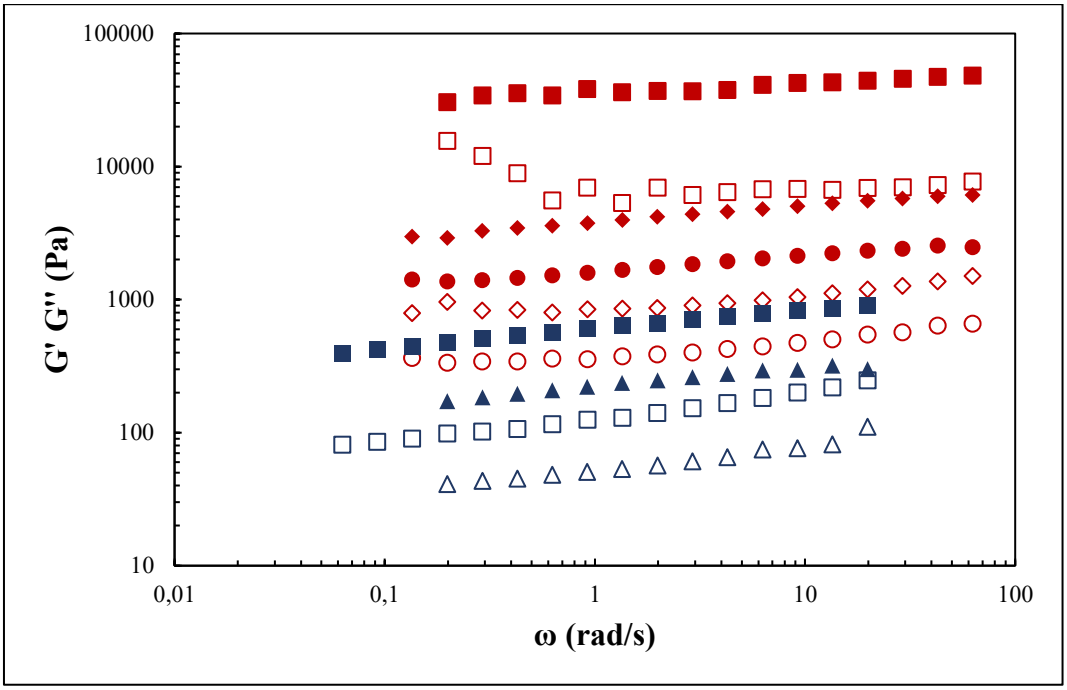


Figure 47: Frequency sweep test referring to 3 pathological liver samples (red symbols) and 2 healthy samples (blue symbols). The fully colored symbols represent the G' moduli while open symbols represent the G'' moduli.

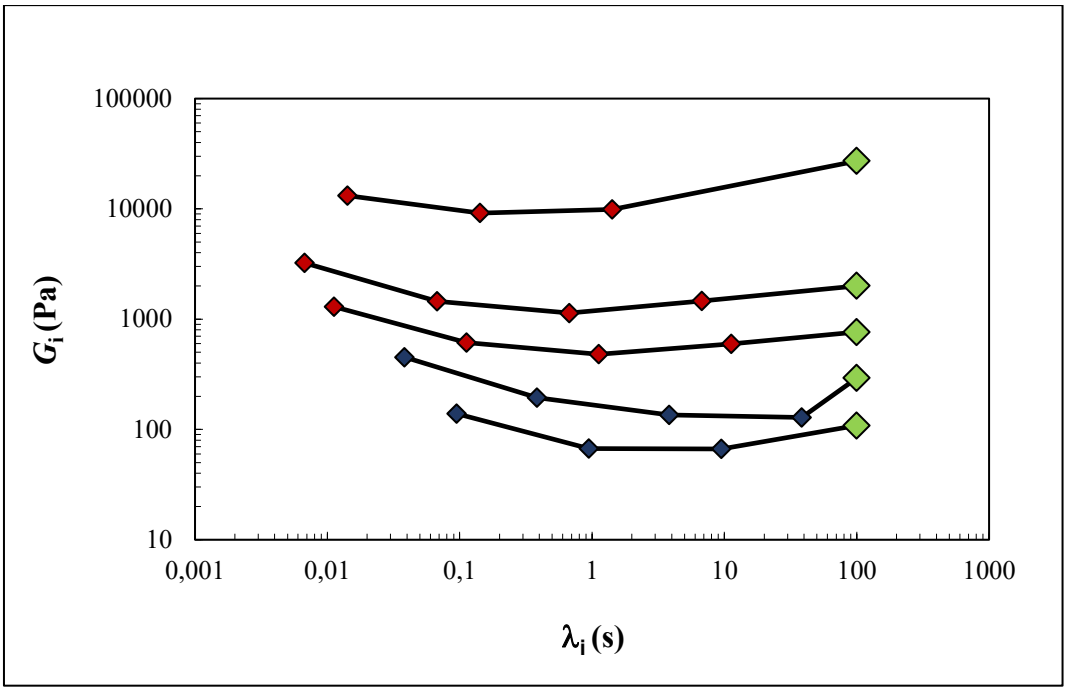


Figure 48: Relaxation spectra referring to 3 pathological liver samples (red symbols) and 2 healthy samples (blue symbols). The green rhombuses represent the elastic contribution of $G_0$, conventionally set at 100s.

The SS and FS tests (Figure 46 and Figure 47) revealed a significant predominance of the elastic modulus (G') over the viscous modulus (G'') in both healthy and pathological liver samples, with G' being approximately five times greater than G''. However, the values of G' and G'' differed between healthy and pathological liver samples, leading to variations in the shear modulus G, which is typically higher in pathological samples.

In the FS graphs (Figure 47), the parallel trend of G' and G'' is evident for both healthy and pathological liver samples. For pathological samples, the dependence of G' and G'' on pulsation (ω) is minimal, as both moduli remain nearly constant. Conversely, healthy samples exhibit a slight decrease in the values of G' and G'' as the frequency decreases. Despite these differences, both pathological and healthy liver samples demonstrate rheological properties similar to gels, characterized by a marked predominance of G' over G'', parallel trends of G' and G'', and minimal dependence on ω. Essentially, the main distinction between healthy and pathological liver samples lies in their shear modulus G, which is generally higher in pathological samples.

For what concerns the relaxation spectrum (Figure 48), those of healthy samples are characterized by lower $G_i$ values and longer relaxation times compared to pathological samples. However, the shape of the relaxation spectrum does not seem to modify between healthy and pathological samples.

Interestingly, we identified another commonality in the rheological characterization of liver samples and gels. Coviello et al. reported a correlation between the shear modulus G and the critical shear modulus $G_c$ in scleroglucan hydrogels (Coviello et al., 2022). Similarly, our pathological and healthy liver samples considered together exhibit a correlation between G and $G_c$ (Figure 49). This correlation suggests that the mechanical properties of the liver tissue are closely linked to those of hydrogels. Such parallelism in rheological behavior between biological tissues and synthetic hydrogels could provide valuable insights into the fundamental mechanisms governing tissue mechanics.

We also found two other correlations between rheological parameters, which are consequential to the G and $G_c$ correlation. Thus, in liver samples there are correlations between G and $\tau_c$ and between G and the work *w* (eq. (*1.38*)) (not shown).

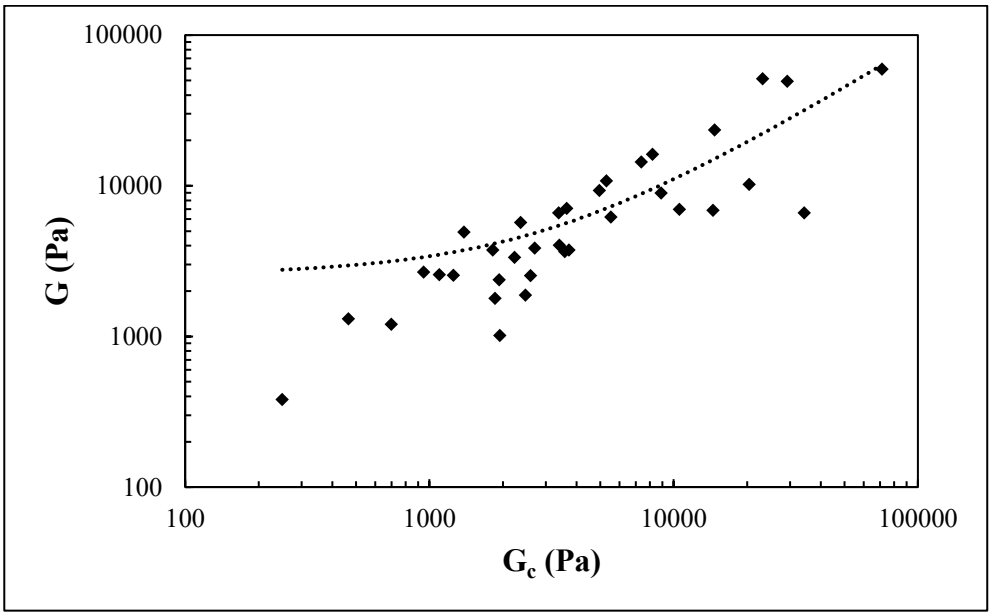


Figure 49: Correlation between G and $G_c$ in healthy and pathological liver samples considered together (Spearman correlation $r = 0.87$ and $p < 0.0001$).

In order to compare the rheological and the histological analyses, a comparison was made between the shear moduli $\Sigma G_i$ obtained from the fitting of FS data and the fibrosis stages provided by the histological analysis of the pathological sample (Table 11). This comparison showed that 10 cases correlated with the degree of fibrosis, while 7 cases with the presence of fibrosis but not on the severity. Therefore in 17 cases correlated with the presence or absence of fibrosis, while in 13 cases did not.

Another comparison was made between the mean G* from FS analysis and the Kleiner-Brunt stages from histological analysis (Table 12). This comparison showed that 13 cases correlated with the degree of fibrosis, while 4 cases correlated with the presence of fibrosis

but not with the severity. Therefore in 17 cases we observed concordance with the presence or absence of fibrosis, while in 13 cases we did not.

Table 11: Comparison between Kleiner-Brunt stages of fibrosis deduced from rheological analyses (shear moduli $\Sigma G_i$) and from histological analyses. Green color indicates the cases with correspondence between the two classifications, while red color represents the cases with no correspondence. Yellow color indicates the cases where the two methods agree on the presence of fibrosis, but not on the severity.

| Sample | $\Sigma G_i$ (Pa) | Kleiner-Brunt stages from rheological analyses | Kleiner-Brunt stages from histological analyses |
|---|---|---|---|
| **1** | 6081,1 | 0 | 0 |
| **2** | 7303,8 | 2 | 0 |
| **3** | 5772,3 | 0 | 1A |
| **4** | 10354,3 | 3 | 1C |
| **5** | 6194,0 | 1 | 1C |
| **6** | 10208,6 | 3 | 0 |
| **7** | 2670,7 | 0 | 0 |
| **8** | 6952,3 | 1 | 1A |
| **9** | 1876,2 | 0 | 1B |
| **10** | 9287,5 | 3 | 1B |
| **11** | 3344,4 | 0 | 1B |
| **12** | 23419,9 | 4 | 1A |
| **13** | 59313,7 | 4 | 2 |
| **14** | 2522,6 | 0 | 1 |
| **15** | 6876,9 | 1 | 0 |
| **16** | 8936,6 | 2 | 1 |
| **17** | 3654,9 | 0 | 1A |
| **18** | 6599,1 | 1 | 1A |
| **19** | 3749,0 | 0 | 0 |
| **20** | 4016,2 | 0 | 0 |
| **21** | 3734,3 | 0 | 0 |
| **22** | 3845,3 | 0 | 0 |
| **23** | 2546,6 | 0 | 0 |
| **24** | 2571,5 | 0 | 1C |
| **25** | 6584,6 | 1 | 0 |
| **26** | 49371,1 | 4 | 1 |
| **27** | 14333,4 | 4 | 0 |
| **28** | 16177,0 | 4 | 0 |
| **29** | 10745,5 | 4 | 0 |
| **30** | 51124,8 | 4 | 1 |

Table 12: Comparison between Kleiner-Brunt stages of fibrosis deduced from rheological analyses (mean G*) and from histological analyses. Green color indicates the cases with correspondence between the two classifications, while red color represents the cases with no correspondence. Yellow color indicates the cases where the two methods agree on the presence of fibrosis, but not on the severity.

| Sample | mean G* (Pa) | Kleiner-Brunt stages from rheological analyses | Kleiner-Brunt stages from histological analyses |
|---|---|---|---|
| **1** | 3719 | 0 | 0 |
| **2** | 4392 | 0 | 0 |
| **3** | 3491 | 0 | 1A |
| **4** | 6450 | 1 | 1C |
| **5** | 3838 | 0 | 1C |
| **6** | 6098 | 0 | 0 |
| **7** | 1046 | 0 | 0 |
| **8** | 4060 | 0 | 1A |
| **9** | 1420 | 0 | 1B |
| **10** | 4571 | 0 | 1B |
| **11** | 4571 | 0 | 1B |
| **12** | 14791 | 4 | 1A |
| **13** | 40532 | 4 | 2 |
| **14** | 1508 | 0 | 1 |
| **15** | 5264 | 0 | 0 |
| **16** | 5115 | 0 | 1 |
| **17** | 1757 | 0 | 1A |
| **18** | 4004 | 0 | 1A |
| **19** | 1947 | 0 | 0 |
| **20** | 2458 | 0 | 0 |
| **21** | 2342 | 0 | 0 |
| **22** | 2349 | 0 | 0 |
| **23** | 1602 | 0 | 0 |
| **24** | 1318 | 0 | 1C |
| **25** | 4062 | 0 | 0 |
| **26** | 30491 | 4 | 1 |
| **27** | 8159 | 2 | 0 |
| **28** | 10104 | 3 | 0 |
| **29** | 6286 | 0 | 0 |
| **30** | 31785 | 4 | 1 |

Moreover, in order to compare the outcomes of the rheological analyses (measure of the mechanical properties of liver tissue *ex vivo*) and those of the elastographic technique (measure of the stiffness of liver tissue *in vivo*), the median elastographic rigidity and the mean G* and $\Sigma G_i$ were compared (Table 13). No correlation was found between these two different methods to evaluate the stiffness (Figure 50 and Figure 51). This may be due to the different measurement methods, one being more direct (rheology) and the other more indirect (elastography). In fact, elastographic measurement, being performed *in vivo*, is affected by many factors (patient's position, fasting, blood pressure) that rheology does not encounter. Moreover, as already discussed, dealing with obese patients, elastographic measurement may also be affected by the thickness of the abdominal wall. Conversely, it is clear that *ex vivo* tissue can differ from *in vivo* tissues as, for example, *ex vivo* tissues is not perfused by physiological fluids. One issue we encountered is that the same stage of fibrosis, as determined by histological analysis, can correspond to significantly different shear modulus values when steatosis is present in the sample. For instance, pathological samples 17 and 12 both exhibited fibrosis stage 1A; however, only sample 17 also showed steatosis, specifically at stage 3. Sample 17 had a shear modulus of 3655 Pa, whereas sample 12 had a shear modulus of 23420 Pa. As already shown in the boxplots of Figure 44, the average shear modulus ± SEM of the pathological samples was (11672 ± 2723) Pa, compared to (2719 ± 728) Pa in healthy samples. This suggests that steatosis reduces the sample stiffness.

Table 13: Comparison between the median elastographic rigidity and the average moduli G* and ΣGi calculated by rheology.

| Sample | Median rigidity (Pa) from elastography | Mean G* (Pa) from rheology | $\Sigma G_i$ (Pa) from rheology |
|---|---|---|---|
| **1** | 4420 | 3719 | 6081 |
| **2** | 5300 | 4392 | 7304 |
| **3** | - | 3491 | 5772 |
| **4** | 3760 | 6450 | 10354 |
| **5** | 6370 | 3838 | 6194 |
| **6** | not executable | 6098 | 10209 |
| **7** | not executable | 1046 | 2671 |
| **8** | 4810 | 4060 | 6952 |
| **9** | 4190 | 1420 | 1876 |
| **10** | 4360 | 4571 | 9287 |
| **11** | - | 4571 | 3344 |
| **12** | 4970 | 14791 | 23420 |
| **13** | 7980 | 40532 | 59314 |
| **14** | not executable | 1508 | 2523 |
| **15** | 5050 | 5264 | 6877 |
| **16** | 4140 | 5115 | 8937 |
| **17** | 9770 | 1757 | 3655 |
| **18** | 4890 | 4004 | 6599 |
| **19** | 4320 | 1947 | 3749 |
| **20** | 5420 | 2458 | 4016 |
| **21** | 3830 | 2342 | 3734 |
| **22** | 6440 | 2349 | 3845 |
| **23** | 3810 | 1602 | 2547 |
| **24** | - | 1318 | 2571 |
| **25** | 8180 | 4062 | 6585 |
| **26** | 8450 | 30491 | 49371 |
| **27** | 6130 | 8159 | 14333 |
| **28** | 5440 | 10104 | 16177 |
| **29** | 6030 | 6286 | 10745 |
| **30** | - | 31785 | 51125 |

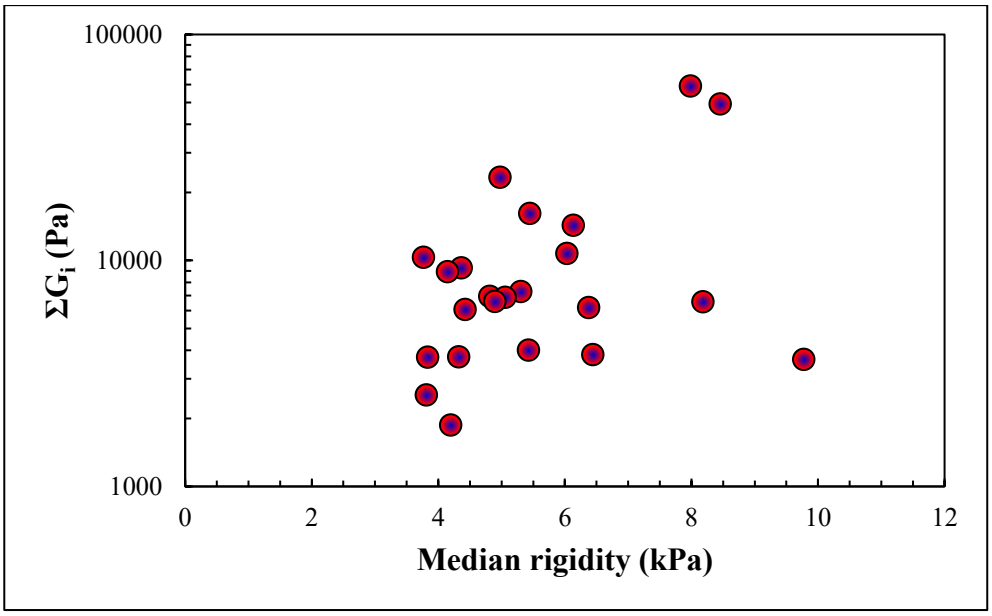


Figure 50: No significant correlation between $\Sigma G_i$ determined by rheology and the median rigidity measured by elastography.

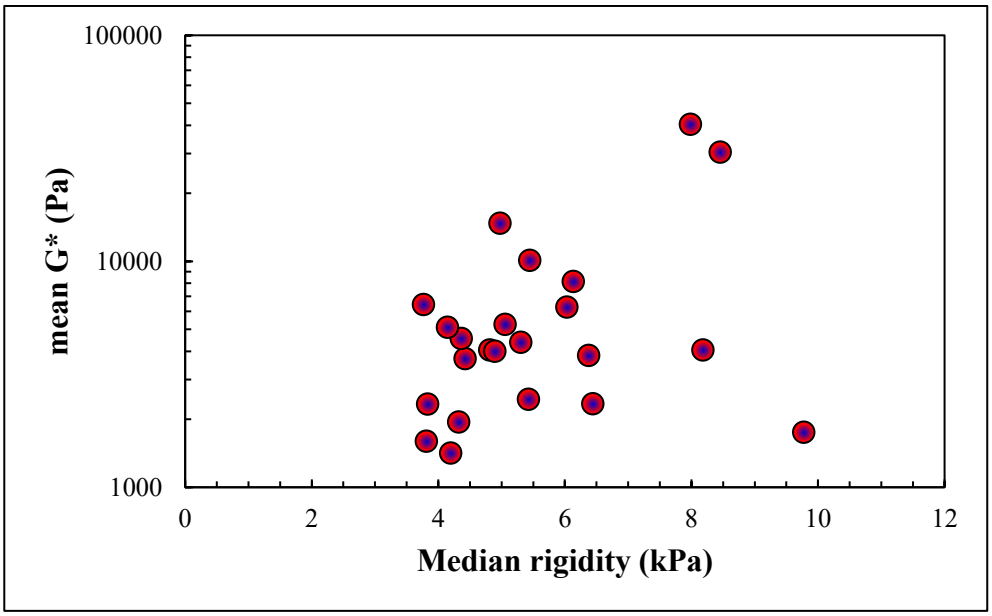


Figure 51: No significant correlation between G* determined by rheology and median rigidity measured with elastography.

## 4.4 LF-NMR characterization of liver samples

Typically, in gel systems, the relaxation time $T_{2m}$ is depressed by the solid surface of the polymeric chains. In liver samples, on the contrary, the main reason for $T_{2m}$ depression is due to the ferromagnetic properties of iron whose presence is considerable. Consequently, the measured $T_{2m}$ is directly proportional to the iron content in the liver samples. To study the relationship between iron concentration and $T_{2m}$, we prepared aqueous solutions with varying concentrations of iron(II) sulfate ($FeSO_4$) and measured, for each solution, $T_{2m}$ at 25°C. The results, depicted in Figure 52, show that as the iron concentration increases, $T_{2m}$ decreases, although in a not linear manner. Therefore, the higher the iron content, the shorter the relaxation time of the hydrogen atoms in the water.

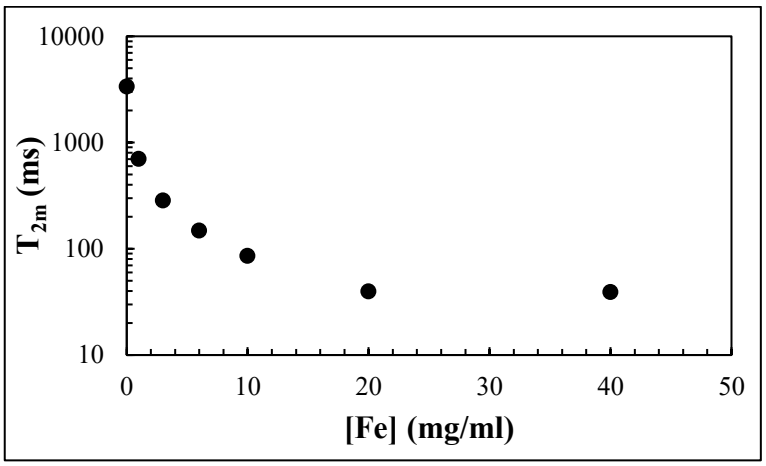


Figure 52: Dependence of the relaxation time $T_{2m}$ on the concentrations of iron(II) sulfate in aqueous solutions.

The relaxation time spectrum as well as $T_{2m}$ or $T_{1m}$ for the liver samples are reported in Table 14 and Table 15. It can be seen that $T_{2m}$ spans in the range 50-100 ms. Such low $T_{2m}$ values in liver samples are due to the presence of iron and its ferromagnetic nature, which allows the rapid relaxation of hydrogens of water molecules. Similarly, $T_{1m}$ values are very low. Analysis of the boxplot in Figure 53 reveals that healthy liver samples exhibit significantly higher $T_{1m}$ and $T_{2m}$ relaxation times compared to pathological samples. This observation suggests that pathological samples possess a higher iron content. This finding is in line with the existing literature, which establishes a correlation between excessive hepatic iron accumulation and liver diseases, such as non-alcoholic fatty liver disease (NAFLD) and non-alcoholic steatohepatitis (NASH) (Fargion et al., 2001; George et al., 1998; Kowdley et al., 2012; Pietrangelo, 2009; Sorrentino et al., 2009).

Table 14: Results of LF-NMR analysis on healthy (blue) and pathological (red) liver samples. $T_{2m}$ is the average mean spin-spin relaxation time, $A_i$% and $T_{2i}$ are the percentages and relaxation times respectively.

| Sample | $T_{2m}$ (ms) | $T_{21}$ (ms) | $T_{22}$ (ms) | $T_{23}$ (ms) | $T_{24}$ (ms) | $A_1$% (-) | $A_2$% (-) | $A_3$% (-) | $A_4$% (-) |
|---|---|---|---|---|---|---|---|---|---|
| 1 | 65,4 | 259,4 | 51,1 | 2,7 | 16,2 | 12,0 | 61,6 | 10,3 | 16,2 |
| 2 | 39,6 | 206,0 | 39,6 | 2,1 | 10,2 | 9,1 | 43,1 | 14,6 | 33,1 |
| 3 | 43,6 | 168,2 | 39,3 | 9,2 | - | 10,1 | 61,0 | 28,9 | - |
| 4 | 40,1 | 198,7 | 45,7 | 14,2 | 4,2 | 11,5 | 23,9 | 36,8 | 27,8 |
| 5 | 52,8 | 203,7 | 49,3 | 17,3 | 4,4 | 12,4 | 43,7 | 32,0 | 11,9 |
| 6 | 45,8 | 178,4 | 42,4 | 2,6 | 14,5 | 10,4 | 54,8 | 8,7 | 26,1 |
| 7 | 43,5 | 146,7 | 31,2 | 3,2 | - | 16,0 | 61,7 | 22,2 | - |
| 8 | 68,8 | 53,6 | 215,2 | 18,7 | 4,5 | 58,2 | 16,0 | 14,5 | 11,4 |
| 9 | 53,8 | 205,9 | 48,8 | 19,5 | 2,0 | 8,1 | 69,1 | 16,9 | 5,9 |
| 10 | 45,3 | 162,2 | 45,8 | 22,3 | 2,5 | 5,6 | 69,3 | 18,8 | 6,2 |
| 11 | 46,3 | 156,1 | 48,9 | 20,2 | 2,0 | 4,1 | 75,6 | 13,4 | 6,8 |
| 12 | 52,8 | 209,3 | 49,7 | 21,9 | 2,2 | 5,9 | 75,7 | 12,8 | 5,7 |
| 13 | 37,2 | 200,3 | 40,6 | 14,7 | 4,9 | 8,0 | 36,1 | 38,6 | 17,3 |
| 14 | 54,6 | 275,6 | 56,9 | 31,6 | 5,2 | 4,6 | 51,8 | 38,9 | 4,8 |
| 15 | 44,8 | 80,5 | 30,6 | - | - | 28,4 | 71,6 | - | - |
| 16 | 54,3 | 144,4 | 41,7 | - | - | 12,2 | 87,8 | - | - |
| 17 | 84,1 | 196,6 | 55,6 | 9,7 | - | 22,0 | 72,3 | 5,6 | - |
| 18 | 317,6 | 1221,4 | 59,5 | 37,0 | 11,3 | 22,7 | 57,9 | 14,7 | 4,7 |
| 19 | 43,5 | 94,8 | 41,2 | 11,1 | 1,6 | 13,9 | 70,6 | 10,0 | 5,5 |
| 20 | 61,2 | 185,5 | 48,0 | 14,5 | 1,5 | 13,2 | 74,0 | 7,6 | 5,3 |
| 21 | 67,3 | 120,7 | 48,3 | 26,2 | - | 28,0 | 66,4 | 5,6 | - |
| 22 | 67,2 | 207,8 | 62,9 | 17,4 | - | 6,0 | 84,5 | 9,5 | - |
| 23 | 49,0 | 189,8 | 46,2 | 9,3 | - | 5,7 | 79,6 | 14,7 | - |
| 24 | 56,2 | 165,9 | 46,2 | 9,3 | - | 11,9 | 76,8 | 11,3 | - |
| 25 | 53,9 | 168,1 | 49,6 | 2,4 | 21,3 | 8,8 | 74,3 | 6,8 | 10,1 |
| 26 | 60,0 | 261,2 | 64,7 | 26,9 | 5,8 | 8,2 | 41,3 | 41,8 | 8,7 |
| 27 | 44,3 | 44,3 | - | - | - | 100,0 | - | - | - |
| 28 | 53,5 | 246,0 | 3,6 | 62,9 | 18,9 | 10,9 | 30,9 | 33,5 | 24,8 |
| 29 | 41,5 | 41,5 | - | - | - | 100,0 | - | - | - |
| 30 | 75,2 | 5,7 | 25,4 | 270,4 | 79,1 | 21,9 | 32,1 | 15,4 | 30,6 |
| 1 | 154,3 | 934,0 | 58,8 | 21,0 | - | 11,3 | 80,0 | 8,7 | - |
| 2 | 45,6 | 127,3 | 43,9 | 11,3 | - | 6,9 | 80,7 | 12,4 | - |
| 3 | - | - | - | - | - | - | - | - | - |
| 4 | 79,5 | 233,3 | 65,7 | 19,8 | - | 10,3 | 82,4 | 7,4 | - |
| 5 | 156,9 | 653,6 | 62,1 | 22,8 | - | 16,7 | 72,9 | 10,4 | - |
| 6 | 67,5 | 99,9 | 55,5 | 2,1 | - | 35,4 | 57,6 | 7,0 | - |
| 7 | 59,8 | 138,1 | 48,5 | 4,4 | - | 15,9 | 77,5 | 6,6 | - |
| 8 | 58,4 | 58,4 | - | - | - | 100,0 | - | - | - |
| 9 | 69,7 | 221,9 | 69,4 | 27,4 | - | 5,2 | 76,4 | 18,4 | - |
| 10 | - | - | - | - | - | - | - | - | - |

Table 15: Results of LF-NMR analysis on healthy (blue) and pathological (red) liver samples. $T_{1m}$ is the average mean spin-lattice relaxation time, $A_i$% and $T_{1i}$ are the percentages and relaxation times respectively.

| Sample | $T_{1m}$ (ms) | $T_{11}$ (ms) | $T_{12}$ (ms) | $T_{13}$ (ms) | $T_{14}$ (ms) | $T_{15}$ (ms) | $A_1$% (-) | $A_2$% (-) | $A_3$% (-) | $A_4$% (-) | $A_5$% (-) |
|---|---|---|---|---|---|---|---|---|---|---|---|
| 1 | 226,0 | 302,3 | 115,7 | 10,9 | - | - | 60,4 | 37,3 | 2,3 | - | - |
| 2 | 166,7 | 279,4 | 121,9 | 3,0 | 56,4 | - | 36,8 | 44,7 | 2,0 | 16,4 | - |
| 3 | 157,2 | 247,3 | 6,4 | 100,3 | - | - | 46,9 | 12,8 | 40,3 | - | - |
| 4 | 166,5 | 272,7 | 112,2 | 50,6 | 2,3 | 46,6 | 39,7 | 46,7 | 8,7 | 2,0 | 3,0 |
| 5 | 166,6 | 271,4 | 104,7 | 32,1 | 12,1 | - | 40,8 | 51,6 | 5,3 | 2,3 | - |
| 6 | 202,2 | 281,7 | 101,2 | 1,8 | 101,4 | - | 56,9 | 33,3 | 1,7 | 8,1 | - |
| 7 | 108,5 | 108,5 | - | - | - | - | 100,0 | - | - | - | - |
| 8 | 203,2 | 259,2 | 97,5 | 4,2 | - | - | 68,1 | 27,2 | 4,7 | - | - |
| 9 | 255,4 | 423,8 | 226,8 | 61,5 | 7,1 | - | 21,8 | 69,9 | 7,1 | 1,2 | - |
| 10 | 274,3 | 306,4 | 118,0 | 10,8 | - | - | 84,0 | 14,1 | 1,9 | - | - |
| 11 | 277,4 | 297,0 | 77,7 | 10,0 | - | - | 91,6 | 6,6 | 1,8 | - | - |
| 12 | 259,3 | 277,1 | 50,0 | - | - | - | 92,2 | 7,8 | - | - | - |
| 13 | 154,9 | 167,2 | 20,1 | - | - | - | 91,6 | 8,4 | - | - | - |
| 14 | 225,0 | 244,1 | 5,9 | - | - | - | 92,0 | 8,0 | - | - | - |
| 15 | 220,5 | 228,2 | 8,0 | - | - | - | 96,5 | 3,5 | - | - | - |
| 16 | 274,5 | 296,5 | 60,7 | - | - | - | 90,7 | 9,3 | - | - | - |
| 17 | 305,2 | 379,1 | 117,5 | 8,5 | - | - | 73,1 | 23,7 | 3,2 | - | - |
| 18 | 290,0 | 290,0 | - | - | - | - | 100,0 | - | - | - | - |
| 19 | 272,6 | 303,5 | 111,7 | 21,7 | - | - | 84,9 | 13,0 | 2,1 | - | - |
| 20 | 265,7 | 304,9 | 119,3 | 19,4 | - | - | 80,5 | 16,5 | 3,0 | - | - |
| 21 | 289,7 | 335,2 | 92,9 | 6,9 | - | - | 82,8 | 12,5 | 4,6 | - | - |
| 22 | 337,8 | 358,5 | 26,8 | - | - | - | 93,8 | 6,2 | - | - | - |
| 23 | 261,1 | 317,3 | 140,0 | 18,5 | - | - | 70,5 | 26,3 | 3,2 | - | - |
| 24 | 268,5 | 333,7 | 130,3 | 3,9 | 3,9 | - | 70,4 | 25,5 | 1,9 | 2,1 | - |
| 25 | 267,9 | 285,8 | 46,7 | - | - | - | 92,5 | 7,5 | - | - | - |
| 26 | 234,9 | 331,1 | 183,6 | 79,6 | 40,8 | - | 44,6 | 43,4 | 6,6 | 5,4 | - |
| 27 | 244,8 | 467,2 | 234,8 | 35,7 | - | - | 10,8 | 81,6 | 7,6 | - | - |
| 28 | 147,0 | 277,4 | 114,7 | 89,5 | 50,3 | 29,4 | 30,5 | 28,6 | 26,7 | 6,9 | 7,2 |
| 29 | 228,6 | 301,6 | 161,9 | 30,9 | 28,5 | - | 53,7 | 40,0 | 3,4 | 2,9 | - |
| 30 | 171,1 | 311,8 | 131,5 | 64,7 | 24,4 | - | 30,9 | 50,1 | 10,5 | 8,5 | - |
| 1 | - | - | - | - | - | - | - | - | - | - | - |
| 2 | 238,8 | 282,5 | 128,1 | 4,5 | - | - | 74,7 | 21,5 | 3,8 | - | - |
| 3 | - | - | - | - | - | - | - | - | - | - | - |
| 4 | 295,0 | 311,4 | 0,8 | - | - | - | 94,7 | 5,3 | - | - | - |
| 5 | 338,9 | 354,9 | 3,1 | - | - | - | 95,4 | 4,6 | - | - | - |
| 6 | 438,5 | 472,2 | 13,9 | - | - | - | 92,6 | 7,4 | - | - | - |
| 7 | 235,7 | 268,5 | 112,5 | 6,6 | - | - | 81,4 | 15,1 | 3,5 | - | - |
| 8 | - | - | - | - | - | - | - | - | - | - | - |
| 9 | 359,5 | 415,8 | 90,6 | - | - | - | 82,7 | 17,3 | - | - | - |
| 10 | 222,1 | 381,3 | 176,5 | 44,5 | 9,1 | 8,3 | 29,9 | 59,7 | 5,0 | 2,4 | 2,9 |

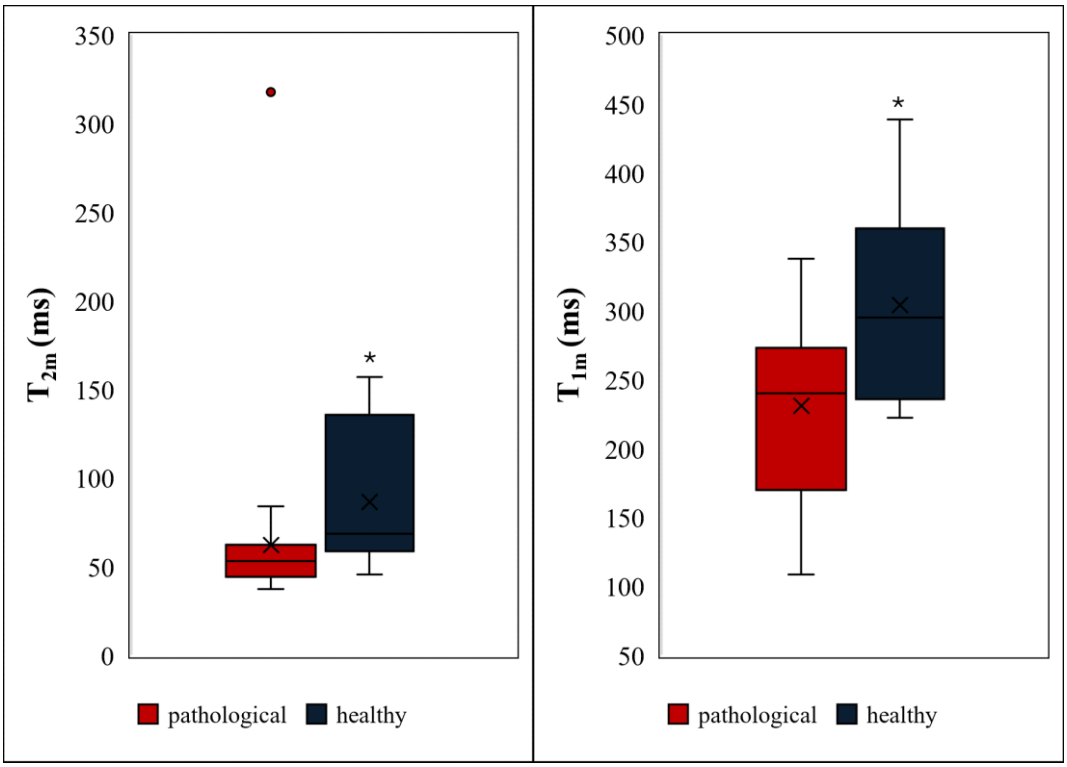


Figure 53: Boxplots with $T_{2m}$ and $T_{1m}$ for pathological (red) and healthy samples (blue). X represents the average value. Statistical significance was determined by comparing pathological and healthy samples: *p < 0.01. Statistical analyses were performed using Mann-Whitney test for $T_{2m}$, because the distribution of data was not gaussian, and Unpaired t test for $T_{1m}$, because the distribution of data was gaussian.

There is a correlation between $T_{2m}$ and $T_{1m}$ measured in both healthy and pathological liver samples (Figure 54). This correlation underscores the descriptive properties of these two parameters.

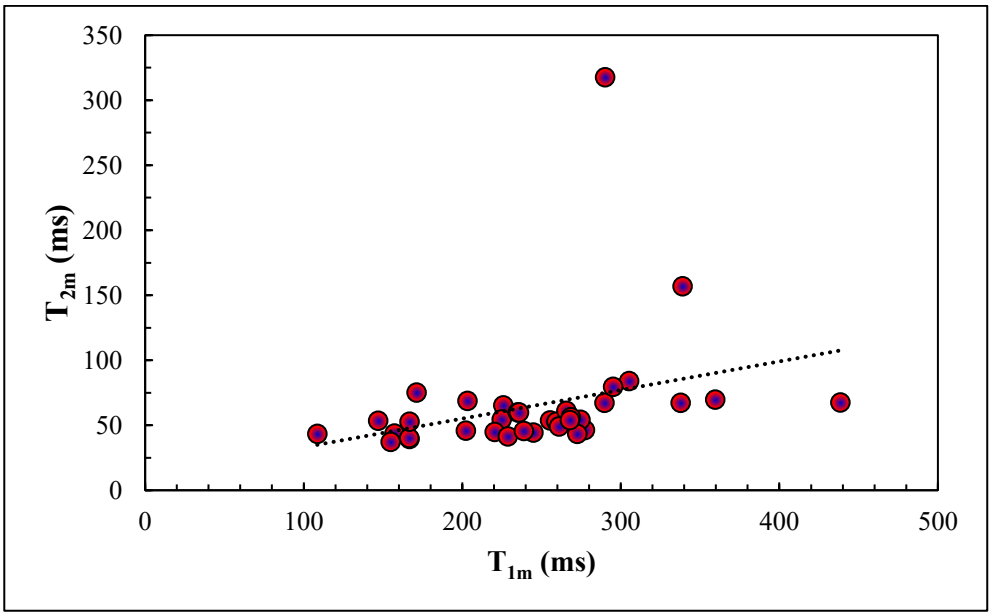


Figure 54: Correlation between $T_{1m}$ and $T_{2m}$ measured in healthy and pathological liver samples considered together (Spearman correlation with r = 0.60 and p < 0.0001).

In liver samples, LF-NMR analysis primarily reflects the iron content rather than providing structural information. However, we identified correlations between $T_{2m}$ and $T_{1m}$ and the results of rheological analysis, which do offer structural insights into the samples. In particular, there are correlations between $T_{2m}$ and mean G* (Figure 55) and similarly between $T_{2m}$ e $\Sigma G_i$ (Figure 56). Moreover, also $T_{1m}$ correlates with mean G* and with $\Sigma G_i$ (Figure 57 and Figure 58). In addition, $T_{1m}$ also correlates with the parameters $G_c$ and $\tau_c$ (Figure 59 and Figure 60).

The correlations between $T_{2m}$ and the mean G* and shear moduli G are inversely proportional. As $T_{2m}$ decreases, the values of both mean G* and G moduli increase. We have already seen that when $T_{2m}$ decreases, the amount of iron in the sample increases. For this reason, this inverse relationship indicates that as $T_{2m}$ decreases, iron content in the sample increases and the stiffness grows. Similarly, $T_{1m}$ exhibit an inverse correlation with mean G* and G. In our samples, increased iron deposition in the liver corresponds to increased liver stiffness, indicating liver health deterioration, as reported in the literature. Indeed, iron excess in the liver can induce fibrosis-promoting signals in the parenchymal and non-parenchymal cells, thus accelerating disease progression (Mehta et al., 2019; Yao et al., 2019). Therefore, the rheological and LF-NMR analysis provide complementary and corroborative data on liver structure and functionality.

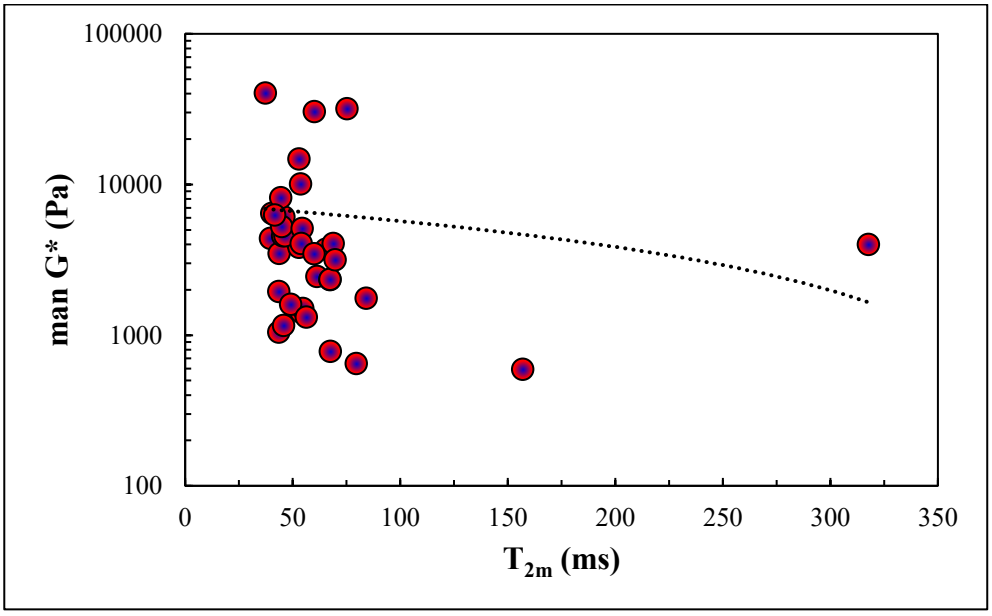


Figure 55: Correlation between $T_{2m}$ and mean G* measured in healthy and pathological liver samples considered together (Spearman correlation with $r = -0.39$ and $p < 0.05$).

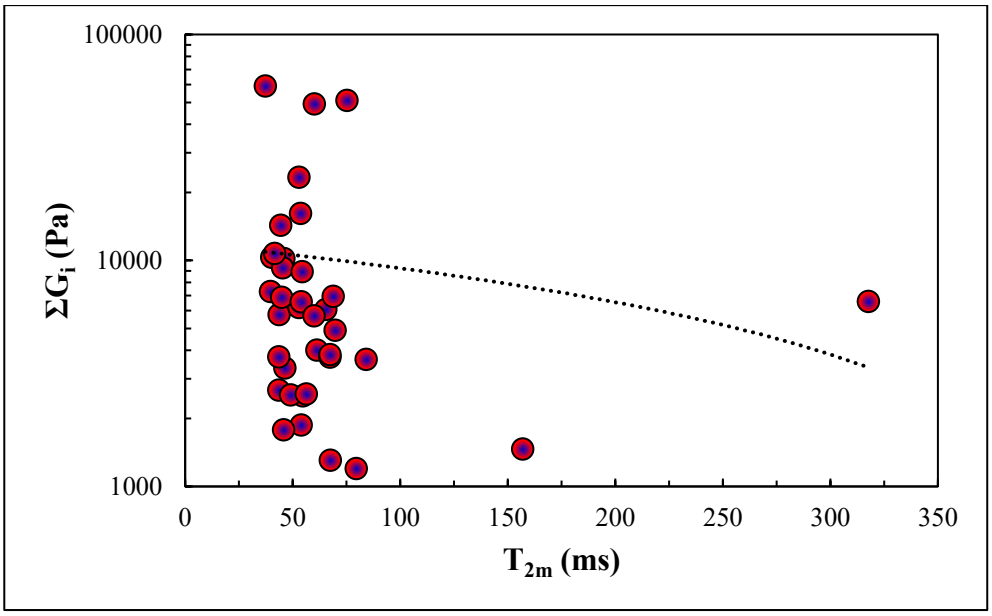


Figure 56: Correlation between $T_{2m}$ and $\Sigma G_i$ measured in healthy and pathological liver samples considered together (Spearman correlation with r = -0.38 and $p < 0.05$).

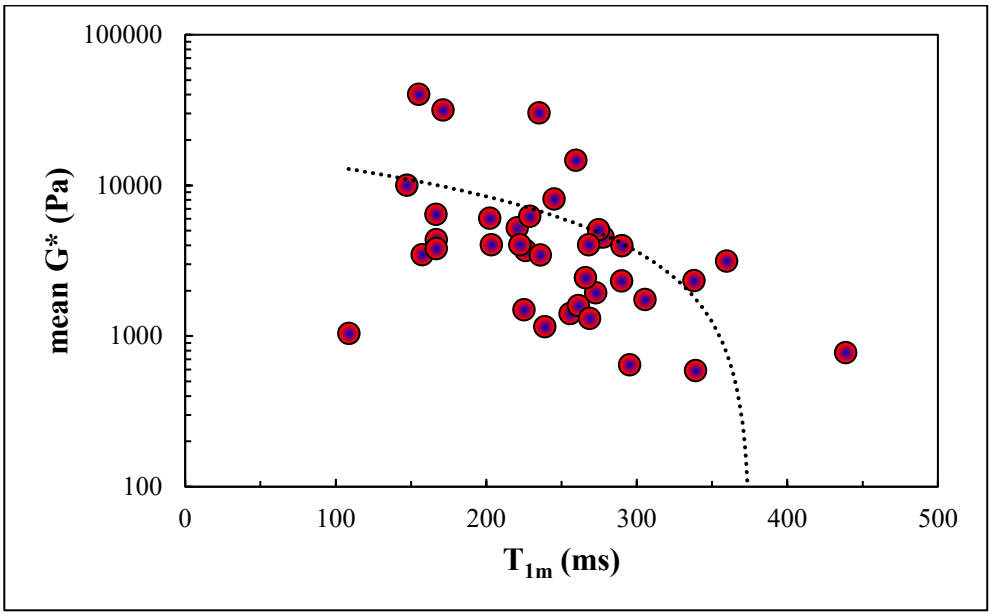


Figure 57: Correlation between $T_{1m}$ and mean G* measured in healthy and pathological liver samples considered together (Spearman correlation with r = -0.46 and $p < 0.005$).

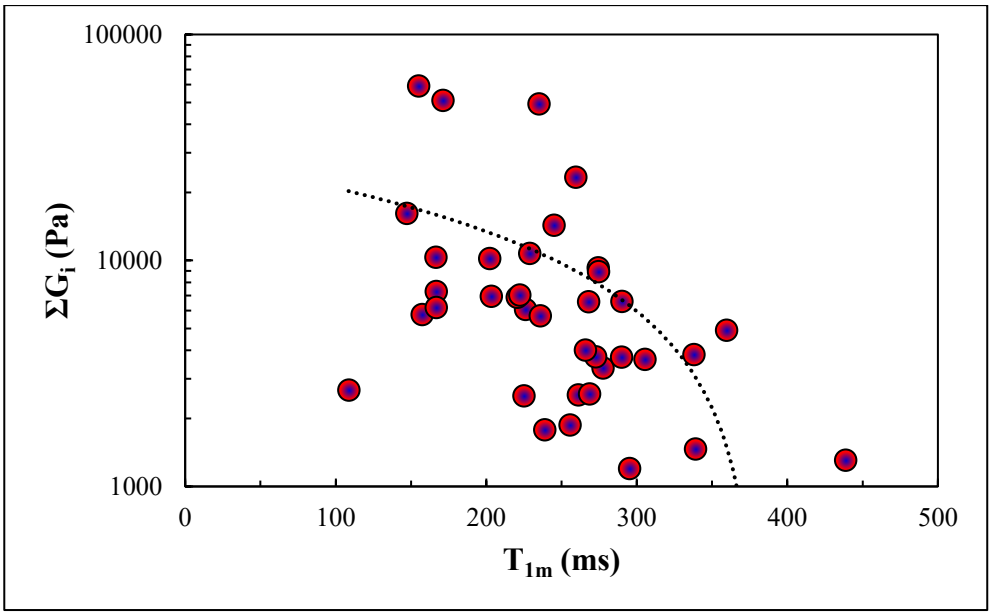


Figure 58: Correlation between $T_{1m}$ and $\Sigma G_i$ measured in healthy and pathological liver samples considered together (Spearman correlation with r = -0.57 and p < 0.005).

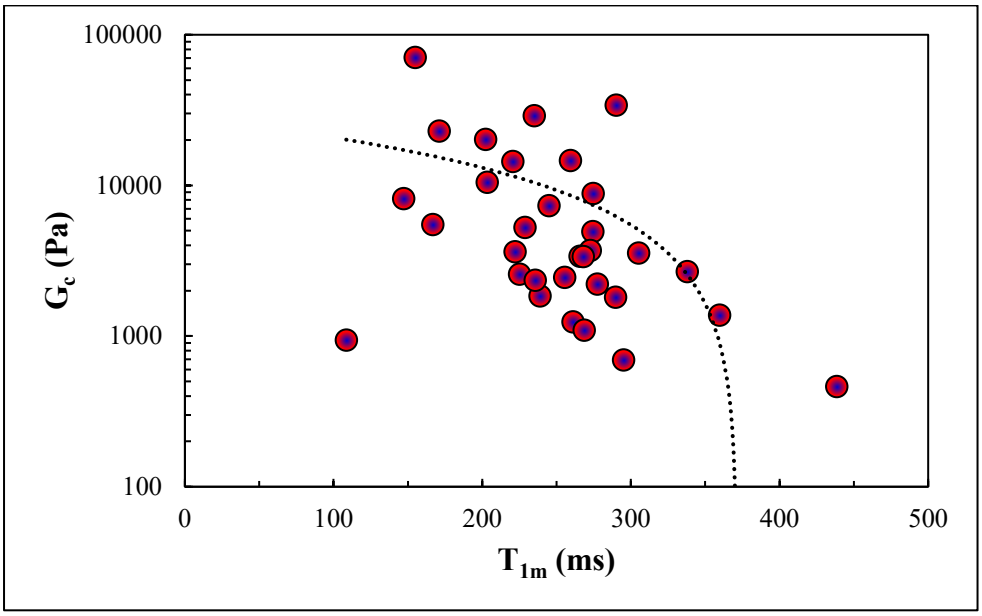


Figure 59: Correlation between $T_{1m}$ and $G_c$ measured in healthy and pathological liver samples considered together (Spearman correlation with r = -0.44 and p < 0.05).

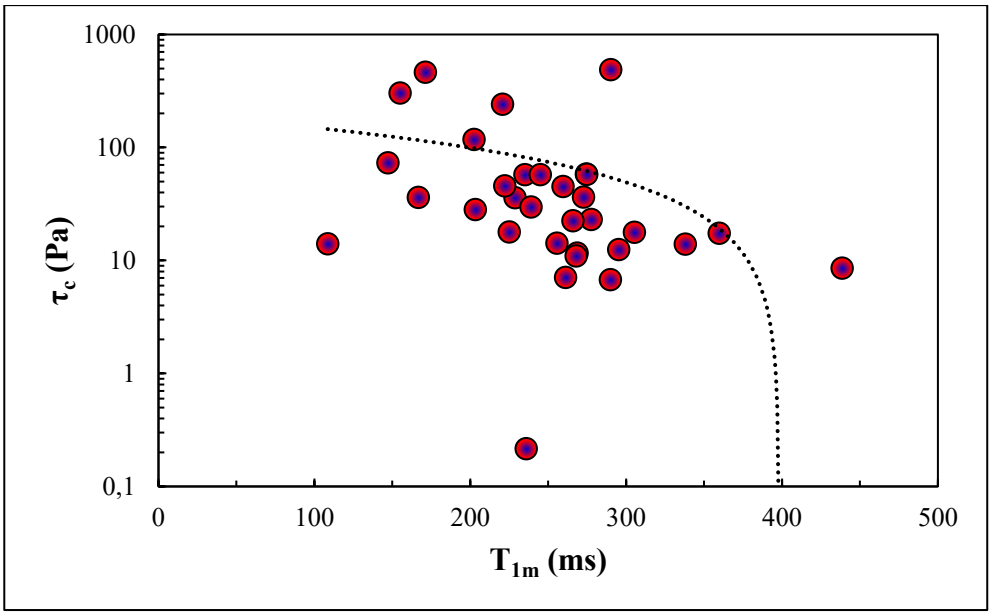


Figure 60: Correlation between $T_{1m}$ and $\tau_c$ measured in healthy and pathological liver samples considered together (Spearman correlation with $r = -0.42$ and $p < 0.05$).

Several factors regulate iron homeostasis, including transferrin, the primary transport protein for ferric iron ($Fe^{3+}$) in the bloodstream. For a subset of our obese patients, the blood concentration of transferrin were known (Table 16). We thus investigated its correlation with LF-NMR and rheological parameters. While transferrin concentrations did not correlate with $T_{2m}$ and $T_{1m}$ relaxation times (not shown), they unexpectedly showed a correlation with mean G* and $\Sigma G_i$ moduli (Figure 61 and Figure 62). Specifically, there is a negative correlation between these parameters: the higher the rheological moduli representing liver stiffness (mean G* and $\Sigma G_i$), the lower the transferrin concentration.

The connection between the liver and the iron is very strong. In fact, the liver is the major site of iron storage in the human body. Iron is stored in the liver in the cores of ferritin shells and as hemosiderin, an insoluble product derived from iron-rich ferritin. Iron can be taken up by the liver by several pathways. The major uptake of iron by hepatocytes is from transferrin. However, an iron overload is toxic and potentially fatal. The liver is particularly susceptible to injury from iron overload, especially when the iron accumulates in hepatocytes. For this reason, iron in the hepatocytes stimulates the translation of ferritin mRNA (to store iron in this protein shell) and represses transcription of DNA for transferrin and transferrin receptors (to limit the arrive in the liver of other iron from the organism) (Bonkovsky, 1991). Thus, in case of iron overload in the liver, the levels of transferrin protein decrease. Meier et al. (Meier et al., 2020) noticed that transferrin is a prognostic factor for survival and mortality in patients with end-stage liver disease. In particular, low serum transferrin levels were associated significantly with increased 90-day mortality.

In this light, it is very interesting that we found a correlation between an increase in liver stiffness in the samples and a decrease in transferrin present in the bloodstream of our patients, both indicating a worsening in liver disease.

Table 16: Hematic concentration of transferrin of some obese patient in comparison with mean G* and $\Sigma G_i$ moduli.

| Patient | mean G* (Pa) | $\Sigma G_i$ (Pa) | Transferrin (mg/dl) |
|---|---|---|---|
| **1** | 3719 | 6081,102 | 338 |
| **2** | 4392 | 7303,79 | 255 |
| **4** | 6450 | 10354,33 | 244 |
| **5** | 3838 | 6193,953 | 331 |
| **10** | 4571 | 9287,473 | 335 |
| **13** | 40532 | 59313,73 | 229 |
| **15** | 5264 | 6876,889 | 351 |
| **16** | 5115 | 8936,604 | 245 |
| **17** | 1757 | 3654,866 | 244 |
| **18** | 4004 | 6599,108 | 257 |
| **19** | 1947 | 3749,029 | 242 |
| **21** | 2342 | 3734,341 | 338 |
| **22** | 2349 | 3845,316 | 322 |
| **23** | 1602 | 2546,569 | 310 |
| **24** | 1318 | 2571,474 | 303 |
| **25** | 4062 | 6584,573 | 244 |
| **26** | 30491 | 49371,06 | 263 |
| **27** | 8159 | 14333,39 | 269 |
| **28** | 10104 | 16177 | 226 |
| **29** | 6286 | 10745,46 | 236 |
| **30** | 31785 | 51124,76 | 233 |

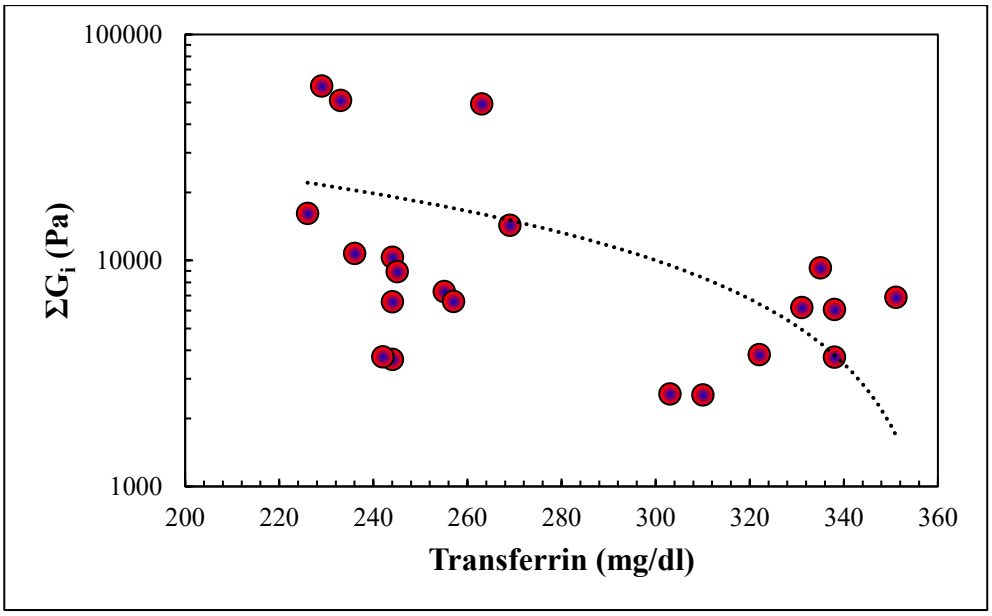


Figure 61: Correlation between transferrin and $\Sigma G_i$ measured in pathological liver samples (Spearman correlation with r = -0.48 and $p < 0.05$).

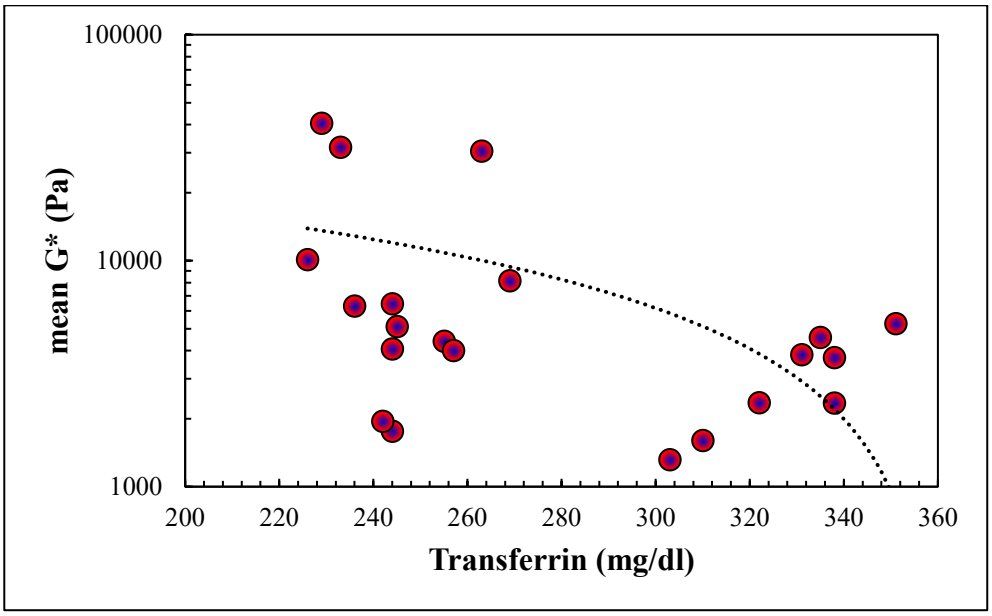


Figure 62: Correlation between transferrin and mean G* measured in pathological liver samples (Spearman correlation with r = -0.45 and $p < 0.05$).

## 4.5 Illness indexes and correlations with rheological and LF-NMR characterization of liver samples

In order to numerically quantify the clinical conditions of patients, we propose the definition of different *disease indices*. Basically, all the considered indices represent, in a Euclidean space at *n* dimensions, the distance of each patient from the normal condition. Thus, whatever the considered indices, while a healthy subject will be associated to a zero index value, patients will be characterized by values greater than zero. Obviously, the bigger the index value, the worse the clinical conditions. In order to have dimensionless indices, each one of the *n* index components is normalized by a reference value, i.e. that pertaining to healthy subjects. Moreover, in so doing, we get the considerable advantage of giving the same numerical importance to each one of the *n* index components. Indeed, the value of each component is normalized with respect to the healthy conditions so that it results a fraction (or a multiple) of the reference value. Accordingly, we defined the BMI index ($I_{BMI}$) (which relies on the Body Mass Index (BMI)), the fibrosis and steatosis index ($I_{FS}$) (which considers the Kleiner-Brunt stages of fibrosis and steatosis defined by histological analyses), the haematochemical index ($I_H$) (which considers the plasma values of glycemia (Glyc), direct bilirubin (BIL DIR), total bilirubin (BIL TOT), triglycerides (TG) and transaminases, i.e. aspartate amino transferase (AST), alanine amino transferase (ALT) and gamma glutamyl transpeptidase (GGT)). Finally, we defined an index that considered all of them, and that we defined the illness index ($I_{ILLNESS}$) (which considers BMI, the histological stages of fibrosis and steatosis and the haematochemical values already mentioned).

In the following, the mathematical definitions of all the indices are reported:

$$I_{BMI} = \sqrt{(BMI_{patient} - 25)/25)^2} \tag{4.2}$$

where 25 was chosen as maximum value of the normal range of BMI, since normal range of BMI goes from 18.5 to 24.9 (Caballero, 2019);

$$I_{FS} = \sqrt{{F_{patient}}^2 + {S_{patient}}^2} \tag{4.3}$$

where $F_{patient}$ and $S_{patient}$ are respectively the stages for fibrosis and steatosis of Kleiner-Brunt of the patients defined by histological analyses. In this case, as the reference value for healthy subjects is zero, this corresponding to the absence of fibrosis and steatosis, the division for "0" is not considered.

$$I_{H\ women} = \sqrt{\begin{array}{l}\left(if\ AST_{patient} > 35;\ then\ \left(\frac{AST_{patient} - 35}{35}\right)^2 ; 0\right) + \\ \left(if\ ALT_{patient} > 35;\ then\ \left(\frac{ALT_{patient} - 35}{35}\right)^2 ; 0\right) + \\ \left(if\ GGT_{patient} > 30;\ then\ \left(\frac{GGT_{patient} - 30}{30}\right)^2 ; 0\right) + \\ \left(if\ Glyc_{patient} > 101;\ then\ \left(\frac{Glyc_{patient} - 101}{101}\right)^2 ; 0\right) + \\ \left(if\ TG_{patient} > 150;\ then\ \left(\frac{TG_{patient} - 150}{150}\right)^2 ; 0\right) + \\ \left(if\ BIL\ TOT_{patient} > 1;\ then\ \left(\frac{BIL\ TOT_{patient} - 1}{1}\right)^2 ; 0\right) + \\ \left(if\ BIL\ DIR_{patient} > 0{,}3;\ then\ \left(\frac{BIL\ DIR_{patient} - 0{,}3}{0{,}3}\right)^2 ; 0\right)\end{array}}$$

(4.4)

where 35, 35, 30, 101, 150, 1, 0.3 (expressed in U/L, U/L, U/L, mg/dl, mg/dl, mmol/L, mmol/L) are respectively the normal range in women for AST, ALT, GGT, Glyc, TG, BIL TOT, BIL DIR (Ciaccio and Lippi, 2020);

$$I_{H\ men} = \sqrt{\begin{array}{l}\left(if\ AST_{patient} > 40;\ then\ \left(\frac{AST_{patient} - 40}{40}\right)^2 ; 0\right) + \\ \left(if\ ALT_{patient} > 40;\ then\ \left(\frac{ALT_{patient} - 40}{40}\right)^2 ; 0\right) + \\ \left(if\ GGT_{patient} > 50;\ then\ \left(\frac{GGT_{patient} - 50}{50}\right)^2 ; 0\right) + \\ \left(if\ Glyc_{patient} > 101;\ then\ \left(\frac{Glyc_{patient} - 101}{101}\right)^2 ; 0\right) + \\ \left(if\ TG_{patient} > 150;\ then\ \left(\frac{TG_{patient} - 150}{150}\right)^2 ; 0\right) + \\ \left(if\ BIL\ TOT_{patient} > 1;\ then\ \left(\frac{BIL\ TOT_{patient} - 1}{1}\right)^2 ; 0\right) + \\ \left(if\ BIL\ DIR_{patient} > 0{,}3;\ then\ \left(\frac{BIL\ DIR_{patient} - 0{,}3}{0{,}3}\right)^2 ; 0\right)\end{array}}$$

(4.5)

where 40, 40, 50, 101, 150, 1, 0.3 (expressed in U/L, U/L, U/L, mg/dl, mg/dl, mmol/L, mmol/L) are respectively the normal range in men for AST, ALT, GGT, Glyc, TG, BIL TOT, BIL DIR (Ciaccio and Lippi, 2020);

$$I_{ILLNESS\ women} = \sqrt{\begin{array}{c} (BMI_{patient} - 25)/25)^2 + \\ {F_{patient}}^2 + {S_{patient}}^2 + \\ \left(if\ AST_{patient} > 35;\ then\ \left(\frac{AST_{patient} - 35}{35}\right)^2 ; 0\right) + \\ \left(if\ ALT_{patient} > 35;\ then\ \left(\frac{ALT_{patient} - 35}{35}\right)^2 ; 0\right) + \\ \left(if\ GGT_{patient} > 30;\ then\ \left(\frac{GGT_{patient} - 30}{30}\right)^2 ; 0\right) + \\ \left(if\ Glyc_{patient} > 101;\ then\ \left(\frac{Glyc_{patient} - 101}{101}\right)^2 ; 0\right) + \\ \left(if\ TG_{patient} > 150;\ then\ \left(\frac{TG_{patient} - 150}{150}\right)^2 ; 0\right) + \\ \left(if\ BIL\ TOT_{patient} > 1;\ then\ \left(\frac{BIL\ TOT_{patient} - 1}{1}\right)^2 ; 0\right) + \\ \left(if\ BIL\ DIR_{patient} > 0{,}3;\ then\ \left(\frac{BIL\ DIR_{patient} - 0{,}3}{0{,}3}\right)^2 ; 0\right) \end{array}} \quad (4.6)$$

where 25 was chosen as maximum value of the normal range of BMI and 35, 35, 30, 101, 150, 1, 0.3 (expressed in U/L, U/L, U/L, mg/dl, mg/dl, mmol/L, mmol/L) are respectively the normal range in women for AST, ALT, GGT, Glyc, TG, BIL TOT, BIL DIR, (Ciaccio and Lippi, 2020);

$$I_{ILLNESS\,men} = \sqrt{\begin{array}{c}(BMI_{patient} - 25)/25)^2 + \\ {F_{patient}}^2 + {S_{patient}}^2 + \\ \left(if\ AST_{patient} > 40;\ then\ \left(\frac{AST_{patient} - 40}{40}\right)^2 ; 0\right) + \\ \left(if\ ALT_{patient} > 40;\ then\ \left(\frac{ALT_{patient} - 40}{40}\right)^2 ; 0\right) + \\ \left(if\ GGT_{patient} > 50;\ then\ \left(\frac{GGT_{patient} - 50}{50}\right)^2 ; 0\right) + \\ \left(if\ Glyc_{patient} > 101;\ then\ \left(\frac{Glyc_{patient} - 101}{101}\right)^2 ; 0\right) + \\ \left(if\ TG_{patient} > 150;\ then\ \left(\frac{TG_{patient} - 150}{150}\right)^2 ; 0\right) + \\ \left(if\ BIL\ TOT_{patient} > 1;\ then\ \left(\frac{BIL\ TOT_{patient} - 1}{1}\right)^2 ; 0\right) + \\ \left(if\ BIL\ DIR_{patient} > 0{,}3;\ then\ \left(\frac{BIL\ DIR_{patient} - 0{,}3}{0{,}3}\right)^2 ; 0\right)\end{array}} \quad (4.7)$$

where 25 was chosen as maximum value of the normal range of BMI and 40, 40, 50, 101, 150, 1, 0.3 (expressed in U/L, U/L, U/L, mg/dl, mg/dl, mmol/L, mmol/L) are respectively the normal range in men for AST, ALT, GGT, Glyc, TG, BIL TOT, BIL DIR (Ciaccio and Lippi, 2020).

Table 17 reports the four indices for the 30 obese patients.

Table 17: Values of the four indices referring to obese patients. $I_{BMI}$ defined by eq. (4.2), $I_{FS}$ defined by eq. (4.3), $I_H$ defined by eq. (4.4) for women and eq. (4.5) for men, $I_{ILLENSS}$ defined by eq. (4.6) for women and eq. (4.7) for men.

| Patient | $I_{BMI}$ | $I_{FS}$ | $I_H$ | $I_{ILLENSS}$ |
|---|---|---|---|---|
| **1** | 0,92 | 1,00 | 0,48 | 1,44 |
| **2** | 0,47 | 1,00 | 0,06 | 1,11 |
| **3** | 0,56 | 1,00 | 1,03 | 1,54 |
| **4** | 0,33 | 1,41 | 1,79 | 2,31 |
| **5** | 0,56 | 1,41 | 0,00 | 1,52 |
| **6** | 0,80 | 1,00 | 0,59 | 1,41 |
| **7** | 0,62 | 1,00 | 0,24 | 1,20 |
| **8** | 0,69 | 3,16 | 0,40 | 3,26 |
| **9** | 0,88 | 1,40 | 0,15 | 1,83 |
| **10** | 0,35 | 1,40 | 0,78 | 1,81 |
| **11** | 0,40 | 1,00 | 0,00 | 1,31 |
| **12** | 0,89 | 1,00 | 0,40 | 1,40 |
| **13** | 0,44 | 2,24 | 0,26 | 2,29 |
| **14** | 0,89 | 1,41 | 0,09 | 1,67 |
| **15** | 0,58 | 0,00 | 0,00 | 0,58 |
| **16** | 0,71 | 1,41 | 0,00 | 1,58 |
| **17** | 0,70 | 3,16 | 2,25 | 3,94 |
| **18** | 0,60 | 1,00 | 0,00 | 1,17 |
| **19** | 0,32 | 0,00 | 1,37 | 1,41 |
| **20** | 0,65 | 1,00 | 0,00 | 1,19 |
| **21** | 0,52 | 2,00 | 0,00 | 2,07 |
| **22** | 0,84 | 1,00 | 0,03 | 1,30 |
| **23** | 0,78 | 1,00 | 0,00 | 1,27 |
| **24** | 0,58 | 1,41 | 0,11 | 1,53 |
| **25** | 0,80 | 1,00 | 0,64 | 1,43 |
| **26** | 0,51 | 2,24 | 0,00 | 2,29 |
| **27** | 0,82 | 0,00 | 0,04 | 0,82 |
| **28** | 0,58 | 1,00 | 4,28 | 4,43 |
| **29** | 0,55 | 0,00 | 0,26 | 0,61 |
| **30** | 0,60 | 1,41 | 0,85 | 1,76 |

Figure 63 displays the distributions of the 4 indices ($I_{BMI}$, $I_{FS}$, $I_H$ and $I_{ILLNESS}$). $I_{BMI}$ is the only index with Gaussian distribution, all the other indices do not have a Gaussian distribution.

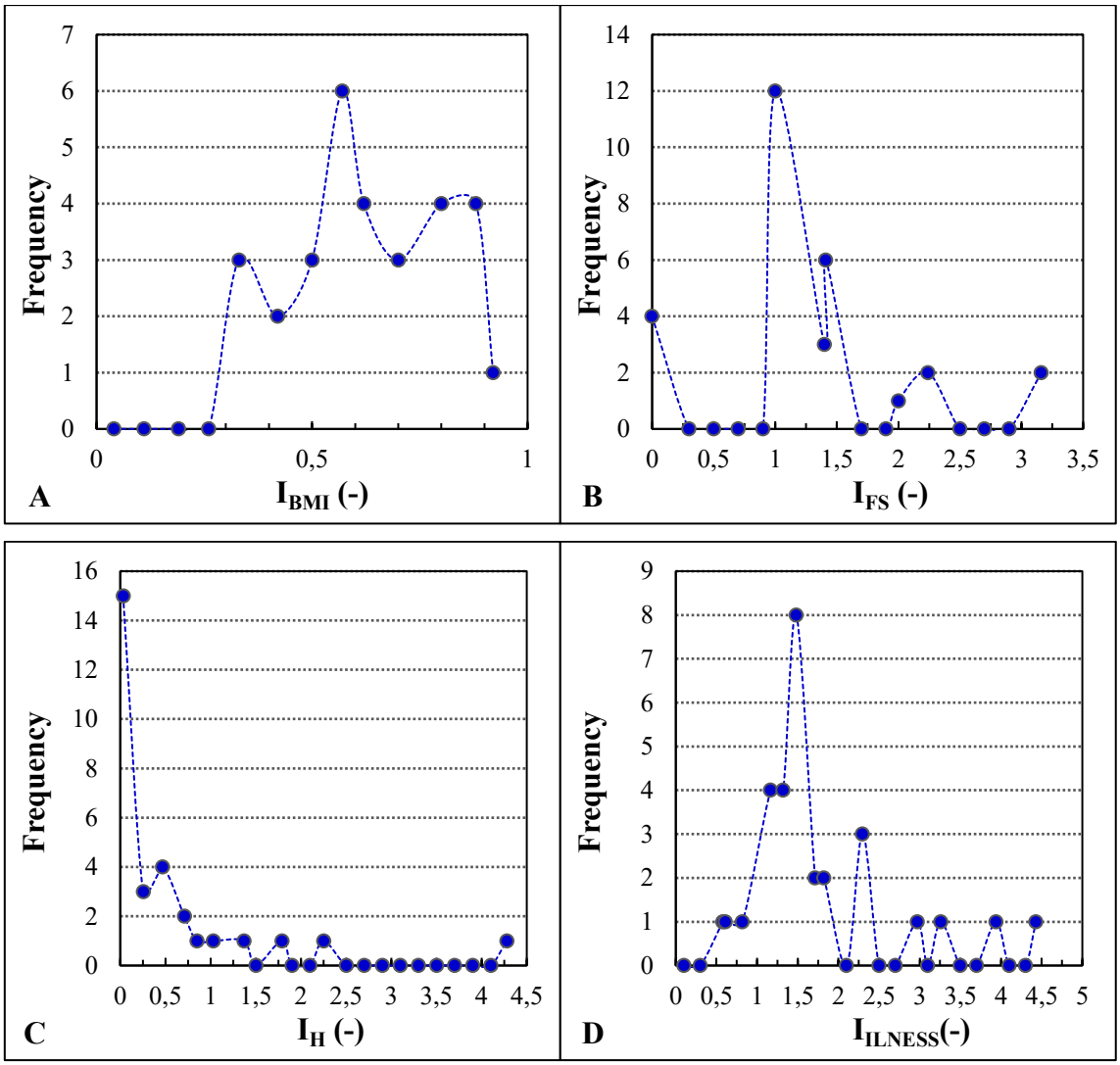


Figure 63: Indices distributions. $I_{BMI}$ is the only index with Gaussian distribution, all the other indices do not have a Gaussian distribution. A) The average value ± st.dev. for $I_{BMI}$ is (0.63 ± 0.18), the upper and the lower confidence limits (95%) are 0.70 and 0.57, respectively. B) The average value ± st.dev. for $I_{FS}$ is (1.25 ± 0.77), the upper and the lower confidence limits (95%) are 1.54 and 0.96, respectively. C) The average value ± st.dev. for $I_H$ is (0.54 ± 0.91), the upper and the lower confidence limits (95%) are 0.87 and 0.20, respectively. D) The average value ± st.dev. for $I_{ILLNESS}$ is (1.75 ± 0.89), the upper and the lower confidence limits (95%) are 2.08 and 1.41, respectively.

Firstly, two correlations between the indices will be reported: $I_{ILLNESS}$-$I_H$ and $I_{ILLNESS}$-$I_{FS}$ (Figure 64 and Figure 65). These correlations between the indices demonstrate their ability to describe obese patients in a concordant manner. $I_{BMI}$ does not correlate with other indices (data not shown).

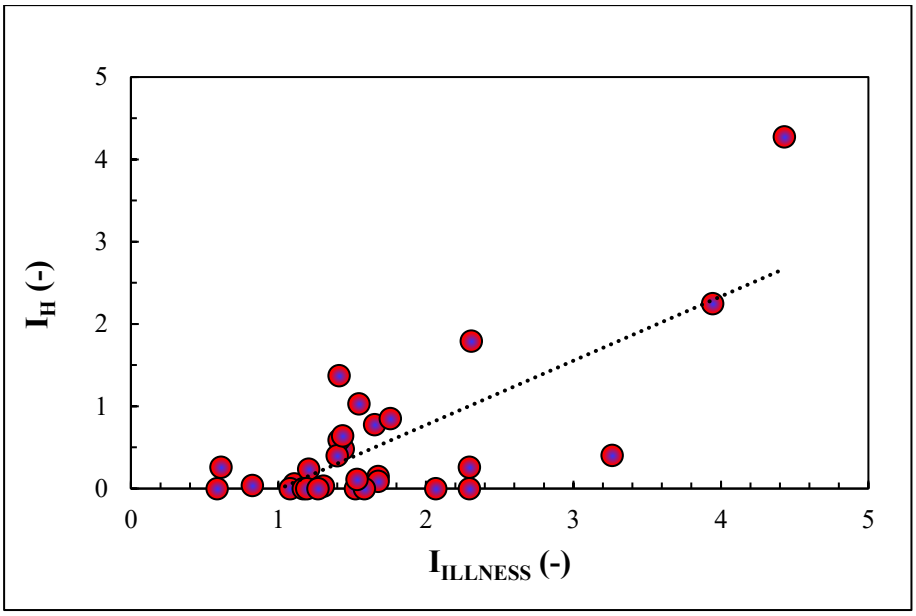


Figure 64: Correlation between $I_{ILLNESS}$ and $I_H$ in obese patients (Spearman correlation with r = 0.46 and p < 0.05).

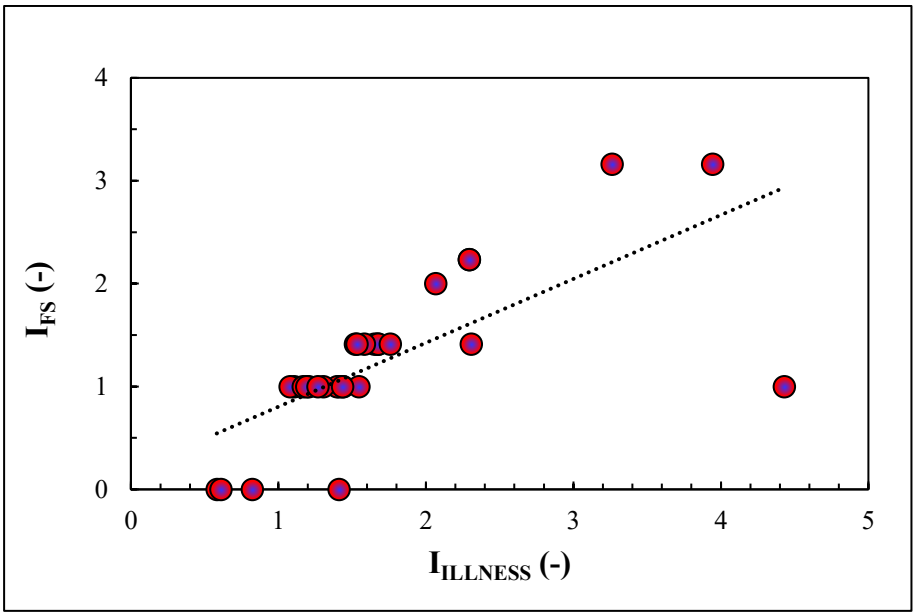


Figure 65: Correlation between $I_{ILLNESS}$ and $I_{FS}$ in obese patients (Spearman correlation with r = 0.80 and p < 0.0001).

These pathological indices were correlated with rheological and LF-NMR parameters. It was seen that critical deformation $\gamma_c$ correlates inversely with $I_{ILLNESS}$ and $I_{FS}$ (Figure 66 and Figure 67). In fact, as the disease index and the fibrosis/steatosis index increase, the liver tissue becomes more rigid and fibrous. As the tissue becomes more fibrous, the critical deformation decreases.

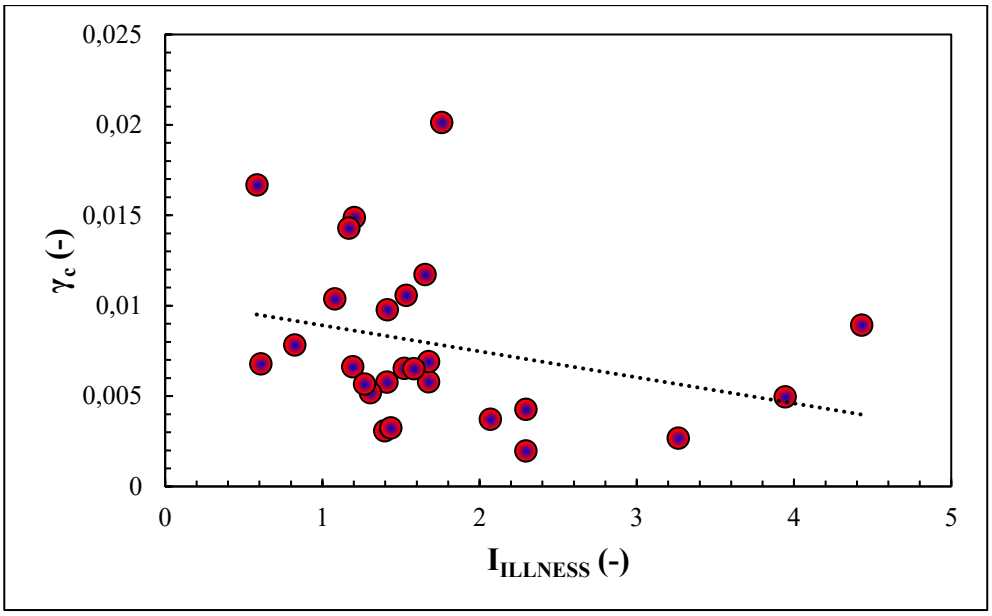


Figure 66: Correlation between $I_{ILLNESS}$ of obese patients and the respective $\gamma_c$ of pathological samples (Spearman correlation with $r = -0.40$ and $p < 0.05$).

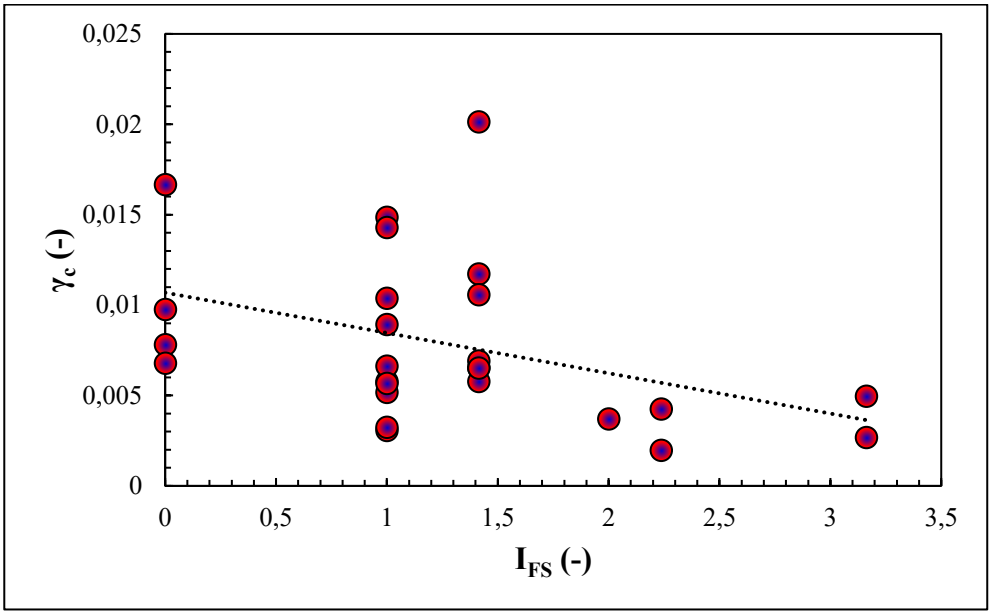


Figure 67: Correlation between $I_{FS}$ and $\gamma_c$ of pathological samples (Spearman correlation with $r = -0.43$ and $p < 0.05$).

Furthermore, we observe that $T_{2m}$ directly correlates with $I_{BMI}$, $I_{FS}$ and with the stages of steatosis of Kleiner-Brunt (measured in histological analyses) (Figure 68, Figure 69 and Figure 70). These correlations indicate that increasing the $I_{BMI}$, $I_{FS}$, the stages of steatosis, there is also an increase in $T_{2m}$ values. To explain these correlations, the alterations in iron metabolism in obese patients must be investigated. While we have seen, both from our results (paragraph 4.4) and from the literature (Mehta et al., 2019; Yao et al., 2019), that iron levels in liver tissue increase with liver tissue stiffness, obesity is associated with iron deficiency.

This is because obese patients have higher hepcidin levels which rise with BMI. Hepcidin is a peptide hormone considered the master regulator of iron homoeostasis, that is produced chiefly by hepatocyte. It is released in response to rising iron saturation of plasma transferrin, increased hepatic iron stores, or inflammation, and negatively feeds back to reduce iron availability by causing degradation of the ferroportin transporter, thereby reducing iron uptake by enterocytes (Hilton et al., 2023). Therefore, we could assert that our obese patients with higher BMI and steatosis are associated with high $T_{2m}$ of the liver samples, because a higher degree of obesity indicates a lower iron content in liver.

$T_{2m}$ does not correlate with $I_{ILLNESS}$ and $I_H$ (data not shown).

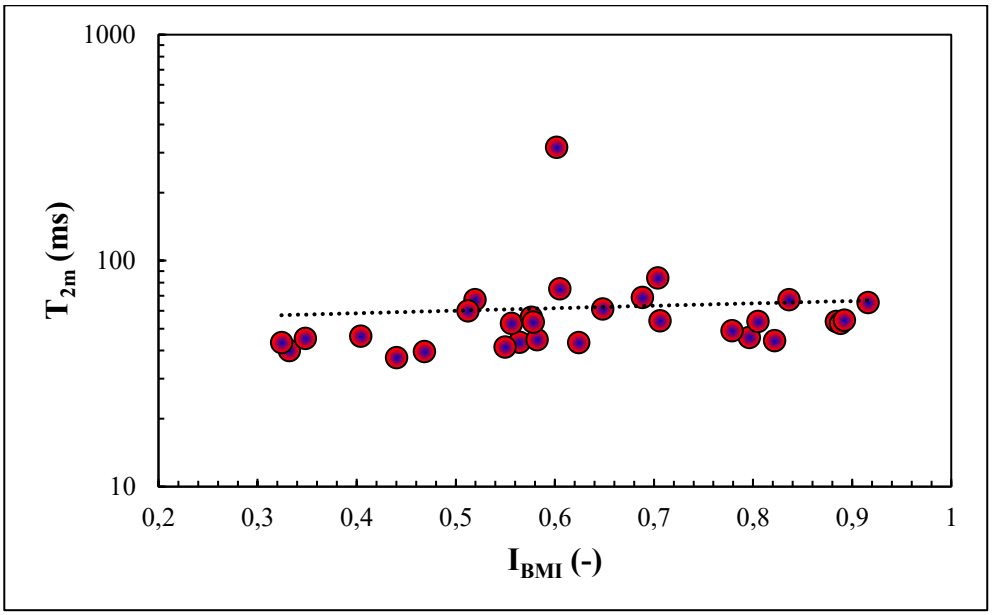


Figure 68: Correlation between $I_{BMI}$ of obese patients and the respective $T_{2m}$ of pathological samples (Spearman correlation with $r = 0.44$ and $p < 0.05$).

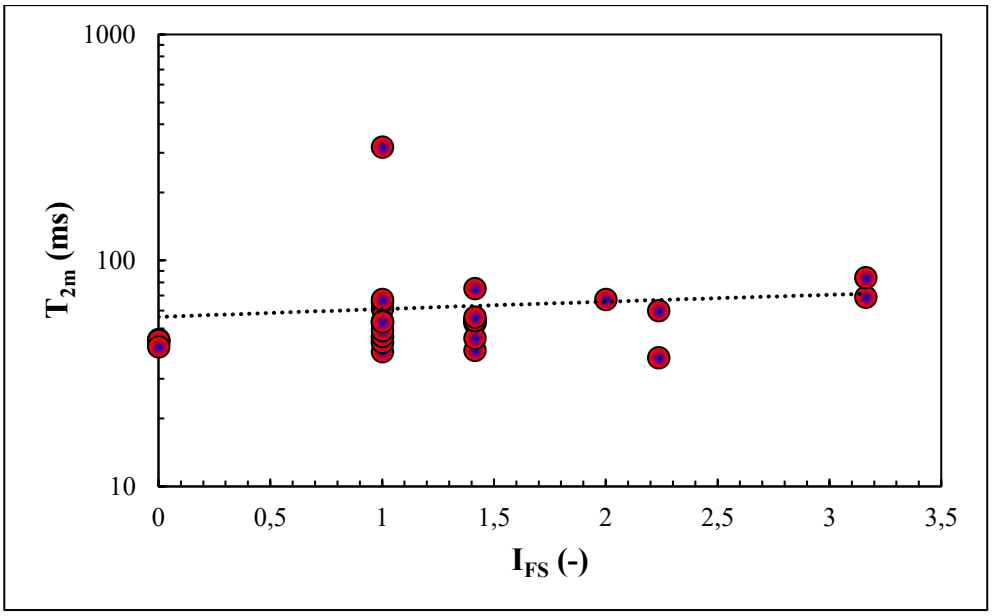


Figure 69: Correlation between $I_{FS}$ and $T_{2m}$ of pathological samples (Spearman correlation with r = 0.38 and p < 0.05).

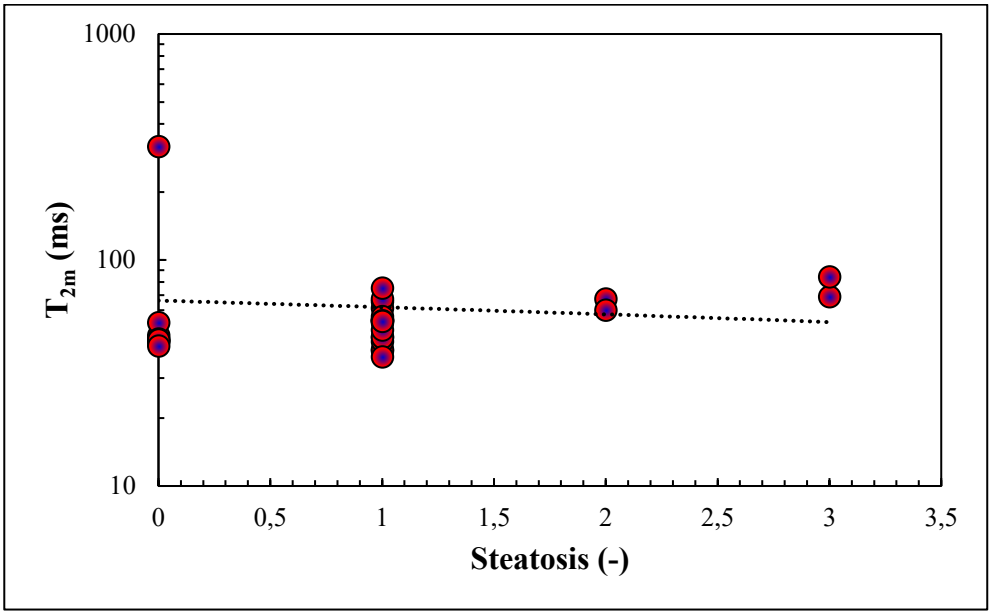


Figure 70: Correlation between steatosis stages deduced from histological analysis and $T_{2m}$ of pathological samples (Spearman correlation with r = 0.46 and p < 0.01).

## 4.6 The composition and the rheological characterization of alginate gels

Hepatic stellate cells (HSCs) are the major promoter of liver fibrosis. These cells, which have the features of fibroblasts, are localized in the liver in the space of Disse. Due to external pathological stimuli, quiescent HSCs trans-differentiate into proliferative and migratory myofibroblasts (cell activation), secreting extracellular matrix (ECM) proteins, a hallmark of LF, resulting in progressive organ failure (Iredale et al., 2013). The production of ECM increases liver stiffness (Kostallari et al., 2022), which in turn contributes to promote HSC

activation and thus liver fibrosis (Olsen et al., 2011). Thus, to test the anti-fibrotic effects of drugs *in vitro*, it is necessary to evaluate their effects on HSCs cultivated on a surface with the same viscoelastic properties of the fibrotic liver. We thus used the rheological properties determined in the liver tissue above described, to generate gel surfaces with comparable properties for *in vitro* tests. Specifically, we selected alginate, a polymer renowned for its non-toxicity and biomimetic qualities.

Different alginate systems were realized in DMEM and cross-linked with various concentrations of calcium ions. In addition, ECM elements, like fibronectin, collagen I or Geltrex (a soluble form of basement membrane extracted from murine Engelbreth-Holm-Swarm tumors) were also mixed with the alginate in different quantities, to favor cell adhesion. To assess if these systems were suitable for cell culture, they were tested with two different cell lines, such as LX2 (a human HSCs cell line) and WS1 (a human fibroblast cell line), with the Dil labelling of the cell membranes (Figure 71 and Figure 72). Geltrex and fibronectin mixed systems were both able to permit WS1 attachment at least up to 72 h. In contrast, for LX2 only the fibronectin mixed with alginate gels allowed cell adhesion up to 72 hours. Systems mixed with collagen I were unsuccessful with both cell types. Thus, alginate gels mixed with fibronectin were used for further *in vitro* testing.

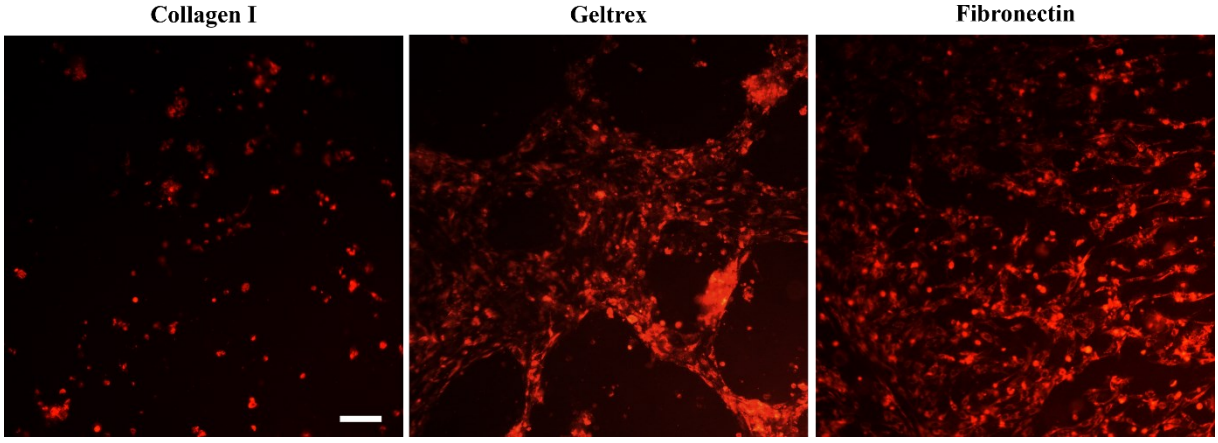


Figure 71: Dil labelling of cell membranes with WS1 cells ($60*10^3$ cells/well in 24 well-palte) seeded on alginate (2% 9 mg/ml $Ca^{++}$) gels mixed with collagen I, Geltrex or fibronectin in ratio 1:10 (ECM element:alginate). Pictures taken with fluorescent microscope at 72 hours from seeding. The scale bar is 100 μm. Only in Geltrex and fibronectin systems is possible to see attached, elongated in shape and viable cells.

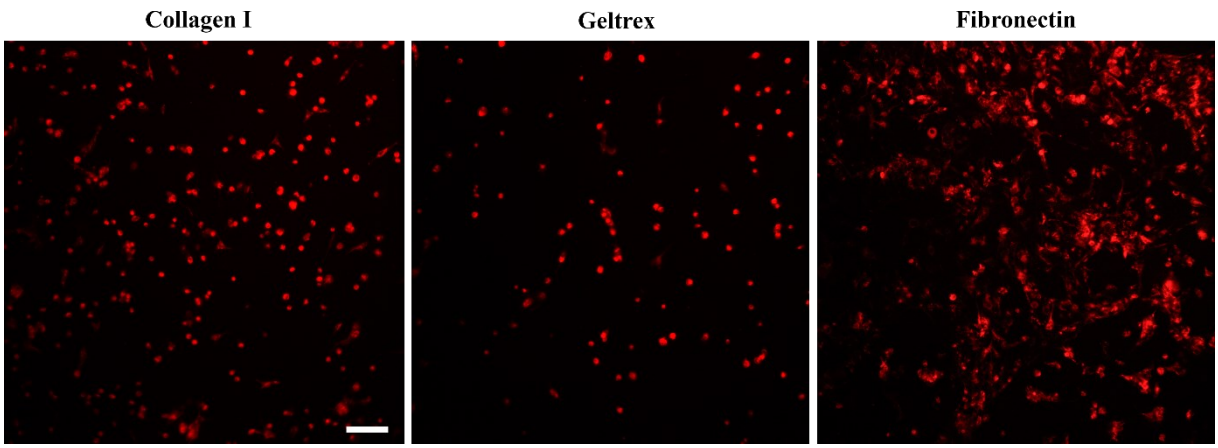


Figure 72: Dil labelling of cell membranes with LX2 cells ($60*10^3$ cells/well in 24 well-palte) seeded on alginate (2% 9 mg/ml $Ca^{++}$) gels mixed with collagen I, Geltrex or fibronectin in ratio 1:10 (ECM element:alginate). Pictures taken with fluorescent microscope at 72 hours from seeding. The scale bar is 100 μm. Only in fibronectin systems is possible to see attached, elongated in shape and viable cells.

The alginate systems with or without fibronectin were characterized by SS tests to delineate the linear viscoelastic region and FS tests to study the mechanical spectrum (Figure 73 and Figure 74). In the SS and FS graphics it is possible to notice that as the concentration of calcium ions increases, the systems are characterized by higher G* moduli. Moreover, also the addition of fibronectin changes slightly the rheology of the system. The best fitting of the Soskey-Winter model on the SS data allows us to evaluate the critical deformation $\gamma_c$ (which marks the upper limit of the viscoelastic field) (Table 18). The best fitting of the generalized Maxwell model to the FS data allows us to evaluate the shear modulus G as well as the relaxation time spectrum as shown in Table 19.

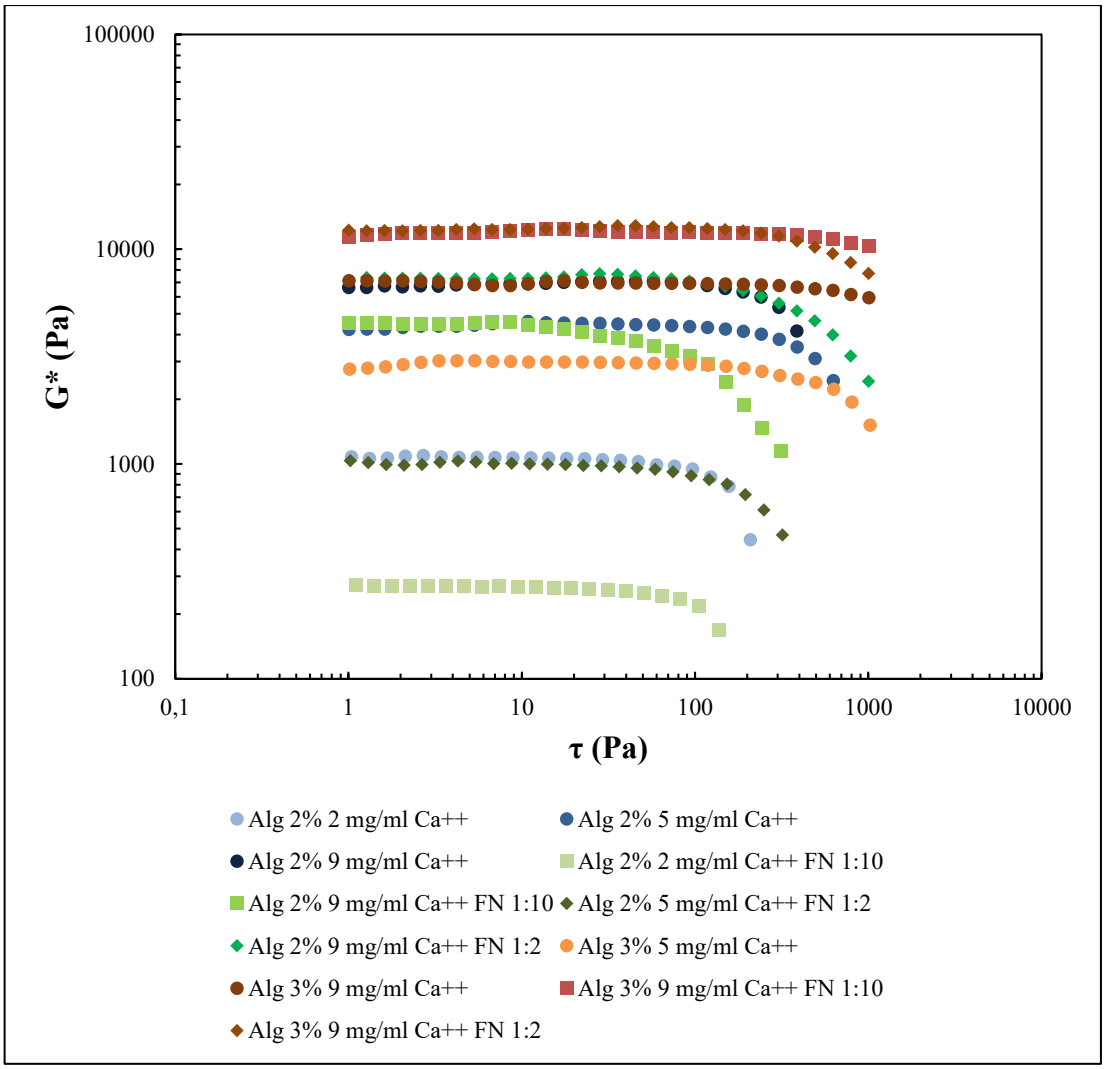


Figure 73: Stress sweep test performed on alginate systems at 1 Hz. The moduli are reported as G* (Pa). The brown-orange symbols represent alginate 3% systems, and the blue-green symbols represent alginate 2% systems.

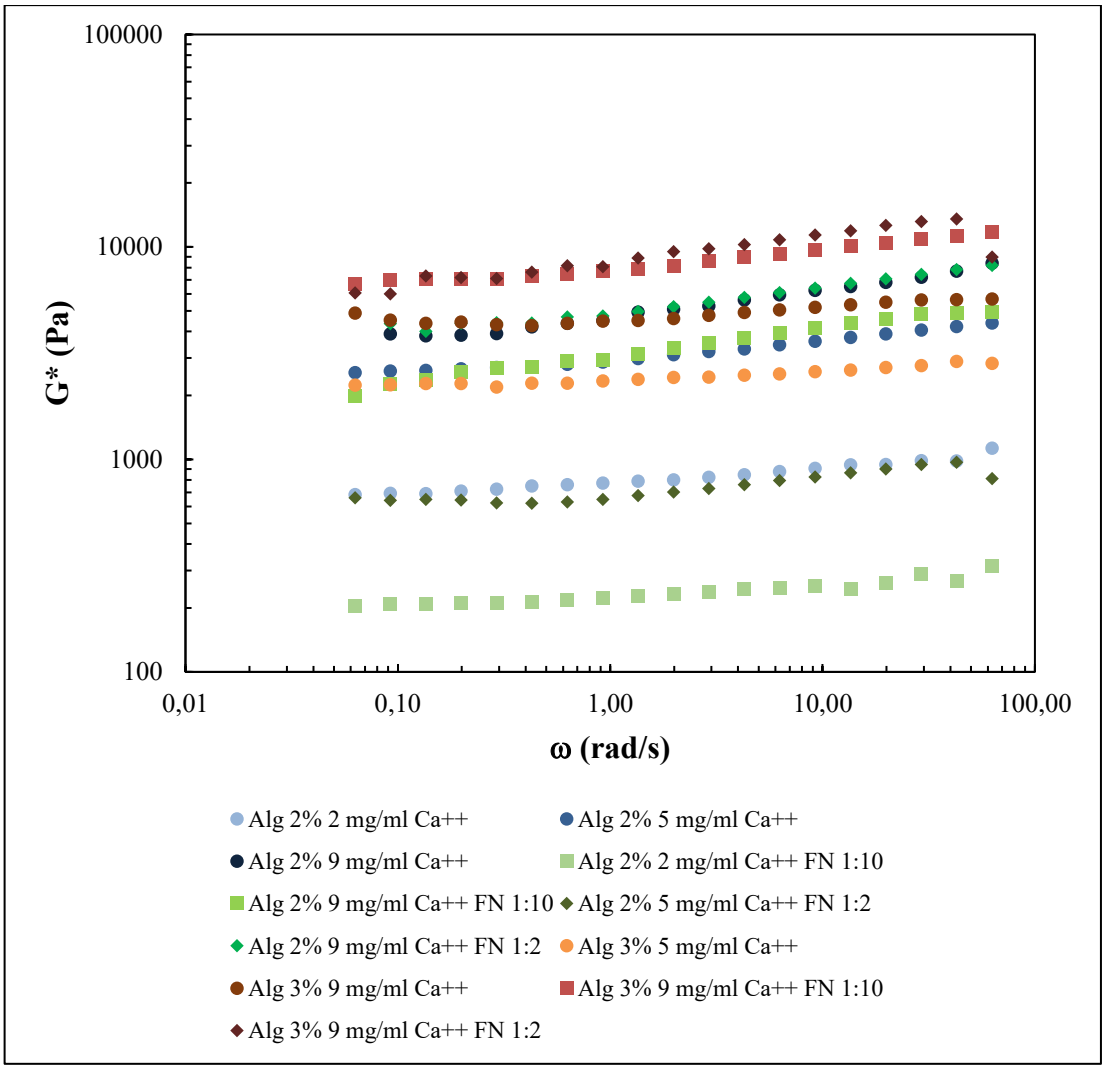


Figure 74: Frequency sweep test performed on alginate systems. The moduli are reported as G* (Pa). The brown-orange symbols represent alginate 3% systems, and the blue-green symbols represent alginate 2% systems.

Table 18: Results of SS analysis on alginate systems. *w* is the work per unit volume necessary to get the critical deformation $\gamma_c$ (eq. (1.38)). $G_c$, $\tau_c$, $\gamma^*_c$ and $G^*_c$ are the fitting results of the Soskey-Winter model (eq. (1.31)).

| Sample | $\gamma_c$ (-) | $G_c$ (Pa) | $\tau_c$ (Pa) | $\gamma^*_c$ (-) | $G^*_c$ (Pa) | $w$ (J/m$^3$) |
|---|---|---|---|---|---|---|
| Alg 2% 2 mg/ml $Ca^{++}$ | 0,0541 | 1109 | 60,0 | 0,0539 | 1113 | 1,62 |
| Alg 2% 5 mg/ml $Ca^{++}$ | 0,0362 | 4137 | 149,6 | 0,0366 | 4091 | 3,02 |
| Alg 2% 9 mg/ml $Ca^{++}$ | 0,0228 | 6519 | 148,9 | 0,0236 | 6297 | 1,94 |
| Alg 2% 2 mg/ml $Ca^{++}$ FN 1:10 | 0,1906 | 265 | 50,5 | 0,1575 | 252 | 3,97 |
| Alg 2% 9 mg/ml $Ca^{++}$ FN 1:10 | 0,0020 | 4267 | 8,6 | 0,0021 | 4167 | 0,01 |
| Alg 2% 5 mg/ml $Ca^{++}$ FN 1:2 | 0,0453 | 1024 | 46,4 | 0,0451 | 1028 | 1,06 |
| Alg 2% 9 mg/ml $Ca^{++}$ FN 1:2 | 0,0087 | 6589 | 57,5 | 0,0089 | 6487 | 0,29 |
| Alg 3% 5 mg/ml $Ca^{++}$ | 0,0582 | 2592 | 150,8 | 0,0584 | 2583 | 5,26 |
| Alg 3% 9 mg/ml $Ca^{++}$ | 0,0592 | 6560 | 388,1 | 0,0599 | 6475 | 13,16 |
| Alg 3% 9 mg/ml $Ca^{++}$ FN 1:10 | 0,0436 | 1319 | 57,5 | 0,0444 | 1297 | 12,15 |
| Alg 3% 9 mg/ml $Ca^{++}$ FN 1:2 | 0,0166 | 11382 | 189,0 | 0,0172 | 11007 | 1,83 |

Table 19: Results of FS analysis on alginate systems. $\Sigma G_i$ is the shear modulus, $G_0$, $G_1$, $G_2$, $G_3$, $G_4$ and $\lambda_1$ are the fitting parameters of the generalized Maxwell model. $\xi$ is the average mesh size of the polymeric network and $\rho_{xs}$ is the crosslinking density.

| Sample | $\lambda_1$ (s) | $G_0$ (Pa) | $G_1$ (Pa) | $G_2$ (Pa) | $G_3$ (Pa) | $G_4$ (Pa) | $G_5$ (Pa) | $\Sigma G_i$ (Pa) | % elasticity | mean G* (Pa) | $\rho_{xs}$ (mol/cm$^3$) | $\xi$ (nm) |
|---|---|---|---|---|---|---|---|---|---|---|---|---|
| Alg 2% 2 mg/ml $Ca^{++}$ | 0,01040 | 424 | 507 | 130 | 192 | 268 | - | 1521 | 28 | 832 | 6,1E-07 | 17,3 |
| Alg 2% 5 mg/ml $Ca^{++}$ | 0,00516 | 1225 | 1661 | 836 | 778 | 648 | 923 | 6072 | 20 | 3239 | 2,5E-06 | 10,9 |
| Alg 2% 9 mg/ml $Ca^{++}$ | 0,00883 | 2034 | 3233 | 1997 | 930 | 2234 | - | 10428 | 20 | 5332 | 4,2E-06 | 9,1 |
| Alg 2% 2 mg/ml $Ca^{++}$ FN 1:10 | 0,00832 | 169 | 160 | 29 | 37 | 44 | - | 439 | 38 | 238 | 1,8E-07 | 26,2 |
| Alg 2% 9 mg/ml $Ca^{++}$ FN 1:10 | 0,01536 | 1216 | 1826 | 1199 | 830 | 1201 | - | 6272 | 19 | 3466 | 2,5E-06 | 10,8 |
| Alg 2% 5 mg/ml $Ca^{++}$ FN 1:2 | 0,02368 | 162 | 294 | 182 | 164 | 341 | - | 1143 | 14 | 742 | 4,6E-07 | 19,0 |
| Alg 2% 9 mg/ml $Ca^{++}$ FN 1:2 | 0,00995 | 2851 | 3277 | 1849 | 1624 | 1112 | - | 10713 | 27 | 5675 | 4,3E-06 | 9,0 |
| Alg 3% 5 mg/ml $Ca^{++}$ | 0,01102 | 1908 | 433 | 306 | 154 | 384 | - | 3184 | 60 | 2464 | 1,3E-06 | 13,5 |
| Alg 3% 9 mg/ml $Ca^{++}$ | 0,01594 | 3547 | 1360 | 748 | 710 | 382 | - | 6747 | 53 | 4863 | 2,7E-06 | 10,5 |
| Alg 3% 9 mg/ml $Ca^{++}$ FN 1:10 | 0,01846 | 4311 | 3404 | 1983 | 1617 | 2349 | - | 13665 | 32 | 8640 | 5,5E-06 | 8,3 |
| Alg 3% 9 mg/ml $Ca^{++}$ FN 1:2 | 0,06038 | 6094 | 5723 | 766 | 2065 | - | - | 14647 | 42 | 9384 | 5,9E-06 | 8,1 |

Stress sweep test results show that the minimal critical stress $\tau_c$ measured (that indicates the exiting from the linear viscoelastic field) is 8,6 Pa. For this reason, the frequency sweep tests on the alginate systems were conducted at 1 Pa.

From the shear moduli reported in Table 19, it is possible to notice that increasing the concentration of calcium ions there is also an increase of G in systems with alginate 2% with or without fibronectin mixed. This is evident also in alginate 3% systems.

In order to appreciate the elastic and viscous modulus trends of these systems in detail, Figure 75, Figure 76, Figure 77 and Figure 78 show the outcomes of their stress and frequency sweep test.

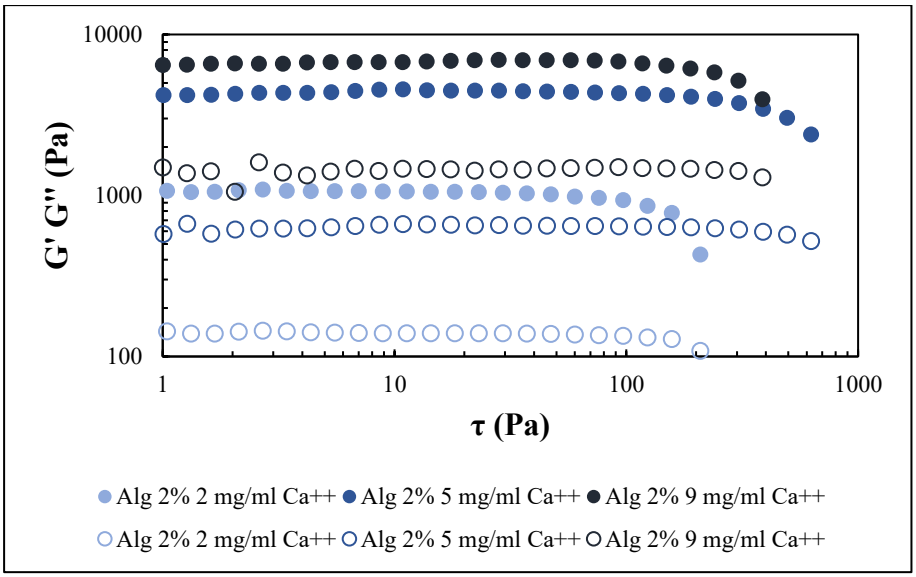


Figure 75: SS test performed on alginate 2% systems with increasing $Ca^{++}$. Filled symbols indicate G' while open symbols indicate G".

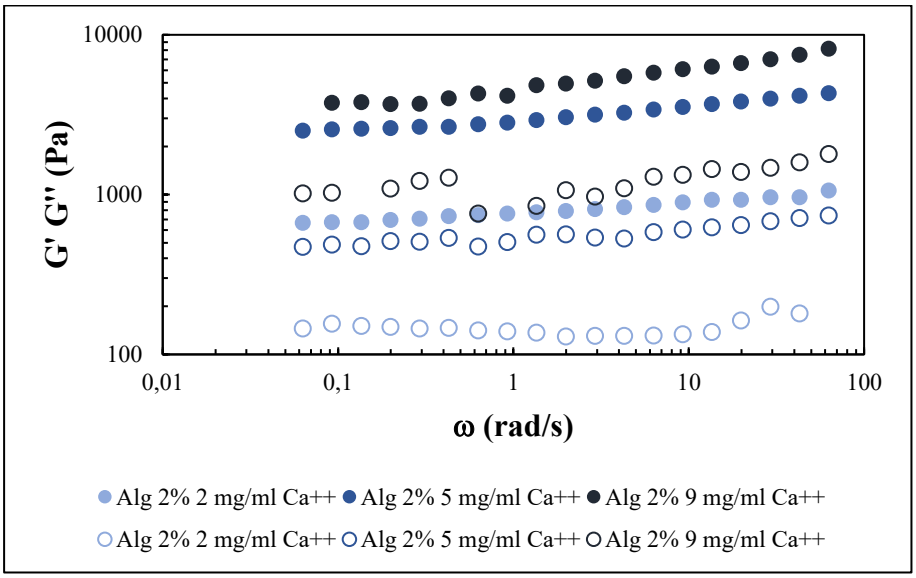


Figure 76: FS test performed on alginate 2% systems with increasing $Ca^{++}$. Filled symbols indicate G' while open symbols indicate G".

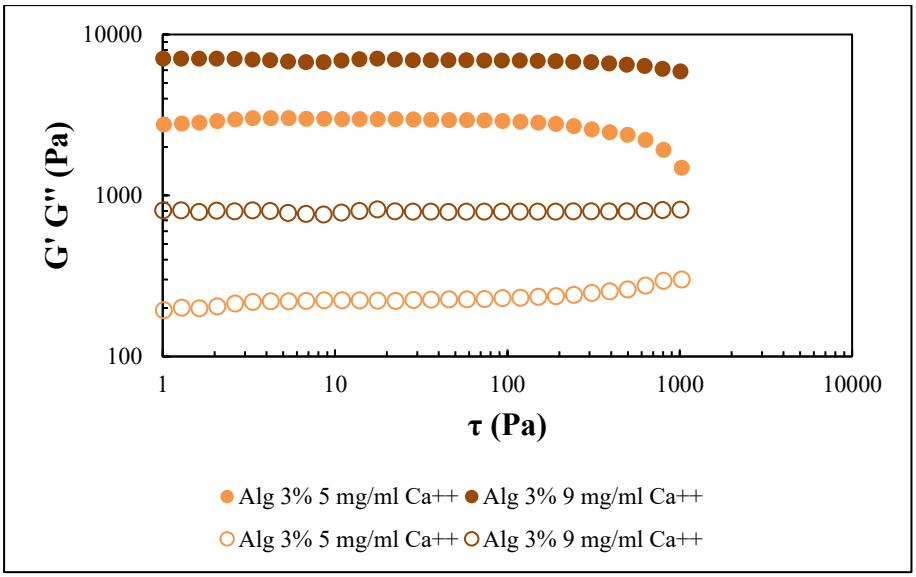


Figure 77: SS test performed on alginate 3% systems with increasing $Ca^{++}$. Filled symbols indicate G' while open symbols indicate G''.

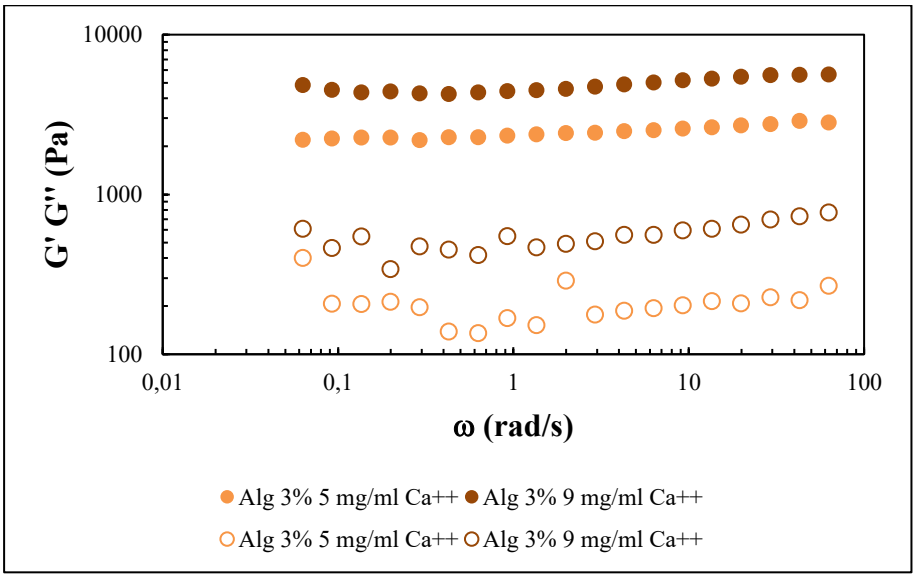


Figure 78: FS test performed on alginate 3% systems with increasing $Ca^{++}$. Filled symbols indicate G' while open symbols indicate G''.

The stress sweep tests, for each type of alginate system, highlight the clear predominance of the elastic component (G') over the viscous component (G''). In both alginate 2 and 3% systems, G' and G'' increase as the calcium ions concentration increases. This is evident also from the frequency sweep tests and from the shear moduli $\Sigma G_i$, which increases as the calcium ions concentration increases. In fact, systems with a higher concentration of calcium ions are more rigid because they possess a greater number of cross-linking points provided by the greater amount of the cross-linking agent. This is also reflected in the average mesh size of the reticulum (Table 19), which decreases as the concentration of calcium ions increases.

Furthermore, the FS tests emphasize the gel nature of all the systems considered as G' is always significantly bigger than G'', as the two moduli are parallel and as they are constant with the pulsation ω. However, in alginate 2% there is a trend of G' and G'', to be downward (when the pulse is reduced, the modules are slightly reduced). Moreover, from the FS tests, by increasing the alginate concentration from 2 to 3%, there is no clear difference in the G' modulus, while there is a difference in G'', which is greater in the 2% alginate systems than in the 3% systems with the same calcium ions considered. This means that there is a greater prevalence of the viscous component in 2% alginate systems, indicating a weaker gel. In fact, Table 19 shows that the % elasticity (eq. (4.1)), spans from 19 to 38% for the 2% alginate while this range spans from 32 to 60 for the 3% alginate gels.

The congruity of the stress and frequency sweep tests is demonstrated by the substantial equivalence between the G' and G'' modules evaluated at small stresses in the stress sweep tests (conducted with a frequency of 1 Hz) and the modules evaluated in the frequency sweep tests at the frequency of 1 Hz (ω = 6.28 rad/s).

In the following pictures (Figure 79, Figure 80, Figure 81 and Figure 82), alginate systems with and without fibronectin (1:10 ratio, fibronectin:alginate) are compared.

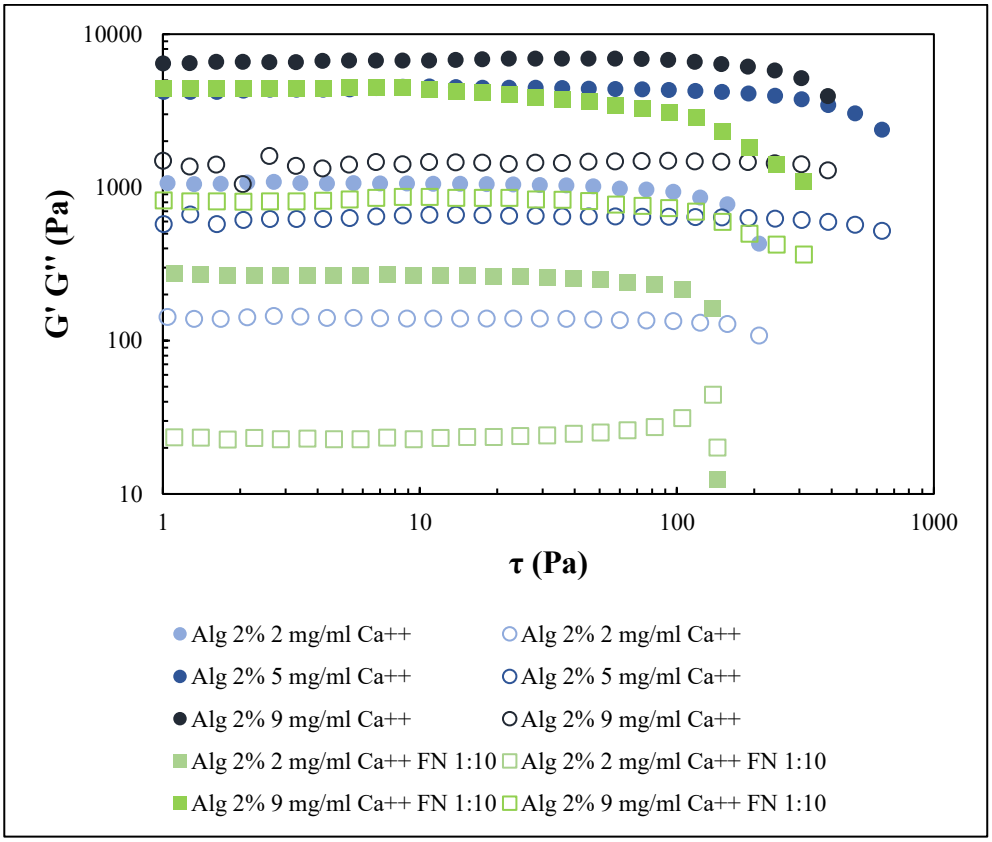


Figure 79: SS test performed on alginate 2% systems (with and without fibronectin) with increasing $Ca^{++}$. Filled symbols indicate G' while open symbols indicate G''.

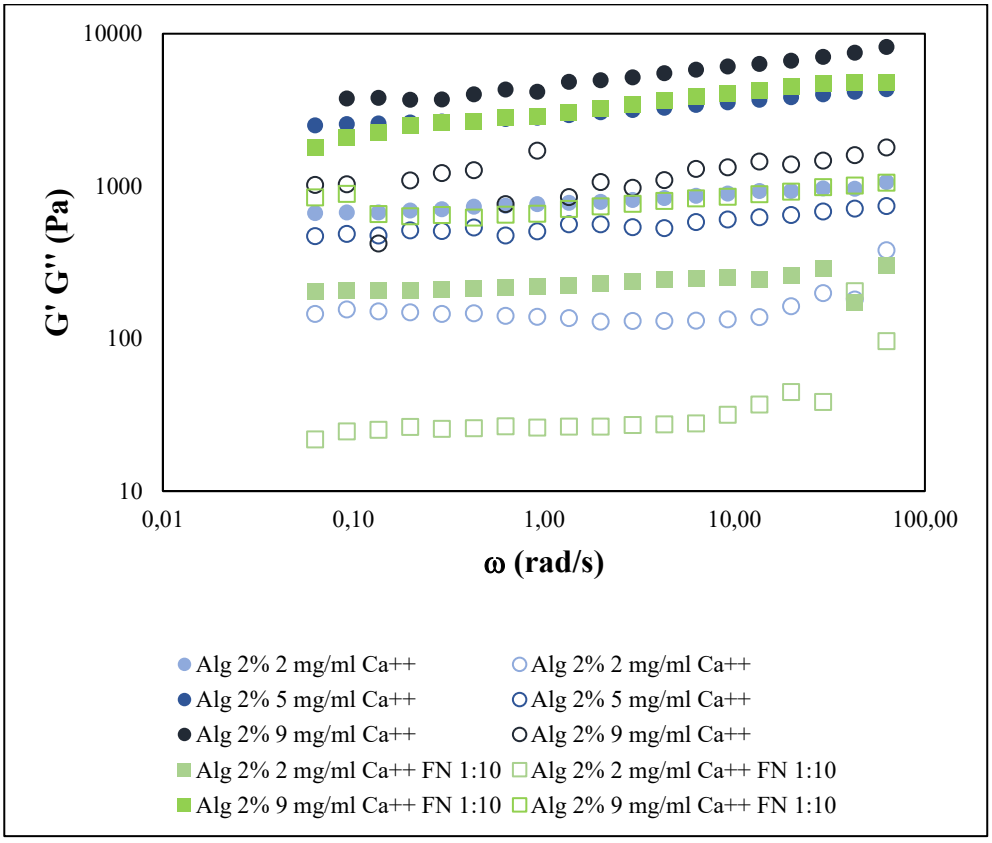


Figure 80: FS test performed on alginate 2% systems (with and without fibronectin) with increasing $Ca^{++}$. Filled symbols indicate G' while open symbols indicate G".

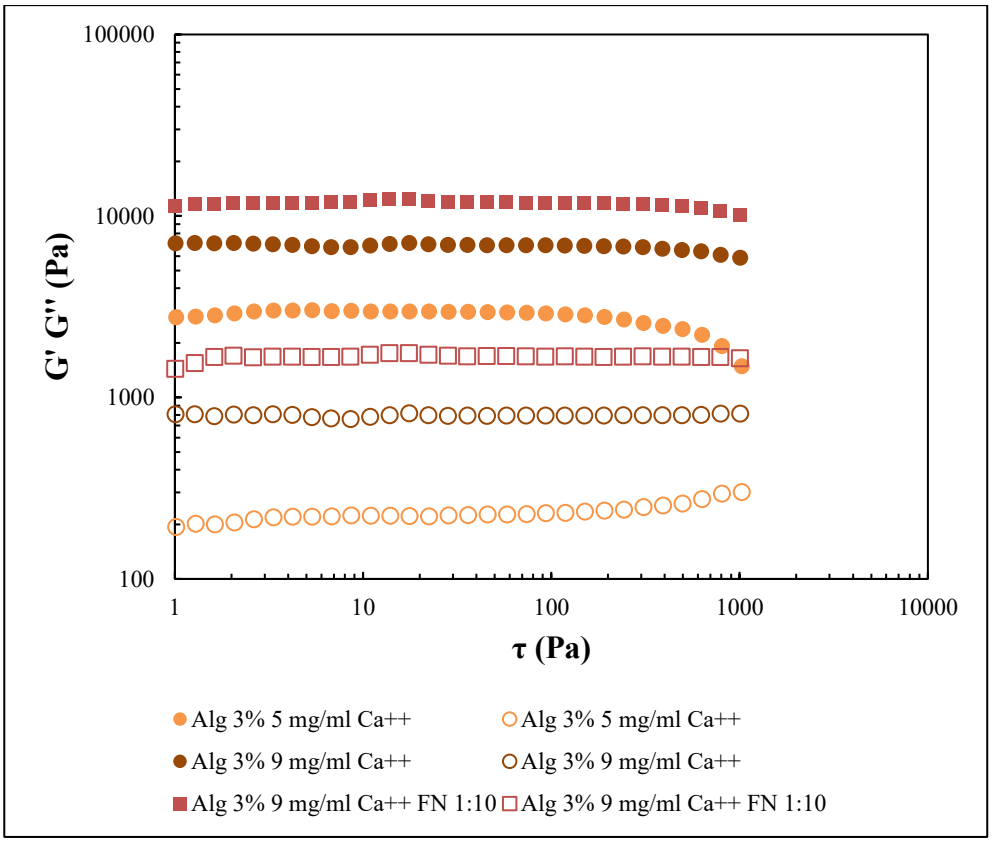


Figure 81: SS test performed on alginate 3% systems (with and without fibronectin) with increasing $Ca^{++}$. Filled symbols indicate G' while open symbols indicate G".

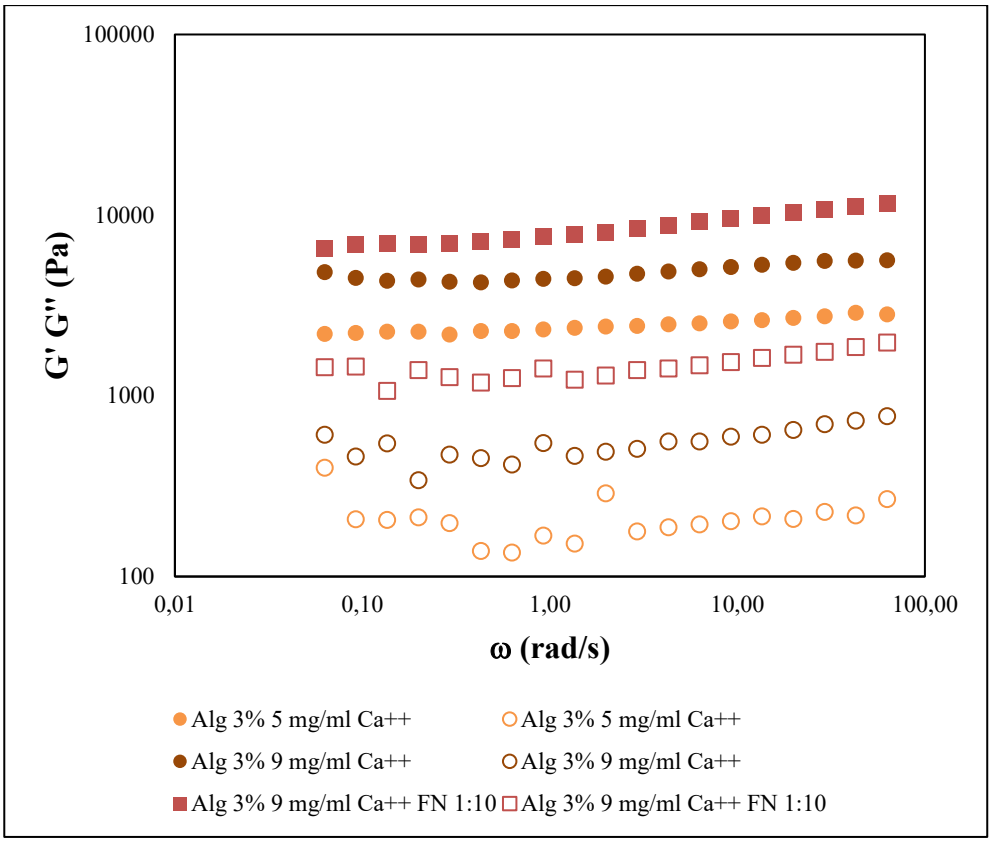


Figure 82: FS test performed on alginate 3% systems (with and without fibronectin) with increasing $Ca^{++}$. Filled symbols indicate G' while open symbols indicate G".

The addition of fibronectin to the alginate systems at a ratio of 1:10 (optimal for cell adhesion), does not change the rheological properties of the systems. In particular, fibronectin does not modify significantly the G' and G" moduli, especially in the systems gelled with a 9 mg/ml $Ca^{++}$ concentration. Indeed, the moduli slightly decrease in the 2% alginate system and slightly increase in the system with 3% alginate. In contrast, in the 2% alginate system gelled with 2 mg/ml $Ca^{++}$ concentration, the addition of fibronectin visibly reduces both moduli.

Figure 83 highlights the existence of a linear correlation between $\Sigma G_i$ and $G_c$ (linear correlation with $r = 0.70$ and $p < 0.05$). Interestingly, a similar correlation was also recently found for weak gels based on scleroglucan and guar-gum (Coviello et al., 2022) and in our liver samples (paragraph 4.3).

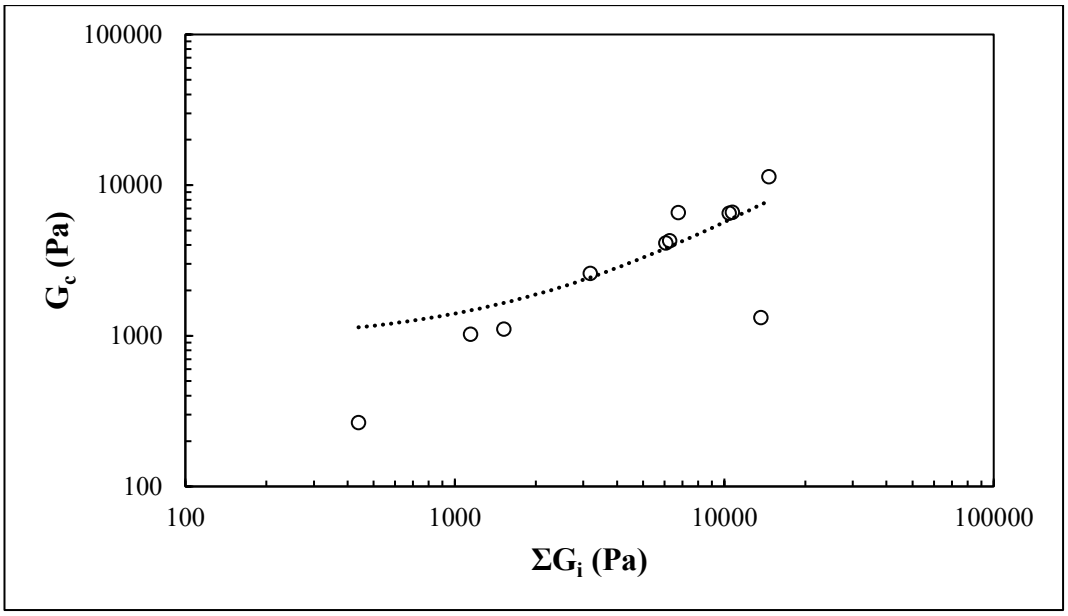


Figure 83: Correlation between $\Sigma G_i$ (Pa) and $G_c$ (Pa) in alginate 2 and 3% systems (linear correlation with $r = 0.70$ and $p < 0.05$).

## 4.7 The LF-NMR characterization of alginate gels

LF-NMR characterization allows the evaluation of the spin-spin relaxation time spectrum and the spin-lattice relaxation spectrum as well as the $T_{2m}$ and $T_{1m}$ shown in Table 20 and Table 21. This technique provides us important nano-microstructure information on polymer systems, like alginate gels. Since $T_{2m}$ is influenced by the surface effect (see paragraph 1.2), this parameter permits to have insights on the surface of contact between the liquid phase (water in this case) and the solid phase (alginate polymer chains). In fact, an increase in $T_{2m}$ corresponds to a decrease in the contact surface area between the liquid phase and the solid phase (in this case the polymer), indicating either an increase in the average mesh size of the polymer network or an increase in the radial size of the polymer chains. Conversely, a decrease in $T_{2m}$ corresponds to an increase in the contact surface between the liquid and solid phase, indicating either a decrease in the average mesh size or a decrease in the radial size of the polymer chains. Thus, the LF-NMR technique is able to provide structural information on the alginate gel that enrich and complete the rheological characterization.

Table 20: Results of LF-NMR analysis on alginate gels. $T_{2m}$ is the average mean spin-spin relaxation time, Ai% and $T_{2i}$ are the percentages and relaxation times respectively.

| Sample | $T_{2m}$ (ms) | $T_{21}$ (ms) | $T_{22}$ (ms) | $T_{23}$ (ms) | $T_{24}$ (ms) | $T_{25}$ (ms) | $A_1$% (-) | $A_2$% (-) | $A_3$% (-) | $A_4$% (-) | $A_5$% (-) |
|---|---|---|---|---|---|---|---|---|---|---|---|
| Alg 2% 2 mg/ml $Ca^{++}$ | 894,6 | 2381,1 | 635,5 | 94,5 | 196,0 | - | 31,2 | 13,0 | 38,7 | 17,2 | - |
| Alg 2% 5 mg/ml $Ca^{++}$ | 922,8 | 2887,0 | 59,7 | 1147,0 | 298,6 | 32,7 | 26,1 | 37,4 | 10,6 | 6,9 | 19,1 |
| Alg 2% 9 mg/ml $Ca^{++}$ | 975,9 | 2660,9 | 841,0 | 160,1 | 49,8 | - | 31,9 | 10,5 | 9,0 | 48,5 | - |
| Alg 2% 2 mg/ml $Ca^{++}$ FN 1:10 | 1140,9 | 2943,9 | 190,6 | 798,1 | 94,3 | - | 33,1 | 24,9 | 11,4 | 30,6 | - |
| Alg 2% 9 mg/ml $Ca^{++}$ FN 1:10 | 1225,2 | 2966,2 | 944,4 | 185,6 | 55,5 | - | 37,0 | 9,2 | 8,2 | 45,6 | - |
| Alg 3% 5 mg/ml $Ca^{++}$ | 642,4 | 2938,0 | 716,0 | 79,7 | 42,2 | - | 19,7 | 3,5 | 15,1 | 61,7 | - |
| Alg 3% 9 mg/ml $Ca^{++}$ | 734,1 | 2938,4 | 892,3 | 117,8 | 34,3 | - | 22,7 | 4,2 | 4,5 | 68,6 | - |
| Alg 3% 9 mg/ml $Ca^{++}$ FN 1:10 | 686,8 | 2811,8 | 895,3 | 151,6 | 33,2 | - | 20,9 | 7,5 | 6,0 | 65,6 | - |

Table 21: Results of LF-NMR analysis on alginate gels. $T_{1m}$ is the average mean spin-lattice relaxation time, $A_i$% and $T_{1i}$ are the percentages and relaxation times respectively.

| Sample | $T_{1m}$ (ms) | $T_{11}$ (ms) | $T_{12}$ (ms) | $T_{13}$ (ms) | $A_1$% (-) | $A_2$% (-) | $A_3$% (-) |
|---|---|---|---|---|---|---|---|
| Alg 2% 2 mg/ml $Ca^{++}$ | 2538,1 | 2636,3 | 173,2 | - | 96,0 | 4,0 | - |
| Alg 2% 5 mg/ml $Ca^{++}$ | 2206,8 | 2811,2 | 1442,6 | 39,1 | 58,5 | 38,9 | 2,6 |
| Alg 2% 9 mg/ml $Ca^{++}$ | 2294,3 | 3712,0 | 1742,5 | 24,1 | 30,1 | 67,4 | 2,4 |
| Alg 2% 2 mg/ml $Ca^{++}$ FN 1:10 | 2581,3 | 2664,4 | 269,1 | - | 96,5 | 3,5 | - |
| Alg 2% 9 mg/ml $Ca^{++}$ FN 1:10 | 2431,3 | 2734,6 | 737,9 | - | 84,8 | 15,2 | - |
| Alg 3% 5 mg/ml $Ca^{++}$ | 1948,3 | 2073,8 | 282,9 | - | 93,0 | 7,0 | - |
| Alg 3% 9 mg/ml $Ca^{++}$ | 1720,9 | 1767,4 | 19,7 | - | 97,3 | 2,7 | - |
| Alg 3% 9 mg/ml $Ca^{++}$ FN 1:10 | 1778,6 | 1915,2 | 25,0 | - | 92,8 | 7,2 | - |

The values of $T_{2m}$ and $T_{1m}$ are higher than those measured for the hepatic samples, this is because alginate hydrogels do not contain ferromagnetic/paramagnetic substances as it happens for the iron contained in the liver. In these hydrogel systems the $T_{2m}$ and $T_{1m}$ reflect, respectively, the spin-spin and spin-lattice relaxation time of the water protons present in the samples. $T_{2m}$ values slightly increase when calcium ions concentration increase. $T_{2m}$ depends on the solid phase in the sample (polymer volume fraction): the greater the contact surface of the solid phase with the liquid phase, the shorter the relaxation time. Consequently, if $T_{2m}$ slightly increases as the calcium ion concentration increases, then the contact surface area between the alginate polymer chains and the water in the sample decreases. This is explained by an increase in the radial size of the polymer chains. In fact, as the calcium ion

concentration rises in the alginate systems (2% alginate, 3% alginate and 2% alginate mixed with fibronectin 1:10), the shear modulus and thus the stiffness of the system increase (Table 19), since the cross-linking points become more numerous and the average mesh sizes smaller (ξ). However, there is also a moderate increase in $T_{2m}$, which indicates that the contact surface between the solid and liquid phase is slightly reduced because there is an increase in the radial size of the polymer chains, which become thicker (see Figure 84). It follows that the rheological and the LF-NMR techniques are focused on two different aspects concerning the characterization of alginate systems.

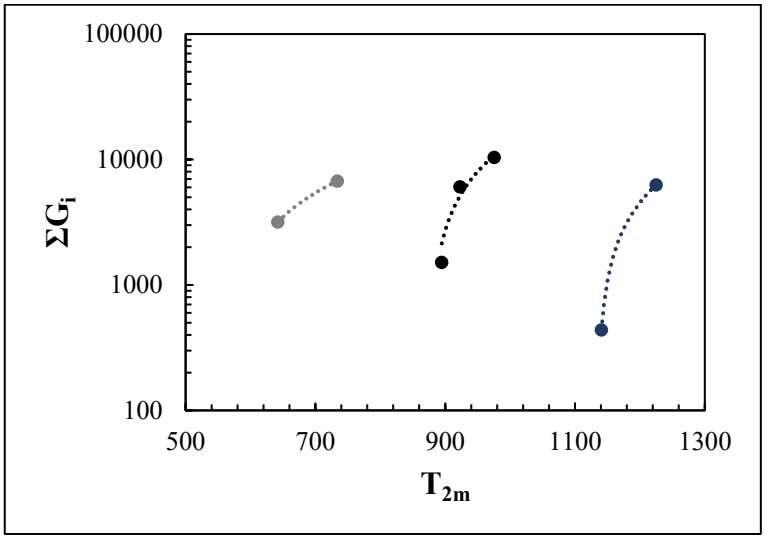


Figure 84: Relationship between $T_{2m}$ and $\Sigma G_i$. The grey symbols represent alginate 3% systems gelled with, starting from the point on the bottom, 5 mg/ml or 9 mg/ml $Ca^{++}$. The black symbols represent alginate 2% systems gelled with, starting from the point on the bottom, 2 mg/ml, 5 mg/ml or 9 mg/ml $Ca^{++}$. The blue symbols represent alginate 2% systems mixed with fibronectin 1:10 gelled with, starting from the point on the bottom, 2 mg/ml or 9 mg/ml $Ca^{++}$.

## 4.8 Selected alginate gel as *in vitro* models

### 4.8.1 Rheological characterization of alginate *in vitro* models

The alginate systems that were selected for in vitro cell tests are the one containing 2% alginate 9 mg/ml $Ca^{++}$ and FN 1:10 (from now on referred as **Alg 2%**), to mimic the healthy liver tissue, and 3% alginate 9 mg/ml $Ca^{++}$ and FN 1:10 (from now on referred as **Alg 3%**), to mimic the fibrotic liver tissue. These systems were chosen for physical nature resembling the normal (Alg 2%) and fibrotic liver (Alg 3%), based on rheological and LF-NMR tests (see paragraph 4.6). In both SS and FS tests, G' and G'' are higher in Alg 3% system than in Alg 2%, indicating that Alg 3% has a stiffer nature (Figure *85* and Figure *86*). Moreover, Alg 3% system is characterized by a higher elastic component than Alg 2%. In fact, the % of elasticity of Alg 3% is 32 while it is 19 for Alg 2%.

Table 22 shows that mean G* and the critical stress $\tau_c$ referring to Alg 3% and to pathological samples are comparable. On the other hand, the shear moduli and the mean G* of Alg 2% system are slightly higher than the average values of these moduli for the healthy samples. Indeed, the inspection of Figure 87 and Figure 88, reveals that this alginate system is positioned in the upper part of the range of values for healthy samples.

Table 22: Comparison between the rheological parameters of the selected alginate systems and the liver samples.

| **Gels** | **$\Sigma G_i$ (Pa)** | **mean G* (Pa)** | **$\tau_c$ (Pa)** |
|---|---|---|---|
| Alg 2% 9 mg/ml $Ca^{++}$ FN 1:10 | 6272 | 3466 | 8,6 |
| Alg 3% 9 mg/ml $Ca^{++}$ FN 1:10 | 13665 | 8640 | 57,5 |
| **Liver samples** | **average of $\Sigma G_i$ (Pa) ± SEM** | **average of mean G* (Pa) ± SEM** | **average of $\tau_c$ (Pa) ± SEM** |
| Healthy liver samples | 2719 ± 728 | 1657 ± 432 | 15 ± 5 |
| Pathological liver samples | 11672 ± 2723 | 7318 ± 1768 | 87 ± 26 |

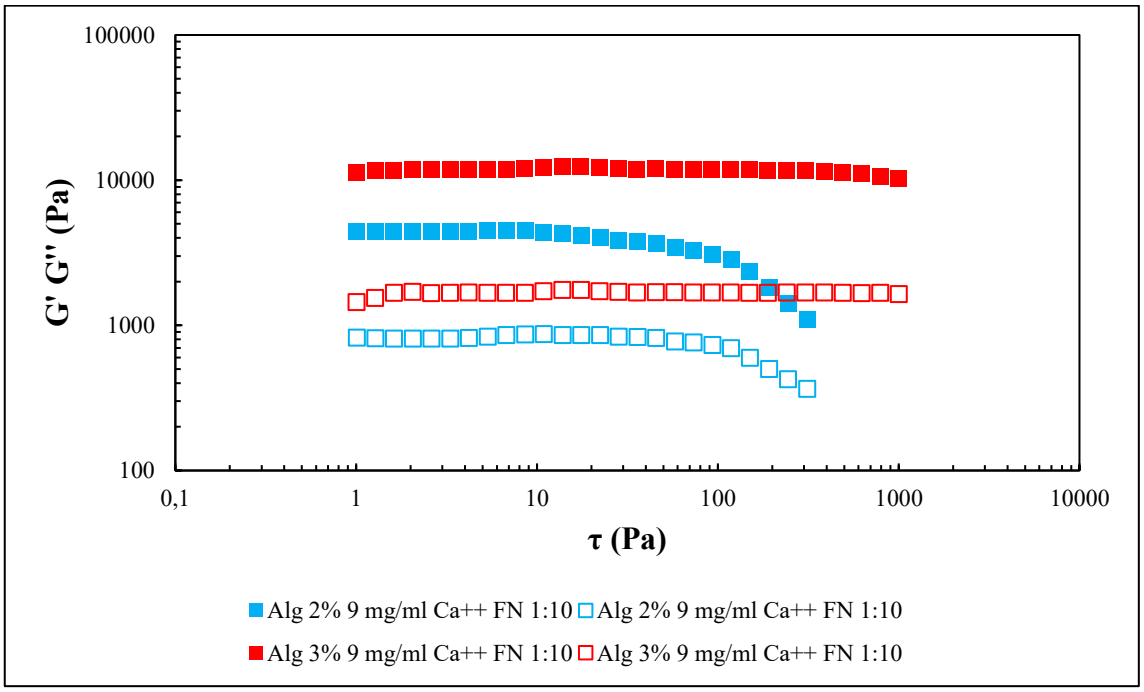


Figure 85: Stress sweep test for the selected alginate systems. Filled symbols indicate G' while open symbols indicate G".

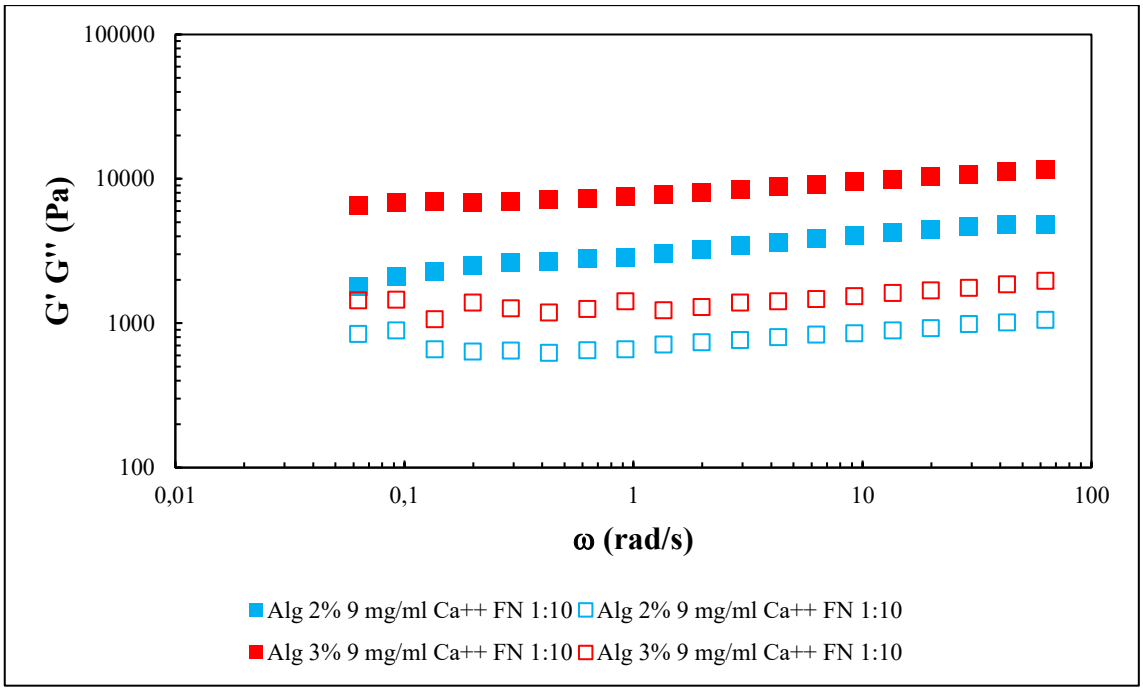


Figure 86: Frequency sweep test for the selected alginate systems. Filled symbols indicate G' while open symbols indicate G''.

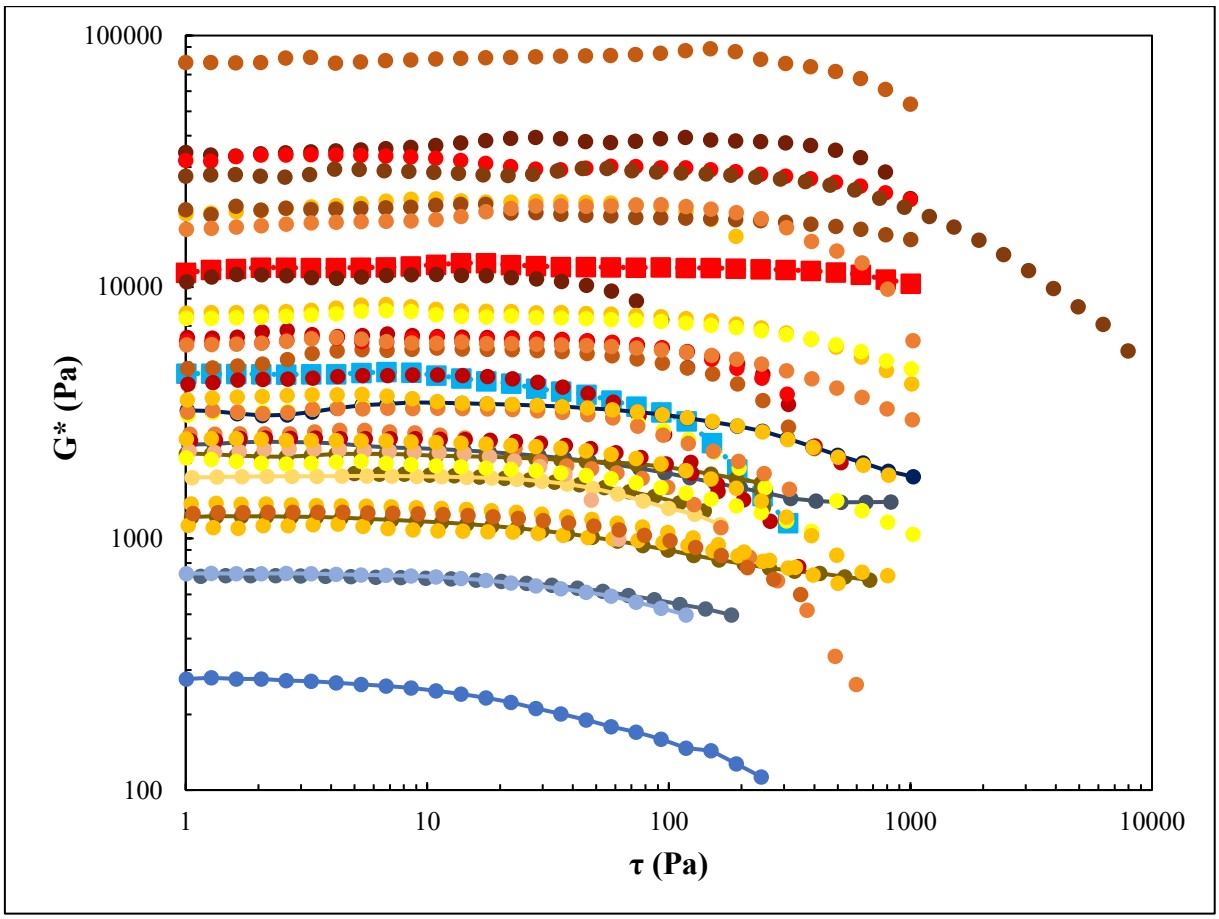


Figure 87: Stress sweep test performed on selected alginate systems and liver samples at 1 Hz. The moduli are reported as G* (Pa). The brown-red-yellow circles not connected by a line represent pathological samples and the blue circles connected by a line represent healthy samples. The blue squares represent the 2% alginate 9 mg/ml Ca++ and FN 1:10 system and the red squares represent the 3% alginate 9 mg/ml Ca++ and FN 1:10 system.

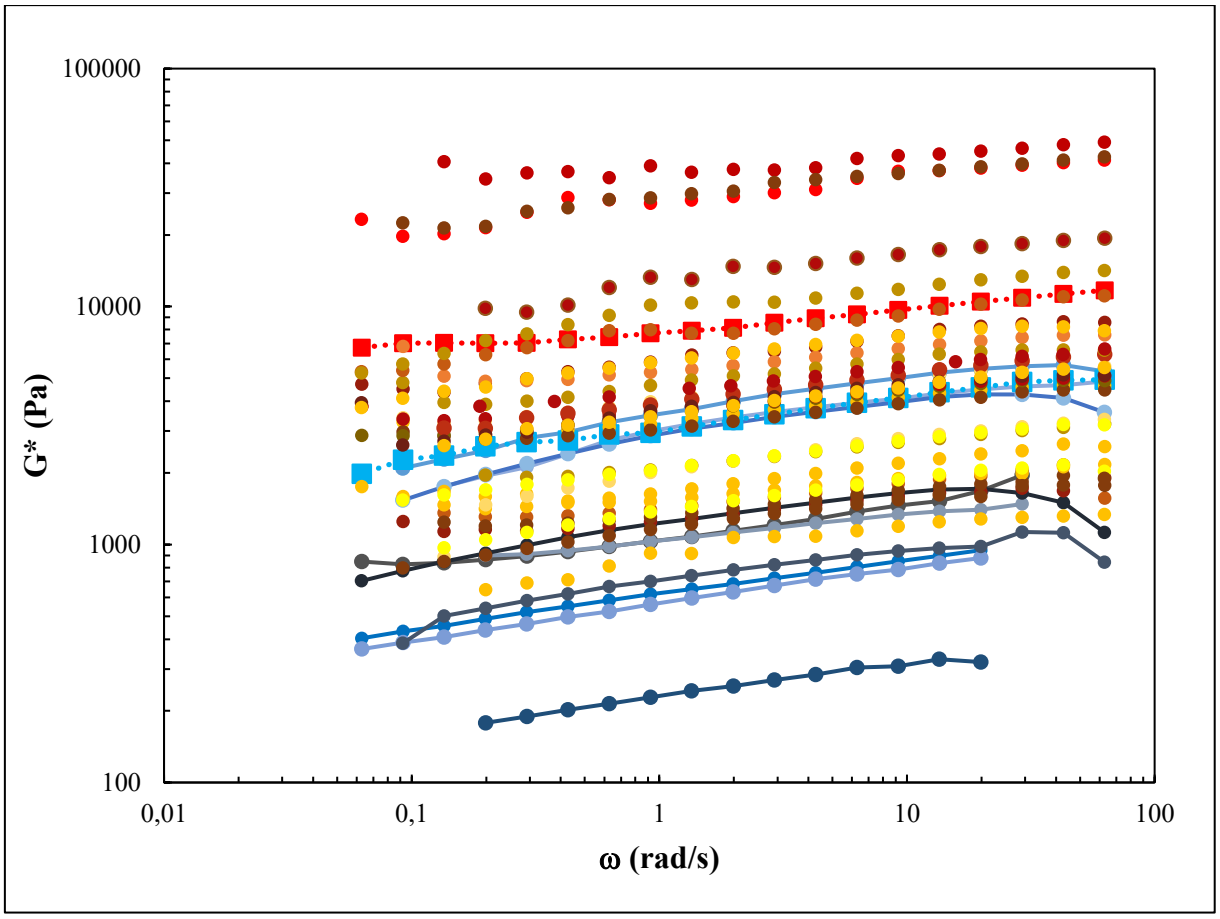


Figure 88: Frequency sweep test performed on selected alginate systems and on the liver samples. The moduli are reported as G* (Pa). The brown-red-yellow circles not connected by a line represent pathological samples and the blue circles connected by a line represent healthy samples. The blue squares represent the 2% alginate 9 mg/ml Ca++ and FN 1:10 system and the red squares represent the 3% alginate 9 mg/ml Ca++ and FN 1:10 system.

### 4.8.2 Effects of alginate *in vitro* models on LX2 cell phenotype (viability assay and morphological analyses)

On the selected alginate systems Alg 2% and Alg 3%, which resemble the normal and fibrotic liver, respectively, it was performed a cell viability assay with LX2 cells for 72 hours (Figure 89). The cells remained viable at least up to 72 hours from seeding in both alginate systems (Alg 2% and Alg 3%). In the Alg 3% gel cells viability was greater compared to those seeded on Alg 2%. This behavior is in line with what occurs *in vivo* where in the fibrotic liver, characterized by increased stiffness (Kostallari et al., 2022), HSCs proliferate faster (Iredale et al., 2013).

Figure 90 shows pictures taken on bright field of LX2 seeded on Alg 2% and Alg 3% at 24 and 48 hours from seeding. In both systems LX2 are in an ideal situation, as they are characterized by their typical elongated shape and have connections with other cells.

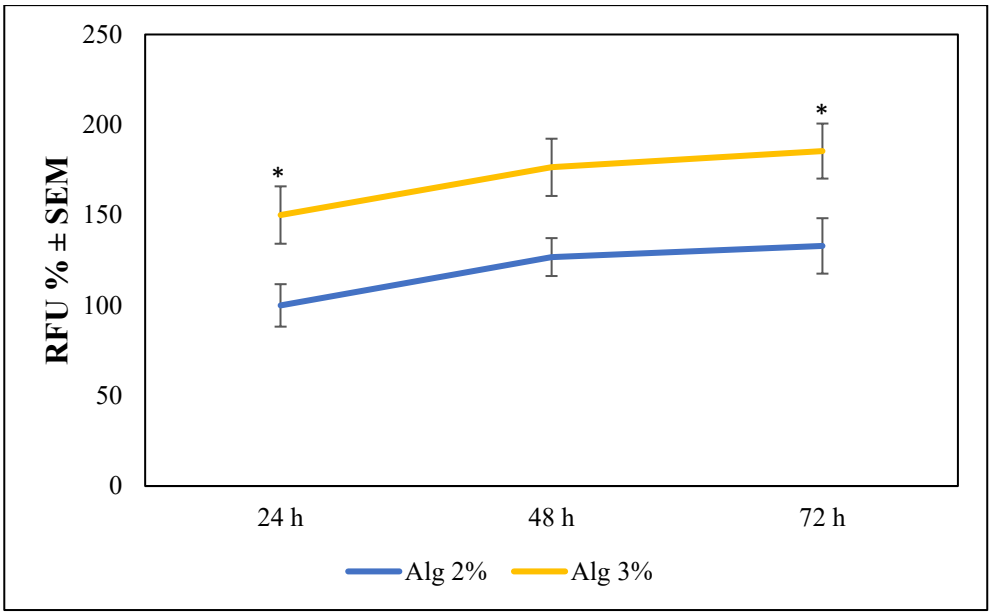


Figure 89: PrestoBlue viability test with LX2 cells ($60*10^3$ cells/well in 24 well-plate) seeded on alginate gels, Alg 2% and Alg 3% (180 µl/well of alginate mixed with fibronectin) (n = 11). The results are expressed as RFU (Relative Fluorescence Units) % ± SEM, where Alg 2% at 24 hours is considered 100%. Statistical significance was determined by comparing cells cultured on Alg 2% versus Alg 3% systems at the same time point (*$p < 0.05$). Depending on data distribution, statistical analyses were performed using either parametric (unpaired t-test) or non-parametric (Mann-Whitney test) tests.

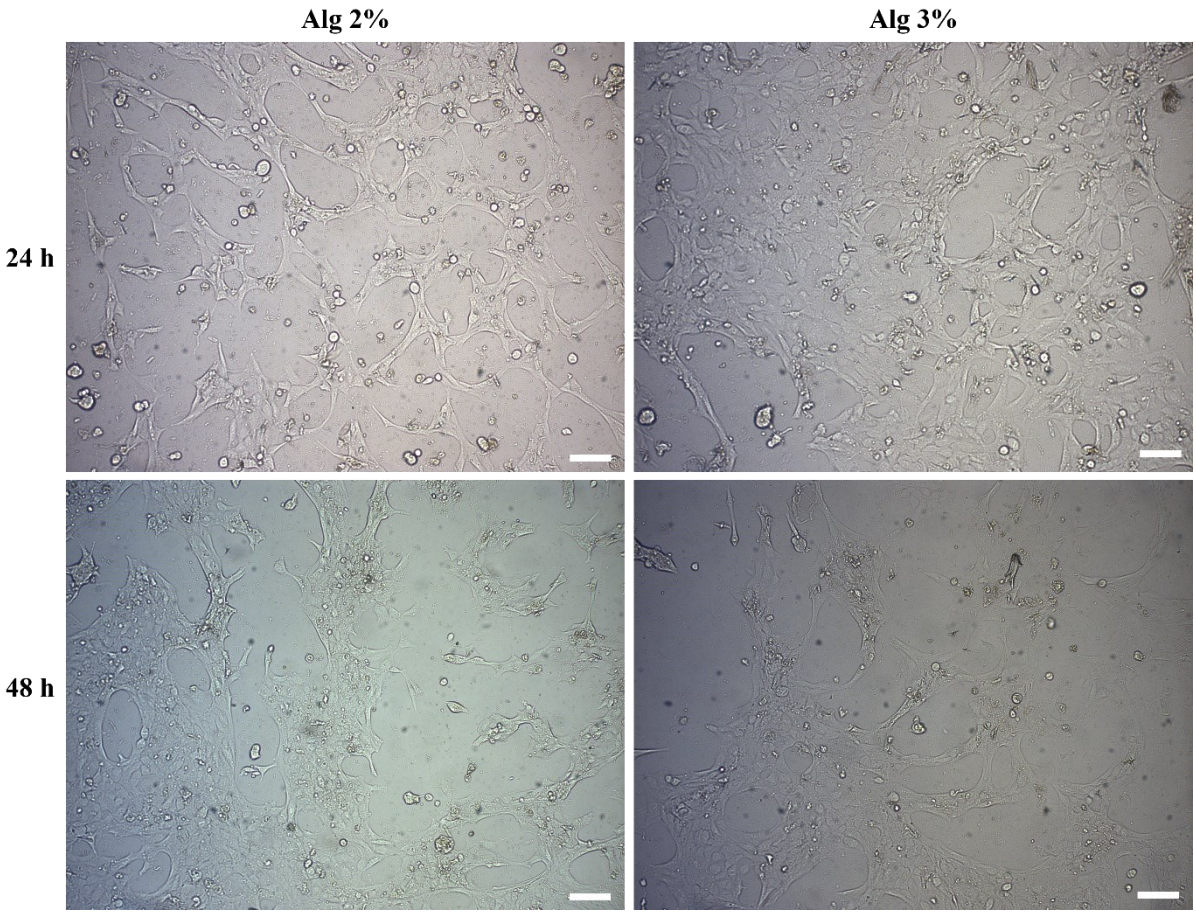


Figure 90: LX2 cells ($120*10^3$ cells/well in 12 well-plate) seeded on alginate gels, Alg 2% and Alg 3%. Bright field pictures taken at 24 and 48 hours from seeding. The scale bar is 100 µm.

The activation of HSCs in fibrotic liver tissue results in a morphological transformation from a star-shaped (more compact and characterized by various cell protrusions) to a myofibroblastic (more elongated) morphology. We therefore studied by microscopic analysis the shape of LX2 cultured on a stiffer surface (Alg 3%) compared to LX2 cultured on a softer surface (Alg 2%). We used two different parameters to study cell morphology: circularity (C) and elongation (AR). The analysis of C and AR (Figure 91) shows a tendency for LX2 cells cultured on Alg 3% to be poorly spherical and more elongated than cells cultured on Alg 2%, suggesting a more activated morphology for cells cultured on the stiffer surface, resembling fibrotic liver.

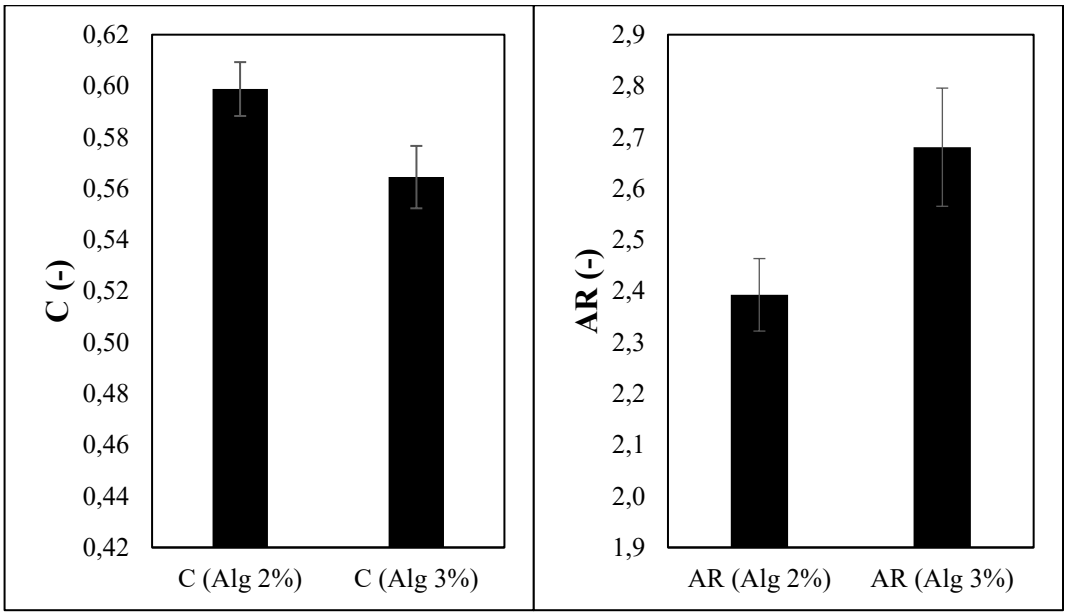


Figure 91: Shape factors C and AR for LX2 cells seeded on Alg 2% and Alg 3% systems. The values are reported as average ± SEM is reported.

### 4.8.3 Molecular effects of alginate *in vitro* models on LX2 (ACTA2 and E2F1 mRNA and protein levels)

To analyze the influence of Alg 2% and Alg 3% on LX2 behavior, RT-qPCR was performed to quantify the expression of ACTA2 and E2F1 mRNA at 24 and 48 hours after seeding on hydrogel substrates. ACTA2 gene encodes for α-SMA (alfa-Smooth Muscle Actin) a typical protein of myofibroblasts. α-SMA, together with collagen I and II, vimentin, fibronectin, are involved in a profibrogenic phenotype of HSCs (Acharya et al., 2021; Le et al., 2023; Olsen et al., 2011). We detected a significant increase in ACTA2 mRNA levels in cells grown on Alg 3% (Figure 92). This indicates that the stiffer gel can mimic the fibrotic

liver stiffness known to promote LX2 cells modification to the myofibroblastic activated phenotype.

E2F1 (E2 promoter binding factor 1) is a transcription factor strongly related to cell proliferation, which promotes the G1/S phase transition (Eletr and Wilkinson, 2011). Moreover, its overexpression has been reported in liver fibrosis (Zhang et al., 2014). We observed a significant increase in its mRNA levels in cells grown on Alg 3% (Figure 93) in line with the phenotype of activated cells (increased proliferation and pro-fibrotic behavior).

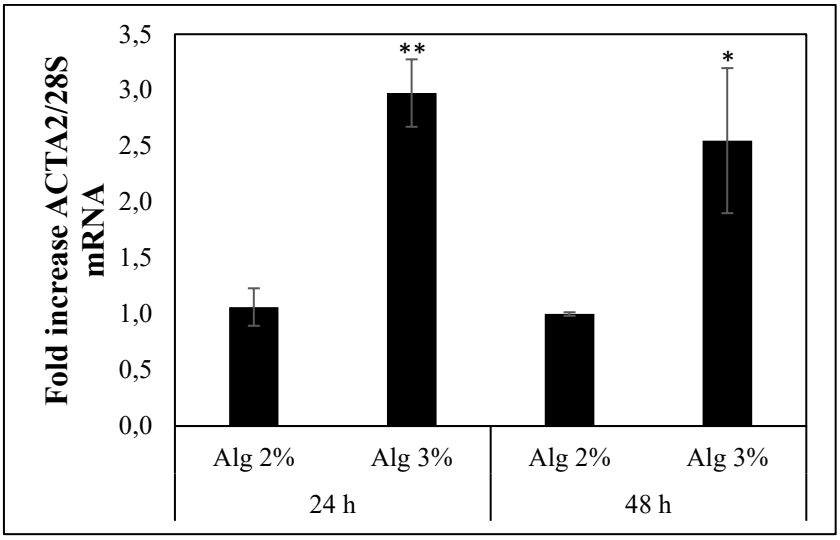


Figure 92: Fold increase (±SEM) mRNA expression of ACTA2 normalized with 28S in LX2 cells grown on Alg 3% compared to Alg 2% (n = 6). Two time points (24 and 48 hours from the seeding) were considered. Statistical significance was determined by comparing Alg 2% versus Alg 3% systems (*p < 0.05, **p < 0.0005, Unpaired t test). LX2 cells were seeded on 12 well-plates (120*$10^3$ cells/well) on alginate gels 2% or 3% m/V with FN 1:10 (300 µl/well).

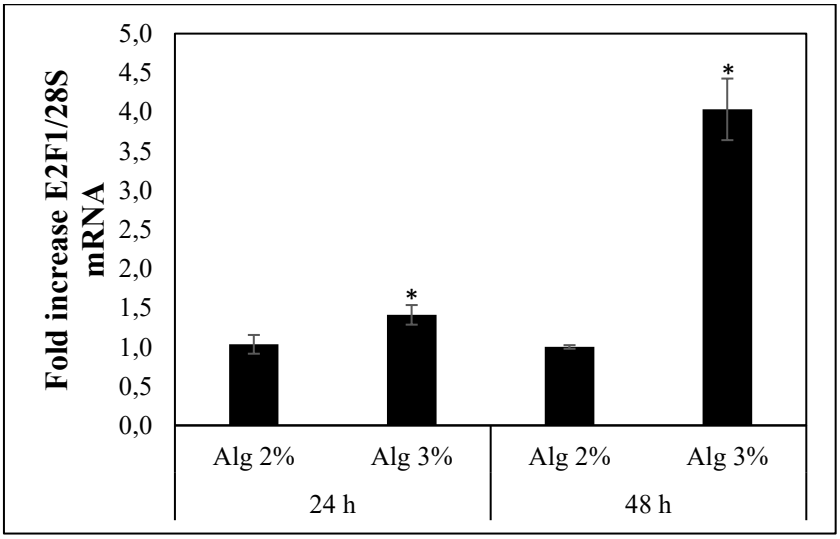


Figure 93: Fold increase (±SEM) mRNA expression of E2F1 normalized with 28S in LX2 cells grown on Alg 3% compared to Alg 2% (n = 6). Two time points (24 and 48 hours from the seeding) were considered. Statistical significance was determined by comparing Alg 2% versus Alg 3% systems (*p < 0.005). Depending on data distribution, statistical analyses were performed using either parametric (unpaired t-test) or non-parametric (Mann-Whitney test) tests. LX2 cells were seeded on 12 well-plates (120*$10^3$ cells/well) on alginate gels 2% or 3% m/V with FN 1:10 (300 µl/well).

To strengthen the data about the mRNA expression levels of α-SMA and E2F1, also the protein levels were evaluated for cells grown on Alg 2% or Alg 3% (Figure 94). For both α-SMA and E2F1, the protein levels show a tendency to increase its levels in LX2 grown on Alg 3% compared to those grown on Alg 2%.

Together, the data reported in Figure 89, Figure 92, Figure 93 and Figure 94 demonstrate that we successfully generated two alginate surfaces whose different viscoelastic properties can mimic the effect of normal and fibrotic liver on LX2 phenotype.

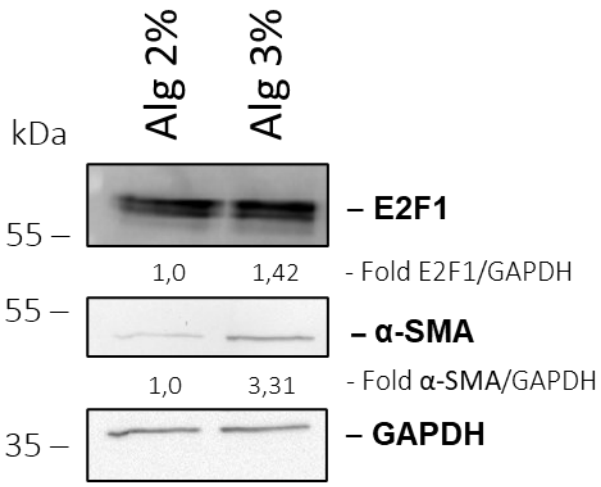


Figure 94: Western Blot with protein bands for α-SMA and E2F1 in LX2 at 24 hours after seeding on Alg 2% or Alg 3%. GAPDH was used as loading control. LX2 cells were seeded on 12 well-plates ($120*10^3$ cells/well) on alginate gels 2% or 3% m/V with FN 1:10 (300 µl/well).

## 4.9 Phenotypic effects of DUBs inhibitors on cells cultured on plastic surfaces

The compound 2C has a deubiquitinase (DUBs) inhibiting activity (Cersosimo et al., 2015). For all the considerations done in paragraph 1.6, 2C and its more soluble derivative DUDC3 deserve an evaluation as antifibrotic agents. 2C and DUDC3 were kindly provide us from the Prof. Fabio Benedetti's group (Prof. Fulvia Felluga and Prof. Sara Drioli in the Department of Pharmaceutical and Chemical Sciences of the University of Trieste). We first tested these compounds on cells seeded on plastic, the simplest and most common model for cultivating cell lines.

### 4.9.1 LX2 uptake test with fluorescent compound (2C-Fl)

To assess the uptake of the 2C compound by LX2 cells, we utilized a fluorescein-labeled variant (2C-Fl) at a concentration of 2 µM (optimal concentration which did not affect visually cell phenotype and could stain most of the cells). Uptake was evaluated at various time points: prior to compound administration, and at 2-, 4-, and 24-hours post-administration (see Figure 95). DAPI staining was employed to visualize the cell nuclei. Starting from the 2-hour time point, the green fluorescent signal becomes localized within the cell cytoplasm and nuclei, indicating an efficient cell uptake.

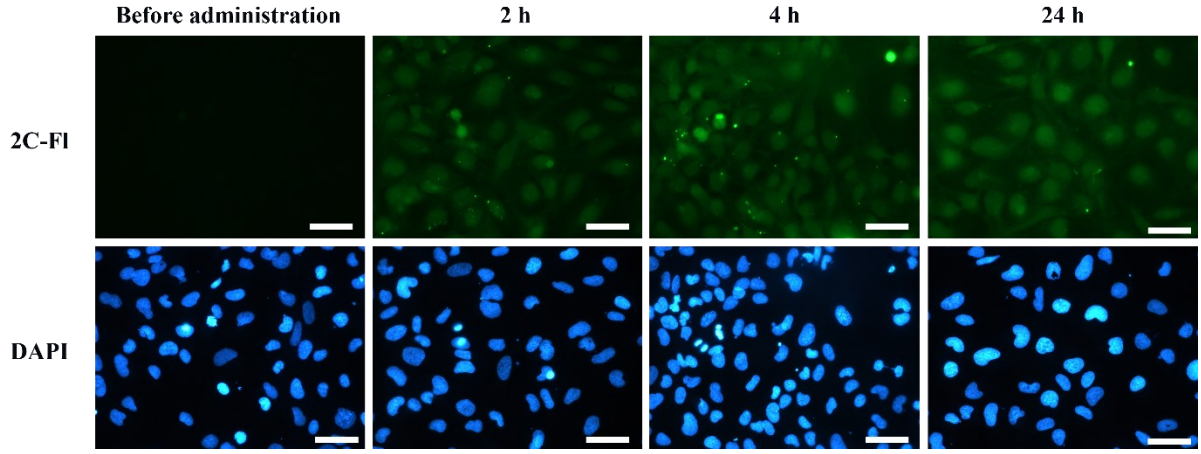


Figure 95: LX2 cells were utilized for the uptake assay. The upper panels illustrate the uptake of the 2C-Fl compound at a concentration of 2 µM at different time points, while the lower panels depict the cell nuclei stained with DAPI. The scale bar indicates 50 µm.

### 4.9.2 DUBs inhibitors effects on cell viability

Cell viability was evaluated over a 72-hour period following initial treatment with varying concentrations of 2C, DUDC3 or VV1 (0.5, 1, 2, 4, 10 µM). VV1 is a compound without DUBs inhibiting activity, which was used as a control compound. Three distinct cell lines were utilized: WS1, LX2, and CFSC (Figure 96, Figure 97 and Figure 98). LX2 and CFSC were chosen as a model for HSCs cells, the main the main cellular players in liver fibrosis. In fact, LX2 are a human HSCs cell line and CFSC are a spontaneously immortalized HSCs cell line derived from adult male cirrhotic rat livers induced by carbon tetrachloride. Instead, WS1 are a human fibroblast cell line, that was chosen because it mimics the phenotype of HSCs when they transdifferentiate into myofibroblasts. The No Treatment (NT) condition was designated as 100% absorbance corresponding to 100% viability. Across all cell types, VV1 did not significantly impact viability. In contrast, both 2C and DUDC3 exhibited a concentration-dependent reduction in cell viability. Notably, CFSC cells demonstrated greater resistance to these treatments compared to LX2 and WS1 and only the highest concentrations

of 2C and DUDC3 significantly affected cell viability. CFSC have different resistance to DUBs inhibitors, probably because these cells from a different species.

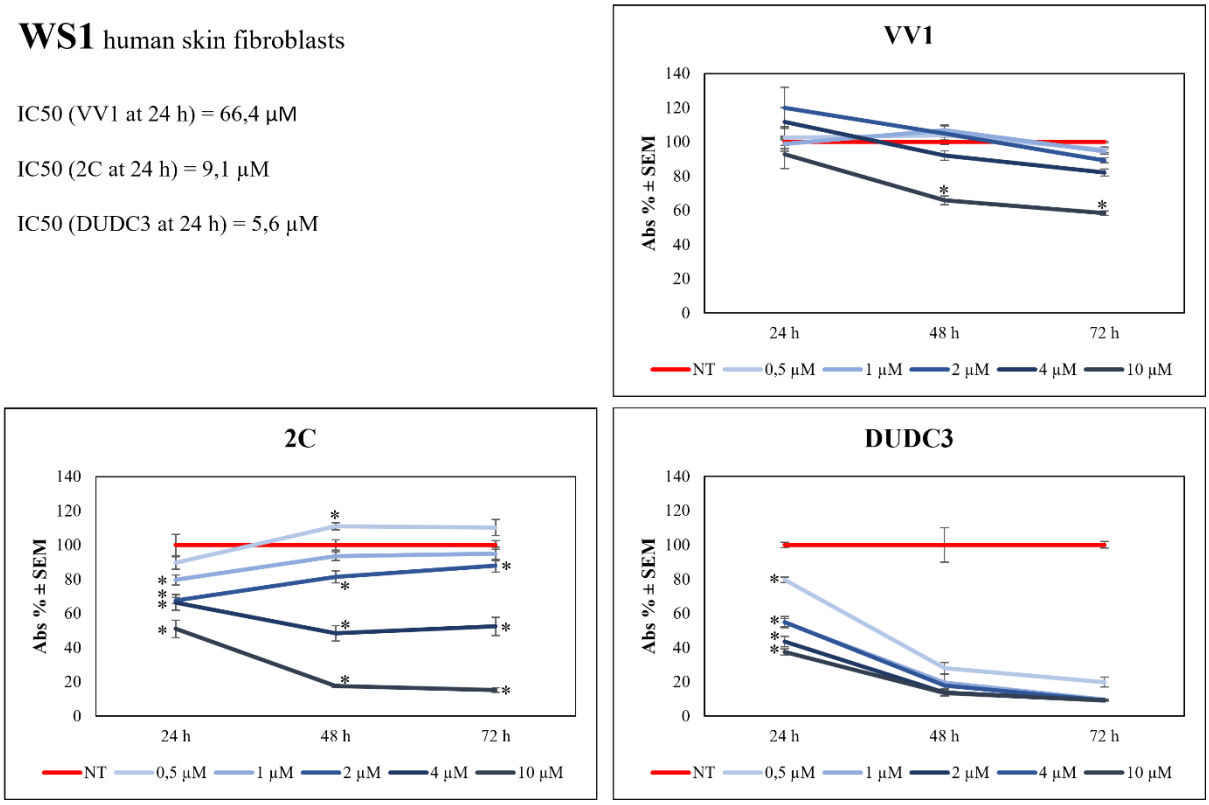


Figure 96: MTT test with WS1 cells, over a 72-hour period following initial treatment with varying concentrations (0.5, 1, 2, 4, 10 µM) of VV1, 2C or DUDC3 (n = 15). The results are reported as Absorbance % ± SEM, where NT condition (red line) is considered 100%. Statistical significance was determined by comparing NT condition vs treatment conditions (*$p < 0.05$). Depending on data distribution, statistical analyses were performed using either parametric (unpaired t-test) or non-parametric (Mann-Whitney test) tests.

**LX2** human hepatic stellate cells

IC50 (VV1 at 24 h) = n.d.

IC50 (2C at 24 h) = 9,1 µm

IC50 (DUDC3 at 24 h) = 3,2 µM

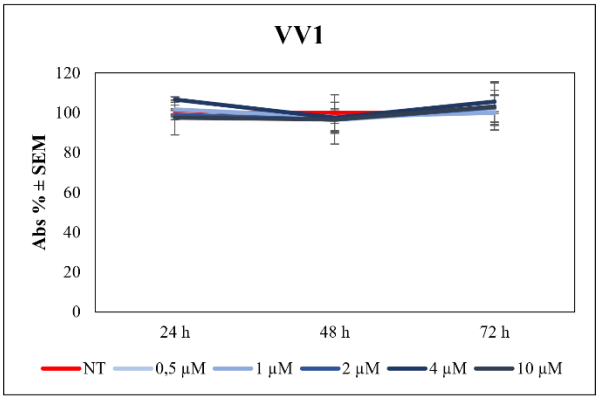


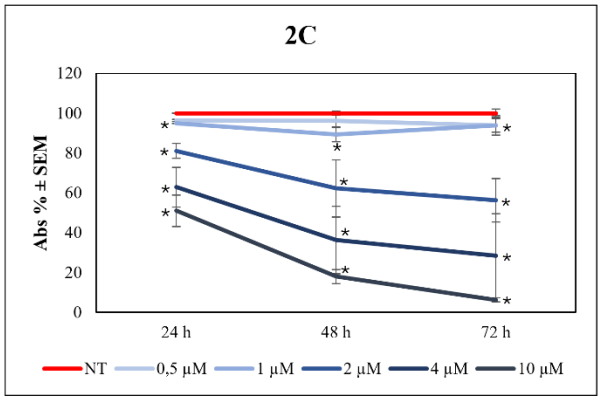


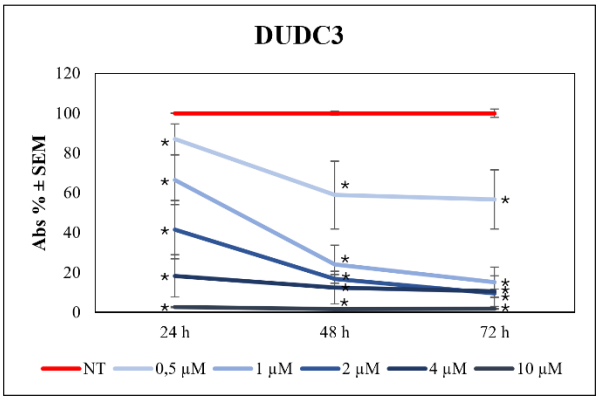


Figure 97: MTT test with LX2 cells, over a 72-hour period following initial treatment with varying concentrations (0.5, 1, 2, 4, 10 µM) of VV1, 2C or DUDC3 (n = 15). The results are reported as Absorbance % ± SEM, where NT condition (red line) is considered 100%. Statistical significance was determined by comparing NT condition vs treatment conditions (*$p < 0.05$). Depending on data distribution, statistical analyses were performed using either parametric (unpaired t-test) or non-parametric (Mann-Whitney test) tests.

**CFSC** (rat hepatic stellate cells)

IC50 (VV1 at 24 h) = n.d.

IC50 (2C at 24 h) = 28,6 µM

IC50 (DUDC3 at 24 h) = 6,8 µM

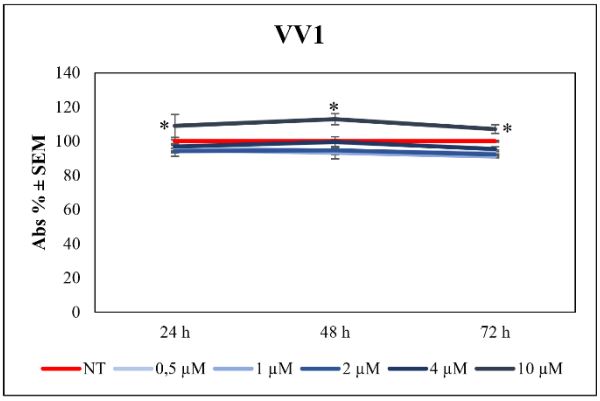


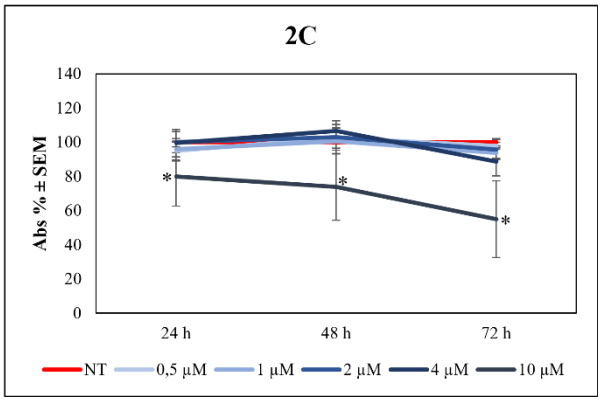


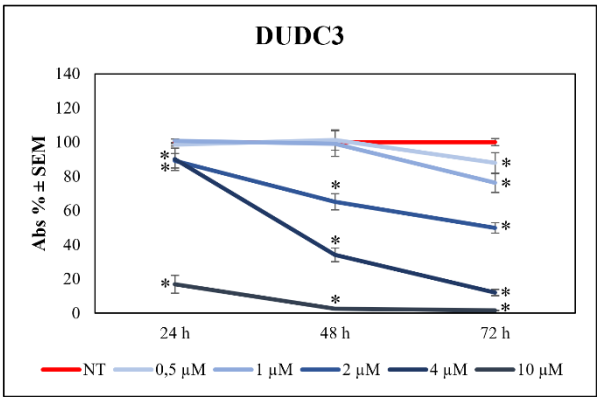


Figure 98: MTT test with CFSC cells, over a 72-hour period following initial treatment with varying concentrations (0.5, 1, 2, 4, 10 µM) of VV1, 2C or DUDC3 (n = 15). The results are reported as Absorbance % ± SEM, where NT condition (red line) is considered 100%. Statistical significance was determined by comparing NT condition vs treatment conditions (*p < 0.05). Depending on data distribution, statistical analyses were performed using either parametric (unpaired t-test) or non-parametric (Mann-Whitney test) tests.

### 4.9.3 Effect of DUBs inhibitors on cell apoptosis

To further explore the phenotypic effects of 2C and DUDC3 on LX2, cell apoptosis was studied (Figure 99). Control treated cells (VV1) showed no significant differences compared to NT cells. 2C compound at 1 µM concentration showed a statistically significant increase in apoptosis induction compared to the NT condition. At higher concentrations, 2C did not elicit significant increase in cell apoptosis. DUDC3, did not show any significant induction of apoptosis at all the concentrations tested.

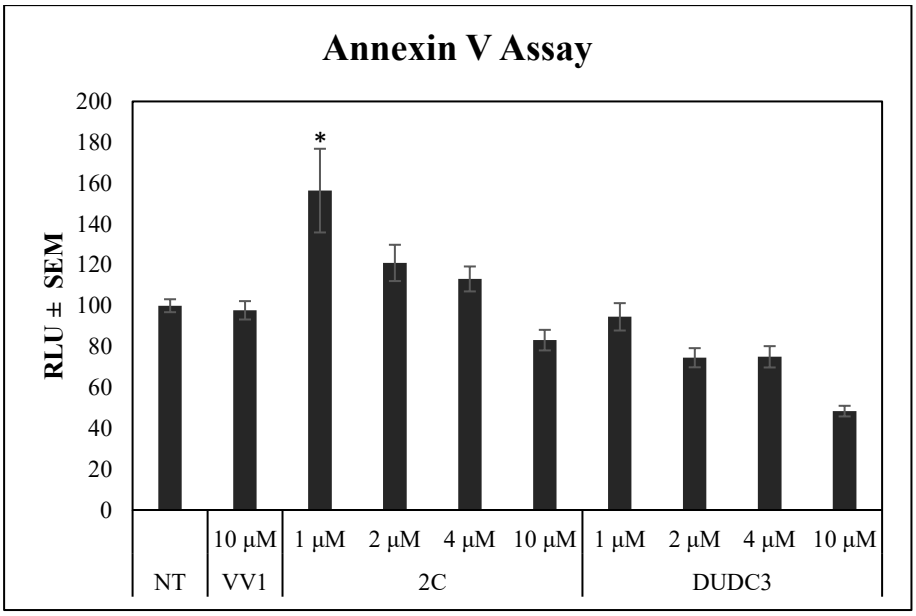


Figure 99: Annexin V Apoptosis assay on LX2 cells 24 hours post-treatment with VV1, 2C or DUDC3 at different concentrations. LX2 cells were seeded in 96 well-plates ($5*10^3$ cells/well), 24 hours after seeding cells were treated and added with the detection reagent of the kit used to perform the Annexin V assay. 24 hours after treatment luminescence of samples was measured. The results are reported as Relative Luminescence Units (RLU) ± SEM, where NT condition is considered 100%. Statistical significance was determined by comparing NT versus treatment conditions (*$p < 0.05$, unpaired t-test).

### 4.9.4 Effect of DUBs inhibitors on cell necrosis

To evaluate the cytotoxicity of DUBs inhibitors treatments on LX2, the LDH test was performed (Figure 100). The results are reported ad Cytotoxicity % (calculated as reported in paragraph 3.22), where Triton treatment is the positive control set at 100% cytotoxicity induction. From the concentration of 2µM, 2C significantly induced cytotoxicity; even more effective was DUDC3, which induced cytotoxicity already at 1µM and displayed cytotoxicity induction more evident than 2C at all the concentrations tested.

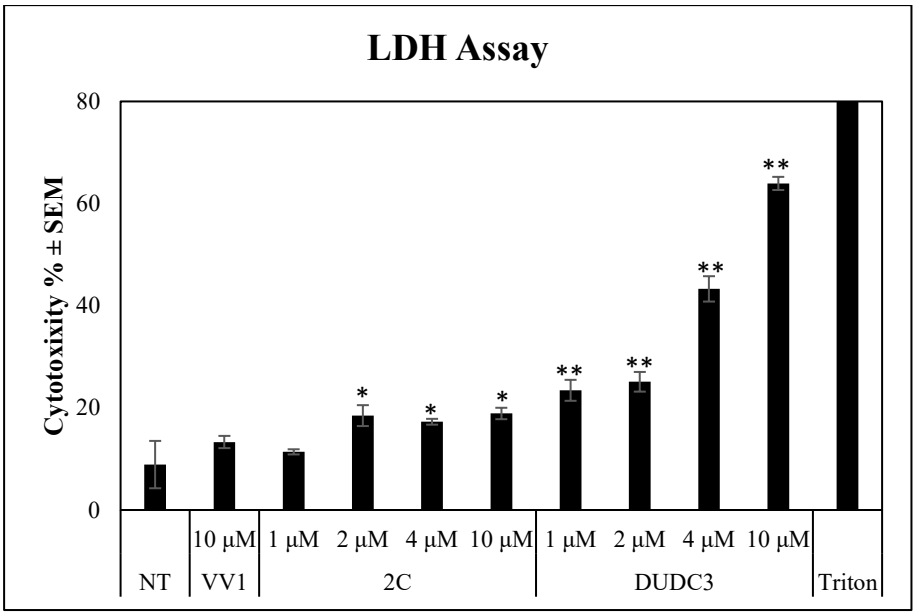


Figure 100: LDH Cytotoxic assay on LX2 cells 24 hours post-treatment with VV1, 2C or DUDC3 at different concentrations. The results are reported as Cytotoxicity % ± SEM, where the positive control (Triton) is considered 100%. Statistical significance was determined by comparing NT versus treatment conditions (*$p < 0.05$, **$p < 0.0005$, unpaired t-test).

### 4.9.5 Effect of DUBs inhibitors on cell autophagy

Autophagy is a process by which cytoplasmic components are delivered into the lysosome for degradation (Levy et al., 2017). Notably, autophagy has been proposed as an alternative mechanism ruling cell death. The induction of cell autophagy was monitored in LX2 cells after DUBs inhibitors treatments, evaluating the protein levels of the two forms of the autophagy marker LC3, i.e. LC3 I (cytosolic form of LC3) and LC3 II (phosphatidylethanolamine (PE) LC3 conjugate form recruited from autophagosomal membranes). LC3 I undergo post-translational modification with PE conjugation during autophagy (Tanida et al., 2008). Our data indicate that the treatments with 2C and DUDC3 at the concentration of 2 µM result in the activation of autophagy, as the LC3B II conjugated form appears in the blot more evidently than in NT and VV1 treated cells (Figure 101).

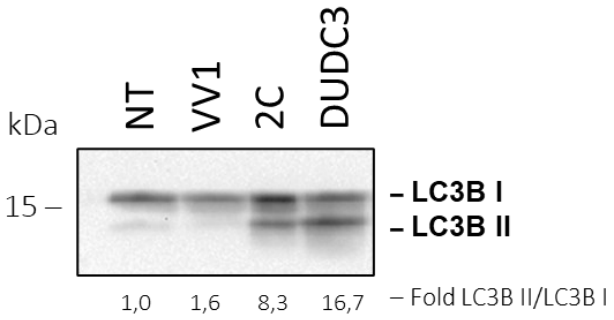


Figure 101: Western Blot protein levels of LC3B I and LC3B II in LX2 cells 24 hours post-treatment with 2 µM of 2C, DUDC3, or VV1, compared to the control NT. The quantification refers to the fold increase of LC3B II form divided by LC3B I form.

Moreover, we evaluated the autophagic flux in LX2 cells treated with DUBs inhibitors (Figure 102). 2C at the highest concentration tested (10 µM) and DUDC3 at all the concentrations present a significantly increased luminescence signal than the NT cells, indicating that these compounds are able to decrease the autophagic flux. Thus, the protein levels of LC3B II indicate an initial activation of the autophagic process by 2C and DUDC3, but the kit results show an inhibition of autophagic flux by DUDC3 and 2C only at high concentrations, suggesting that these compounds might be late inhibitors of the autophagic flux.

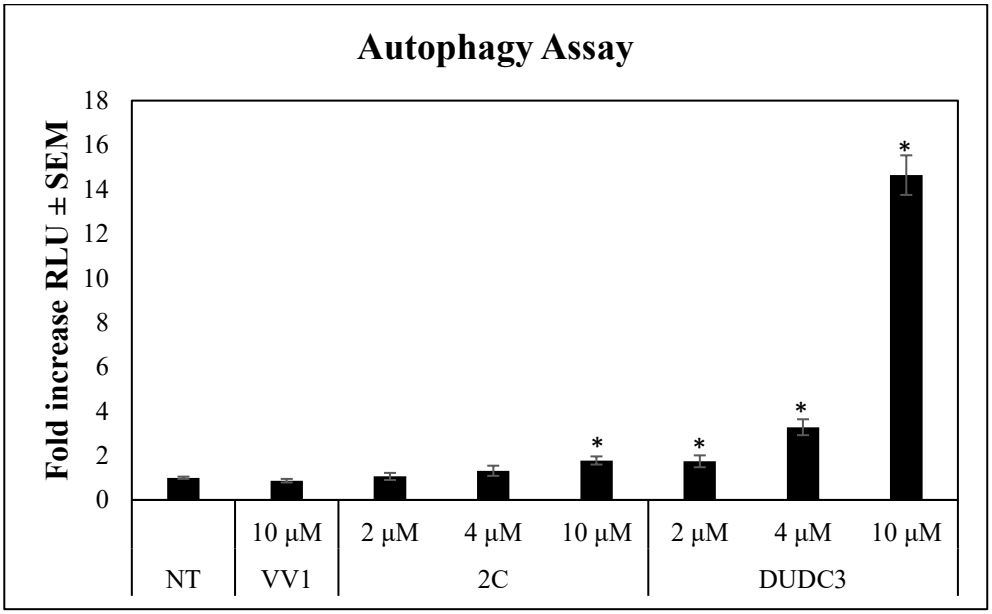


Figure 102: Autophagy LC3 HiBiT Reporter Assay on LX2 cells 24 hours post-treatment with VV1, 2C or DUDC3 at different concentrations. The results are reported as Fold increase of Relative Luminescence Units (RLU) ± SEM, where NT condition is considered the control. An increased luminescence reflects a decreased autophagic flux. Statistical significance was determined by comparing NT versus treatment conditions (*$p < 0.05$, unpaired t-test).

## 4.10 Molecular effects of DUBs inhibitors on cells cultured on plastic surfaces

### 4.10.1 mRNA levels of ACTA2 and E2F1 in LX2 treated with DUBs inhibitors

As pointed out before, the most relevant fibrotic marker in HSCs is α-SMA (Khomich et al., 2019). We observed a strong reduction in ACTA2 expression (gene encoding for α-SMA protein) in LX2 cells 24 and 48 hours following 2C and DUDC3 treatments (Figure 103). Given that α-SMA is necessary for the contraction and motility of transdifferentiated myofibroblasts, this result is of extreme relevance and support the concept of the anti-fibrotic effect of 2C and DUDC3.

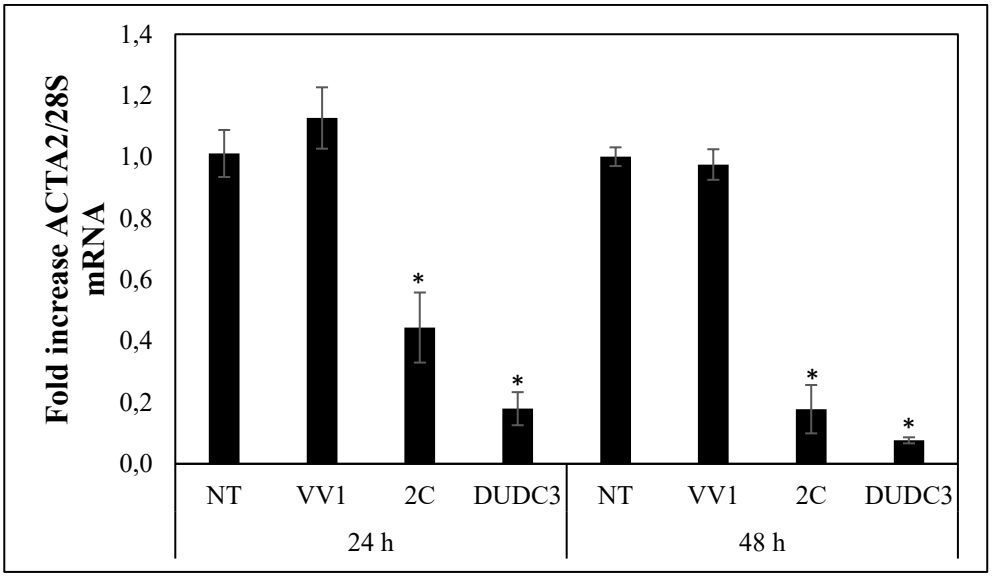


Figure 103: Fold increase (± SEM) mRNA expression of ACTA2 normalized with 28S in LX2 cells treated with 2 μM of VV1, 2C, or DUDC3, compared to not treated (NT) cells (n = 6). Two time points (24 and 48 hours after treatments) were considered. Statistical significance was determined by comparing treatments versus NT condition (*$p < 0.05$, Mann-Whitney test).

Another gene implicated to liver fibrosis is the E2F1 transcription factor, also strongly related to cell proliferation (Eletr and Wilkinson, 2011; Zhang et al., 2014). 24 hours after treatment, E2F1 mRNA levels were significantly reduced in DUDC3-treated LX2 compared to VV1-treated cells and NT. At 48 hours both in 2C- and DUDC3-treated cells, E2F1 expression was significantly reduced (Figure 104). In line with the viability data (Figure 97), DUDC3 appeared to be more potent than 2C.

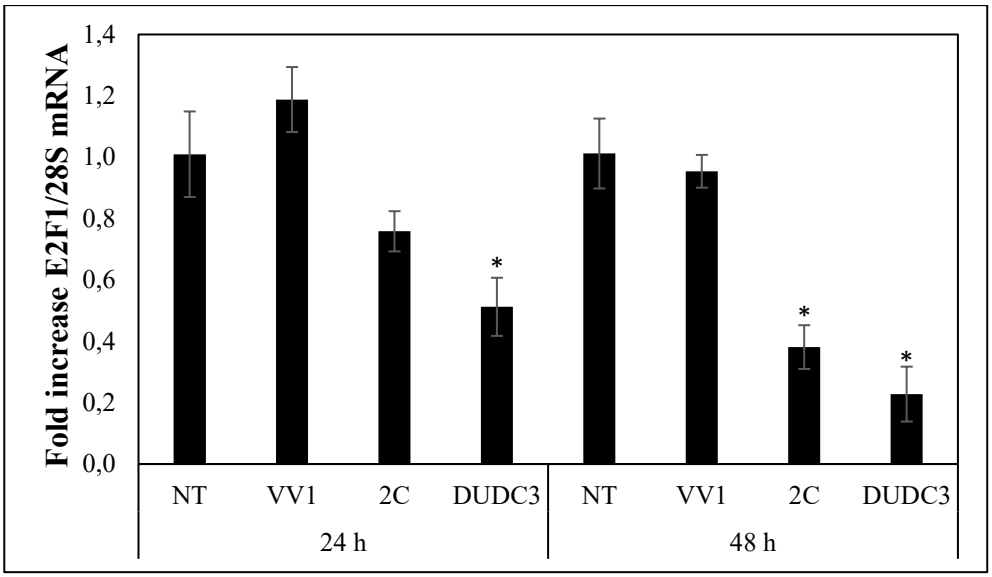


Figure 104: Fold increase (± SEM) mRNA expression of E2F1 normalized with 28S in LX2 cells treated with 2 μM of VV1, 2C, or DUDC3, compared to not treated (NT) cells (n = 6). Two time points (24 and 48 hours after treatments) were considered. Statistical significance was determined by comparing treatments versus NT condition (*p < 0.05, Mann-Whitney test).

### 4.10.2 Protein levels of other fibrotic markers in LX2 treated with DUBs inhibitors

Given the relevance of fibronectin, collagen I and α-SMA as marker in the genesis and progression of liver fibrosis (Acharya et al., 2021; Le et al., 2023; Olsen et al., 2011), the protein levels of these markers were analyzed (Figure 105). Regarding fibronectin and collagen I, we detected a clear reduction of their protein levels in LX2 cells treated with 4 μM 2C and 1 μM DUDC3 compared to NT cells.

For what concerns α-SMA, we observed a significant reduction in its protein levels after the treatment with 2C (1, 2 or 4 μM) or DUDC3 (0,2 or 1 μM) compared to NT and VV1-treated cells (Figure 106), in line with the mRNA results (Figure 103).

2C and its derivative DUDC3 can inhibit several cysteine-dependent deubiquitinating enzymes. Thus, they interfere with protein degradation by the ubiquitin-proteasome system, causing accumulation of polyubiquitinated proteins, proteotoxic stress and apoptosis (Cersosimo et al., 2015). The accumulation of polyubiquitinated proteins induced by 2C (4 μM) and DUDC3 (1 μM) is clearly visible from the bands reported in Figure 105. This proves the expected mechanism of action of our DUBs inhibitors in the cellular model considered.

PARP (poly ADP-ribose polymerase) enzyme plays a crucial role in many processes, including DNA repair and cell death (Soldani and Scovassi, 2002). Moreover, the cleavage of PARP indicates the activation of the mitochondrial apoptotic pathway (Deng et al., 2018). At the concentrations of 2/4 μM of 2C and 1 μM of DUDC3, we detected the formation of the cleaved PARP, indicating the activation of apoptosis. Notably, with regard to 2C, these results

confirm those obtained evaluating apoptosis via the measurement of Annexin V assay (Figure 99). For DUDC3, this accordance does not occur as Annexin V test did not show significant apoptosis. Further testing is necessary to clarify this aspect.

Beside the dose-response effect on protein levels just displayed, we evaluated also a time response effect with other two markers, i.e. E2F1 and vimentin (Figure 107). Vimentin is another marker of liver fibrosis (Le et al., 2023) and surprisingly it did not decreased its protein values after DUBs treatments (Figure 108). In contrast, for E2F1 we observe a significant reduction in its protein levels 48 hours after the treatment with 2C and DUDC3 compared to NT and VV1 (Figure 109). Moreover, as seen for the mRNA levels (Figure 104), DUDC3 was more efficient in reducing the protein level of E2F1 both 24 and 48 hours following compound treatment. At 24 hours, we only noticed a tendency towards a decrease with 2C treatment.

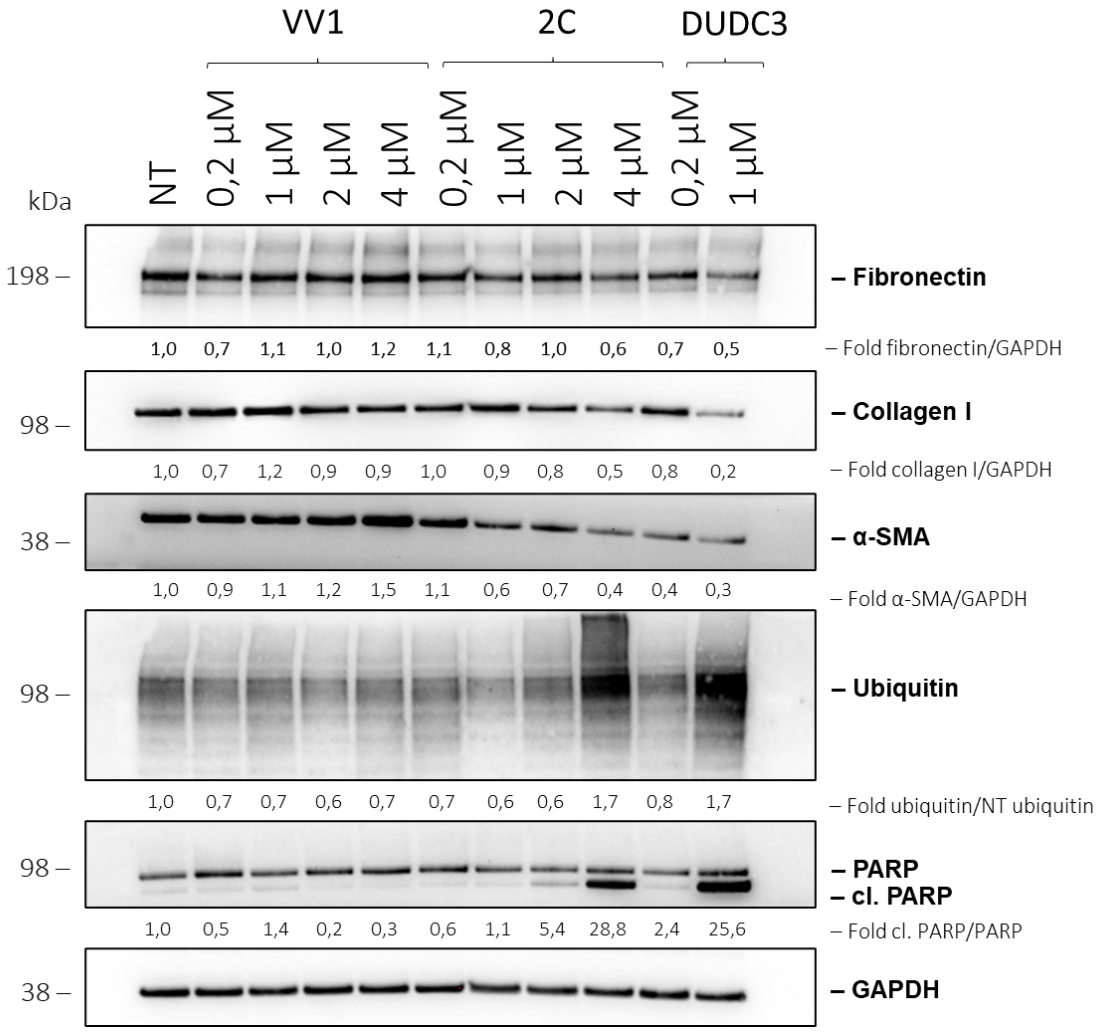


Figure 105: Western Blot protein levels of fibronectin, collagen I, α-SMA, ubiquitin, PARP, cl. PARP in LX2 cells 24 hours post-treatment with VV1 (0,2-1-2-4 µM), 2C (0,2-1-2-4 µM), or DUDC3 (0,2-1 µM), compared to the control NT. GAPDH was used as loading control.

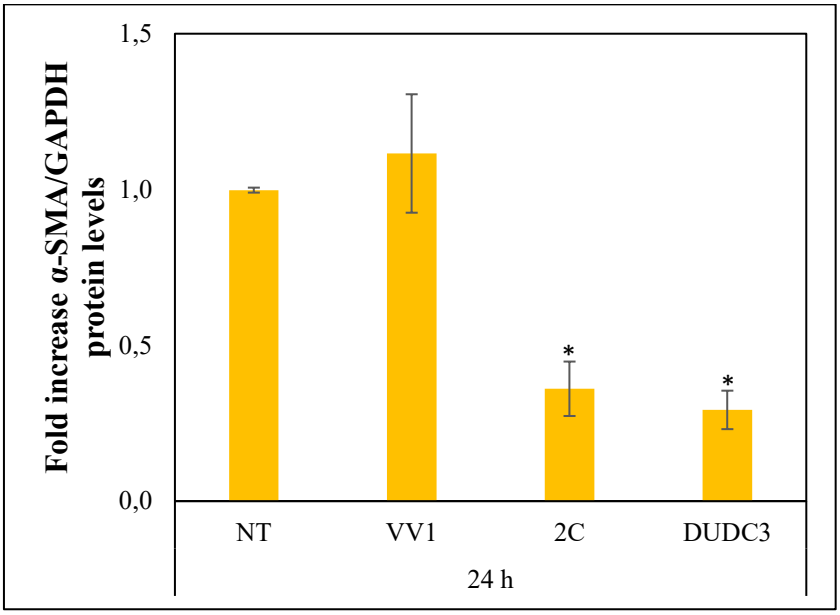


Figure 106: Fold increase (± SEM) of α-SMA/GAPDH protein levels in LX2 cells at 24 hours after treatment with 2 µM of VV1, 2C, or DUDC3, compared to not treated cells (NT) (n = 3). Statistical significance was determined by comparing treatments versus NT condition (*p < 0.05, Mann-Whitney test).

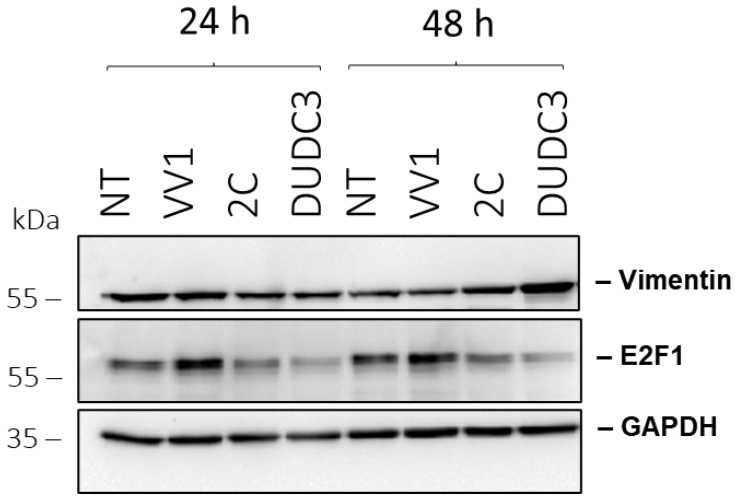


Figure 107: Western Blot protein levels of vimentin and E2F1 in LX2 cells at 24 and 48 hours post-treatment with 2 µM of VV1, 2C, or DUDC3, compared to the control NT. GAPDH was used as loading control.

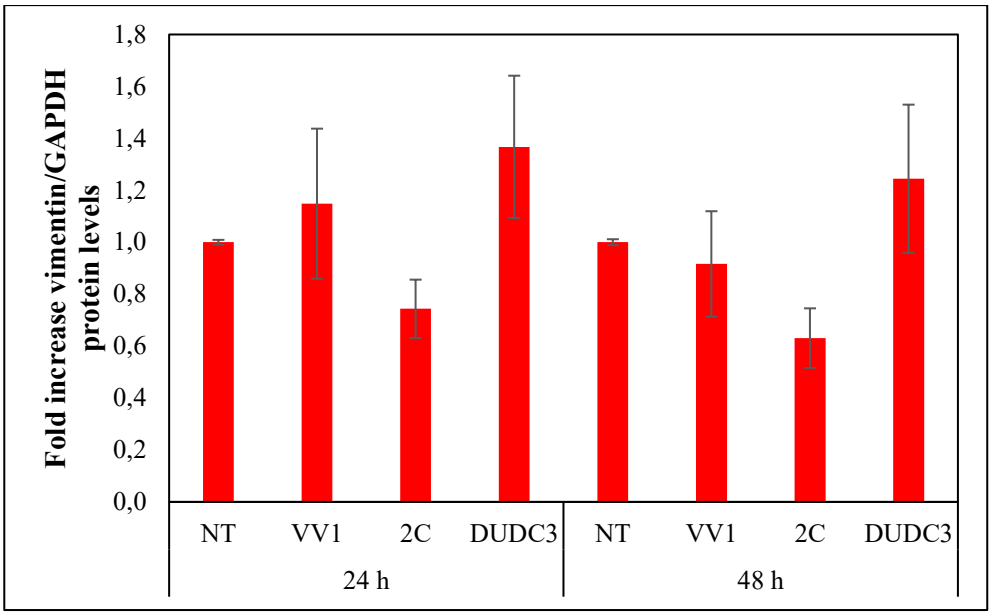


Figure 108: Fold increase (± SEM) of vimentin/GAPDH protein levels in LX2 cells at 24 and 48 hours post-treatment with 2 µM of VV1, 2C, or DUDC3, compared to not treated cells (NT) (n = 3).

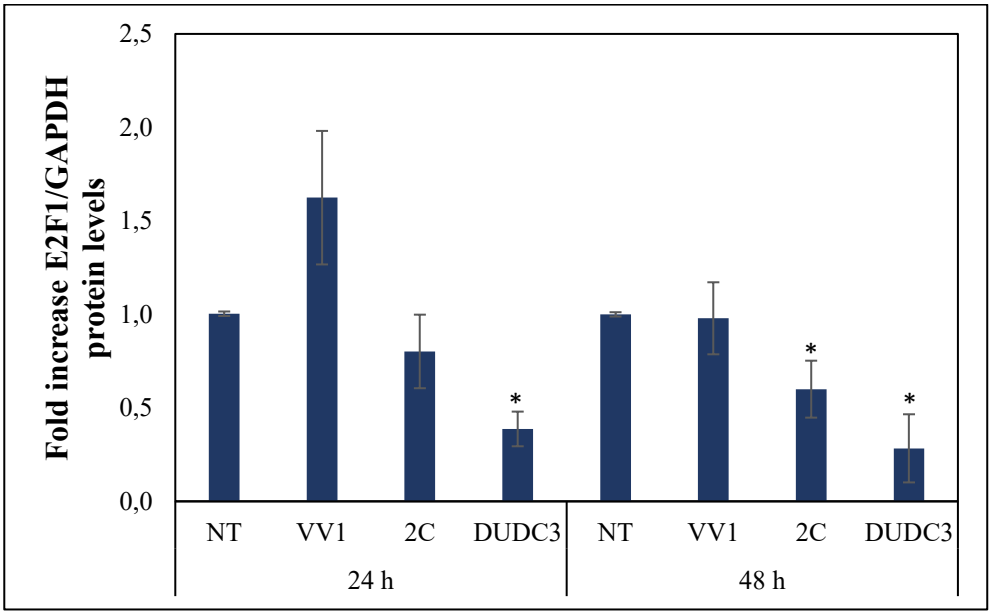


Figure 109: Fold increase (± SEM) of E2F1/GAPDH protein levels in LX2 cells at 24 and 48 hours post-treatment with 2 µM of VV1, 2C, or DUDC3, compared to not treated cells (NT) (n = 3). Statistical significance was determined by comparing treatments versus NT condition (*$p < 0.05$, Mann-Whitney test).

### 4.10.3 Immunofluorescence in LX2 cells treated with 2C

β-tubulin, vimentin, fibronectin and collagen I, all involved in the fibrosis, were investigated by immunofluorescence to study possible alteration of their intracellular organization/localization (Figure 110 and Figure 111). Compared to untreated and VV1-treated cells, 2C treated cells show a different distribution of these cytoskeleton components/fibrosis markers, resulting in a morphological change in the cells. In particular,

fibronectin and vimentin have a predominantly cytoplasmic distribution in NT and VV1-treated cells, while in the 2C-treated cells they are predominantly close to the nucleus. While the meaning of this observation deserves further investigations, it is important to note the subverted cytoskeleton organization induced by the DUBs inhibitors. Moreover, while WB data do not show significant variation in the levels of vimentin (Figure 105 and Figure 108), the immunofluorescence data suggest that the effect may be an alteration in its cellular distribution.

On the other hand, β-tubulin apparently suggests a change in the dimension of the LX2, while collagen I has no major visible effects.

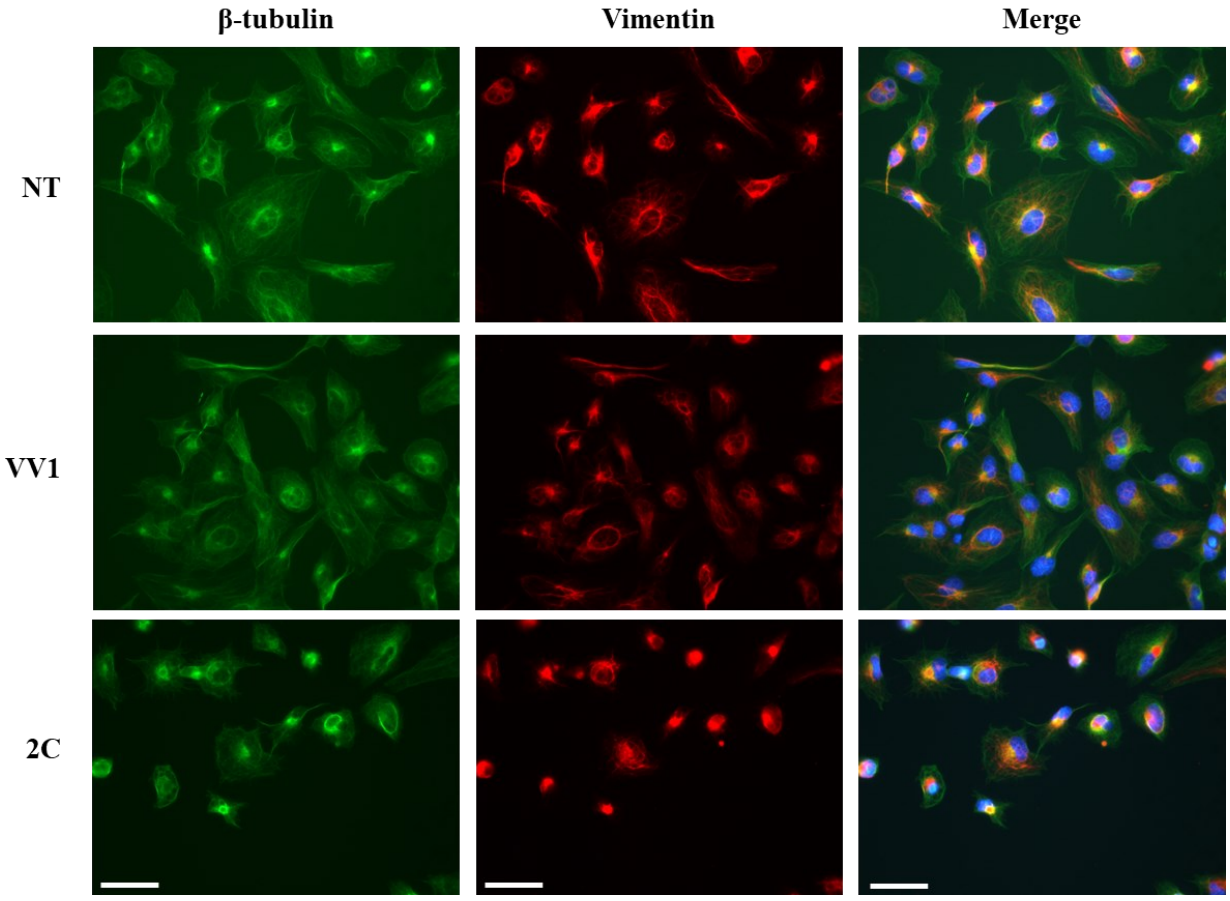


Figure 110: Immunofluorescence test with β-tubulin (green), vimentin (red) and DAPI (blue) staining in LX2 cells treated from 24 hours with 2 μM VV1 or 2C compounds or in not treated (NT) cells. The scale bar is 50 μm. The pictures in the right column represent the merge of β-tubulin, vimentin and DAPI channels.

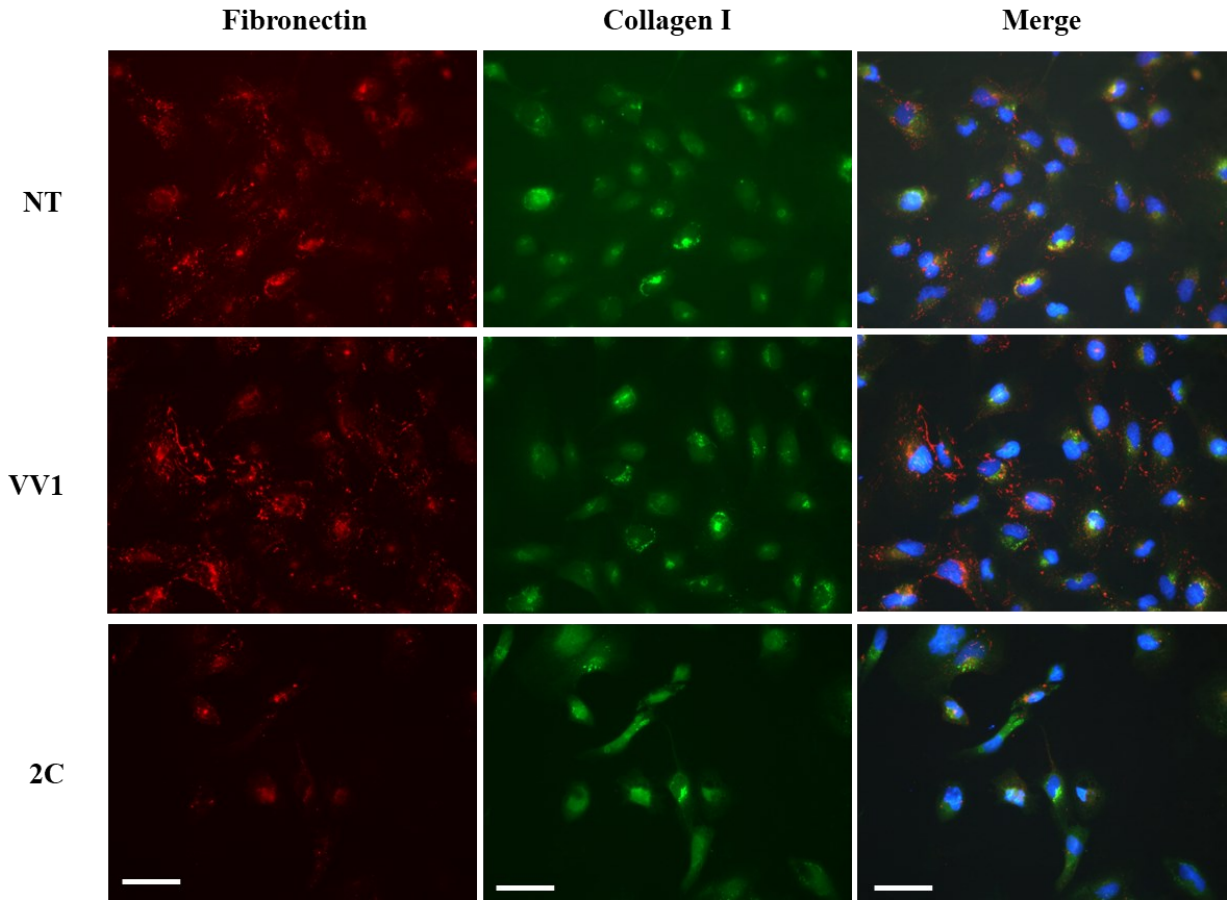


Figure 111: Immunofluorescence test with collagen I (green), fibronectin (red) and DAPI (blue) staining in LX2 cells treated from 24 hours with 2 µM VV1 or 2C compounds or in not treated (NT) cells. The scale bar is 50 µm. The pictures in the right column represent the merge of collagen I, fibronectin and DAPI channels.

## 4.11 Phenotypic effects of DUBs inhibitors on LX2 cells cultured in 3D spheroids

Traditional 2D cell cultures have different advantages (e.g. simplicity of realization, cheapness), but fall in replicating the complex *in vivo* environment of liver tissue. On the other hand, 3D cell cultures, such as spheroids, provide a more accurate representation of the liver's microenvironment, because they allow for better simulation of cell-cell interaction and cell-matrix interactions, which are crucial for studying the progression of liver fibrosis. The 3D models enhance the predictive power of drug testing. For these reasons, we realized with LX2 cells 3D spheroids in collagen I.

3D spheroids were treated with DUBs inhibitors 2C and DUDC3 and the control compound VV1 after 24 hours from the seeding. As reported in Figure 112, VV1 compound affects viability of LX2 cells in 3D-culture systems only at the highest concentration tested (40 µM), while 2C and DUDC3 compounds significantly affect the viability at all the

concentrations tested. Moreover, 2C and DUDC3 show a dose-response effect. In Table 23 the IC50 values calculated from this text are reported.

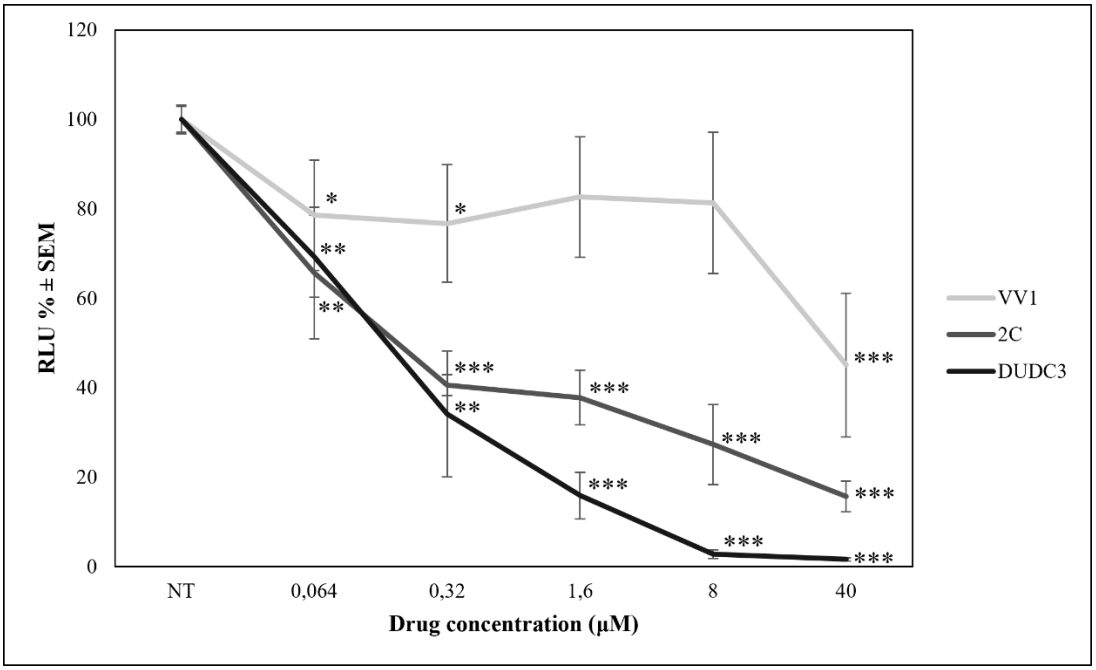


Figure 112: Viability assay (CellTiter test) conducted on LX2 3D spheroids 96 hours post-treatment with DUBs inhibitors (n = 9). 3D spheroids contained 2.0 * $10^3$ LX2 cells in collagen I (2 mg/ml). The results are reported as Relative Luminescence Units (RLU) ± SEM, where NT condition is considered 100%. Statistical significance was determined by comparing NT with treatment conditions: *p < 0.01, **p < 0.001, and ***p < 0.0001. Depending on data distribution, statistical analyses were performed using either parametric (unpaired t-test) or non-parametric (Mann-Whitney test) methods.

Table 23: IC50 for VV1, 2C and DUDC3 calculated from a CellTiter test conducted with LX2 cells cultivated in 3D spheroids.

| Compounds | IC50 (µM) |
|---|---|
| VV1 | >> 40 |
| 2C | 1.36 |
| DUDC3 | 0.16 |

Figure 113 shows how the treatment with 2C and, especially, DUDC3 compounds is also able to interfere with the morphology of the cells, compared with cells treated with VV1 control compound. In fact, the cells treated with DUDC3 appear more rounded in shape, probably indicating that they are undergoing cell death.

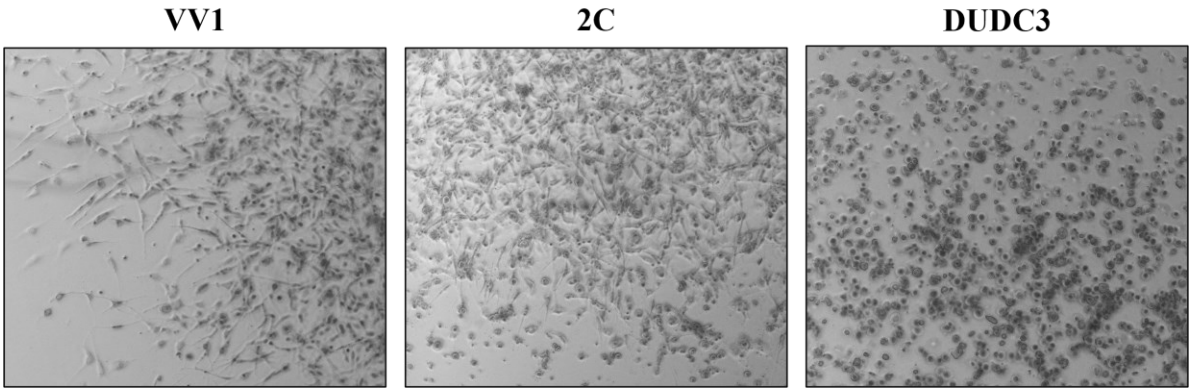


Figure 113: 3D-spheroids of LX2 in collagen I (2 mg/ml) treated with VV1, 2C and DUDC3 (the concentration used is 5 μM for each compound). The pictures were taken 24 hours after treatment, by means of the visible microscope Nikon Eclipse TS100.

## 4.12 Phenotypic and molecular effects of DUBs inhibitors on LX2 cells cultured on alginate *in vitro* models

### 4.12.1 Effects of DUBs inhibitors on cell viability in LX2 cultured on alginate *in vitro* models

DUBs inhibitors compounds were tested also in LX2 grown on alginate systems (Alg 2%, considered to mimic the healthy liver tissue, and Alg 3%, considered to mimic the fibrotic liver tissue). The optimal concentration considered was of 2 μM for VV1, 2C and DUDC3. Higher concentrations were not tested as they damage excessively the cells, and no analysis can be conducted. Both 2C and DUDC3 show a significantly reduction in cell viability compared to VV1 (Figure 114 and Figure 115). Moreover, both the compounds were more effective at 24-hour time point in Alg 3% systems than in Alg 2%, indicating probably a major activity in the *in vitro* model that mimics the liver tissue.

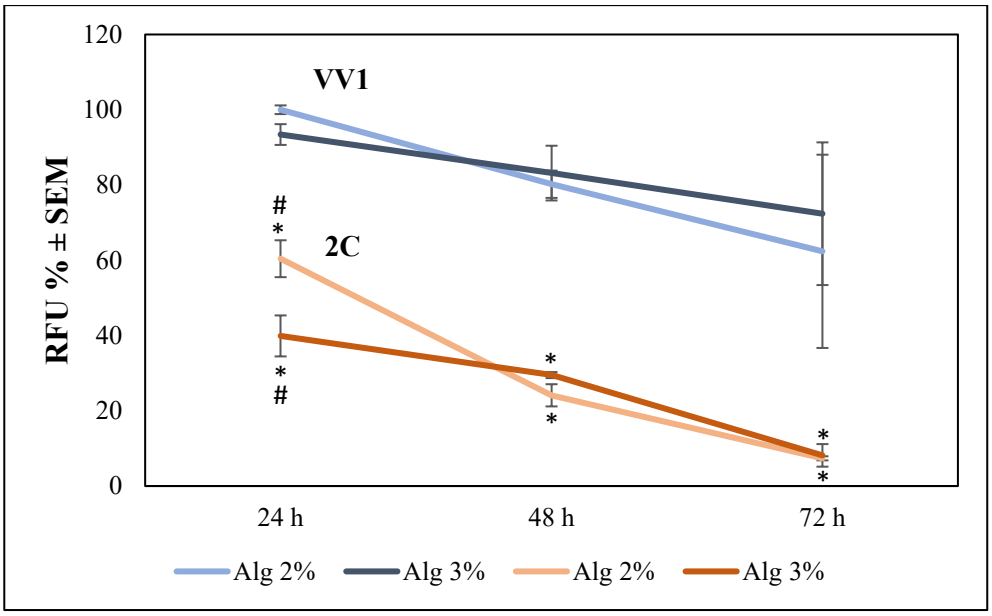


Figure 114: PrestoBlue viability test with LX2 grown on alginate systems (Alg 2% and Alg 3%) over a 72-hour period following initial treatment with 2 µM VV1 or 2C compounds (n = 6). The results are reported as Relative Luminescence Units (RLU) ± SEM, where the VV1-treated cells on Alg 2% at 24 hours were designated as 100% RFU corresponding to 100% viability. Statistical significance was determined by comparing 2C treatments versus VV1-treated cells grown in the same alginate *in vitro* model and at the same time point (*p < 0.005, unpaired t-test). Statistical significance was also determined by comparing 2C-treated cells on Alg 2% at 24 hours vs 2C-treated cells on Alg 3% at 24 hours (#p < 0.005, unpaired t-test).

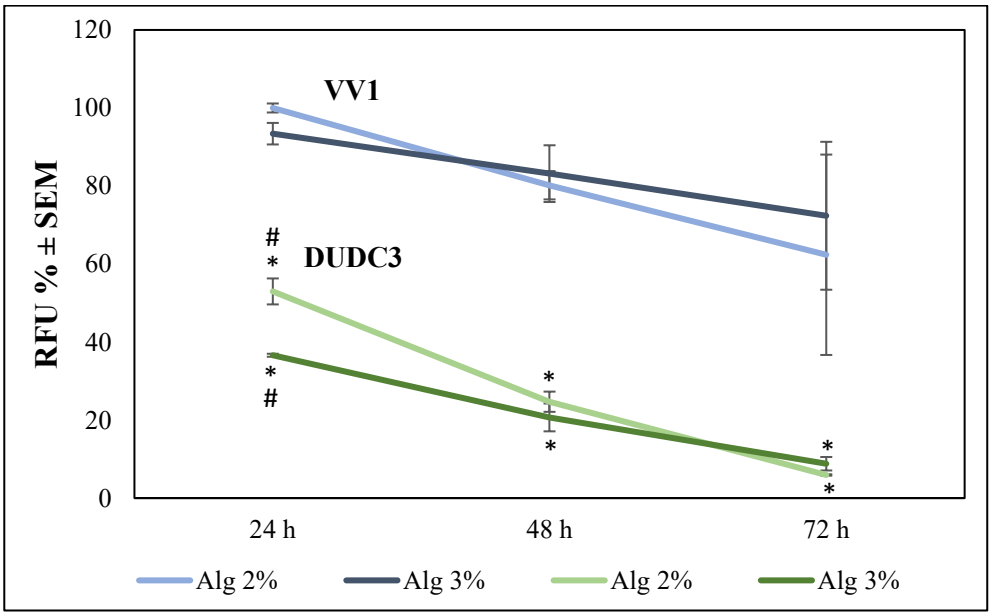


Figure 115: PrestoBlue viability test with LX2 grown on alginate systems (Alg 2% and Alg 3%) over a 72-hour period following initial treatment with 2 µM VV1 or DUDC3 compounds (n = 6). The results are reported as Relative Luminescence Units (RLU) ± SEM, where the VV1-treated cells on Alg 2% at 24 hours were designated as 100% RFU corresponding to 100% viability. Statistical significance was determined by comparing DUDC3 treatments versus VV1-treated cells grown in the same alginate *in vitro* model and at the same time point (*p < 0.005, unpaired t-test). Statistical significance was also determined by comparing DUDC3-treated cells on Alg 2% at 24 hours vs DUDC3-treated cells on Alg 3% at 24 hours (#p < 0.0001, unpaired t-test).

### 4.12.2 Molecular effects of DUBs inhibitors on LX2 cells cultured on alginate *in vitro* models (mRNA levels of ACTA2 and MMP9)

The mRNA levels of ACTA2 were investigated in LX2 cells grown on alginate systems (Alg 2%, considered to mimic the healthy liver tissue, and Alg 3%, considered to mimic the fibrotic liver tissue) following treatment with 2 µM of VV1, 2C, or DUDC3. 2C and DUDC3 were able to significantly reduce ACTA2 expression in cells cultured on both Alg 2% and Alg 3% (Figure 116).

We also studied the expression levels of MMP9. MMP9, belonging to the matrix metalloproteinase family, can remodel ECM in different pathological conditions including liver fibrosis. The balance between MMP and ECM protein is important for liver homeostasis and MMP9 expression is detected in the early stages of hepatic fibrogenesis (Jeng et al., 2020). Both 2C and DUDC3 decrease significantly MMP9 mRNA levels in both Alg 2% and Alg 3% systems (Figure 117), supporting their anti-fibrotic effect.

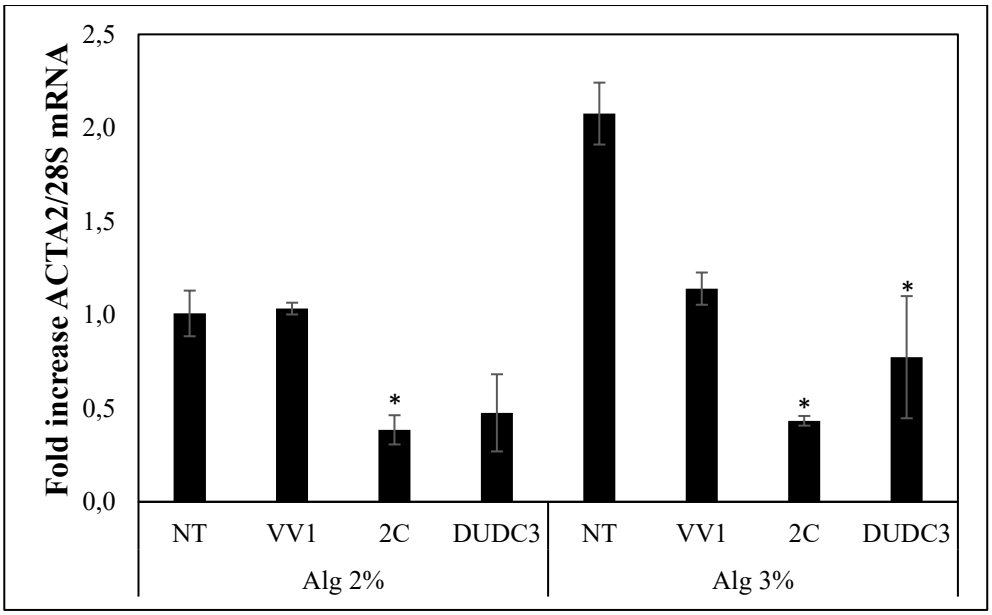


Figure 116: Fold increase (± SEM) mRNA levels of ACTA2 normalized with 28S in LX2 cells grown on Alg 2% and Alg 3%, treated from 24 hours with 2 µM of VV1, 2C, or DUDC3, compared to not treated (NT) cells grown on Alg 2% (n = 3). Statistical significance was determined by comparing treatments versus NT condition (*p < 0.05, Mann-Whitney test).

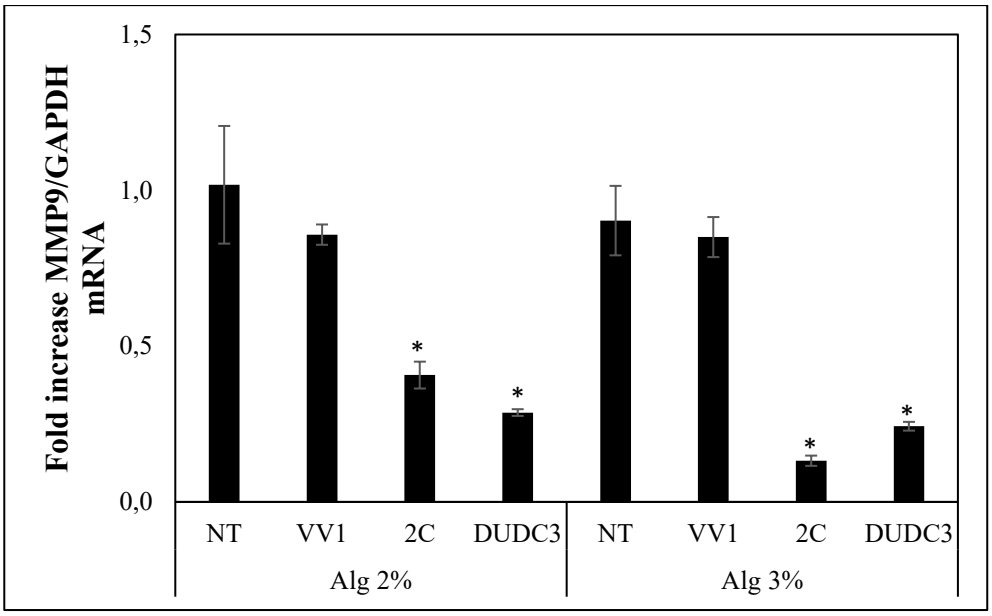


Figure 117: Fold increase (± SEM) mRNA levels of MMP9 normalized with GAPDH in LX2 cells grown on Alg 2% and Alg 3%, treated from 24 hours with 2 µM of VV1, 2C, or DUDC3, compared to not treated (NT) cells grown on Alg 2% (n = 3). Statistical significance was determined by comparing treatments versus NT condition (*p < 0.05, Mann-Whitney test).

## 4.13 Phenotype of primary mouse HSCs (mHSCs)

After having shown the effect of our DUBs inhibitors on the HSCs cell line LX2, we wanted to explore the effects in primary isolated HSCs. As a first test, we followed the activation process, which is known to occur in primary HSC cultured on plastic (Yin et al., 2013). Indeed, a stiff surface induces the trans-differentiation process of HSCs (Olsen et al., 2011). The knowledge of this time point at which trans-differentiation occurs in our vitro set up is relevant to deeply understand the effects of DUBS inhibitors. To this end, freshly isolated primary mouse HSCs (mHSCs) were seeded on cover slip glasses and subjected to ORO staining at two different time point, i.e. 2 days and 9 days after seeding, considered adequate to study cells trans-differentiation. From Figure 118 is possible to observe how mHSCs, 2 days after seeding, appear with the typical extensions, resembling the classical star shape. Moreover, they have a great amount of red lipid droplets, i.e. the storage of vitamin A (evidenced by the ORO staining). After 9 days, cells appear modified in their shape becoming stretched and enlarged, with the typical morphology of the myofibroblasts. Moreover, they have lost many of their lipid droplets whose lipid content is used to generate the energy required by the trans-differentiation process.

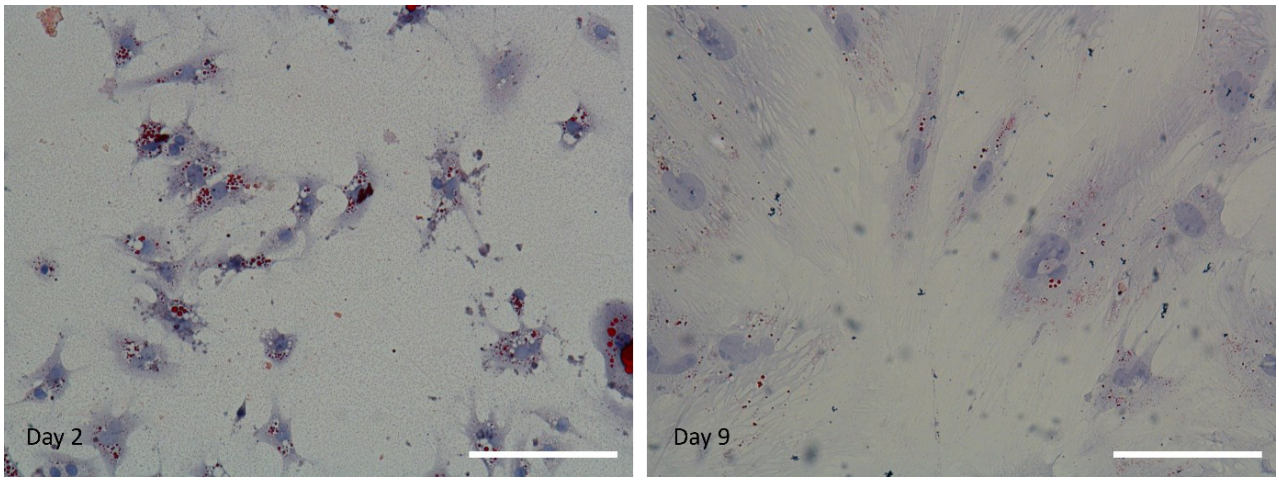


Figure 118: ORO staining of mouse primary HSCs at 2 days and 9 days from the isolation and seeding.

## 4.14 Levels of activation markers in primary mHSCs

To further analyze the activation of primary mouse HSCs seeded on plastic, we also assessed the protein levels of two activation markers, namely fibronectin and collagen I (Figure 119). These markers show higher levels in cells cultured 7 days on plastic than in those cultured 3 days. Moreover, these cells show also to secrete more fibronectin and collagen I after 7 days of culture rather than after 3 days. These observations further confirm the trans-differentiation process.

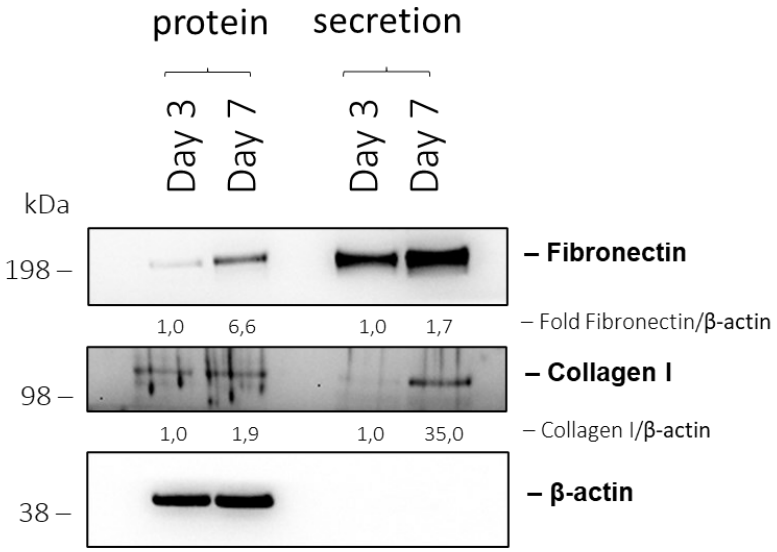


Figure 119: Western Blot protein levels of fibronectin and collagen I in primary mHSCs cultured on a plastic surface for 3 and 7 days after isolation. β-actin was used as loading control and to normalize the protein bands. The secretion protein bands were normalized with Ponceau bands.

## 4.15 Effects of DUBs inhibitors on the viability of primary mHSCs

The MTT assay was employed to evaluate primary mHSCs viability 48 hours after treatment with varying concentrations of VV1, 2C, or DUDC3 (0.5, 1, 2, 4, 10 μM). The treatments were administered 1 day or 7 days after seeding; thus, the viability test was performed at day 3 or day 9, respectively (Figure 120). The design of this experiment aimed to the exploration of the effect on the viability of mHSCs treated with DUBs inhibitors in the transdifferentiated or non-transdifferentiated phenotype. 2C reduced the viability only at day 3 with the highest concentration tested. DUDC3 exhibited a concentration-dependent reduction in cell viability at day 3, while at day 9 cells become more resistant as the viability was reduced at the highest concentration tested (10 μM). The pictures in Figure 121 reflect the results of the viability test. In fact, cells at day 9 are all viable across all the condition, instead of cells at day 3 in which cells are affected in morphology and viability by DUBs inhibitor, in particular DUDC3.

The fact that primary mouse HSC are more sensible to DUBs inhibitors few days after seeding (day 1) may be due to the fact at this time point the cells still need to adapt to the novel environment (2D plastic surface). Possibly, the adaptation process does not allow an effective defense against DUBs inhibitors. However, once adapted, cells become more resistant via mechanisms whose nature deserve further investigation. Obviously, to fully understanding the effects of our DUB inhibitors on “adapted” mHSC we need to explore the effects at longer time points. Despite this, our data show that our DUB inhibitors are effective also on primary HSCs, a relevant observation for future *in vivo* studies.

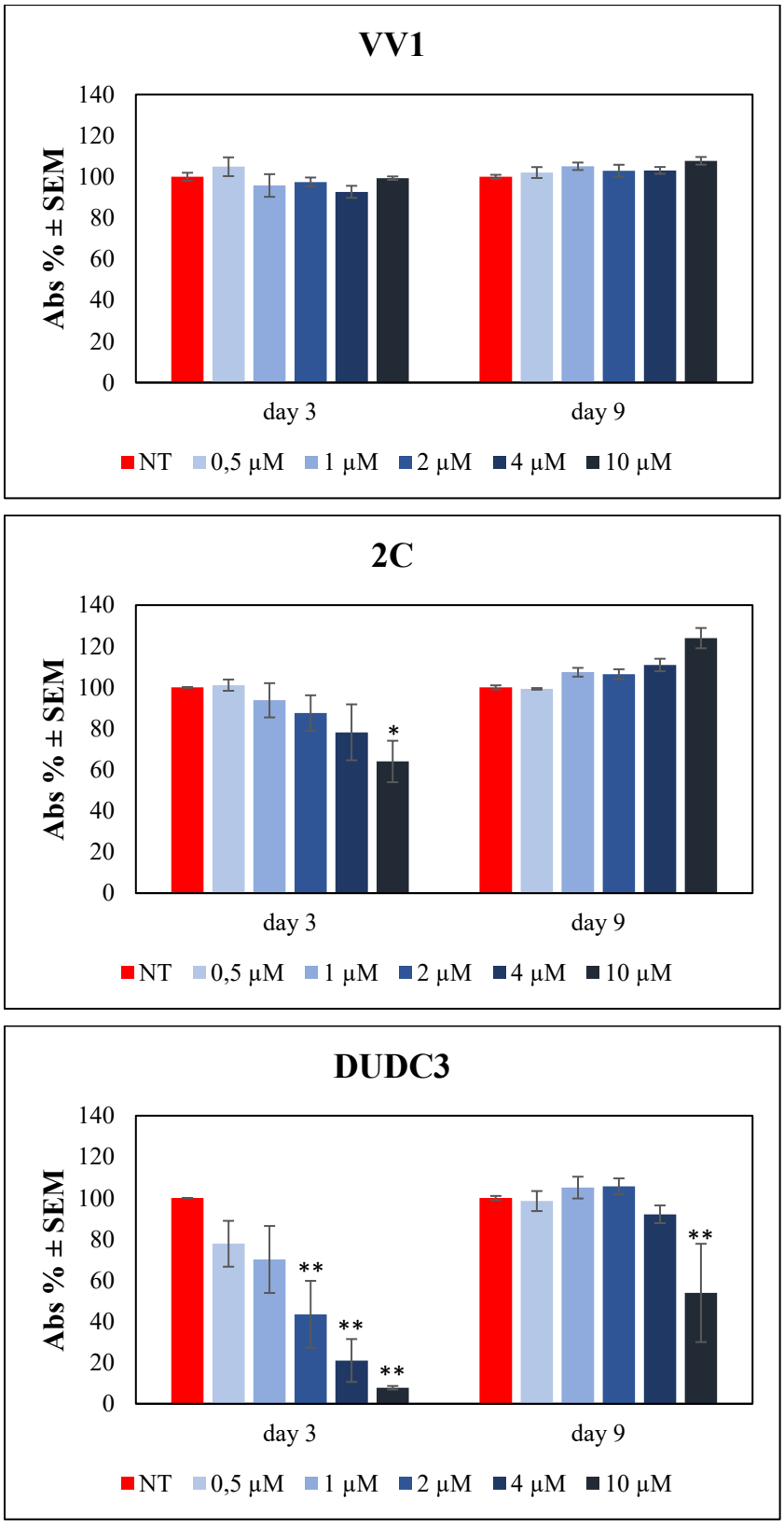


Figure 120: MTT test with primary mHSCs after 48 hours from treatment with varying concentrations (0.5, 1, 2, 4, 10 µM) of VV1, 2C, or DUDC3 (n = 15). The treatments were administered 1 day or 7 days after isolation and seeding of primary mHSCs. The results are reported as Absorbance % ± SEM, where NT condition (red color) is considered 100%. Statistical significance was determined by comparing NT condition vs treatment conditions (*$p < 0.05$, **$p < 0.01$). Depending on data distribution, statistical analyses were performed using either parametric (unpaired t-test) or non-parametric (Mann-Whitney test) tests.

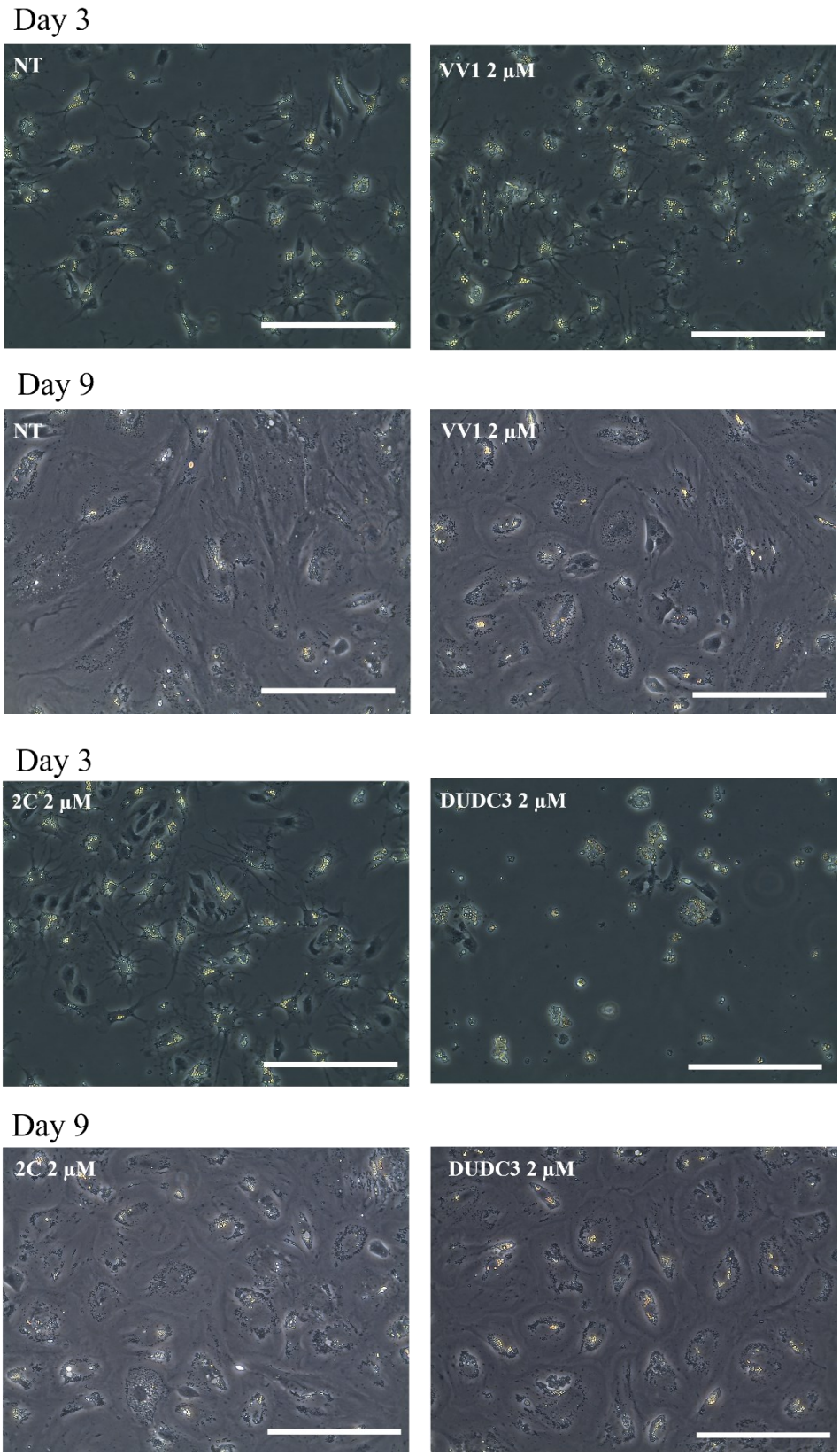


Figure 121: Bright field pictures of primary mHSCs treated 1 day or 7 days after isolation. Cells were treated with 2 µM of VV1, 2C, or DUDC3. 48 hours after treatment, namely at day 3 and day 9, the pictures were taken. The scale bar represents 200 µm.

## 4.16 Effect of DUBs inhibitors on α-SMA in primary mHSCs

α-SMA protein levels were determined in primary mHSCs treated after 7 days of culture. mHSCs were treated with 2 μM of VV1, 2C, or DUDC3. After 48 hours from treatment protein were extracted and used to perform Western Blot (Figure 122). Compared to VV1 treated cells, we observed a reduction in the protein level following DUDC3 treatment.

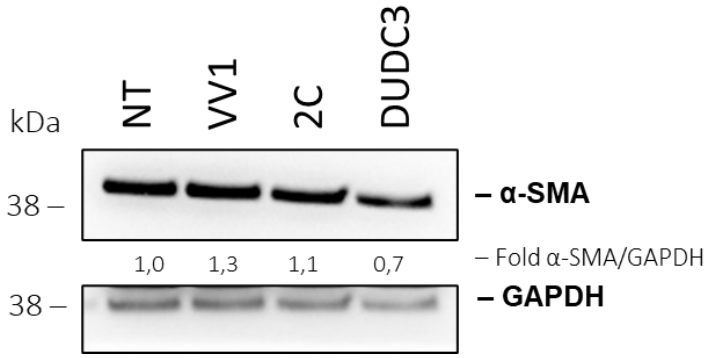


Figure 122: Western Blot protein levels of α-SMA in primary mHSCs treated after being cultured for 7 days after isolation. mHSCs were treated with 2 μM of VV1, 2C, or DUDC3. GAPDH was used as loading control and to normalize the protein bands. Not treated cells (NT) are considered the control.

# 5. Discussion and conclusions

The liver is a critical organ for metabolism in human beings, which plays an essential role in an abundance of physiological processes and is vulnerable to endogenous or exogenous injuries. After the damage to the liver, a type of aberrant wound healing response known as liver fibrosis (LF) may occur; the phenomenon consists of an excessive accumulation of extracellular matrix (ECM) (Pei et al., 2023). LF is a chronic damage and inflammation of the liver that can result from numerous causes and, if not adequately treated, can progress to cirrhosis, portal hypertension and eventually hepatocellular carcinoma (HCC) (Dhar et al., 2020). The principal causes that lead to chronic liver injury are hepatitis viruses (i.e. HBV, HCV), alcohol abuse and metabolic disorders, that can cause nonalcoholic fatty liver disease (NAFLD) and its more aggressive form nonalcoholic steatophepatitis (NASH) (Mazza et al., 2017). From 2009 to 2019, among the etiologies, NAFLD has increased markedly and in the same period the incidence and prevalence of liver cirrhosis worldwide increased and in 2017 liver cirrhosis caused more than 1.32 million deaths, accounting for 2.4% of global deaths (Lan et al., 2023). Liver fibrosis is therefore of particular interest to national health systems also in terms of costs. However, so far, there are no drugs approved either by the Food and Drug Administration (FDA) or by the European Medicines Agency (EMA), hence there is an urge to develop liver antifibrotic therapies (Kumar et al., 2021; Zhang et al., 2023). The most efficient therapeutic approach to liver fibrosis consists of the elimination of the main causes. However, this approach has limited effectiveness, as some causes cannot be fully eliminated. Moreover, in cases of end stage fibrosis, the only available treatment is liver transplantation (Pei et al., 2023). Therefore, novel therapeutic agents need to be explored to stop the development of early liver fibrosis or to reverse the fibrosis process to achieve liver fibrosis resolution.

In the development of effective strategies for treating liver fibrosis, pre-clinical and clinical evaluations are essential. The development of innovative *in vitro* models may enhance the discovery of compounds with anti-fibrotic properties (Mazza et al., 2017). One of the main aims of this thesis, in fact, is to design and develop *in vitro* models for the study of liver fibrosis. These models consist of hydrogel surfaces that can mimic the viscoelastic properties of liver tissue, both under physiological and pathological conditions. Rheological properties of the liver tissue during the aberrant fibrogenesis are important because liver fibrosis tissue is characterized by excessive accumulation of ECM (Dhar et al., 2020); moreover, the production of ECM increases liver stiffness (Kostallari et al., 2022), which in turn contributes

to promote HSC activation and thus liver fibrosis (Olsen et al., 2011). In literature there is a lack of proper information about the mechanical characteristics of the human liver tissue. Only some studies conducted on porcine liver tissue are available (Jugé et al., 2023; Nicolle et al., 2010; Wex et al., 2014). Thus, to have a better insight on human liver tissue rheological properties, we characterized healthy and pathological liver samples by means of the rheometer. The pathological samples came from obese patients and exhibited varying degrees of fibrosis and steatosis as evaluated histologically (Table 5). In contrast, healthy samples were obtained from normal liver enucleated from large cancer resection tissue.

The oscillatory tests reveal a significant predominance of the elastic modulus (G') over the viscous modulus (G'') in both healthy and pathological liver samples. However, the values of G' and G'' differ between healthy and pathological liver samples, leading to variations in the shear modulus G, which is typically higher in pathological samples. In fact, the parameters $G^*$, $\Sigma G_i$, and $\tau_c$ are significantly lower in healthy liver samples than in pathological ones (Figure 44 and Figure 45). Increased stiffness in pathological samples is associated with pathological changes, lower stiffness attains to healthy liver tissue. These significant differences suggest that the rheological parameters can effectively differentiate between the two tissue types and provide biomechanical insights into liver tissue condition.

Both pathological and healthy liver samples demonstrated rheological properties similar to gels, characterized by a marked predominance of G' over G'', parallel trends of G' and G'', and minimal dependence on ω. Interestingly, we identified another commonality in the rheological characterization of liver samples and gels. Coviello et al. reported a correlation between the shear modulus G and the critical shear modulus $G_c$ in scleroglucan hydrogels (Coviello et al., 2022). Similarly, our pathological and healthy liver samples considered together exhibited a correlation between G and $G_c$ (Figure 49). Such parallelism between rheological behavior of biological tissues and polymeric hydrogels could provide valuable insights into the strategies to realize *in vitro* models to study liver fibrosis and anti-fibrotic molecules.

Comparing the mean $G^*$ and $\Sigma G_i$ moduli obtained by the rheological analyses with the median rigidity obtained from the elastographic technique (routine clinical test performed on the patients we considered) we did not find a correlation (Figure 50 and Figure 51). This may be due to the different measurement methods. In fact, elastographic measurement, which is performed *in vivo*, is affected by a whole series of factors (patient's position, fasting, blood pressure, abdominal wall thickness) that rheology does not encounter, being performed *ex vivo* on explanted liver sample. Obviously, it is sure that the rheological properties of *in vivo*

tissue can differ from those of *ex vivo* tissue because, for example *ex vivo* tissues are not pervaded by moving fluids. However, we believe that our rheological tests are far more precise and informative than elastography, even if they can be performed only on the explanted liver sample.

LF-NMR characterization of liver samples provides the values of $T_{2m}$ and $T_{1m}$, which are strongly influenced by the amount of iron contained, being iron a ferromagnetic material. Healthy liver samples exhibited significantly higher $T_{1m}$ and $T_{2m}$ relaxation times compared to pathological samples (Figure 53). This observation suggests that pathological samples, on average, possess a higher iron content. Moreover, $T_{2m}$ and $T_{1m}$ measured in liver samples correlates inversely with mean G* and $\Sigma G_i$ moduli measured by rheological characterization (Figure 55, Figure 56, Figure 57 and Figure 58). This means that samples characterized by low $T_{2m}/T_{1m}$, and thus by high iron deposition, are also characterized by elevated mean G* and $\Sigma G_i$ moduli, indicating a high stiffness of liver tissue. Our data suggest that increased stiffness correlates with increased iron deposition. In line with this, there is the observation that an iron excess in the liver can induce fibrosis-promoting signals in the parenchymal and non-parenchymal cells, thus accelerating disease progression (Mehta et al., 2019; Yao et al., 2019). Moreover, in NAFLD, NASH, alcoholic liver disease and HCV infection, increased hepatic iron is very common, more than other liver diseases, such as autoimmune or cholestatic liver diseases (Kowdley, 2016; Mehta et al., 2019). The excess of iron can accelerate the progression of liver fibrosis to cirrhosis and HCC, because iron catalyzes the formation of toxic hydroxyl radicals, which mediate cellular damage potentially augmenting fibrosis progression (Mehta et al., 2019; Yao et al., 2019). However, it is not yet fully clear whether iron overload is the cause or the consequence in liver fibrosis. According to Kowdley (Kowdley, 2016), liver fibrosis may also be the cause of iron accumulation. A hormone synthesized by the liver called hepcidin regulates iron absorption in the gut. Receptors on hepatocytes sense the amount of iron in circulation and accordingly up- or downregulate the production of hepcidin. Hepcidin binds to enterocytes to the basolateral transporter ferroportin, following which ferroportin is internalized and degraded by lysosomes. Consequently, the iron export out of the gut epithelium to the blood circulation is reduced, leading to reduction in iron levels in tissues (Hilton et al., 2023; Kowdley, 2016). Liver injury could potentially lead to a reduction in the production of hepcidin from hepatocytes or a reduction in the sensing of iron by the liver. This may explain how the increased iron accumulation in the liver tissue can occur (Kowdley, 2016).

Another important correlation we observed, deals with the protein transferrin that carries iron in the blood. Our data indicate an inverse correlation between the levels of transferrin and the mean G* and $\Sigma G_i$ moduli, showing that the higher the rheological moduli representing liver stiffness, the lower the transferrin concentration (Figure 61 and Figure 62). This observation is in line with the knowledge that in case of iron overload in the liver, the levels of transferrin protein decrease, to limit the iron transport to the tissues, including the liver. In this regard, transferrin is considered a prognostic factor for survival and mortality in patients with end-stage liver disease (Meier et al., 2020). In particular, low serum transferrin levels are associated with increased 90-day mortality. On the other hand, also a high degree of stiffness in liver tissue is associated with high higher severity in liver disease (Semmler et al., 2023).

Our data indicate that $T_{2m}$ directly correlates with $I_{BMI}$, $I_{FS}$ and with the stages of steatosis measured in histological samples according to Kleiner-Brunt (Figure 68, Figure 69 and Figure 70). Notably, our patients have variable degrees of obesity and this pathological condition is known to associate with iron deficiency due to the reduced hepcidin levels (Hilton et al., 2023). We could therefore suppose that the increase of the $T_{2m}$ values in our obese patients depends, at least in part, to the reduced iron content in the liver. Thus, in line with the literature (Mehta et al., 2019; Yao et al., 2019), on the one hand we observe (paragraph 4.4) that iron levels in liver increase with liver tissue stiffness. On the other hand, again in accordance with the literature (Hilton et al., 2023), we show (paragraph 4.5) that iron levels in liver decrease with the BMI of the patients. Taken together, our data indicate that the combination of rheological and LF-NMR analyses provides complementary and corroborative data on liver structure that reflects in organ functionality.

The analysis performed on the liver samples allowed us to precisely define the viscoelastic properties of the normal and pathological liver. These data were employed to generate cell-culturing surfaces able to mimic the viscoelastic properties of the normal and pathological conditions. For this purpose, we used alginate polymers because of their excellent peculiarities including biocompatibility and versatility.

Following the rheological and LF-NMR characterization of different alginate hydrogels generated using different alginate concentrations and amount of $Ca^{++}$ necessary to induce the gelation, we selected two systems that better resemble the rheological properties of the healthy and pathological liver tissue. Moreover, the selected alginate hydrogels were mixed with fibronectin (in ratio 1:10, fibronectin:alginate) to favor cell adhesion. Our data indicate that alginate hydrogels generated with an alginate concentration of 2% and 3% (crosslinked

by a solution containing 9 mg/ml calcium ions) well resembled the healthy and fibrotic liver tissue, respectively. We then characterized the phenotype of our cellular model (LX2) cultured on the different surfaces. LX2 cultured on Alg 3% surface proliferated faster than those cultured on Alg 2% and this was evident from the viability assay results (Figure 89). Moreover, we observed an increase of the mRNA/protein levels of E2F1 (Figure 93 and Figure 94), an important proliferation but also fibrotic marker (Zhang et al., 2014). Additionally, LX2 cultured on Alg 3% system showed higher mRNA/protein levels of α-SMA (Figure 92 and Figure 94), an important hallmark of liver fibrosis (Acharya et al., 2021). Taken together these results prove that the Alg 3% can induce the phenotypic and molecular modification occurring *in vivo* in the fibrotic liver; in contrast, Alg 2% maintains the cells in a more quiescent phenotype. Of course, being LX2 a cell line and not primary cells, a certain degree of activation is present also when cultured on Alg 2%. Despite this, our system with appropriate viscoelastic properties can generate data with an increased predictive power for *in vivo* test. In the future we plan to repeat the experiments using primary freshly isolated HSCs, although the isolation procedure is not easy and the amount of cell which can be recovered is generally modest.

The other important aim of our research activity was to evaluate the anti-fibrotic effects of 2C compound, a deubiquitinase (DUBs) inhibitor (Cersosimo et al., 2015), and its derivative DUDC3. DUDC3 was chosen among many other derivatives of 2C for its potent anti-proliferative effect we previously observed in ovarian cancer cells (Maddaloni et al., 2024). Inhibiting DUBs, 2C impairs the ubiquitin-proteosome system causing the accumulation of polyubiquitinated proteins, leading to proteotoxic stress and cell apoptosis (Cersosimo et al., 2015; Iuliano et al., 2022; Maddaloni et al., 2024). 2C showed proapoptotic activity in different cancer cell lines of glioblastoma and ovarian cancer cell (Cersosimo et al., 2015; Maddaloni et al., 2024). Furthermore, 2C interferes the expression of E2F1 (Maddaloni et al., 2024), an activator that can promote HCC (Farra et al., 2019) and LF (Zhang et al., 2014).

We tested these compounds on cells seeded on plastic, the simplest and most common model for cultivating cell lines. We first proved that the molecules used can effectively enter the cells and for this purpose 2C labelled with fluorescein was delivered to LX2 resulting in an excellent uptake (Figure 95). Similar results (data not shown) were obtained for the other cell lines considered, i.e. immortalized murine HSCs (CFSC) and immortalized human fibroblast (WS1). Although with different quantitative effects, 2C/DUDC3 could reduce cell viability in a dose and time dependent manner in all cell types (Figure 96, Figure 97 and,

Figure 98). This observation allows to exclude that the effect overserved is cell-dependent and thus confers to our work a more general validity and predictive power for *in vivo* experiments.

Our data suggest that in LX2 the reduction of cell viability is probably due to apoptosis for 2C treatment at the lowest concentrations (~ 1 μM) (Figure 99); necrosis induction seems instead to be the major driver for the highest concentrations of 2C and for all the concentrations of DUDC3 (Figure 100). 2C and DUDC3 also seem to promote a type of cell death named autophagy (Figure 101) at least by judging from the appearance of the cleaved form of the autophagy marker LC3BII. However, an additional test, which explores the final pathway of autophagy, does not confirm the completion of the autophagy process (Figure 102). Whereas further testing will be necessary to clarify this aspect, it is possible that 2C/DUDC3 can trigger the initial stage of autophagy but, for reasons to be determined, the process does not reach completion.

The phenotypic effect above discussed for LX2 are most likely related to the ability of 2C/DUDC3 to inhibit deubiquitination as shown by the fact that there is an accumulation of polyubiquitinated proteins induced by 2C and DUDC3 (Figure 105). In addition, our compounds decrease the protein levels of the fibrotic markers α-SMA and E2F1 (Figure 106 and Figure 109). These results support the concept of the anti-fibrotic effect of 2C and DUDC3. Notably, by immunofluorescence assay (Figure 110 and Figure 111) we also noticed that 2C is able to rearrange the distribution of cytoskeleton proteins, i.e. β-tubulin and vimentin, and the ECM protein fibronectin; fibronectin mediates cell-ECM and ECM-ECM interactions during fundamental events such as development, wound healing and fibrosis (Schwarzbauer and DeSimone, 2011). Thus, the effect of our drugs on cell phenotype may also depend on the rearrangements of cytoskeleton proteins via mechanisms that deserve further investigation.

We tested the DUBs inhibitors also in 3D spheroids, that provide a more accurate representation of the cell-cell and cell-matrix interaction than plastic surfaces. Also in this model, 2C and DUDC3 reduced the viability of LX2, showing a dose-response effect (Figure 112). This observation fully confirms the data obtained with cells cultured on plastic conferring to the results a remarkable level of solidity.

DUBs inhibitors compounds were tested also in LX2 grown on the alginate *in vitro* models that we designed to mimic healthy (Alg 2%) or fibrotic (Alg 3%) liver tissue (Figure 114 and Figure 115). Both 2C and DUDC3 show a significantly reduction in cell viability compared to VV1, the control compound, confirming the data of plastic 2D culture and the 3D spheroids models. 24 hours after treatment these compounds seem to be more effective in

reducing the viability in Alg 3% systems than in Alg 2%. This probably indicates a major effectiveness in situation of increased cell proliferation. Moreover, 2C and DUDC3 were able to decrease the mRNA levels of ACTA2 and MMP9. ACTA2 is a maker of fibrotic activation and MMP9 is a matrix metalloproteinase whose expression is detected in the early stages of liver fibrogenesis (Figure 116 and Figure 117).

Lastly, we evaluated the DUBs inhibitor effects also in primary mouse HSCs (mHSCs). We observed that primary mHSCs cells after 7-9 days after seeding on plastic surfaces transdifferentiate to an activated phenotype. We test our compound on both non-activated and activated mHSCs. 2C and DUDC3 affected the viability of mHSCs mostly in non-activated than in activated ones (Figure 120). The fact that primary mHSC are more sensible to DUBs inhibitors few days after seeding (day 1) may be due to the fact at this time point the cells still need to adapt to the novel environment. However, once adapted, cells seem to become more resistant via mechanisms whose nature deserve further investigation. Obviously, to fully understanding the effects of our DUB inhibitors on "adapted" mHSC we need to explore the effects at longer time points. Despite this, DUDC3 was able to reduce α-SMA protein levels in activated mHSCs (Figure 122). Thus, our phenotypic and molecular effects data show that our DUBs inhibitors are effective also on primary HSCs, a relevant observation for future *in vivo* studies. Together the four *in vitro* models considered (cell line culture on plastic surface, cell culture on alginate surface, cell cultured in 3D and primary cells culture on plastic surface) make our *in vitro* data reliable and with a significant predictive power for the *in vivo* tests.

Despite the demonstrated effectiveness, *in vivo* our DUBs most likely can exert their effect also on cells different from the HSCs possibly resulting in unwanted side effects. Thus, to confer a more specific action *in vivo*, we are developing targeted delivery systems in collaboration with Prof. Giorgia Pastorin (University of Singapore). Finally, we are collaborating with the research group of Prof. Nhung Hai Truong (Faculty of Biology and Biotechnology, VNUHCM – University of Science, Ho Chi Minh City, Vietnam), that is testing our DUBs inhibitors in *in vivo* models of liver fibrosis (project code: VN21GR01 financed by the Minister of External Affairs and of the International Collaboration – MAECI).

# References


Abrami, M., Chiarappa, G., Farra, R., Grassi, G., Marizza, P., Grassi, M., 2018. Use of low-field NMR for the characterization of gels and biological tissues. ADMET DMPK 6, 34. https://doi.org/10.5599/admet.6.1.430

Abrami, M., Maschio, M., Conese, M., Confalonieri, M., Gerin, F., Dapas, B., Farra, R., Adrover, A., Torelli, L., Ruaro, B., Grassi, G., Grassi, M., 2021. Combined use of rheology and portable low-field NMR in cystic fibrosis patients. Respir. Med. 189, 106623. https://doi.org/10.1016/j.rmed.2021.106623

Abrami, M., Maschio, M., Conese, M., Confalonieri, M., Salton, F., Gerin, F., Dapas, B., Farra, R., Adrover, A., Milcovich, G., Fornasier, C., Biasin, A., Grassi, M., Grassi, G., 2022. Effect of chest physiotherapy on cystic fibrosis sputum nanostructure: an experimental and theoretical approach. Drug Deliv. Transl. Res. 12, 1943–1958. https://doi.org/10.1007/s13346-022-01131-8

Acharya, P., Chouhan, K., Weiskirchen, S., Weiskirchen, R., 2021. Cellular Mechanisms of Liver Fibrosis. Front. Pharmacol. 12, 671640. https://doi.org/10.3389/fphar.2021.671640

Adams, D.H., Eksteen, B., 2006. Aberrant homing of mucosal T cells and extra-intestinal manifestations of inflammatory bowel disease. Nat. Rev. Immunol. 6, 244–251. https://doi.org/10.1038/nri1784

Affo, S., Yu, L.-X., Schwabe, R.F., 2017. The Role of Cancer-Associated Fibroblasts and Fibrosis in Liver Cancer. Annu. Rev. Pathol. Mech. Dis. 12, 153–186. https://doi.org/10.1146/annurev-pathol-052016-100322

Amernia, B., Moosavy, S.H., Banookh, F., Zoghi, G., 2021. FIB-4, APRI, and AST/ALT ratio compared to FibroScan for the assessment of hepatic fibrosis in patients with non-alcoholic fatty liver disease in Bandar Abbas, Iran. BMC Gastroenterol. 21, 453. https://doi.org/10.1186/s12876-021-02038-3

Antao, A.M., Tyagi, A., Kim, K.-S., Ramakrishna, S., 2020. Advances in Deubiquitinating Enzyme Inhibition and Applications in Cancer Therapeutics. Cancers 12, 1579. https://doi.org/10.3390/cancers12061579

Arezzini, B., Lunghi, B., Lungarella, G., Gardi, C., 2003. Iron overload enhances the development of experimental liver cirrhosis in mice. Int. J. Biochem. Cell Biol. 35, 486–495. https://doi.org/10.1016/s1357-2725(02)00298-4

Asrani, S.K., Devarbhavi, H., Eaton, J., Kamath, P.S., 2019. Burden of liver diseases in the world. J. Hepatol. 70, 151–171. https://doi.org/10.1016/j.jhep.2018.09.014

Augst, A.D., Kong, H.J., Mooney, D.J., 2006. Alginate Hydrogels as Biomaterials. Macromol. Biosci. 6, 623–633. https://doi.org/10.1002/mabi.200600069

Baiz, D., 2014. Bortezomib effect on E2F and cyclin family members in human hepatocellular carcinoma cell lines. World J. Gastroenterol. 20, 795. https://doi.org/10.3748/wjg.v20.i3.795

Bard, J.A.M., Goodall, E.A., Greene, E.R., Jonsson, E., Dong, K.C., Martin, A., 2018. Structure and Function of the 26S Proteasome. Annu. Rev. Biochem. 87, 697–724. https://doi.org/10.1146/annurev-biochem-062917-011931

Barr, R.G., 2018. Shear wave liver elastography. Abdom. Radiol. 43, 800–807. https://doi.org/10.1007/s00261-017-1375-1

Bilston, L.E., 2018. Soft tissue rheology and its implications for elastography: Challenges and opportunities. NMR Biomed. 31, e3832. https://doi.org/10.1002/nbm.3832

Boccatonda, A., Andreetto, L., D'Ardes, D., Cocco, G., Rossi, I., Vicari, S., Schiavone, C., Cipollone, F., Guagnano, M.T., 2023. From NAFLD to MAFLD: Definition,

Pathophysiological Basis and Cardiovascular Implications. Biomedicines 11, 883. https://doi.org/10.3390/biomedicines11030883
Bonkovsky, H.L., 1991. Iron and the Liver. Am. J. Med. Sci. 301, 32–43. https://doi.org/10.1097/00000441-199101000-00006
Bridle, K.R., Crawford, D.H.G., Ramm, G.A., 2003. Identification and characterization of the hepatic stellate cell transferrin receptor. Am. J. Pathol. 162, 1661–1667. https://doi.org/10.1016/S0002-9440(10)64300-3
Brownstein, K.R., Tarr, C.E., 1977. Spin-lattice relaxation in a system governed by diffusion. J. Magn. Reson. 1969 26, 17–24. https://doi.org/10.1016/0022-2364(77)90230-X
Caballero, B., 2019. Humans against Obesity: Who Will Win? Adv. Nutr. 10, S4–S9. https://doi.org/10.1093/advances/nmy055
Caliari, S.R., Perepelyuk, M., Cosgrove, B.D., Tsai, S.J., Lee, G.Y., Mauck, R.L., Wells, R.G., Burdick, J.A., 2016. Stiffening hydrogels for investigating the dynamics of hepatic stellate cell mechanotransduction during myofibroblast activation. Sci. Rep. 6, 21387. https://doi.org/10.1038/srep21387
Cameron, Andrew.R., Frith, Jessica.E., Cooper-White, Justin.J., 2011. The influence of substrate creep on mesenchymal stem cell behaviour and phenotype. Biomaterials 32, 5979–5993. https://doi.org/10.1016/j.biomaterials.2011.04.003
Campana, L., Esser, H., Huch, M., Forbes, S., 2021. Liver regeneration and inflammation: from fundamental science to clinical applications. Nat. Rev. Mol. Cell Biol. 22, 608–624. https://doi.org/10.1038/s41580-021-00373-7
Carthew, P., Edwards, R.E., Smith, A.G., Dorman, B., Francis, J.E., 1991. Rapid induction of hepatic fibrosis in the gerbil after the parenteral administration of iron-dextran complex. Hepatol. Baltim. Md 13, 534–539.
Castilho-Fernandes, A., De Almeida, D.C., Fontes, A.M., Melo, F.U.F., Picanço-Castro, V., Freitas, M.C., Orellana, M.D., Palma, P.V.B., Hackett, P.B., Friedman, S.L., Covas, D.T., 2011. Human hepatic stellate cell line (LX-2) exhibits characteristics of bone marrow-derived mesenchymal stem cells. Exp. Mol. Pathol. 91, 664–672. https://doi.org/10.1016/j.yexmp.2011.09.002
Cersosimo, U., Sgorbissa, A., Foti, C., Drioli, S., Angelica, R., Tomasella, A., Picco, R., Semrau, M.S., Storici, P., Benedetti, F., Berti, F., Brancolini, C., 2015. Synthesis, Characterization, and Optimization for in Vivo Delivery of a Nonselective Isopeptidase Inhibitor as New Antineoplastic Agent. J. Med. Chem. 58, 1691–1704. https://doi.org/10.1021/jm501336h
Chai, Q., Jiao, Y., Yu, X., 2017. Hydrogels for Biomedical Applications: Their Characteristics and the Mechanisms behind Them. Gels 3, 6. https://doi.org/10.3390/gels3010006
Chaudhuri, O., Gu, L., Darnell, M., Klumpers, D., Bencherif, S.A., Weaver, J.C., Huebsch, N., Mooney, D.J., 2015. Substrate stress relaxation regulates cell spreading. Nat. Commun. 6, 6365. https://doi.org/10.1038/ncomms7365
Chen, Q., Shen, Y., Zheng, J., 2021. A review of cystic fibrosis: Basic and clinical aspects. Anim. Models Exp. Med. 4, 220–232. https://doi.org/10.1002/ame2.12180
Ciaccio, M., Lippi, G., 2020. Biochimica Clinica e Medicina di Laboratorio, III Edizione. ed. EdiSES Università.
Ciotti, S., Sgarra, R., Sgorbissa, A., Penzo, C., Tomasella, A., Casarsa, F., Benedetti, F., Berti, F., Manfioletti, G., Brancolini, C., 2018. The binding landscape of a partially-selective isopeptidase inhibitor with potent pro-death activity, based on the bis(arylidene)cyclohexanone scaffold. Cell Death Dis. 9, 184. https://doi.org/10.1038/s41419-017-0259-1
Coviello, T., Alhaique, F., Di Meo, C., Matricardi, P., Montanari, E., Zoratto, N., Grassi, M., Abrami, M., 2022. Scleroglucan and guar gum: The synergistic effects of a new

polysaccharide system. Express Polym. Lett. 16, 410–426. https://doi.org/10.3144/expresspolymlett.2022.30
Csepregi, R., Lemli, B., Kunsági-Máté, S., Szente, L., Kőszegi, T., Németi, B., Poór, M., 2018. Complex Formation of Resorufin and Resazurin with B-Cyclodextrins: Can Cyclodextrins Interfere with a Resazurin Cell Viability Assay? Molecules 23, 382. https://doi.org/10.3390/molecules23020382
Deng, Y., Li, Xudan, Li, Xuan, Zheng, Z., Huang, W., Chen, L., Tong, Q., Ming, Y., 2018. Corilagin induces the apoptosis of hepatocellular carcinoma cells through the mitochondrial apoptotic and death receptor pathways. Oncol. Rep. https://doi.org/10.3892/or.2018.6396
Dhar, D., Baglieri, J., Kisseleva, T., Brenner, D.A., 2020. Mechanisms of liver fibrosis and its role in liver cancer. Exp. Biol. Med. 245, 96–108. https://doi.org/10.1177/1535370219898141
Draper, N.R., Smith, H., 1998. Applied regression analysis, 3rd ed. ed, Wiley series in probability and statistics. J. Wiley & sons, New York Chichester Weinheim [etc.].
Du Roure, O., Saez, A., Buguin, A., Austin, R.H., Chavrier, P., Siberzan, P., Ladoux, B., 2005. Force mapping in epithelial cell migration. Proc. Natl. Acad. Sci. 102, 2390–2395. https://doi.org/10.1073/pnas.0408482102
Eletr, Z.M., Wilkinson, K.D., 2011. An Emerging Model for BAP1's Role in Regulating Cell Cycle Progression. Cell Biochem. Biophys. 60, 3–11. https://doi.org/10.1007/s12013-011-9184-6
Elmore, S., 2007. Apoptosis: A Review of Programmed Cell Death. Toxicol. Pathol. 35, 495–516. https://doi.org/10.1080/01926230701320337
European Association for the Study of the Liver, Clinical Practice Guideline Panel, EASL Governing Board representative, 2021. EASL Clinical Practice Guidelines on non-invasive tests for evaluation of liver disease severity and prognosis – 2021 update. J. Hepatol. 75, 659–689. https://doi.org/10.1016/j.jhep.2021.05.025
European Association for the Study of the Liver, European Association for the Study of Diabetes, European Association for the Study of Obesity, 2016. EASL–EASD–EASO Clinical Practice Guidelines for the management of non-alcoholic fatty liver disease. J. Hepatol. 64, 1388–1402. https://doi.org/10.1016/j.jhep.2015.11.004
Evans, N., Minelli, C., Gentleman, E., LaPointe, V., Patankar, S., Kallivretaki, M., Chen, X., Roberts, C., Stevens, M., 2009. Substrate stiffness affects early differentiation events in embryonic stem cells. Eur. Cell. Mater. 18, 1–14. https://doi.org/10.22203/eCM.v018a01
Fargion, S., Mattioli, M., Ludovica Fracanzani, A., Sampietro, M., Tavazzi, D., Fociani, P., Taioli, E., Valenti, L., Fiorelli, G., 2001. Hyperferritinemia, iron overload, and multiple metabolic alterations identify patients at risk for nonalcoholic steatohepatitis. Am. J. Gastroenterol. 96, 2448–2455. https://doi.org/10.1111/j.1572-0241.2001.04052.x
Farra, R., Dapas, B., Grassi, M., Benedetti, F., Grassi, G., 2019. E2F1 as a molecular drug target in ovarian cancer. Expert Opin. Ther. Targets 23, 161–164. https://doi.org/10.1080/14728222.2019.1579797
Farshi, P., Deshmukh, R.R., Nwankwo, J.O., Arkwright, R.T., Cvek, B., Liu, J., Dou, Q.P., 2015. Deubiquitinases (DUBs) and DUB inhibitors: a patent review. Expert Opin. Ther. Pat. 25, 1191–1208. https://doi.org/10.1517/13543776.2015.1056737
Field-Smith, A., Morgan, G.J., Davies, F.E., 2006. Bortezomib (Velcade?) in the treatment of multiple myeloma. Ther. Clin. Risk Manag. 2, 271–279. https://doi.org/10.2147/tcrm.2006.2.3.271

Flory, P.J., 1953. Principles of polymer chemistry, The George Fisher Baker non-resident lectureship in chemistry at Cornell university. Cornell university press, Ithaca (N.Y.) London.

Foty, R., 2011. A Simple Hanging Drop Cell Culture Protocol for Generation of 3D Spheroids. J. Vis. Exp. 2720. https://doi.org/10.3791/2720

Gardi, C., Arezzini, B., Fortino, V., Comporti, M., 2002. Effect of free iron on collagen synthesis, cell proliferation and MMP-2 expression in rat hepatic stellate cells. Biochem. Pharmacol. 64, 1139–1145. https://doi.org/10.1016/s0006-2952(02)01257-1

George, D.K., Goldwurm, S., Macdonald, G.A., Cowley, L.L., Walker, N.I., Ward, P.J., Jazwinska, E.C., Powell, L.W., 1998. Increased hepatic iron concentration in nonalcoholic steatohepatitis is associated with increased fibrosis. Gastroenterology 114, 311–318. https://doi.org/10.1016/S0016-5085(98)70482-2

Gong, Z., Szczesny, S.E., Caliari, S.R., Charrier, E.E., Chaudhuri, O., Cao, X., Lin, Y., Mauck, R.L., Janmey, P.A., Burdick, J.A., Shenoy, V.B., 2018. Matching material and cellular timescales maximizes cell spreading on viscoelastic substrates. Proc. Natl. Acad. Sci. 115. https://doi.org/10.1073/pnas.1716620115

González-Domínguez, Á., Visiedo-García, F.M., Domínguez-Riscart, J., González-Domínguez, R., Mateos, R.M., Lechuga-Sancho, A.M., 2020. Iron Metabolism in Obesity and Metabolic Syndrome. Int. J. Mol. Sci. 21, 5529. https://doi.org/10.3390/ijms21155529

Grassi, M., Grassi, G., Lapasin, R., Colombo, I., 2006. Understanding Drug Release and Absorption Mechanisms: A Physical and Mathematical Approach. CRC Press. https://doi.org/10.1201/9781420004656

Hilton, C., Sabaratnam, R., Drakesmith, H., Karpe, F., 2023. Iron, glucose and fat metabolism and obesity: an intertwined relationship. Int. J. Obes. 47, 554–563. https://doi.org/10.1038/s41366-023-01299-0

Houglum, K., Bedossa, P., Chojkier, M., 1994. TGF-beta and collagen-alpha 1 (I) gene expression are increased in hepatic acinar zone 1 of rats with iron overload. Am. J. Physiol. 267, G908-913. https://doi.org/10.1152/ajpgi.1994.267.5.G908

Huebsch, N., Arany, P.R., Mao, A.S., Shvartsman, D., Ali, O.A., Bencherif, S.A., Rivera-Feliciano, J., Mooney, D.J., 2010. Harnessing traction-mediated manipulation of the cell/matrix interface to control stem-cell fate. Nat. Mater. 9, 518–526. https://doi.org/10.1038/nmat2732

Iredale, J.P., 2001. Hepatic Stellate Cell Behavior during Resolution of Liver Injury. Semin. Liver Dis. 21, 427–436. https://doi.org/10.1055/s-2001-17557

Iredale, J.P., Thompson, A., Henderson, N.C., 2013. Extracellular matrix degradation in liver fibrosis: Biochemistry and regulation. Biochim. Biophys. Acta BBA - Mol. Basis Dis. 1832, 876–883. https://doi.org/10.1016/j.bbadis.2012.11.002

Iuliano, L., Dalla, E., Picco, R., Mallavarapu, S., Minisini, M., Malavasi, E., Brancolini, C., 2022. Proteotoxic stress-induced apoptosis in cancer cells: understanding the susceptibility and enhancing the potency. Cell Death Discov. 8, 407. https://doi.org/10.1038/s41420-022-01202-2

Iwakiri, Y., 2014. Pathophysiology of Portal Hypertension. Clin. Liver Dis. 18, 281–291. https://doi.org/10.1016/j.cld.2013.12.001

Jeng, K.-S., Lu, S.-J., Wang, C.-H., Chang, C.-F., 2020. Liver Fibrosis and Inflammation under the Control of ERK2. Int. J. Mol. Sci. 21, 3796. https://doi.org/10.3390/ijms21113796

Jugé, L., Foley, P., Hatt, A., Yeung, J., Bilston, L.E., 2023. Ex vivo bovine liver nonlinear viscoelastic properties: MR elastography and rheological measurements. J. Mech. Behav. Biomed. Mater. 138, 105638. https://doi.org/10.1016/j.jmbbm.2022.105638

Khanam, A., Saleeb, P.G., Kottilil, S., 2021a. Pathophysiology and Treatment Options for Hepatic Fibrosis: Can It Be Completely Cured? Cells 10, 1097. https://doi.org/10.3390/cells10051097

Khanam, A., Saleeb, P.G., Kottilil, S., 2021b. Pathophysiology and Treatment Options for Hepatic Fibrosis: Can It Be Completely Cured? Cells 10, 1097. https://doi.org/10.3390/cells10051097

Khomich, O., Ivanov, A.V., Bartosch, B., 2019. Metabolic Hallmarks of Hepatic Stellate Cells in Liver Fibrosis. Cells 9, 24. https://doi.org/10.3390/cells9010024

Kisseleva, T., Cong, M., Paik, Y., Scholten, D., Jiang, C., Benner, C., Iwaisako, K., Moore-Morris, T., Scott, B., Tsukamoto, H., Evans, S.M., Dillmann, W., Glass, C.K., Brenner, D.A., 2012. Myofibroblasts revert to an inactive phenotype during regression of liver fibrosis. Proc. Natl. Acad. Sci. 109, 9448–9453. https://doi.org/10.1073/pnas.1201840109

Kleiner, D.E., Brunt, E.M., Van Natta, M., Behling, C., Contos, M.J., Cummings, O.W., Ferrell, L.D., Liu, Y.-C., Torbenson, M.S., Unalp-Arida, A., Yeh, M., McCullough, A.J., Sanyal, A.J., Nonalcoholic Steatohepatitis Clinical Research Network, 2005. Design and validation of a histological scoring system for nonalcoholic fatty liver disease. Hepatology 41, 1313–1321. https://doi.org/10.1002/hep.20701

Kobayashi, Y., Okamura, N., Tsukune, M., Fujie, M.G., Tanaka, M., 2020. Non-minimum phase viscoelastic properties of soft biological tissues. J. Mech. Behav. Biomed. Mater. 110, 103795. https://doi.org/10.1016/j.jmbbm.2020.103795

Kopač, T., Abrami, M., Grassi, M., Ručigaj, A., Krajnc, M., 2022. Polysaccharide-based hydrogels crosslink density equation: A rheological and LF-NMR study of polymer-polymer interactions. Carbohydr. Polym. 277, 118895. https://doi.org/10.1016/j.carbpol.2021.118895

Kostallari, E., Wei, B., Sicard, D., Li, J., Cooper, S.A., Gao, J., Dehankar, M., Li, Y., Cao, S., Yin, M., Tschumperlin, D.J., Shah, V.H., 2022. Stiffness is associated with hepatic stellate cell heterogeneity during liver fibrosis. Am. J. Physiol.-Gastrointest. Liver Physiol. 322, G234–G246. https://doi.org/10.1152/ajpgi.00254.2021

Kowdley, K.V., 2016. Iron Overload in Patients With Chronic Liver Disease. Gastroenterol. Hepatol. 12, 695–698.

Kowdley, K.V., Belt, P., Wilson, L.A., Yeh, M.M., Neuschwander-Tetri, B.A., Chalasani, N., Sanyal, A.J., Nelson, J.E., for the NASH Clinical Research Network., 2012. Serum ferritin is an independent predictor of histologic severity and advanced fibrosis in patients with nonalcoholic fatty liver disease. Hepatology 55, 77–85. https://doi.org/10.1002/hep.24706

Kumar, S., Duan, Q., Wu, R., Harris, E.N., Su, Q., 2021. Pathophysiological communication between hepatocytes and non-parenchymal cells in liver injury from NAFLD to liver fibrosis. Adv. Drug Deliv. Rev. 176, 113869. https://doi.org/10.1016/j.addr.2021.113869

Lan, Y., Wang, H., Weng, H., Xu, X., Yu, X., Tu, H., Gong, K., Yao, J., Ye, S., Shi, Y., Sheng, J., 2023. The burden of liver cirrhosis and underlying etiologies: results from the Global Burden of Disease Study 2019. Hepatol. Commun. 7, e0026–e0026. https://doi.org/10.1097/HC9.0000000000000026

Lapasin, R., Pricl, S., 1995. Rheology of Industrial Polysaccharides: Theory and Applications. Springer US, Boston, MA. https://doi.org/10.1007/978-1-4615-2185-3

Le, T.V., Phan-Thi, H.-T., Huynh-Thi, M.-X., Dang, T.M., Holterman, A.X.L., Grassi, G., Nguyen-Luu, T.-U., Truong, N.H., 2023. Autophagy Inhibitor Chloroquine Downmodulates Hepatic Stellate Cell Activation and Liver Damage in Bile-Duct-Ligated Mice. Cells 12, 1025. https://doi.org/10.3390/cells12071025

Lee, K.Y., Mooney, D.J., 2012. Alginate: Properties and biomedical applications. Prog. Polym. Sci. 37, 106–126. https://doi.org/10.1016/j.progpolymsci.2011.06.003
Levy, J.M.M., Towers, C.G., Thorburn, A., 2017. Targeting autophagy in cancer. Nat. Rev. Cancer 17, 528–542. https://doi.org/10.1038/nrc.2017.53
Li, Z., Dranoff, J.A., Chan, E.P., Uemura, M., Sévigny, J., Wells, R.G., 2007. Transforming growth factor-β and substrate stiffness regulate portal fibroblast activation in culture. Hepatology 46, 1246–1256. https://doi.org/10.1002/hep.21792
Liu, ShiZuo, Yao, S., Yang, H., Liu, ShuaiJie, Wang, Y., 2023. Autophagy: Regulator of cell death. Cell Death Dis. 14, 648. https://doi.org/10.1038/s41419-023-06154-8
Locke, G.A., Cheng, D., Witmer, M.R., Tamura, J.K., Haque, T., Carney, R.F., Rendina, A.R., Marcinkeviciene, J., 2008. Differential activation of recombinant human acetyl-CoA carboxylases 1 and 2 by citrate. Arch. Biochem. Biophys. 475, 72–79. https://doi.org/10.1016/j.abb.2008.04.011
Maddaloni, M., Farra, R., Dapas, B., Felluga, F., Benedetti, F., Berti, F., Drioli, S., Vidali, M., Cemazar, M., Kamensek, U., Brancolini, C., Murano, E., Maremonti, F., Grassi, M., Biasin, A., Rizzolio, F., Cavarzerani, E., Scaggiante, B., Bulla, R., Balduit, A., Ricci, G., Zito, G., Romano, F., Bonin, S., Azzalini, E., Baj, G., Tierno, D., Grassi, G., 2024. In Vitro and In Vivo Evaluation of the Effects of Drug 2c and Derivatives on Ovarian Cancer Cells. Pharmaceutics 16, 664. https://doi.org/10.3390/pharmaceutics16050664
Mann, H.B., Whitney, D.R., 1947. On a Test of Whether one of Two Random Variables is Stochastically Larger than the Other. Ann. Math. Stat. 18, 50–60. https://doi.org/10.1214/aoms/1177730491
Marcellin, P., Kutala, B.K., 2018. Liver diseases: A major, neglected global public health problem requiring urgent actions and large-scale screening. Liver Int. 38, 2–6. https://doi.org/10.1111/liv.13682
Mazza, G., Al-Akkad, W., Rombouts, K., 2017. Engineering in vitro models of hepatofibrogenesis. Adv. Drug Deliv. Rev. 121, 147–157. https://doi.org/10.1016/j.addr.2017.05.018
McKnight, P.E., Najab, J., 2010. Mann-Whitney U Test, in: Weiner, I.B., Craighead, W.E. (Eds.), The Corsini Encyclopedia of Psychology. Wiley. https://doi.org/10.1002/9780470479216.corpsy0524
Mehta, K.J., Coombes, J.D., Briones-Orta, M., Manka, P.P., Williams, R., Patel, V.B., Syn, W.-K., 2018. Iron Enhances Hepatic Fibrogenesis and Activates Transforming Growth Factor-β Signaling in Murine Hepatic Stellate Cells. Am. J. Med. Sci. 355, 183–190. https://doi.org/10.1016/j.amjms.2017.08.012
Mehta, K.J., Farnaud, S.J., Sharp, P.A., 2019. Iron and liver fibrosis: Mechanistic and clinical aspects. World J. Gastroenterol. 25, 521–538. https://doi.org/10.3748/wjg.v25.i5.521
Meier, J.A., Bokemeyer, A., Cordes, F., Fuhrmann, V., Schmidt, H., Hüsing-Kabar, A., Kabar, I., 2020. Serum levels of ferritin and transferrin serve as prognostic factors for mortality and survival in patients with end-stage liver disease: A propensity score-matched cohort study. United Eur. Gastroenterol. J. 8, 332–339. https://doi.org/10.1177/2050640619891283
Mevissen, T.E.T., Komander, D., 2017. Mechanisms of Deubiquitinase Specificity and Regulation. Annu. Rev. Biochem. 86, 159–192. https://doi.org/10.1146/annurev-biochem-061516-044916
Nanda, I., Schröder, S.K., Steinlein, C., Haaf, T., Buhl, E.M., Grimm, D.G., Weiskirchen, R., 2022. Rat Hepatic Stellate Cell Line CFSC-2G: Genetic Markers and Short Tandem Repeat Profile Useful for Cell Line Authentication. Cells 11, 2900. https://doi.org/10.3390/cells11182900
Nandi, D., Tahiliani, P., Kumar, A., Chandu, D., 2006. The ubiquitin-proteasome system. J. Biosci. 31, 137–155. https://doi.org/10.1007/BF02705243

Nevzorova, Y.A., Bangen, J.-M., Hu, W., Haas, U., Weiskirchen, R., Gassler, N., Huss, S., Tacke, F., Sicinski, P., Trautwein, C., Liedtke, C., 2012. Cyclin E1 controls proliferation of hepatic stellate cells and is essential for liver fibrogenesis in mice. Hepatol. Baltim. Md 56, 1140–1149. https://doi.org/10.1002/hep.25736

Nicolle, S., Vezin, P., Palierne, J.-F., 2010. A strain-hardening bi-power law for the nonlinear behaviour of biological soft tissues. J. Biomech. 43, 927–932. https://doi.org/10.1016/j.jbiomech.2009.11.002

Olsen, A.L., Bloomer, S.A., Chan, E.P., Gaça, M.D.A., Georges, P.C., Sackey, B., Uemura, M., Janmey, P.A., Wells, R.G., 2011. Hepatic stellate cells require a stiff environment for myofibroblastic differentiation. Am. J. Physiol.-Gastrointest. Liver Physiol. 301, G110–G118. https://doi.org/10.1152/ajpgi.00412.2010

Ortiz, C., Schierwagen, R., Schaefer, L., Klein, S., Trepat, X., Trebicka, J., 2021. Extracellular Matrix Remodeling in Chronic Liver Disease. Curr. Tissue Microenviron. Rep. 2, 41–52. https://doi.org/10.1007/s43152-021-00030-3

Park, J., Cho, J., Song, E.J., 2020. Ubiquitin-proteasome system (UPS) as a target for anticancer treatment. Arch. Pharm. Res. 43, 1144–1161. https://doi.org/10.1007/s12272-020-01281-8

Park, J.-S., Ma, H., Roh, Y.-S., 2021. Ubiquitin pathways regulate the pathogenesis of chronic liver disease. Biochem. Pharmacol. 193, 114764. https://doi.org/10.1016/j.bcp.2021.114764

Pei, Q., Yi, Q., Tang, L., 2023. Liver Fibrosis Resolution: From Molecular Mechanisms to Therapeutic Opportunities. Int. J. Mol. Sci. 24, 9671. https://doi.org/10.3390/ijms24119671

Pietrangelo, A., 2009. Iron in NASH, chronic liver diseases and HCC: How much iron is too much? J. Hepatol. 50, 249–251. https://doi.org/10.1016/j.jhep.2008.11.011

Promega, U.K., 2024. Autophagy LC3 HiBiT Reporter Assay System (https://www.promega.co.uk/products/cell-health-assays/autophagy/autophagy-assay/?catNum=GA2550).

Ramm, G.A., Crawford, D.H., Powell, L.W., Walker, N.I., Fletcher, L.M., Halliday, J.W., 1997. Hepatic stellate cell activation in genetic haemochromatosis. Lobular distribution, effect of increasing hepatic iron and response to phlebotomy. J. Hepatol. 26, 584–592. https://doi.org/10.1016/s0168-8278(97)80424-2

Ruddell, R.G., Hoang-Le, D., Barwood, J.M., Rutherford, P.S., Piva, T.J., Watters, D.J., Santambrogio, P., Arosio, P., Ramm, G.A., 2009. Ferritin functions as a proinflammatory cytokine via iron-independent protein kinase C zeta/nuclear factor kappaB-regulated signaling in rat hepatic stellate cells. Hepatol. Baltim. Md 49, 887–900. https://doi.org/10.1002/hep.22716

Ryaboshapkina, M., Hammar, M., 2017. Human hepatic gene expression signature of non-alcoholic fatty liver disease progression, a meta-analysis. Sci. Rep. 7, 12361. https://doi.org/10.1038/s41598-017-10930-w

Sacco, P., Baj, G., Asaro, F., Marsich, E., Donati, I., 2020. Substrate Dissipation Energy Regulates Cell Adhesion and Spreading. Adv. Funct. Mater. 30, 2001977. https://doi.org/10.1002/adfm.202001977

Santos, M., Moreira, R., 2007. Michael Acceptors as Cysteine Protease Inhibitors. Mini-Rev. Med. Chem. 7, 1040–1050. https://doi.org/10.2174/138955707782110105

Schurz, J., 1991. Rheology of polymer solutions of the network type. Prog. Polym. Sci. 16, 1–53. https://doi.org/10.1016/0079-6700(91)90006-7

Schwarzbauer, J.E., DeSimone, D.W., 2011. Fibronectins, Their Fibrillogenesis, and In Vivo Functions. Cold Spring Harb. Perspect. Biol. 3, a005041–a005041. https://doi.org/10.1101/cshperspect.a005041

Semmler, G., Yang, Z., Fritz, L., Köck, F., Hofer, B.S., Balcar, L., Hartl, L., Jachs, M., Stopfer, K., Schedlbauer, A., Neumayer, D., Maurer, J., Müllner-Bucsics, T., Simbrunner, B., Scheiner, B., Trauner, M., Mandorfer, M., Reiberger, T., Bauer, D.J.M., 2023. Dynamics in Liver Stiffness Measurements Predict Outcomes in Advanced Chronic Liver Disease. Gastroenterology 165, 1041–1052. https://doi.org/10.1053/j.gastro.2023.06.030

Shaid, S., Brandts, C.H., Serve, H., Dikic, I., 2013. Ubiquitination and selective autophagy. Cell Death Differ. 20, 21–30. https://doi.org/10.1038/cdd.2012.72

Sheka, A.C., Adeyi, O., Thompson, J., Hameed, B., Crawford, P.A., Ikramuddin, S., 2020. Nonalcoholic Steatohepatitis: A Review. JAMA 323, 1175. https://doi.org/10.1001/jama.2020.2298

Snyder, N.A., Silva, G.M., 2021. Deubiquitinating enzymes (DUBs): Regulation, homeostasis, and oxidative stress response. J. Biol. Chem. 297, 101077. https://doi.org/10.1016/j.jbc.2021.101077

Soldani, C., Scovassi, A.I., 2002. Poly(ADP-ribose) polymerase-1 cleavage during apoptosis: an update. APOPTOSIS 7, 321–328. https://doi.org/10.1023/A:1016119328968

Sorrentino, P., D'Angelo, S., Ferbo, U., Micheli, P., Bracigliano, A., Vecchione, R., 2009. Liver iron excess in patients with hepatocellular carcinoma developed on non-alcoholic steato-hepatitis. J. Hepatol. 50, 351–357. https://doi.org/10.1016/j.jhep.2008.09.011

Soskey, P.R., Winter, H.H., 1984. Large Step Shear Strain Experiments with Parallel-Disk Rotational Rheometers. J. Rheol. 28, 625–645. https://doi.org/10.1122/1.549770

Stroffolini, T., Sagnelli, E., Gaeta, G.B., Sagnelli, C., Andriulli, A., Brancaccio, G., Pirisi, M., Colloredo, G., Morisco, F., Furlan, C., Almasio, P.L., Almasio, P.L., Gaeta, G.B., Sagnelli, E., Stroffolini, T., Andriulli, A., Babudieri, S., Brancaccio, G., Cacopardo, B., Colloredo, G., Coppola, N., De Luca, M., Furlan, C., Licata, A., Morisco, F., Pirisi, M., Pisaturo, M., Rosina, F., Russello, M., Sagnelli, C., Santantonio, T., Smedile, A., 2017. Characteristics of liver cirrhosis in Italy: Evidence for a decreasing role of HCV aetiology. Eur. J. Intern. Med. 38, 68–72. https://doi.org/10.1016/j.ejim.2016.10.012

Taimr, P., 2003. Activated stellate cells express the TRAIL receptor-2/death receptor-5 and undergo TRAIL-mediated apoptosis. Hepatology 37, 87–95. https://doi.org/10.1053/jhep.2003.50002

Tanida, I., Ueno, T., Kominami, E., 2008. LC3 and Autophagy, in: Deretic, V. (Ed.), Autophagosome and Phagosome, Methods in Molecular Biology™. Humana Press, Totowa, NJ, pp. 77–88. https://doi.org/10.1007/978-1-59745-157-4_4

Tayler, M.C.D., Ward-Williams, J., Gladden, L.F., 2019. Ultralow-field nuclear magnetic resonance of liquids confined in ferromagnetic and paramagnetic materials. Appl. Phys. Lett. 115, 072409. https://doi.org/10.1063/1.5110658

Tildy, B.E., Rogers, D.F., 2015. Therapeutic Options for Hydrating Airway Mucus in Cystic Fibrosis. Pharmacology 95, 117–132. https://doi.org/10.1159/000377638

Troeger, J.S., Mederacke, I., Gwak, G., Dapito, D.H., Mu, X., Hsu, C.C., Pradere, J., Friedman, R.A., Schwabe, R.F., 2012. Deactivation of Hepatic Stellate Cells During Liver Fibrosis Resolution in Mice. Gastroenterology 143, 1073-1083.e22. https://doi.org/10.1053/j.gastro.2012.06.036

Van Grunsven, L.A., 2017. 3D in vitro models of liver fibrosis. Adv. Drug Deliv. Rev. 121, 133–146. https://doi.org/10.1016/j.addr.2017.07.004

Varca, A.C., Casalena, D., Chan, W.C., Hu, B., Magin, R.S., Roberts, R.M., Liu, X., Zhu, H., Seo, H.-S., Dhe-Paganon, S., Marto, J.A., Auld, D., Buhrlage, S.J., 2021. Identification and validation of selective deubiquitinase inhibitors. Cell Chem. Biol. 28, 1758-1771.e13. https://doi.org/10.1016/j.chembiol.2021.05.012

Weiskirchen, R., Weimer, J., Meurer, S.K., Kron, A., Seipel, B., Vater, I., Arnold, N., Siebert, R., Xu, L., Friedman, S.L., Bergmann, C., 2013. Genetic characteristics of the human hepatic stellate cell line LX-2. PloS One 8. https://doi.org/10.1371/journal.pone.0075692

Wertz, I.E., Murray, J.M., 2019. Structurally-defined deubiquitinase inhibitors provide opportunities to investigate disease mechanisms. Drug Discov. Today Technol. 31, 109–123. https://doi.org/10.1016/j.ddtec.2019.02.003

Wex, C., Stoll, A., Fröhlich, M., Arndt, S., Lippert, H., 2014. Mechanics of fresh, frozen-thawed and heated porcine liver tissue. Int. J. Hyperthermia 30, 271–283. https://doi.org/10.3109/02656736.2014.924161

Wilson, C.L., Murphy, L.B., Leslie, J., Kendrick, S., French, J., Fox, C.R., Sheerin, N.S., Fisher, A., Robinson, J.H., Tiniakos, D.G., Gray, D.A., Oakley, F., Mann, D.A., 2015. Ubiquitin C-terminal hydrolase 1: A novel functional marker for liver myofibroblasts and a therapeutic target in chronic liver disease. J. Hepatol. 63, 1421–1428. https://doi.org/10.1016/j.jhep.2015.07.034

Xu, L., Hui, A.Y., Albanis, E., Arthur, M.J., O'Byrne, S.M., Blaner, W.S., Mukherjee, P., Friedman, S.L., Eng, F.J., 2005. Human hepatic stellate cell lines, LX-1 and LX-2: new tools for analysis of hepatic fibrosis. Gut 54, 142–151. https://doi.org/10.1136/gut.2004.042127

Yan, Y., Zeng, J., Xing, L., Li, C., 2021. Extra- and Intra-Cellular Mechanisms of Hepatic Stellate Cell Activation. Biomedicines 9, 1014. https://doi.org/10.3390/biomedicines9081014

Yao, J., Dai, Y., Zhang, J., Zhang, X., Zheng, R., 2019. Association between Serum Ferritin Level and Nonalcoholic Fatty Liver Disease in a Non-Obese Chinese Population: a Cross-Sectional Study. Clin. Lab. 65. https://doi.org/10.7754/Clin.Lab.2019.181250

Ye, Y., Wang, H., Gao, J., Kostallari, E., 2022. Editorial: Chronic Liver Disease: New Targets and New Mechanisms. Front. Mol. Biosci. 9, 963630. https://doi.org/10.3389/fmolb.2022.963630

Yeung, T., Georges, P.C., Flanagan, L.A., Marg, B., Ortiz, M., Funaki, M., Zahir, N., Ming, W., Weaver, V., Janmey, P.A., 2005. Effects of substrate stiffness on cell morphology, cytoskeletal structure, and adhesion. Cell Motil. Cytoskeleton 60, 24–34. https://doi.org/10.1002/cm.20041

Yin, C., Evason, K.J., Asahina, K., Stainier, D.Y.R., 2013. Hepatic stellate cells in liver development, regeneration, and cancer. J. Clin. Invest. 123, 1902–1910. https://doi.org/10.1172/JCI66369

Younossi, Z.M., Koenig, A.B., Abdelatif, D., Fazel, Y., Henry, L., Wymer, M., 2016. Global epidemiology of nonalcoholic fatty liver disease—Meta-analytic assessment of prevalence, incidence, and outcomes. Hepatology 64, 73–84. https://doi.org/10.1002/hep.28431

Yu, H., Lim, K.P., Xiong, S., Tan, L.P., Shim, W., 2013. Functional Morphometric Analysis in Cellular Behaviors: Shape and Size Matter. Adv. Healthc. Mater. 2, 1188–1197. https://doi.org/10.1002/adhm.201300053

Yuan, X., Sun, Y., Cheng, Q., Hu, K., Ye, J., Zhao, Y., Wu, J., Shao, X., Fang, L., Ding, Y., Sun, X., Shi, X., Xue, B., 2020. Proteomic analysis to identify differentially expressed proteins between subjects with metabolic healthy obesity and non-alcoholic fatty liver disease. J. Proteomics 221, 103683. https://doi.org/10.1016/j.jprot.2020.103683

Zhang, C.-Y., Liu, S., Yang, M., 2023. Treatment of liver fibrosis: Past, current, and future. World J. Hepatol. 15, 755–774. https://doi.org/10.4254/wjh.v15.i6.755

Zhang, Y., Xu, N., Xu, J., Kong, B., Copple, B., Guo, G.L., Wang, L., 2014. E2F1 is a novel fibrogenic gene that regulates cholestatic liver fibrosis through the Egr-1/SHP/EID1 network. Hepatology 60, 919–930. https://doi.org/10.1002/hep.27121

Zhao, J., Bai, J., Peng, F., Qiu, C., Li, Y., Zhong, L., 2023. USP9X-mediated NRP1 deubiquitination promotes liver fibrosis by activating hepatic stellate cells. Cell Death Dis. 14, 40. https://doi.org/10.1038/s41419-022-05527-9

# Acknowledgements

Firstly, I want to express my sincere thanks to my supervisors Prof. Mario Grassi and Prof. Gabriele Grassi. They supported, suggested and encouraged me every day in these three years. And, moreover, they will continue! Thank you!

I would like to thank all the professionals that collaborate with our research group: Prof. Silvia Palmisano, Dott.ssa Michela Giuricin, Prof. Fabrizio Zanconati, Dott.ssa Deborah Bonazza, Prof. Fabio Benedetti, Prof. Fulvia Felluga, Prof. Sara Drioli and Prof. Flavio Rizzolio.

I thank a thousand of times Barbara, who supported and helped me in my biological experiments and results. I learned with her a lot of techniques and how to manage a laboratory and emergencies, too! You are a friendly shoulder you can always count on!

I want to thank Michela for her availability and Prof. Dario Voinovich for having always a wise advice for me.

For my Erasmus period in Aachen, I really thank Prof. Ralf Weiskirchen and his group that welcomed and guided me: Marinela, Paola, Sarah, Anastasia and Steffen. Thanks a lot for the stock of Lindt chocolate! In particular, thousand thanks to Steffen and Marinela, who supported (and also endured) me in my infinite German experiments.

I thank my lunch companions Eleonora, Federica and Solange for our recharging breaks. Eleonora, thanks also for our walks till the fountain of youth to fill the water bottles. These steps are essential to ease the heart from daily stresses.

I want to thank my first classmates in the study of rheology, Claudia, Eleonora and Giulia. Claudia introduced me to cell culture for my first time. I will always be grateful to you!

In this PhD research period, I was very honored to teach to my thesis students: Lorena, Laura, Federico and Maddalena. Thank for your dedication and company! Good luck for your future!

I thank my colleagues Caterina for our in-depth talks about our future programs, Salvatore for hosting me with Prof. Flavio Rizzolio in C.R.O. Aviano, Domenico for his kindness and Thanh for coming from Vietnam to stay with us for a period. Thanh, thanks for all the sweets and teas! I hope to come in Vietnam one day!

Now let’s get sentimental.

Thanks to all my friends, Iris, Enxhi, Beatrice, Valentina, Elena, Elena and to my hearth friends, “i trollini”: Letizia, Priscilla, Michela, Carlo, Frutt, Andre, Piove, Pippo, Lallo, Simone, Beppe, Luca. We are all round the world, but always together.

Thanks to all my relatives and my grandmothers Franca and Agnese, who constantly asked me for updates on my work. Thanks to my grandfathers and Teresa that help me every day from haven.

Thanks to Claudia, Marisa, Camilla and Angelo for our recharging chats and boardgames!

Thanks to Gabriella, Elvino and Erika for supporting me and for our Sunday lunches!

Mam and Dad, you are always by my side in all my choices, thank you, thank you, thank you! You are my strength!

Edi, my little big brother, one of the most enterprising men I know, I want to wish you all the best for your future. *Per aspera ad astra.*

Marco, amore mio, thanks for being my favorite adventure buddy and life companion! Thank you for being my number one fan and the ever-present supporter in the writing of this thesis! To our endless laughs and adventures!